Active Control of Rotating Stall in a Three-Stage Axial Compressor

by

Joel M. Haynes

GTL Report #218

June 1993

GAS TURBINE LABORATORY
MASSACHUSETTS INSTITUTE OF TECHNOLOGY
CAMBRIDGE, MASSACHUSETTS

Active Control of Rotating Stall in a Three-Stage Axial Compressor

by

Joel M. Haynes

GTL Report #218 June 1993

This work was supported by the U.S. Air Force Office of Scientific Research, Major Daniel Fant, technical monitor.

ACTIVE CONTROL OF ROTATING STALL IN A THREE-STAGE AXIAL COMPRESSOR

by

JOEL M. HAYNES

ABSTRACT

Stall inception in a three-stage axial compressor has been suppressed over a range of previously unstable operating points through the feedback of velocity perturbations to the inlet flow field. Perturbations were generated using 12 individually actuated guide vanes at the compressor inlet. The operating range was extended by 7.8% to a slope of 0.9 on the pressure rise characteristic. Over this range data describing the compressor's pressure rise and torque were collected.

Flow field measurements upstream of the compressor revealed the excitation of spatial harmonics in the annular flow field before stall inception. With or without feedback, a spatial mode was observed to grow into a stall cell without a discontinuity of amplitude or position. The decrease in the stall inception mass flow as a result of damping the critical spatial mode indicated the importance of spatial modes in the stall inception process in this compressor. Destabilization was originally caused by the first mode. After stabilizing an under-damped mode, the flow range was extended until the next sequential mode became unstable.

The independent behavior of the modes before stall inception is described by four versions of a small disturbance model of compressor dynamics adapted from that of Moore and Greitzer. The two more sophisticated versions are presented here for the first time. The models require a description of the compressor's geometry, knowledge of its pressure rise characteristic, and some versions require a lag parameter characterizing the pressure rise response lag. The response lag parameter which enabled the models to most accurately predict the open-loop compressor dynamics was consistent with published values. The open-loop modal dynamics were determined experimentally and could be accurately described by the dynamics represented in the simplest model. The open-loop dynamics were measured for the first three modes over a range of stable and formerly unstable operating points. The more elaborate models gave accurate predictions of the closed-loop compressor performance, and the most accurate one predicted the flow range extension with less than 1.5% error.

Acknowledgments

I am indebted to many for their support, instruction, guidance, and grace which has helped me complete this research project. Individually none of this would have been possible, and ultimately all of our own efforts come to nothing without the grace of another. Because of this I consider having had the opportunity to work together with so many skilled, intelligent, and dedicated people who are willing to help others a great blessing. I would like to thank those who made this thesis possible.

My advisor, Professor A. H. Epstein, has been dedicated to my completion of this project, and I thank him for his guidance, instructions, and advice which helped navigate me through my first research experience. I also am indebted to him for his foresight, design skills, and support which enabled me to accomplish so much. I also thank Professor E. M. Greitzer for his support, feedback, and simply the opportunity to work with him. By example, he has taught me much about what it means to ask good questions as a researcher and get to the heart of a matter.

In the lab I received valued assistance from many individuals. In particular I am deeply indebted to Jim Paduano for teaching me so many things about which I had known nothing beforehand. Jim's patience, knowledge, and support were invaluable towards helping me learn and accomplish so much in so little time. The compressor would never have operated as well as it did without the excellent work of Viktor Dubrowski, and I am also indebted to him for his ingenuity and experience in machining many things for this project. Besides this I enjoyed working with him and appreciate his concern for students. I also thank Jim Nash for his casting of the servo-controlled guide vanes, and Roy Andrews for his modifications to the rig. I thank Dave Devor for helping me through so many computer problems and Dave Stenberg for tackling the tedious problems associated with programming the A/D. Dr. Gerry Guenette is thanked for endowing me with some of his laboratory wisdom and software know-how which helped me avoid or learn from mistakes. I also thank Phil Lavrich for his helpful directions about using the compressor facility.

Besides these, I am especially indebted to fellow students and friends for their partnership in getting the compressor rig fully operational. I thank Isaac Lee for his tremendous help in assembling the SGV ring, setting up instrumentation, and helping me perform some of my experiments. I also thank John Ito for his patience and dedication in helping me conduct experiments - even over the 4th of July weekend. Robert Wickham too helped me conduct experiments, and he deserves much of the credit for getting the torque meter operational enabling me to obtain torque measurements.

Apart from dealing with hardware issues, I received immense guidance and understanding from many people which helped me deal with such a complicated problem. I thank all of those who attended the weekly active-control meetings and shared their insights with the rest of us. In particular I thank Jim Paduano who helped me grasp many of the concepts surrounding active control. I also thank Gavin Hendricks for teaching me many things about modeling a compressor and for helping me grow in my understanding of fluid mechanics. In addition to these, I thank Fred Newman, Dan Gysling, and Jon Simon from whom I learned many things either by talking informally or otherwise.

Several people deserve thanks for their support in preparing this thesis. Primarily, "Graphics Boy" John Ito made writing this thesis several orders of magnitude easier by his dedicated support and careful attention to detail in helping format text and draw and format many diagrams. His willingness to work even later than myself some nights was a tremendous encouragement. John's friendship and support were invaluable in the process of completing this thesis. I also thank Jim Paduano for his proof-reading of Chapters 3 to 5 and his help in preparing some of the figures in this thesis. Diana Park is also appreciated for her talented drawing skills in generating many of the detailed drawings. I would also like to thank Chris Van Schalkwyk for his help in completing this project, especially for his proof-reading of Chapters 3 to 5.

I am especially thankful to those who helped me survive life at MIT. Thanks be to God! who grants us a refreshing, satisfying, exciting, surprising, and longsuffering life through the knowledge of Jesus Christ and through His powerful working by the Holy Spirit. You really are awesome as far as I can tell from even what little bit I know of you at this time. Thanks for being there to deal with my failures and enabling me to be free in an environment that is so high-pressure. I also must thank my parents, Paul and Carolyn Haynes, for their encouragement and support throughout my life and even while I am far away. I want to thank my wonderful housemates, Andrew, Frank, Rob, Dave O, Dave Y, and Alan, who have cooked dinner for me and have bared with me especially during the last few weeks of writing this thesis. I also want to thank Jim, Randall, and Daniel for their encouragement. Much thanks goes to Jeff Grandy and Dave Bakhash who went running with me to keep me healthy even when things were busy. I also want to thank all the people in the GTL who have make working here a positive experience.

This project was supported by the U.S. Air Force Office of Scientific Research (contract #AFOSR-90-0059C). Major Daniel Fant is thanked for granting support to this project.

Table of Contents

Abstract . . . 2
Acknowledgments . . . 3
List of Figures . . . 8
List of Tables . . . 13
Nomenclature . . . 14

1 **Introduction** . . . 18

1.1 Compressor Instabilities . . . 18
1.2 Stall Inception . . . 23
1.3 Stall Inception Modeling . . . 25
1.4 Rotating Stall Prevention . . . 27
1.5 Purpose & Scope of Thesis . . . 30

2 **Experimental Setup** . . . 32

2.1 Introduction . . . 32
2.2 Low Speed Three-Stage Compressor with IGV Actuators . . . 33
2.3 Compressor Instrumentation . . . 41
2.3.1 Hot-Wire Probes & Anemometers . . . 41
2.3.2 Scanivalve & Pressure Probes . . . 41
2.3.3 Torque Sensor . . . 43
2.3.4 Tachometer . . . 43
2.3.5 Servo Motors . . . 43
2.4 Data Filtering, Acquisition, & Processing . . . 44
2.4.1 Low Pass Filters . . . 44
2.4.2 Metrabyte A/D . . . 44
2.4.3 Analogic A/D . . . 44
2.4.4 A/D for VAXStation II . . . 45
2.4.5 Computer Hardware . . . 45
2.5.6 Software Considerations . . . 45
2.5.7 Servo Motor Motion Control . . . 46
2.5 Experimental Technique . . . 46
2.5.1 Hot-Wire Calibration . . . 46
2.5.2 Flow Coefficient Evaluation . . . 46
2.6 Measurement of State Variables and Error Analysis . . . 48
2.6.1 Time Averaged Measurements . . . 48
2.6.2 Real Time Measurements . . . 51
2.7 A Systems Description of the Actively Controlled Compressor . . . 52

3 **Modeling Higher Spatial Mode Dynamics in a Compressor with Active Modal Stabilization** 55

3.1 Compressor Model 55
3.1.1 Assumptions 55
3.1.2 Notation 61
3.1.2.1 Nondimensionalization 61
3.1.2.2 Independent Variables 61
3.1.2.3 Dependent Variables 62
3.1.2.4 Parameters Characterizing the Compressor 62
3.1.2.5 Parameter Perturbations 63
3.1.2.6 Spatial Fourier Coefficients (SFC's) 64
3.1.3 Compressor Model Equations and their Solution, Model 1 64
3.1.4 Evaluation of Parameters 67
3.1.5 Discretization 70

3.2 Additional Dynamic Considerations 73
3.2.1 Time Lags in the Feedback Path 73
3.2.2 Zero Order Hold (ZOH) Feedback 77
3.2.3 Closed Loop Actuator Dynamics 77

3.3 Modeling Unsteady Losses in the Compressor, Model 2 79
3.3.1 Model Development 79
3.3.2 Discussion and Evaluation of Parameters, Model 2 82

3.4 Modeling Compressor Flow Deviation & Blockage Effects, Model 3 . . . 83
3.4.1 Model Development 83
3.4.2 Discussion and Evaluation of Parameters, Model 3 88

3.5 Modeling Lag in Pressure Rise Due to Changes in Flow Angle, Model 4 . . 90
3.5.1 Model Development 90
3.5.2 Discussion and Evaluation of Parameters, Model 4 94

4 **Open-Loop Compressor Characterization** 98

4.1 Characterization of Open-Loop Spatial Mode Dynamics 98
4.1.1 Identification Methodology 98
4.1.1.1 Spatial Mode Transfer Function Identification 99
4.1.1.2 Parametric Estimation of Spatial Mode Transfer Functions 100
4.1.2 Identification Results 109

4.2 Prediction of Open-Loop Dynamics 114
4.2.1 Model 1 114
4.2.2 Model 2 - Unsteady Losses 116
4.2.3 Model 3 - Unsteady Losses & Other Flow Response Lags . . . 119
4.2.4 Model 4 - Flow Response Lags to $\delta\phi$ and $\delta\gamma$ 119

5 **Active Stabilization of a Three-Stage Low Speed Compressor** 131

5.1 Stall Inception if the Uncontrolled Compressor 134
5.1.1 Axial Velocity Flow Field at Stall Inception 135
5.1.2 Power Spectrum Density (PSD) of the Pre-Stall Flow Field . . . 139
5.1.2.1 Upstream PSD Measurements 140
5.1.2.2 Variations in Mode Strength within the Compressor . . 142
5.1.3 IGV Restaggering 144

5.2 Experimental Optimization of the Closed-Loop Controller 145
5.2.1 Controller Parameter Estimates 147
5.2.2 Experimental Optimization of Gain 150
5.2.3 Experimental Optimization of Phase 150
5.2.4 Limitations on Stabilization 155

5.3 Optimal Closed-Loop Compressor Performance 156

5.4 Modeling Closed-Loop Compressor Performance 163

6 **Summary, Conclusions, and Recommendations** 179

6.1 Summary 179

6.2 Conclusions 180

6.3 Recommendations for Future Work 181

References 183

Appendix A **Data Collection Log** 186

Appendix B **Additional Torque, Modal Dynamics, and Flow Field Data** . . 188

Appendix C **Estimating the Ideal Pressure Rise Response to Flow Perturbations** 214

List of Figures

1.1 Compressor Surge 20
1.2 Stall Cell in Compressor 21
1.3 Compressor Characteristic 22
1.4 Fully Developed Stall Cell in Three-Stage Axial Compressor [5] 22
1.5 Conceptual Increase in Compressor's Stable Operating Range from A to A' due to Active Control 24
1.6 Progression of Short Length Scale Stall Inception 26
1.7 Modal Disturbances 28
1.8 Single-Stage Compressor Speedline 29

2.1 Side View Schematic of Three-Stage Compressor Test Facility 34
2.2 Compressor Blading Specifications 35
2.3 Twelve Motors Mounted on IGV Ring 38
2.4 Three-Stage Axial Compressor with New IGV Ring 39
2.5 Servo-Controlled Guide Vane Design 40
2.6 Layout of Compressor Instrumentation 42
2.7 Closed-Loop Control of DC Servo Motors 47
2.8 Pressure Data Acquisition Equipment 50
2.9 Closed-Loop Control Feedback Path 54

3.1 Stations in a 2-D Axial Compressor Model 56
3.2 Parabolic Fit to Pumping Characteristic 69
3.3 Compressor Slope Calculated from Extended and Unextended Characteristics . 69
3.4 ψ vs ϕ for $-1.9° < \gamma < 23.1°$ in 5° Intervals 71
3.5 $\partial\psi/\partial\gamma$ Calculated from Extended and Unextended Characteristics 71
3.6 Model of Closed-Loop Dynamics 74
3.7 Servo Motor Closed-Loop Transfer Function 78
3.8 SGV Actuator Model Compared with Measured Transfer Function 78
3.9 Plot of ψ, ψ_T, and $L_{u,ss}$ 84
3.10 Plot of Parameters $\partial L_{uR,ss} / \partial\phi$, $\partial L_{uS,ss} / \partial\phi$, and $\partial\psi_T / \partial\phi$ 84
3.11 Plot of ψ, ψ_T, $L_{d,ss}$, and $L_{u,ss}$ 89
3.12 Plot of Parameters $\partial L_{uR,ss} / \partial\phi$, $\partial L_{uS,ss} / \partial\phi$, and $\partial\psi_i / \partial\phi$ 89
3.13 Effect of SGV Unsteadiness on Flow into First Blade Row 91

3.14 Plot of Parameters $\partial\psi_i / \partial\phi$, $\partial\psi / \partial\phi$, and $\partial L_{SGV,ss} / \partial\phi$ 95

4.1 Estimate of Compressor Transfer Function for Mode 1 at $\phi = .49$ 101
4.2 Estimate of Compressor Transfer Function for Mode 2 at $\phi = .49$ 102
4.3 Estimate of Compressor Transfer Function for Mode 3 at $\phi = .49$ 103
4.4 Estimate of Compressor Transfer Function for Mode 1 at $\phi = .45$ 107
4.5 Frequency Response Associated with the Poles and Zeros of Model 2 108
that are Not Represented in Model 1 ($\phi = .46$ in this case)
4.6 Stall Cell Growth Rate σ_n with a Parabolic Curve Fit 110
4.7 Stall Cell Frequency ω_n with Linear Fit 110
4.8 Poles and Zeros of the First Spatial Mode 112
4.9 Poles and Zeros of the Second Spatial Mode 112
4.10 Poles and Zeros of the Third Spatial Mode 113
4.11 1st, 2nd, and 3rd Mode Stability Predicted by Model 1 115
Compared with Experimental Data
4.12 1st, 2nd, and 3rd Mode Disturbance Frequency Predicted by Model 1 115
Compared with Experimental Data
4.13 1st, 2nd, and 3rd Mode Stability Predicted by Model 2 117
Compared with Experimental Data
4.14 1st, 2nd, and 3rd Mode Disturbance Frequency Predicted by Model 2 117
Compared with Experimental Data
4.15 1st, 2nd, and 3rd Mode Stability Predicted by Model 3 120
Compared with Experimental Data
4.16 1st, 2nd, and 3rd Mode Disturbance Frequency Predicted by Model 3 120
Compared with Experimental Data
4.17 Poles and Zeros of 1st, 2nd, and 3rd Spatial Modes 122-127
Predicted by Models 1, 2, and 3

5.1 Stall Inception Flow Field around Compressor Annulus at Midspan 136
Measured Upstream of the IGV's when $\overline{\phi} = .46$
5.2 Magnitudes and Phases of the First Three Spatial Fourier Coefficients 137
Calculated from the Stall Inception Flow Field at Midspan
5.3 PSD of the 1st, 2nd, and 3rd Modes Measured Upstream of the IGV's 141
during Operation near ϕ_{stall} in the Absence of Active Control
5.4 Axial Variation in Mode Strength Measured at 3 Radial Positions 143
5.5 Radially Averaged 1st Mode Strength Upstream and Inside the Compressor . .143
5.6 Radial Variation in 1st Mode Strength 143
Measured Downstream of the Second Rotor
5.7 Unstalled Steady-State Compressor Performance 146
for SGV Stagger Angles Ranging from -16.9° to 68.1° in 5° Intervals

5.8 Constant R_1 Root Locus Representing 1st Mode Compressor Dynamics . . . 148
at 2% above ϕ_{stall} for Variable Closed-Loop Phase β_1 (R_1 = 5.0)

5.9 Constant R_2 Root Locus Representing 2nd Mode Compressor Dynamics . . . 149
at 2% above ϕ_{stall} for Variable Closed-Loop Phase β_2 (R_2 = 3.1)

5.10 Constant R_3 Root Locus Representing 3rd Mode Compressor Dynamics . . . 149
at 2% above ϕ_{stall} for Variable Closed-Loop Phase β_3 (R_3 = 1.1)

5.11 Variation in Mode Strength near Stall with First Mode Gain 151
during 1st and 2nd Mode Active Control

5.12 Variation in Mode Strength near Stall with Second Mode Gain 151
during 1st and 2nd Mode Active Control

5.13 Variation in Mode Strength near Stall with Third Mode Gain 152
during 1st, 2nd, and 3rd Mode Active Control

5.14 Experimental Determination of Optimal First Mode Phase $\beta_{1\,opt}$ 153

5.15 Experimental Determination of Optimal Second Mode Phase $\beta_{2\,opt}$ 153

5.16 Experimental Determination of Optimal Second Mode Phase $\beta_{3\,opt}$ 154

5.17 Compressor Speedline with Extended Flow Range due to Active Control . . . 157
Compared with Zeroth Mode Restagger of SGV's by 5°

5.18 Stall Inception Flow Field around Compressor Annulus at Midspan during . . 158
1st Mode Control Measured Upstream of the IGV's when $\overline{\phi}$ = .45

5.19 Magnitudes and Phases of the First Three Spatial Fourier Coefficients 159
Calculated from the Stall Inception Flow Field at Midspan during
1st Mode Control

5.20 Stall Inception Flow Field around Compressor Annulus during Optimal . . . 161
1st and 2nd Mode Control Measured Upstream of the IGV's when $\overline{\phi}$ = .43

5.21 Magnitudes and Phases of the First Three Spatial Fourier Coefficients 162
Calculated from the Stall Inception Flow Field at Midspan
during 1st and 2nd Mode Control

5.22 Stall Inception Flow Field around Compressor Annulus during Optimal 1st, . .164
2nd, and 3rd Mode Control Measured Upstream of the IGV's when $\overline{\phi}$ = .43

5.23 Magnitudes and Phases of the First Three Spatial Fourier Coefficients 165
Calculated from the Stall Inception Flow Field at Midspan
during 1st, 2nd, and 3rd Mode Control

5.24 Comparison of Model 1 Prediction and Experimental Measurement of $\phi_{1\,neut}$. 168
for Mode 1 during Active Control with Reduced 1st Mode Gain, R_1 = 2.5

5.25 Comparison of Model 1 Prediction and Experimental Measurement of $\phi_{2\,neut}$. 168
for Mode 2 during Active Control with Reduced 2nd Mode Gain, R_2 = 1.0

5.26 Comparison of Model 2 Prediction and Experimental Measurement of $\phi_{1\,neut}$. 168
for Mode 1 during Active Control with Reduced 1st Mode Gain, R_1 = 2.5

5.27 Comparison of Model 2 Prediction and Experimental Measurement of $\phi_{2\,neut}$. 169
for Mode 2 during Active Control with Reduced 2nd Mode Gain, R_2 = 1.0

5.28 Comparison of Model 3 Prediction and Experimental Measurement of $\phi_{1\,neut}$. 170
for Mode 1 during Active Control with Reduced 1st Mode Gain, $R_1 = 2.5$
5.29 Comparison of Model 3 Prediction and Experimental Measurement of $\phi_{2\,neut}$. 170
for Mode 2 during Active Control with Reduced 2nd Mode Gain, $R_2 = 1.0$
5.30 Comparison of Model 4 Prediction and Experimental Measurement of $\phi_{1\,neut}$. 171
for Mode 1 during Active Control with Reduced 1st Mode Gain, $R_1 = 2.5$
5.31 Comparison of Model 4 Prediction and Experimental Measurement of $\phi_{2\,neut}$. 171
for Mode 2 during Active Control with Reduced 2nd Mode Gain, $R_2 = 1.0$
5.32 Comparison of Model Predictions of $\phi_{1\,neut}$ with Experimental 172
Measurements of ϕ_{neut}
5.33 Comparison of Model Predictions of $\phi_{2\,neut}$ with Experimental 173
Measurements of ϕ_{neut}
5.34 Comparison of Model Predictions of $\phi_{3\,neut}$ with Experimental 174
Measurements of ϕ_{neut}
5.35 Flow Coefficient at Neutral Stability Predicted by Model 1 175
for Modes 1, 2, and 3 using Optimal Closed-Loop Phase for Values of Gain
Incremented from $R_n = 0$ to the Maximum Stable Value
5.36 Flow Coefficient at Neutral Stability Predicted by Model 2 176
for Modes 1, 2, and 3 using Optimal Closed-Loop Phase for Values of Gain
Incremented from $R_n = 0$ to the Maximum Stable Value
5.37 Flow Coefficient at Neutral Stability Predicted by Model 3 177
for Modes 1, 2, and 3 using Optimal Closed-Loop Phase for Values of Gain
Incremented from $R_n = 0$ to the Maximum Stable Value
5.38 Flow Coefficient at Neutral Stability Predicted by Model 4 178
for Modes 1, 2, and 3 using Optimal Closed-Loop Phase for Values of Gain
Incremented from $R_n = 0$ to the Maximum Stable Value

B.1 Compressor Torque Characteristic for SGV Stagger Angles 189
Ranging from -1.9° to 23.1° in 5° Intervals
B.2 Compressor Isentropic Pressure Rise Characteristic, Calculated from Torque . 189
Characteristic, for SGV Angles Ranging from -1.9° to 23.1° in 5° Intervals
B.3 Estimate of Compressor Transfer Function for Mode 1 at $\phi = .49$ 190
B.4 Estimate of Compressor Transfer Function for Mode 1 at $\phi = .47$ 191
B.5 Estimate of Compressor Transfer Function for Mode 1 at $\phi = .45$ 192
B.6 Estimate of Compressor Transfer Function for Mode 1 at $\phi = .43$ 193
B.7 Estimate of Compressor Transfer Function for Mode 2 at $\phi = .49$ 194
B.8 Estimate of Compressor Transfer Function for Mode 2 at $\phi = .47$ 195
B.9 Estimate of Compressor Transfer Function for Mode 2 at $\phi = .45$ 196
B.10 Estimate of Compressor Transfer Function for Mode 2 at $\phi = .43$ 197
B.11 Estimate of Compressor Transfer Function for Mode 3 at $\phi = .49$ 198

B.12 Estimate of Compressor Transfer Function for Mode 3 at $\phi = .47$ 199

B.13 Estimate of Compressor Transfer Function for Mode 3 at $\phi = .45$ 200

B.14 Estimate of Compressor Transfer Function for Mode 3 at $\phi = .43$ 201

B.15 Stall Inception Flow Field around Compressor Annulus at 20% Span 202
Measured Upstream of the IGV's when $\overline{\phi} = .46$

B.16 Magnitudes and Phases of the First Three Spatial Fourier Coefficients 203
Calculated from the Stall Inception Flow Field at 20% Span

B.17 Stall Inception Flow Field around Compressor Annulus at 50% Span 204
Measured Upstream of the IGV's when $\overline{\phi} = .46$

B.18 Magnitudes and Phases of the First Three Spatial Fourier Coefficients 205
Calculated from the Stall Inception Flow Field at 50% Span

B.19 Stall Inception Flow Field around Compressor Annulus at 80% Span 206
Measured Upstream of the IGV's when $\overline{\phi} = .46$

B.20 Magnitudes and Phases of the First Three Spatial Fourier Coefficients 207
Calculated from the Stall Inception Flow Field at 80% Span

B.21 Stall Inception Flow Field around Compressor Annulus at 20% Span 208
during Optimal 1st and 2nd Mode Control
Measured Upstream of the IGV's when $\overline{\phi} = .43$

B.22 Magnitudes and Phases of the First Three Spatial Fourier Coefficients 209
Calculated from the Stall Inception Flow Field at 20% Span
during Optimal 1st and 2nd Mode Control

B.23 Stall Inception Flow Field around Compressor Annulus at 50% Span 210
during Optimal 1st and 2nd Mode Control
Measured Upstream of the IGV's when $\overline{\phi} = .43$

B.24 Magnitudes and Phases of the First Three Spatial Fourier Coefficients 211
Calculated from the Stall Inception Flow Field at 50% Span
during Optimal 1st and 2nd Mode Control

B.25 Stall Inception Flow Field around Compressor Annulus at 80% Span 212
during Optimal 1st and 2nd Mode Control
Measured Upstream of the IGV's when $\overline{\phi} = .43$

B.26 Magnitudes and Phases of the First Three Spatial Fourier Coefficients 213
Calculated from the Stall Inception Flow Field at 80% Span
during Optimal 1st and 2nd Mode Control

C.1 Rotor Velocity Triangle 217

List of Tables

2.1 MIT Three-Stage Axial Compressor Design Parameters 36
3.1 Parameter Values & Expressions which Characterize the High Reaction Build of the MIT Three-Stage Axial Compressor and were Used in the Compressor Models 97
4.1a First Mode Parameter Identification Data 128
4.1b Second Mode Parameter Identification Data 129
4.1c Third Mode Parameter Identification Data 130
A.1 Data Collection Log 187

Nomenclature

Symbols

$A(s)$	actuator transfer function (3.30)
A_0	hot-wire calibration constant (2.1)
A_1	hot-wire calibration constant (2.1)
$b_{r,n}$, $b_{i,n}$, $g_{i,n}$	control power parameters for the n^{th} mode (3.21)
b_R	nondimensional rotor blade chord (3.3)
b_S	nondimensional stator blade chord (3.4)
b_{SGV}	nondimensional servo guide vane blade chord (3.5)
C_x	axial velocity (2.1; Appendix C)
$D(s)$	feedback time lag transfer function (3.26)
E	anemometer output voltage (2.1)
$G_n(s)$	compressor transfer function (3.23)
i	$\sqrt{-1}$
L_{dR}	pressure loss across the rotors due to deviation and blockage (3.43)
L_{dS}	pressure loss across the stators due to deviation and blockage (3.43)
$L_{d,ss}$	steady-state pressure loss across the compressor from deviation and blockage (3.43)
L_{SGV}	pressure loss across the compressor associated with changes in $\delta\gamma$ (3.56)
$L_{SGV,ss}$	steady-state pressure loss across the compressor (3.56)
L_{uR}	pressure loss across the rotors due to viscous losses (3.32)
L_{uS}	pressure loss across the stators due to viscous losses (3.32)

$L_{u,ss}$	steady-state pressure loss across the compressor from viscous losses (3.32)
m	hot-wire calibration constant (2.1)
n	mode number
P_t	total pressure (Section 3.1.2.3)
P_s	static pressure (Section 3.1.2.3)
R	mean radius of the compressor (Section 3.1.2.1)
R_n	controller feedback gain (6.1; Figure 3.6)
Re	Reynolds number based on (2.2)
s	Laplace transform variable
t	time
$\bar{t}$	nondimensional time (Section 3.1.2.2)
U	mean rotor blade velocity (Section 3.1.2.1)
$\tilde{u}_{c,n}$	commanded SGV deflection for the n^{th} spatial mode (Figure 3.6)
V	flow speed (2.1)
$\vec{V}$	flow velocity vector (Appendix C)
v	tangential velocity component (Appendix C)
$\tilde{y}_n$	measured axial velocity disturbance for the n^{th} mode (Figure 3.6)
$\hat{Z}$	closed-loop control parameters vector (6.3)
ZOH(s)	zero order hold transfer function (3.29)
z	z-transform variable

Greek symbols

α	blade exit metal angle (Figure 2.2; Table 2.1)
β_n	controller feedback phase (6.1; Figure 3.6)
γ	SGV stagger angle (Section 2.6.2, 3.1.2.3)
$\bar{\gamma}$	nominal stagger angle of SGV blades (3.5)
γ_R	rotor blade stagger angle (Table 2.1)
γ_S	stator blade stagger angle (Table 2.1)

$\tilde{\gamma}$	n^{th} spatial Fourier coefficient of $\delta\gamma$
ζ	damping coefficient for actuator response (3.30)
η	nondimensional axial position (3.1.2.2)
η_{HW}	nondimensional axial location of hot-wires (Section 3.1.2.4)
$\hat{\Theta}_n$	open-loop dynamics parameter vector (4.6)
θ	angular position in radians (Section 3.1.2.2)
κ	leading edge metal angle (Figure 2.2, Table 2.1)
λ	rotor fluid inertia (3.3)
μ	total fluid inertia in the compressor (3.6)
μ_C	compressor fluid inertia (3.4)
μ_{SGV}	servo guide vane fluid inertia (3.5)
ρ	air density (Section 3.1.2.1)
σ_n	growth rate of mode n (3.21)
T	nondimensional torque coefficient (2.4; Section 2.6.1)
τ	nondimensional time delay
Φ	local flow potential (Section 3.1.2.3)
ϕ	axial flow coefficient (Section 2.6.1)
$\overline{\phi}$	annulus averaged axial flow coefficient
$\tilde{\phi}_n$	n^{th} spatial Fourier coefficient of $\delta\phi$
$\delta\phi$	nondimensional flow disturbance (Section 2.6.2)
ψ	steady-state total-to-static pressure rise coefficient (Section 2.6.1, 3.1.2.4)
ψ_T	steady-state isentropic total-to-static pressure rise coefficient (3.1)
ψ_i	steady-state total-to-static pressure rise coefficient (3.2)
ω	rate of rotor rotation (Section 2.6.1)
ω_n	rate of rotation of mode n (3.21)
ω_N	natural frequency of actuators (3.30)
ω_{RS}	rate of stall cell rotation (Section 1.1)

Operators, superscripts, and subscripts

$\delta(\cdot)$	small perturbation of the argument
$(\tilde{\ })$	spatial Fourier coefficient
$(\dot{\ })$	derivative with respect to nondimensionalized time, τ
$(\cdot)_n$	n^{th} mode version of the argument
$(\cdot)^*$	complex conjugate
$(\cdot)_r$	real part of argument
$(\cdot)_i$	imaginary part of argument
$\lvert \cdot \rvert$	absolute value
$\angle(\cdot)$	phase angle (argument) of complex number
$\mathrm{Re}\{ \cdot \}$	real part
$\mathrm{Im}\{ \cdot \}$	imaginary part
Σ	summation

Acronyms

A/D	analog to digital
DFT	discrete Fourier transform
ID	identification
IDFT	inverse discrete Fourier transform
IGV	inlet guide vane
IV	instrumental variable
PID	proportional-integral-derivative
RIV	refined instrumental variable
SFC	spatial Fourier coefficient
SGV	servo-controlled guide vane

CHAPTER 1

Introduction

Increasing the range of operating conditions over which a compressor can maintain stable airflow will help engines that utilize compressors run safely over a wider range of operating conditions and could improve their performance at formerly inefficient operating points. To make this physically realizable, the flow phenomena which cause airflow instabilities when the compressor is supposed to produce a high pressure rise under low air flow conditions need to be dampened so that stability can be maintained. This thesis describes the research that was conducted to stabilize of one type of airflow instability and extend the range of operating conditions that are stable.

1.1 Compressor Instabilities

An understanding of the fluid dynamic behavior of a compressor is needed in order to guarantee its successful performance in an engine and to better guide the design process. Already in 1941 at the time of the first gas turbine powered aircraft it was recognized that a compressor can exhibit instabilities in the air flow during conditions of high pressure rise and low air flow. These instabilities are a topic of current interest because compressor stages are being designed to perform close to the upper limits of possible pressure rise. Emmons [1] was the first to identify rotating stall as an instability distinguishable from compressor surge. Although these instabilities are often coupled, they will be described separately, and although they are common to both axial and centrifugal compressors, only axial compressors will be considered in this thesis.

Surge is an axisymmetric time-varying flow oscillation in a compression system. During compressor surge pressure builds up in the plenum chamber while air flows

through the compressor in a spatially uniform fashion around the annulus, Figure 1.1. The air decelerates just before plenum pressure reaches its peak. During the subsequent "blow down" of the plenum, the air may actually reverse direction and flow out the inlet of the compressor. The frequency of these oscillations is at least an order of magnitude lower than the rotating stall frequency. Surge is hazardous because it can overstress the casing and compressor blades [2], strain the blades so that the rotating blades (rotors) collide with the stationary blades (stators), or blow out the flame in the combustor. In this research, the compression system was designed with a small plenum volume to compressor duct volume ratio, i.e. a low B parameter, to prevent surge from developing and to facilitate the study of rotating stall phenomena. However, it should be noted that active and passive suppression of surge has already been demonstrated [3,4]. So conceivably, in an engine, a surge suppression system could be implemented while stabilization of rotating stall was pursued independently.

Rotating stall is a localized disturbance in the compressor flow field that propagates around the annulus at some fraction of the rotor's rotational speed. When the flow pattern of the stall is fully developed, its shape changes very little with time although it continues to rotate around the annulus. Therefore, it introduces no net fluctuation in the compressor mass flow but rather a continuous shifting of the flow pattern at a rotational rate ω_{RS}. High response measurements of axial velocity by Lavrich [5], Figure 1.2, reveal the shape of the fully developed stall cell in the compressor being used in this research at an average $\phi = 0.183$. Below the transition point where the fully developed stall cell first forms, $\phi = 0.46$, the stall cell's rotational frequency is 46% of the rotor frequency. Rotating stall is hazardous because it stresses the compressor blading, greatly decreases compressor efficiency, can cause critical temperatures in the turbine and compressor, can induce surge, and can only be corrected, if at all, by greatly increasing the mass flow and powering down the compressor. Figure 1.3, illustrating the annulus averaged pressure rise and mass flow, is used to

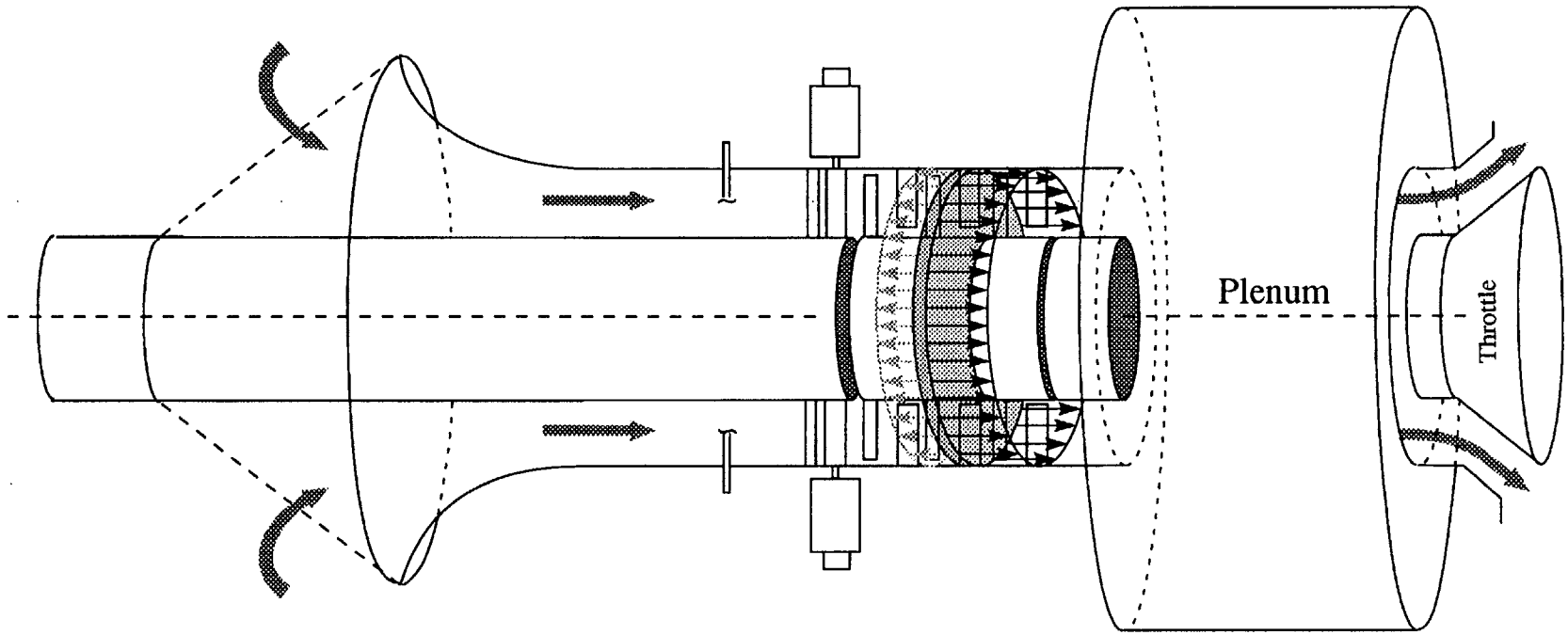

Figure 1.1: Compressor Surge

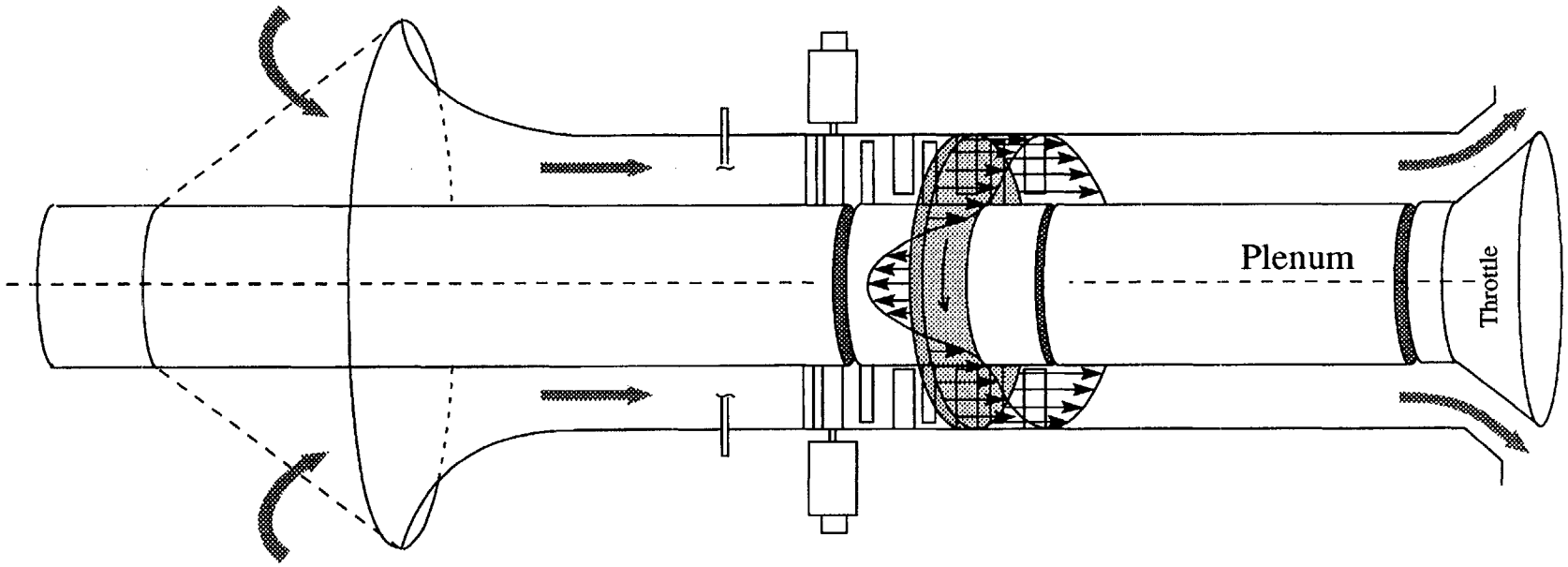

Figure 1.2: Stall Cell in Compressor

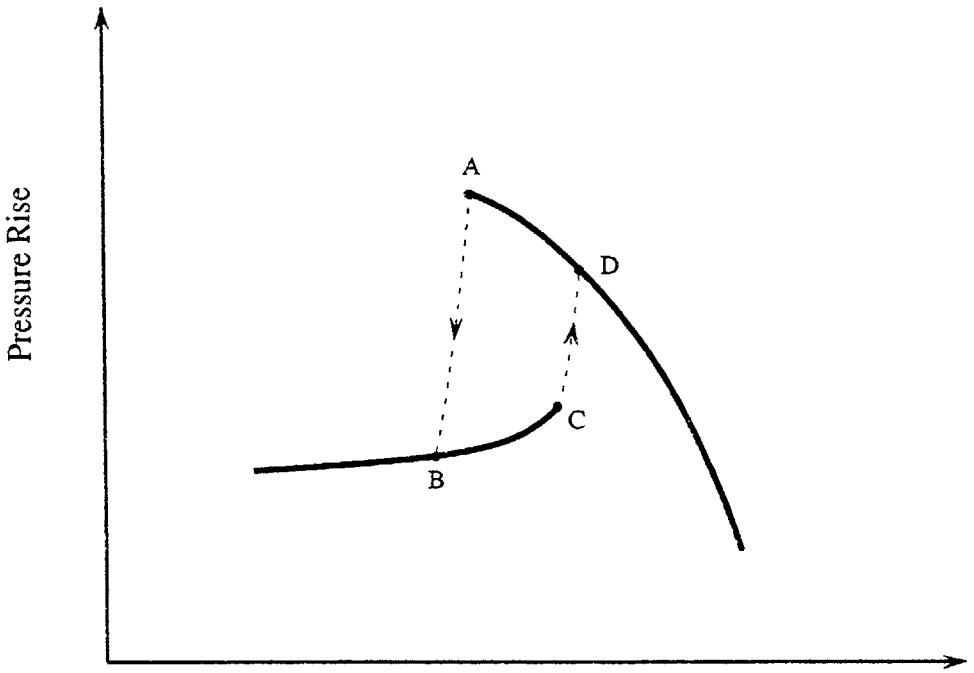

Figure 1.3: Compressor Characteristic

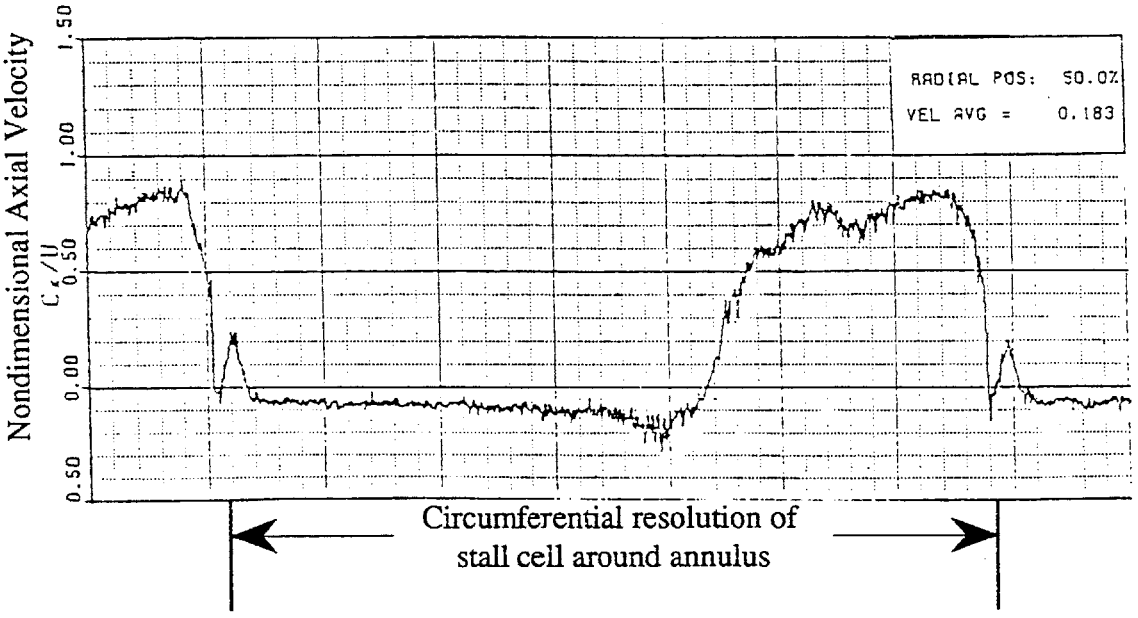

Figure 1.4: Fully Developed Stall Cell in Three-Stage Axial Compressor [5]

clarify this last point. A compressor operating with a high pressure rise at position A goes into rotating stall. The new operating point, point B, lies on the intersection of the throttle line for point A and the compressor characteristic. This operating point has decreased mass flow and a greatly decreased pressure rise. To recover from stall and restore proper compressor performance the operating point must be changed to point C from which the transition to a better operating point, D, can occur. Point D lies on the throttle line of point C.

1.2 Stall Inception

The focus of this research is the stabilization the compressor flow field as the compressor begins, or is about to begin, the transition from point A to point B. During this transition, one or more stall cells develop in the compressor flow field, and the compressor blades see a highly unsteady flow. Figure 1.4 shows the flow pattern when operating at point B; the compressor is in "deep stall." Understanding and modeling the deep stall flow field of the compressor can be useful in the design process, but the goal of this research is to maintain a steady flow around the annulus and to postpone the transition into deep stall so that it will occur at a lower mass flow. This new stall point corresponds to point A'. Figure 1.5 illustrates the desired compressor behavior.

This shift in the stalling mass flow is desirable because it increases the effective flow range over which the compressor can be operated. Typically, the peak operating point at which the compressor can be safely operated is point E (Figure 1.5). The gap in the flow range between point E and the stall point is called the stall margin; it exists for reasons of safety to allow for flow unsteadiness and possible nonaxisymmetric flow into the compressor. The extension of the compressor characteristic to point A' would increase the stall margin, thereby adding an increased factor of safety to the compressor's stable operation. Avoiding the onset of rotating stall means avoiding the detrimental effects described above. Alternatively, a new operating point with a higher pressure rise

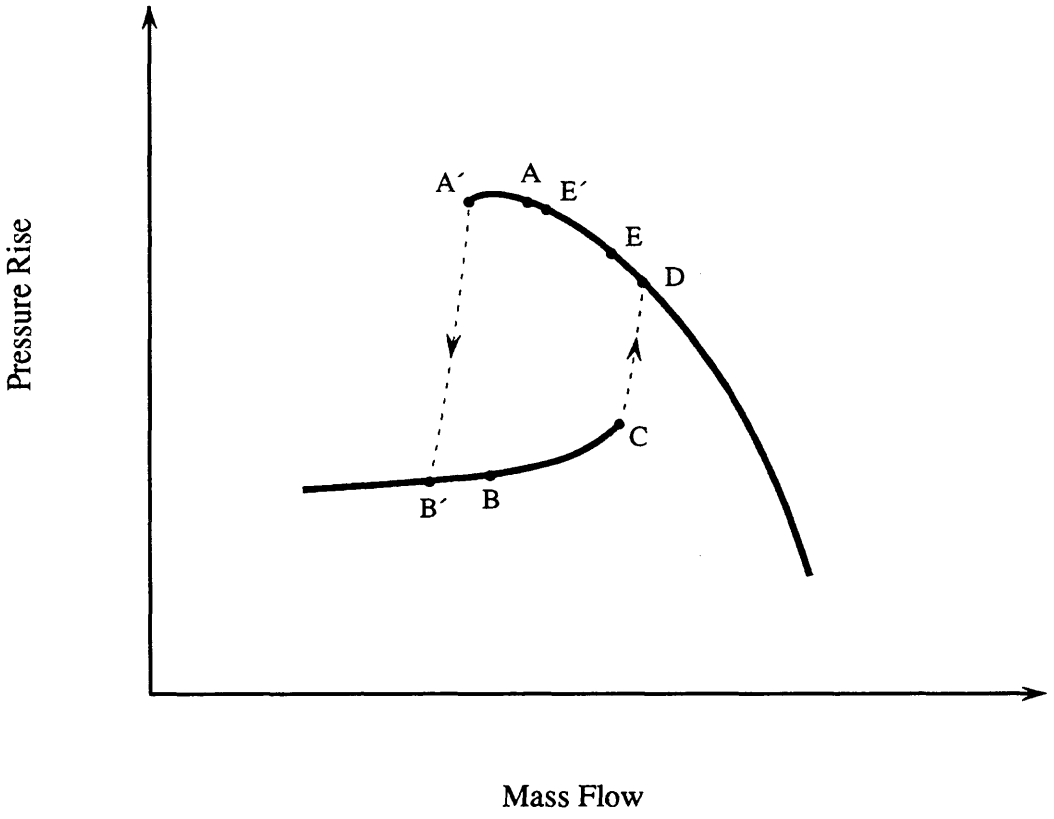

Figure 1.5: Conceptual Increase in Compressor's Stable Operating Range from A to A' due to Active Control

could be chosen with the same safety margin as before; this new operating point may also be closer to the peak efficiency operating conditions in some cases.

A fluid dynamic understanding of the cause(s) of rotating stall inception has been the focus of much research in recent years. The concept of a localized flow anomaly triggering stall inception by causing stalled flow in a single blade passage of a blade row has been supported by Day [6]. By this mechanism, the stalled blade passage causes a change in the adjacent blades' air flow incidence angles at time $t = t_1$. The adjacent blade in the direction opposite of rotor rotation sees an increased incidence angle which causes it to stall at $t = t_2$ and this stall cell triggers the stalling of the next blade passage in the direction of rotor rotation in the same way at $t = t_3$. The adjacent blade in the direction of rotor rotation sees a decreased incidence angle, and if the blade is stalled at $t = t_2$ the decreased incidence angle helps it to recover at $t = t_3$. Figure 1.6 illustrates this using flow velocity vectors $\vec{V}$. It is supposed that blades initially stall more rapidly than they recover. This allows the stalled zone to grow in circumferential extent while it propagates around the annulus. Day's observations of small disturbances of short circumferential extent propagating around the annulus and growing into rotating stall support this conception; however, this is not the cause of rotating stall on all compressors because rotating stall has been observed to develop by another mechanism as well.

1.3 Stall Inception Modeling

A theory of small amplitude rotating stall disturbances developed by Moore [7] and a more complete theory of post-stall transients in compressors by Moore and Greitzer [8] are the basis for understanding a different mechanism of rotating stall inception. They theorize that compressor instabilities grow from small amplitude disturbances, and for this reason the linearized form of the inception equations should accurately describe their initial growth. The inception equations suggest that rotating stall will develop as a result of small flow disturbances that are spatially periodic around the annulus and growing in amplitude. Any spatially periodic disturbance can be

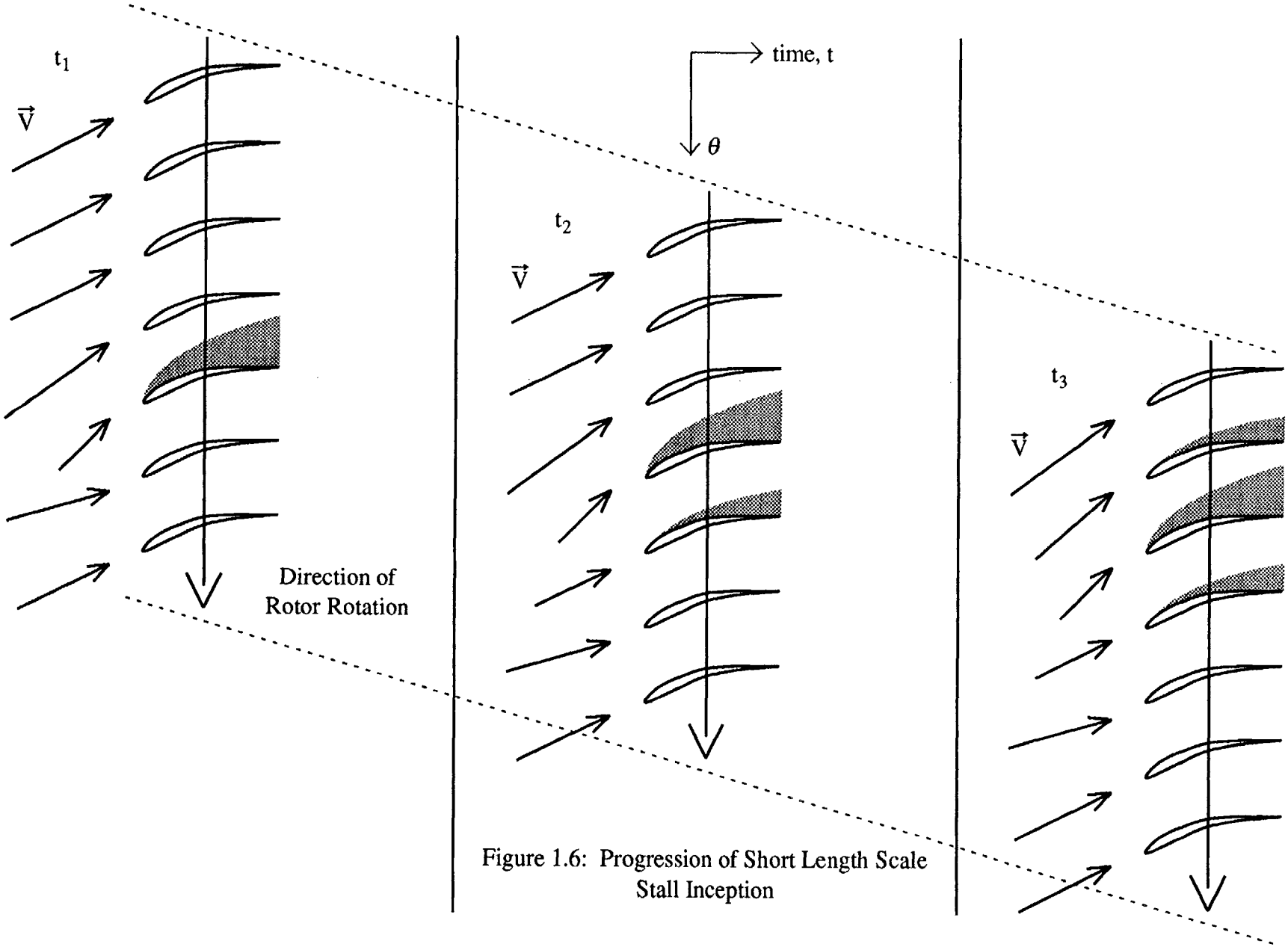

Figure 1.6: Progression of Short Length Scale Stall Inception

represented mathematically as the sum of several pure harmonics, i.e. several spatial modes. Figure 1.7 illustrates first, second, and third spatial mode disturbances. The validity of this model has received much attention recently and has been supported by the findings of McDougall et al [9], Longley [10], and Garnier [11]. This has provided the basis for developing a controller to prevent the onset of rotating stall in axial compressors.

1.4 Rotating Stall Prevention

Strategies for the prevention of rotating stall apart from this model have focused on the avoidance of undesirable compressor operation states rather than on the stabilization of normally unstable states. One way this has been accomplished is by modifying the compressor design. Compressors have been designed to surge before they stall in many cases because recovery is potentially easier, and some compressors have been designed with casing treatments at the tips of the rotors [12] which delay the onset of some types of stall but also hurt compressor efficiency. However, these design alterations do not address the problem of stabilizing an unstable flow and extending the flow range of the compressor. Stall avoidance has also been implemented by altering the compressor characteristic via bleed valves [13] or rapid stator restaggering [14], but these methods result in greater inefficiencies and avoid the problem of flow stabilization.

Based on the Moore-Greitzer model, the prevention of modal disturbances should postpone rotating stall inception to a point of lower mass flow. Epstein et al [15] were the first to suggest that modal disturbance generators could be used with real-time feedback control to dampen the modal disturbances that would normally grow into a fully developed stall cell. Paduano [16] was the first to implement a proportional control system of this type on a single-stage compressor using an array of 12 Inlet Guide Vane (IGV) actuators around the compressor inlet annulus. Figure 1.8 shows the compressor characteristic of Paduano's compressor and the sequence of flow range extensions achieved by the suppression of the first three spatial modes. Day [17] has also reported a

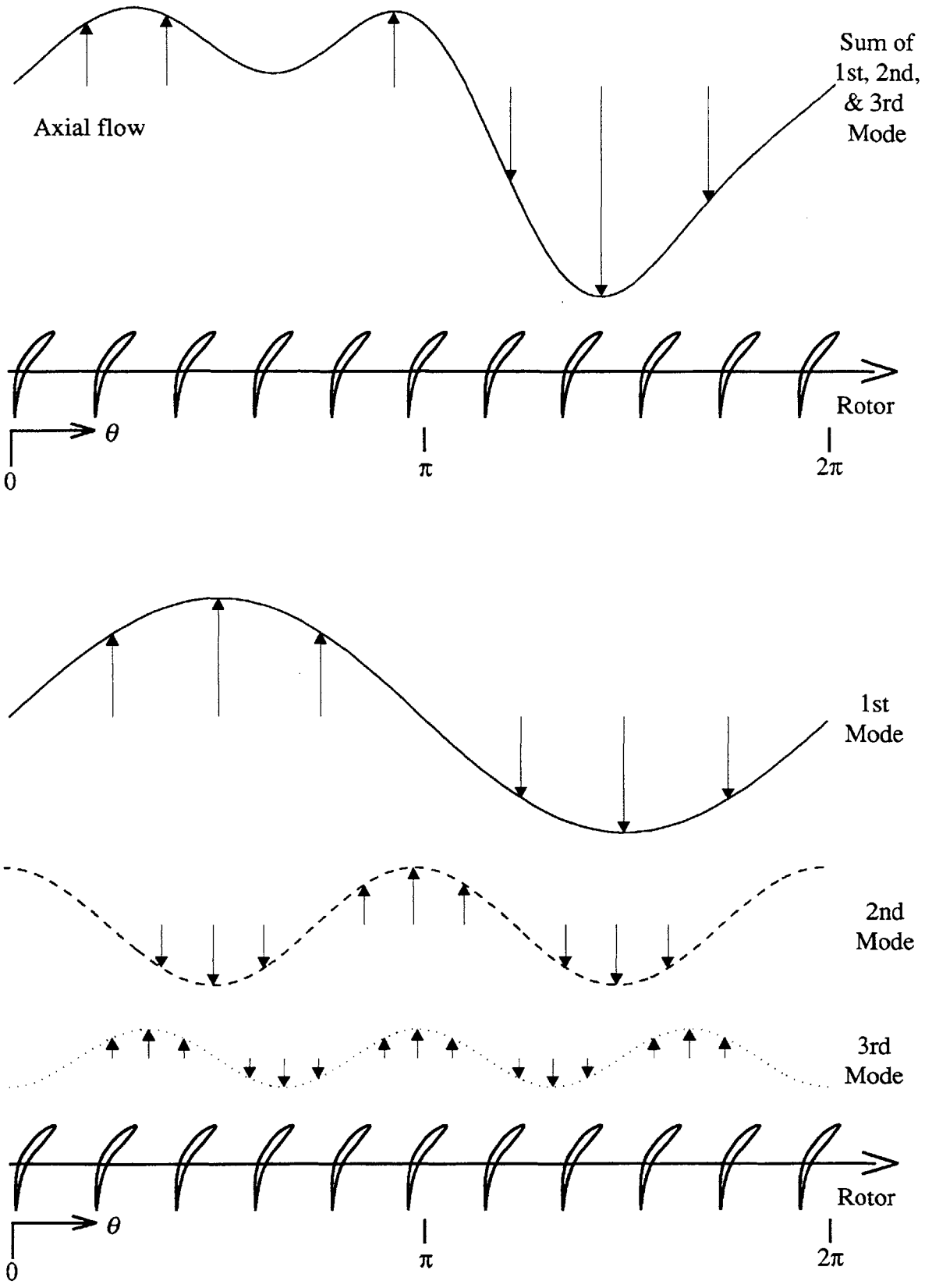

Figure 1.7: Modal Disturbances

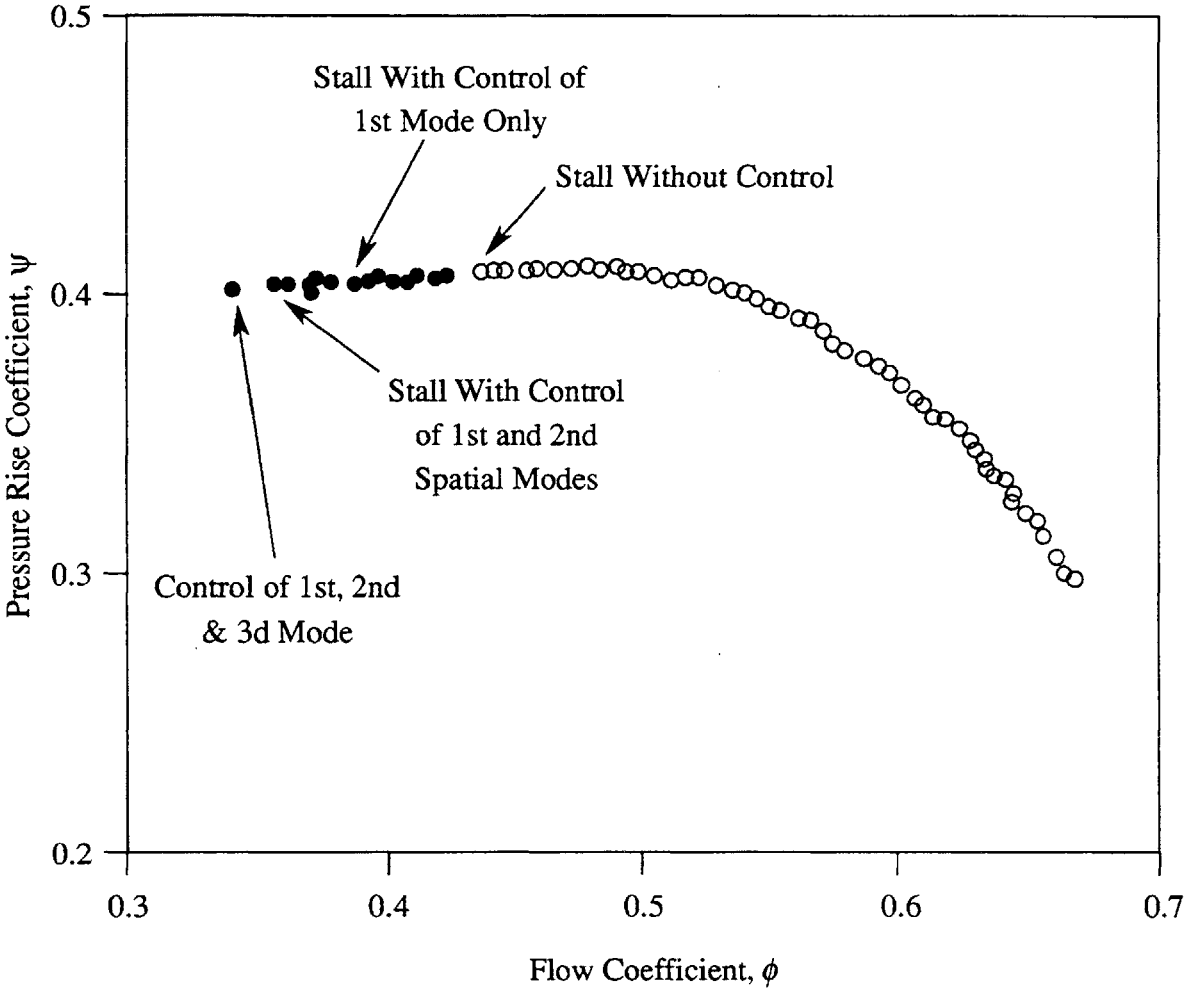

Figure 1.8 Single-Stage Compressor Speedline

successful extension of the flow range, but this was done on a four-stage compressor equipped with an array of 12 fast acting air injection valves capable of blowing on the tips of the first stage rotor blades. The radial flow variations introduced by Day's control system did not conform to the Moore-Greitzer inception model, and inherent nonlinearities in his control system prevented him from implementing truly proportional damping of modal disturbances. Nevertheless, Day was able to suppress first mode disturbances. Contemporary with Day's research, investigation of the effectiveness of an active IGV control system like Paduano's but on a three-stage compressor was begun.

1.5 Purpose & Scope of Thesis

Multistage experiments were deemed necessary to prove that stall stabilization is possible for multistage compressors. The feasibility of using modal disturbances in the compressor inlet to dampen modal disturbances existing downstream of the first rotor had to be demonstrated to further validate the Moore-Greitzer model and justify the use of active control on a variety of compressor designs. The percentage of flow range extension, the maximum effective damping of each mode by the controller, the maximum compressor characteristic slope to which the multistage compressor could be stabilized, and the predictability of each of these improvements were also important points of interest.

This thesis is organized with the intent of communicating and contextualizing the results of the multistage active control experiments and with the hope of giving some enlightenment to future work in the area of active control of compressors. Chapter 2 describes the multistage compressor active control facility with special attention given to the details that distinguish it from the single-stage experiments of Paduano. Chapter 3 highlights the simplest form of the linearized dynamic equations that model the compressor with IGV's as modal actuators; this chapter also presents the models for other components of the closed-loop system and a modified form of the original compressor model. Chapter 4 is an overview of the open-loop higher mode dynamics

that were measured and modeled. Chapter 5 presents the details of the compressor flow field and performance before and after control was implemented and presents the results of modeling the compressor under closed-loop control. Appendix A is added to give a detailed record of the conditions under which measurements were made, and Appendix B is added to show further data describing the compressor behavior.

CHAPTER 2

Experimental Setup

To study active control of a multistage compressor, an existing three-stage low speed research compressor facility was modified by introducing independent IGV actuators upstream of the first rotor. The IGV actuators allowed the creation of annular perturbation waves as well as localized changes in the compressor pressure rise across the first rotor. This chapter discusses the configuration of the experiment. Section 2.2 gives a description of the compressor and its modifications for active control experiments. Section 2.3 describes the equipment for sensing the actuators' position and the compressor's state of operation. Section 2.4 details the electronic equipment used in data collection and processing. Section 2.5 gives the details of important experimental techniques used in calibration and data collection. Section 2.6 describes how equipment was implemented into subsystems used for state variable identification; an error analysis is given for each state variable. The last section, 2.7, gives a description of the startup sequence of events and the signal flow path for active control experiments; the parts of the configuration that vary between experiments are noted.

2.1 Introduction

The active control experiments described in this thesis were performed at the MIT Gas Turbine Laboratory using the low speed three-stage compressor facility. The lab's experience in actively controlling a single stage compressor assisted the rapid creation of an actively controlled three-stage facility. All equipment used in the experiment will be mentioned here and important characteristics will be noted. Further

details of the equipment used in active control and details of the compressor facility may be found in the references [16,18,19].

2.2 Low Speed Three-Stage Compressor with IGV Actuators

The MIT GTL low speed three-stage compressor facility was designed and built by Eastland [18] using a Pratt & Whitney research compressor. The compressor was originally used by P&W to research blading design for the rear stages of the JT9D compressor [20]. Later the compressor was modified by Gamache [19] for reverse flow studies. The exhaust fan in the exit duct added by Gamache was not turned on during these active control experiments, and the fan was allowed to turn freely during operation of the compressor. Eastland and Gamache provide prolific documentation of the basic design of the three-stage compressor facility. Figure 2.1 illustrates the layout of the facility.

The research compressor has a constant cross-sectional area, A_C, with a hub-to-tip ratio of .88, making it a good candidate for testing a 2-D flow model in which radial variations have been neglected. The compressor blading was chosen to be the same build used by Garnier [11] in his study of rotating waves as rotating stall inception indicators. The documented evidence of pre-stall waves with this build made it ideal for initial active control experiments. This build was originally prescribed by Pratt & Whitney [21] for Gamache as a high reaction blading design which he used in his reverse flow studies, referenced as build #2 [19]. This build has also been studied by Lavrich [5] in his investigation of time resolved measurements during rotating stall. He documents that before rotating stall the first stage is the first to show a drop in pressure rise followed by the second and then the third as the flow is decreased. Hence, the first blade row is the most heavily stalled. The basic design parameters describing the compressor and this specific build are listed in Table 2.1; Figure 2.2 illustrates some of these specifications.

For active control experiments the compressor needed to be modified so that annularly distributed disturbances could be created in the flow field. Compressor

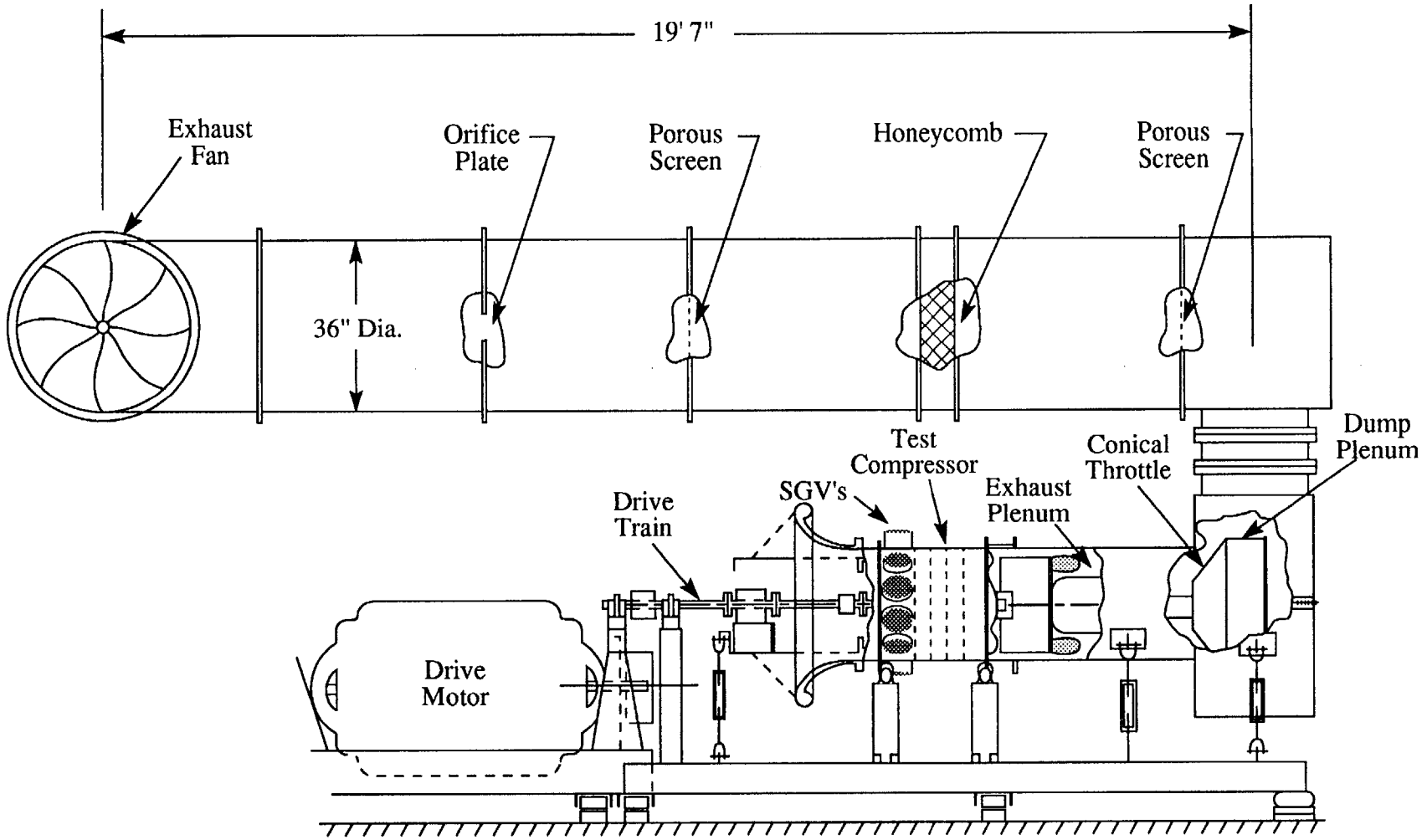

Fig. 2.1: Side View Schematic of Three-Stage Compressor Test Facility

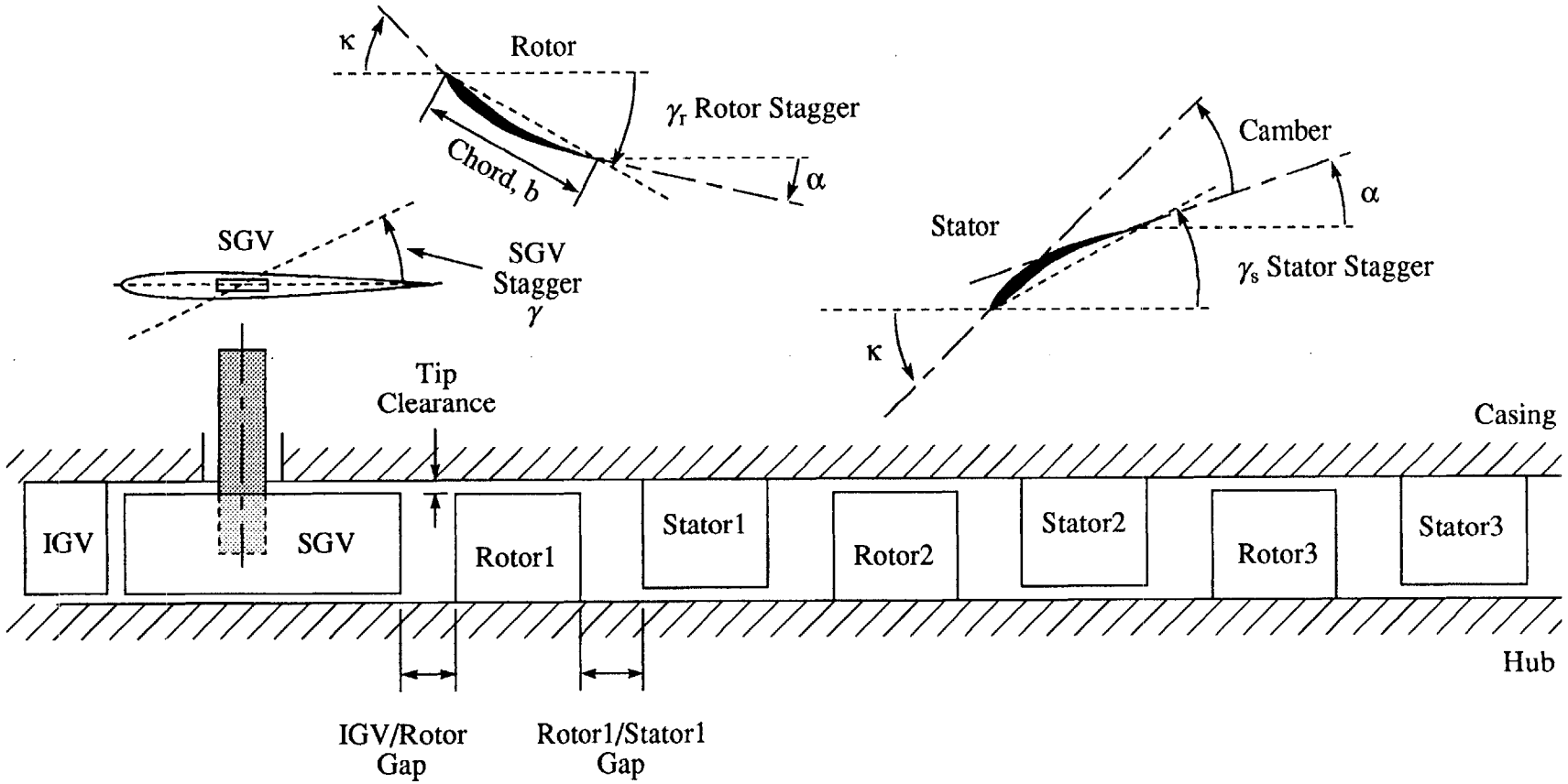

Figure 2.2: Compressor Blading Specifications

Tip Diameter (mm.)	610.
Hub-to-Tip Ratio	0.88
Design Average Reaction	0.75
Design Flow Coefficient	0.59
Pressure Rise Coefficient (@design)	2.03
Efficiency (@design)	84.3%
Stalling Flow Coefficient	0.460

	No. of Blades	Chord (mm.)	Camber (degrees)	Stagger $\gamma, \gamma_R, \gamma_S$ (degrees)	Tip Clearance* (mm)	Leading Edge Blade Angle*, κ (degrees)	Trailing Edge Blade Angle*, α (degrees)
Inlet Guide Vanes	125	20.1	11.0	8.1		0	10.0
IGV to SGV Gap		6.					
SGVs	12	81.2	0.0	8.1		8.1	8.1
SGV to R1 Gap		13.					
Rotor 1	54	45.2	17.0	42.8	0.97	50.0	41.0
R1 to S1 Gap		20.					
Stator 1	85	31.4	27.0	11.0	0.81	18.0	-1.0
S1 to R2 Gap		20.					
Rotor 2	55	44.8	18.0	43.5	0.94	54.5	36.5
R2 to S2 Gap		20.					
Stator 2	88	31.3	25.0	12.0	0.94	27.5	2.5
S2 to R3 Gap		20.					
Rotor 3	49	50.7	20.0	44.6	0.89	58.0	38.0
R3 to S3 Gap		18.					
Stator 3	90	31.4	53.0	5.5	0.86	36.5	-17.0

*Measured by Gamache [19]

Table 2.1: MIT Three-Stage Axial Compressor Design Parameters

modeling demonstrated the success of IGV actuators; this in conjunction with their low cost and ease of implementation made them the most desirable means of actuation. Prior GTL familiarity and experience with IGV actuators in active control experiments also encouraged this choice. Their success in affecting the rear stages of the compressor, however, remained to be shown.

To implement IGV control, a new IGV mounting ring was designed for the three-stage compressor. On this new casing the original IGV blades were mounted in a position further upstream than in the original design but were positioned to swirl the flow by the same amount specified in the build. In the space that was created between the original IGV's and the first rotor, twelve evenly spaced guide vanes were mounted to twelve servo motors which attached to the new IGV mounting ring. The rotational freedom of each IGV was constrained by a mechanical stop limiting each blade's rotation to $\pm 70°$; the stop was important in preventing damage to the blade and in positioning. A front view of the new IGV ring is shown in Figure 2.3, and Figure 2.4 illustrates the IGV ring's integration into the original compressor design. The servo-controlled guide vanes, SGV's, are NACA 65-009's with zero camber and a design chord of 81.2 mm. The long chord length was an important factor in meeting the design criterion for a moderate SGV solidity using only a few motors. The control effectiveness of IGV's was studied by Silkowski [22], and his results were used to determine the blade count and solidity which in turn sets the aspect ratio. On the three-stage compressor the SGV solidity was .54, slightly less than the .60 solidity of the SGV's in the single-stage control experiments. The SGV's were cast out of epoxy (specific gravity = 0.7) just as they were for the single-stage compressor. However, since these blades have a smaller radial length, they have a lower moment of inertia, about 1.60×10^{-6} kg-m^2. Using the same type of servo motor actuators, these blades perform with a higher bandwidth than those used on the single-stage compressor; Figure 3.8 illustrates the frequency response of an SGV. Figure 2.5 shows a single SGV and its important design characteristics. In the active

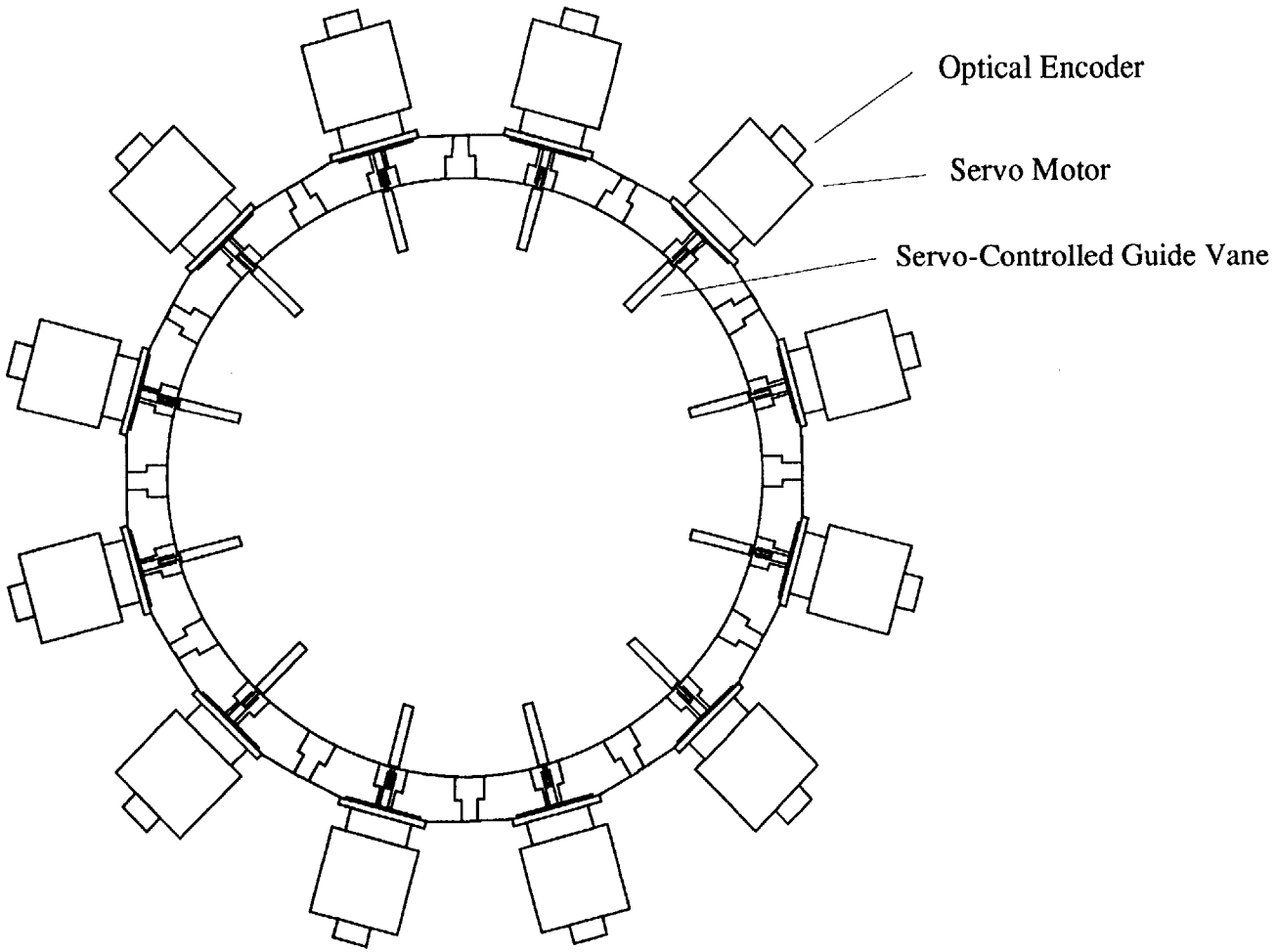

Figure 2.3: Twelve Motors Mounted on IGV Ring

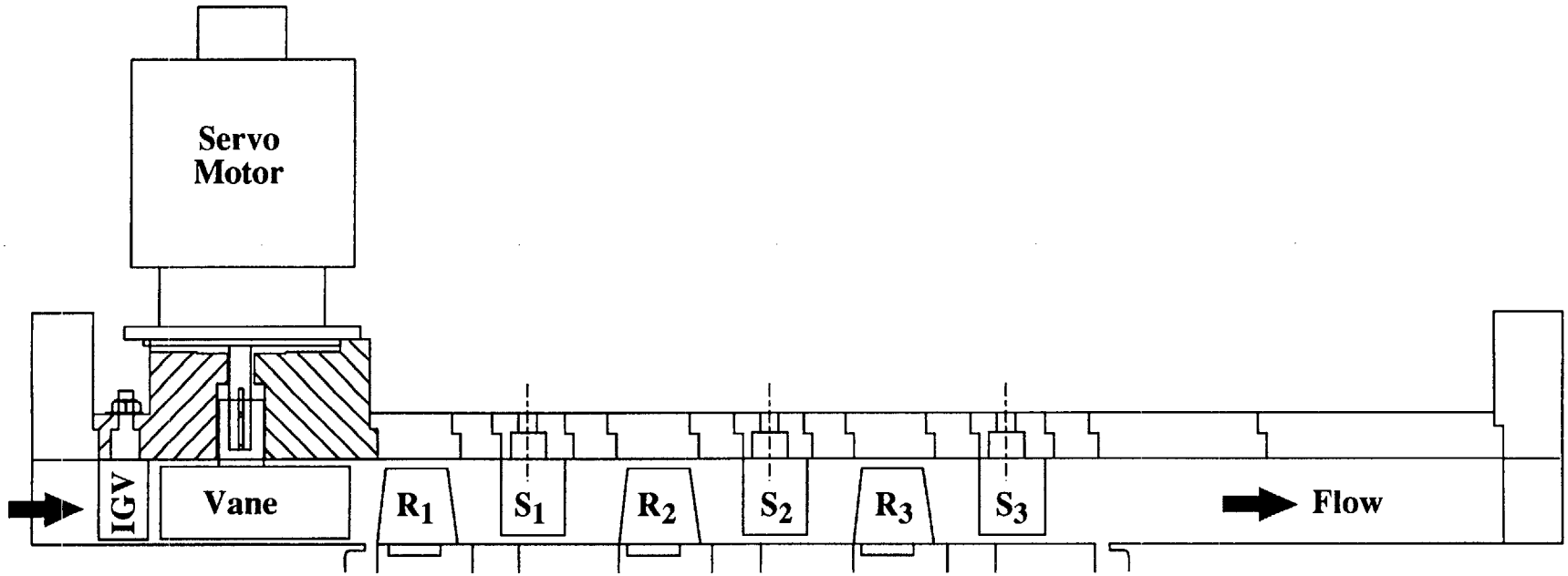

Figure 2.4: Three-Stage Axial Compressor with New IGV Ring

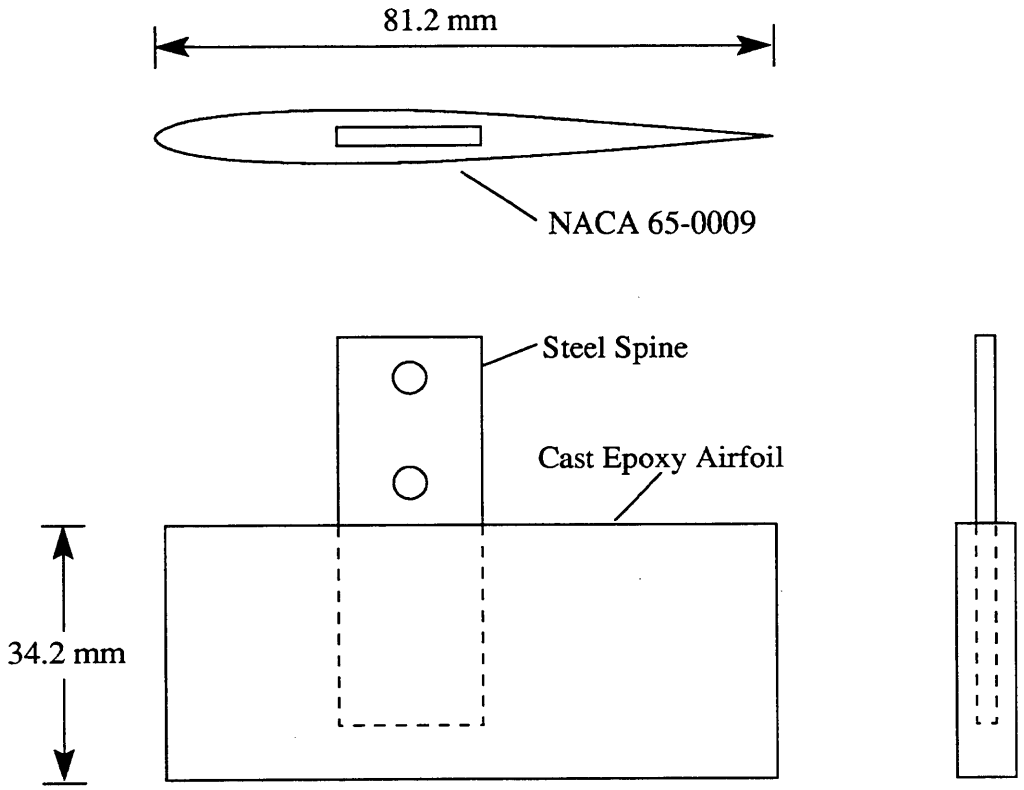

Figure 2.5: Servo-Controlled Guide Vane Design

control experiments the SGV's were positioned at a stagger angle that matched that of the IGV's.

2.3 Compressor Instrumentation

The instrumentation for flow velocity measurements and pressure measurements was distributed around the compressor annulus. Figure 2.6 documents the location of all the instrumentation ports used in the active control experiments. Other instrumentation was positioned in ways described below.

2.3.1 Hot-Wire Probes & Anemometers

A Dantec 56C17 CTA Bridge and 56C01 CTA Unit comprised the flow anemometer unit used in flow velocity measurements. The bandwidth of this equipment is reported by the manufacturer to be 50 kHz which is well above the requirements of this experiment. Intrusive flow measurements were made using Dantec 55-P11 hot-wire probes. These probes have a 20 μm diameter tungsten wire about 1.2 mm in length. The anemometer's output is a voltage signal proportional to the current provided to the probe. The current to the probe is continuously adjusted during operation so that the resistance through the tungsten wire remains constant. The resistance in the wire is related to its temperature which in turn is determined by the air convection across the wire. The relationship between output voltage and air flow velocity is given by King's law [23],

$$E^2 = A_0 + A_1 V^m, \tag{2.1}$$

where E is the output voltage, V is flow velocity, and A_0, A_1, and m are calibration constants. The hot-wires were calibrated before each run and sometimes during a run. Section 2.5.1 describes the details of this procedure.

2.3.2 Scanivalve & Pressure Probes

Steady-state measurements in the compressor were made using a Scanivalve. The scanivalve consists of one Spectra strain-gauge-type transducer which can sequentially sample pressures from up to 48 pressure probes. The scanivalve was

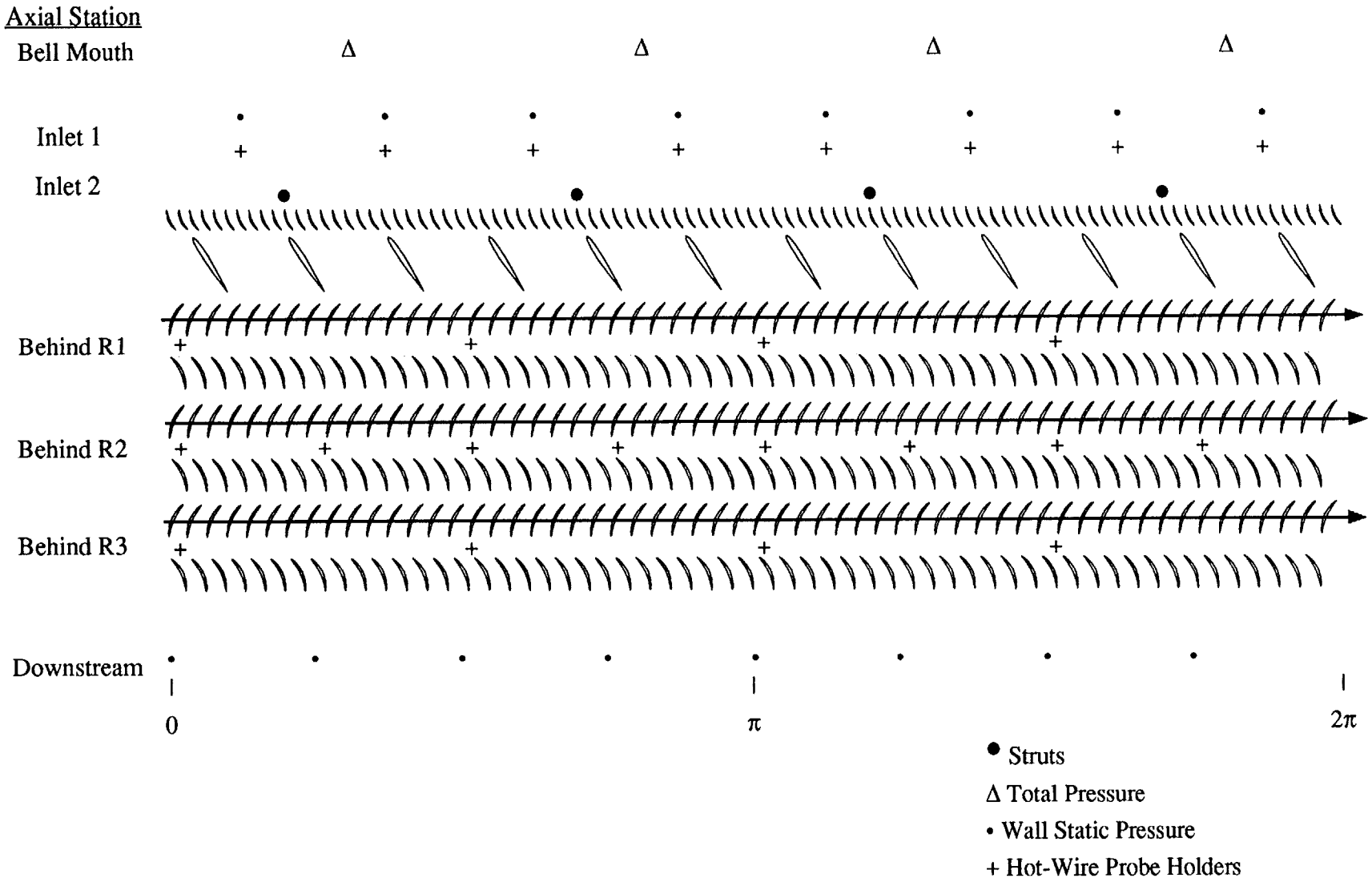

Figure 2.6: Layout of Compressor Instrumentation

calibrated using an MKS Baratron unit. Each pressure measurement was made by averaging 100 readings of the scanivalve signal 0.2 seconds after it connected with the pressure tap. The delay was intended to allow any pressure transients to die out.

Wall static pressure taps were used for all static pressure measurements. Four kiel-head probes positioned at 50% span within the bell mouth inlet were used for total pressure measurements. These probes are highly insensitive to flow angle which insures accurate measurements. The probes were connected to the Scanivalve using 1/4 inch tubing.

2.3.3 Torque Sensor

A Lebow 1105H-5K slip ring torque sensor was attached to the compressor drive shaft. A Lebow 7530-100 signal conditioning unit excited the strain gauge bridge in the torque sensor and amplified the signal.

2.3.4 Tachometer

Speed sensing was provided by the Lebow torque sensor equipped with a 60 tooth gear and a magnetic pickup. The pulse signal from the magnetic pickup was read by a frequency counter which directly registered RPM.

2.3.5 Servo Motors

Each SGV was positioned using a low-inertia DC servo motor mounted on the IGV ring. The motors are Pacific Scientific 4VM62-220-1 permanent-magnet servo motors, and they have a moment of inertia of 3.8×10^{-6} kg-m^2. The motors are air cooled by a vacuum blower that pulls air through the core of each motor at a rate of 1 standard cubic foot per minute. This allows them to operate with a maximum power dissipation of 100 watts. The RMS current rating for the motors is 7.2 amps. Typical power dissipation in the active control experiments was 10 watts.

2.4 Data Filtering, Acquisition, & Processing

2.4.1 Low Pass Filters

A 4-pole Bessel filter, model 744PL-4 manufactured by Frequency Devices, filtered each anemometer signal. The upstream flow measurements were filtered with a 1.0 kHz cutoff frequency so that the lag in the control system introduced by the filters would be negligible. Although this is above the Nyquist frequency (250 Hz), it has been shown that only noise exists in the spectral content of the compressor flow between 250 Hz and the rotor blade passing frequency [5]. Flow measurements behind the rotors were filtered with a 200 Hz cutoff frequency to eliminate much of the high frequency noise associated with the blade passing frequencies which range from 1960 Hz to 2200 Hz.

2.4.2 Metrabyte A/D

For some experiments the filtered anemometer signals and other signals were read by an HP Vectra computer via a Metrabyte DASH-16F A/D converter mounted in an expansion slot. The Metrabyte A/D performed direct memory access (DMA) sampling at 100 kHz and could make 12 bit conversions of 0 to 5 V signals for up to 16 channels. The 12 bit A/D enabled an average flow resolution of 0.106 m/s per A/D count.

2.4.3 Analogic A/D

To obtain better resolution of the flow disturbances and enable downstream flow measurements to be made simultaneously, the Metrabyte A/D was replaced by an Analogic HSDAS-16 A/D converter with an AMUX-64-X 64 channel multiplexer. The Analogic A/D had an aggregate sampling rate of 200 kHz and made 16 bit conversions of 0 to 5 V signals for 32 channels. The 16 bit A/D enabled an average flow resolution of 0.0085 m/s per A/D count.

2.4.4 A/D for VAXstation II

The VAXstation II computer was equipped with a Data Translations DT3382 A/D. The A/D sampling rate was set to 1 kHz. This A/D was used for the Scanivalve pressure signal and the torque sensor signal.

2.4.5 Computer Hardware

A Hewlett Packard Vectra 80486-based microcomputer operating at 25 MHz and equipped with 8 Mb of RAM, an A/D, and 4 servo motion control boards conducted the real-time control of the compressor. The HP Vectra was also equipped with an 80487 math coprocessor to speed calculations.

A VAXstation II workstation controlled the operation of the Scanivalve via an IEEE bus making it convenient to store and then process all pressure measurements on the VAX. The pressure measurements were communicated to the HP Vectra during the calibration routines via a serial communication line.

2.4.6 Software Considerations

Software requirements for the active control experiments included A/D interface routines, motion control board interface routines, calibration routines, and the compressor feedback control program. Most of these programs were used in the single-stage control experiments [16] and were either modified to account for the unique characteristics of the three-stage compressor or used in their original form. The closed-loop feedback rate in the compressor feedback control program remained at 500 Hz.

The Analogic A/D assembly language interface routines were modified for the three-stage compressor control experiments, but functionally they performed in the same mode of operation as the Metrabyte routines. Notable differences are that the channels were read in a single pass at a 200 kHz 'fast clock' rate instead of at 100 kHz, and a 16-bit table look-up was performed instead of a 12-bit, which allowed for greater resolution of the flow signal.

2.4.7 Servo Motor Motion Control

The DC servo motors were controlled using four Galil DMC-430 servo motion control boards. Three motors were monitored and controlled by each board. The shaft position was monitored by the boards using an optical encoder on each DC motor shaft, and a ± 10 Volt current command from the control boards was sent to an amplifier which powered the motors. Blade positioning was handled independent of the 486 processor by a processor on the DMC-430; this greatly decreased the computational demands on the 486 processor. The processor implemented a discrete time version of PID control set to user specifications. Two different blade settings were used in the three-stage active control experiments. The DMC-430 conducted the closed-loop discrete time control at 2 kHz. Figure 2.7 illustrates the signal flow path for the positioning of an SGV. Further details about servo control boards and amplifiers are given by Paduano [16].

2.5 Experimental Technique

2.5.1 Hot-Wire Calibration

The hot-wires were calibrated by making multiple measurements of the flow velocity and corresponding measurements of the average hot-wire signal based on 2500 data points. A total of 14 to 15 different data points were taken at 1800 RPM and 2400 RPM. This data was used to calculate the calibration coefficients in King's Law (Equation 2.1). Some data was taken at 1800 RPM so that the hot-wires would be accurately calibrated for flow coefficients at or below the stalling flow coefficient. Sometimes a hot-wire deteriorated during a run. In that case it would be replaced, and all of the hot-wires would be recalibrated.

2.5.2 Flow Coefficient Evaluation

Flow coefficient data presented here always consists of an average of three measurements. If the flow coefficient exhibited slow and small amplitude fluctuations, three sequential measurements during the low flow were used. In cases when the neutral

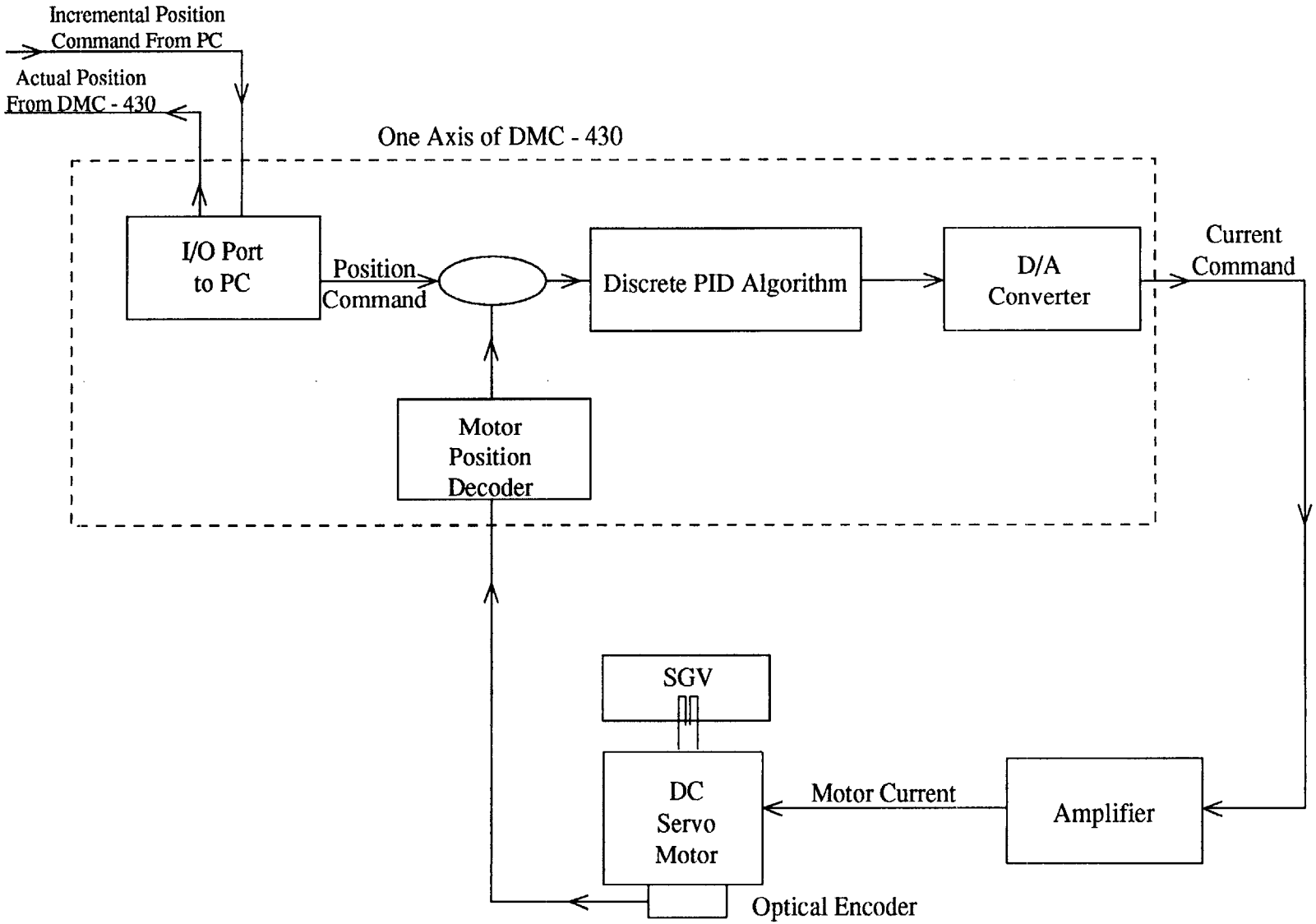

Figure 2.7: Closed-Loop Control of DC Servo Motors

stability flow coefficient was being measured, the compressor had to remain in a stable state at that flow coefficient for at least 45 seconds for the measurements to take place.

2.6 Measurement of State Variables & Error Analysis

2.6.1 Time Averaged Measurements

- Rotor Frequency ω - The readout from the frequency counter was read directly by the VAX using the IEEE bus. This measurement had a precision of $\pm$ 1 RPM. In all of the active control experiments the desired compressor speed was set to 2400 RPM. The speed was set manually. It shifted when there were large changes in flow coefficient and also drifted over time. Variations of only $\pm$ 5 RPM were tolerated over the full range of flow coefficients. This allowed for a maximum error of 0.25% in the operating speed of the compressor during an experiment.

- Flow Coefficient ϕ - The flow coefficient of the compressor was calculated from the total to static pressure difference in the inlet modified by a calibration factor C(Re). Both the static and total pressures around the inlet were annulus averaged. The axial flow velocity calibration equation had the form:

$$C_x = C(Re)\sqrt{\frac{2(P_t - P_s)}{\rho}} \qquad (2.2)$$

This is divided by the mean rotor blade speed to calculate the flow coefficient, $\phi = C_x/U$. The velocity of a uniform flow field is corrected with a calibrated function of Reynolds number which accounts for changes in blockage due to boundary layer growth. This calibration has an estimated bias of $\pm$ 2%; it is not evident in the data since all flow measurements were made using the same calibration. For individual experiments the precision of the flow coefficient, measured in the way

described above, was calculated to be ± 0.28% when operating near the stall point. However, variations in conditions from one experiment to the next resulted in a precision of ± 1.77% between experiments. To accommodate these fluctuations when making comparisons between experiments, data describing changes in the flow coefficient were calculated as a percent of the stalling flow coefficient of each experiment. When flow coefficient data were compared or used in a calculation, they were calculated by multiplying the percentages by an exemplary stalling flow coefficient. When modeling the compressor, the compressor characteristic with the exemplary stalling flow coefficient was used for reasons of consistency.

- Pressure Rise ψ - The nondimensional pressure rise across the compressor was defined to be

$$\psi = \frac{P_{s\,downstream} - P_{t\,upstream}}{\rho U^2} \tag{2.3}$$

where ρ is the density of the air. The upstream total and the downstream static pressures were computed based on an average of measurements made around the annulus. Figure 2.8 illustrates the equipment configuration for acquiring pressure data. For individual experiments the precision of the ψ measurements was calculated to be ± 0.24%. From one experiment to the next, ψ was calculated to have a precision of ± 1.65% due to changing conditions.

- Torque T - When the compressor was operating in a steady state the analog torque signal was observed to oscillate about a fixed DC value at a regular frequency. Gamache believed this was due to the flexible couplings at both ends of the torque sensor oscillating in response to an unsteady driving force [19]. An average value of the torque signal generated by the Lebow 7530 signal conditioning unit was obtained by the VAX A/D by averaging

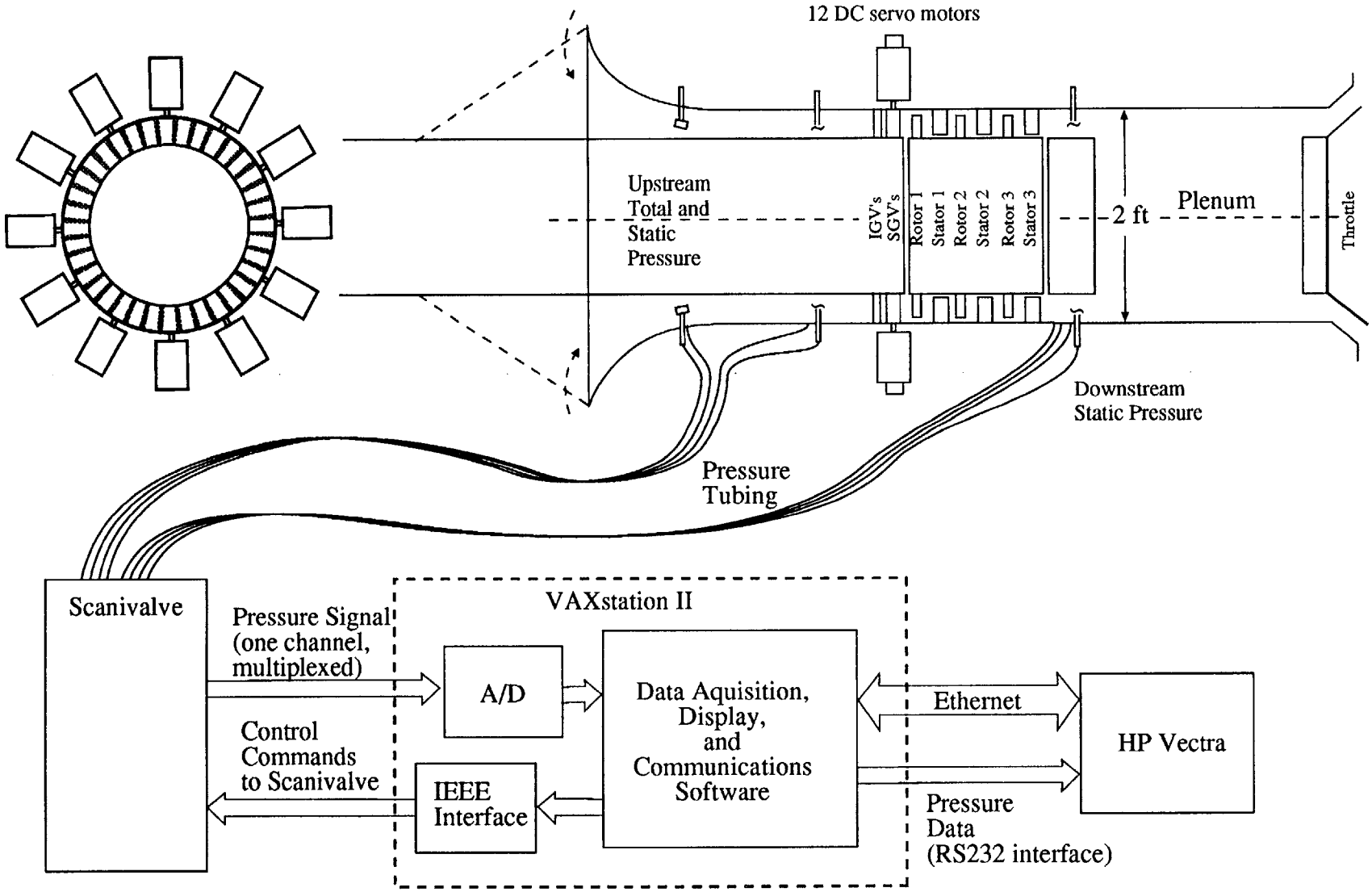

Figure 2.8: Pressure Data Acquisition Equipment

400 samples over a period of 16 shaft rotations. The measured compressor torque accounts for both the work done on the flow (true torque) and the energy dissipated by the bearings (tare torque). The torque measurements were corrected for the tare torque of the compressor according to the calibration given by Christianson [20] who removed the compressor blading and measured the torque as a function of shaft speed. Torque measurements are nondimensionalized according to the formula:

$$T = \frac{\text{true torque}}{\rho U^2 A_C R} \tag{2.4}$$

where R is the mean radius of the compressor. The precision of torque measurements was calculated to be $\pm$ 0.30%.

2.6.2 Real Time Measurements

- Flow Disturbance $\delta\phi$ – The Metrabyte A/D introduced noise in the flow signal on the order of 1 to 3 A/D counts; this gives flow resolution of 0.32 m/s. Due to noise and crosstalk, the precision of the Analogic A/D was on the order of 7 A/D counts. To evaluate the contribution of anemometer and filter noise as well, scattering in the signal was measured with the anemometers shunted with fixed resistances. The precision of the flow measurements was shown to be between 23 and 27 A/D counts depending on the anemometer. This results in a meaningful flow resolution of 0.23 m/s.

  Around the inlet annulus, 8 hot-wires were positioned 5 rotor blade chords, i.e. 0.60 compressor radii, upstream of the first rotor. In a potential flow field, disturbances decay exponentially with distance from their source; so, the measured signal was a damped version of the actual disturbance in the compressor. It is significant that higher spatial modes in the damped signal upstream will be much weaker than lower spatial modes

because the decay is also exponential with mode number. Weaker higher modes are the best guarantee against spatial aliasing although there is a penalty in the signal strength of lower modes. Garnier found that spatial aliasing on this compressor was not a problem if the hot-wires were at least 0.5 compressor radii upstream of the first blade row [11].

Eight hot-wires around the annulus can resolve the first three spatial Fourier modes. These modes (n = 1, 2, 3) were computed and used in proportional feedback control. The signal-to-noise ratio of these measurements needed to be high in order to single out a particular mode. Near the instability point of each mode the highest recorded signal to noise ratios measured without going into rotating stall were 46 dB for the first mode, 29 dB for the second mode, and 23 dB for the third mode.

- SGV Stagger Angle γ – SGV positions are measured with optical encoders and monitored by the servo motion control boards. The optical encoders have 4096 count resolution; so the position is known with an precision of $\pm 0.044°$. The accuracy of the SGV position was influenced by their calibration. Before each run the distance from the stop to an index position on the encoder was measured and the precalculated distance from the index position to the zero stagger angle was used to position the SGV's. The bias in the SGVs' actual flow position is $\pm 0.62°$.

2.7 A Systems Description of the Actively Controlled Compressor

Active control of the compressor involved many of the sub-systems described above working together. In an experiment the compressor was operated at 2400 RPM and the IGV's initially positioned at the design stagger angle. The operating point of the compressor was changed by closing the throttle. The pressure rise and flow coefficient of the compressor were monitored using the VAX. When the flow coefficient was

within 2% of the stall point, the throttle was held in position, and the control system was turned on. Figure 2.9 diagrams the closed-loop feedback path. Upstream modal disturbances were detected with the array of hot-wires around the annulus. The anemometer signals were filtered and then read by the A/D on the microcomputer. Using a low pass digital filter, the computer monitored the mean flow coefficient and was able to calculate the perturbation velocity at each hot-wire station. A discrete Fourier transform, DFT, of the perturbation velocities into spatial modes was then performed. A control law was applied for each mode, and then an inverse discrete Fourier transform, IDFT, was used to determine the contribution of each mode to the 12 SGV displacements. The SGV commands were then sent to the motion control boards. The digital control loop was repeated at a rate of 500 Hz. After the control system was turned on, the throttle could be closed further. When the compressor went into rotating stall, the control system was turned off and the throttle was opened.

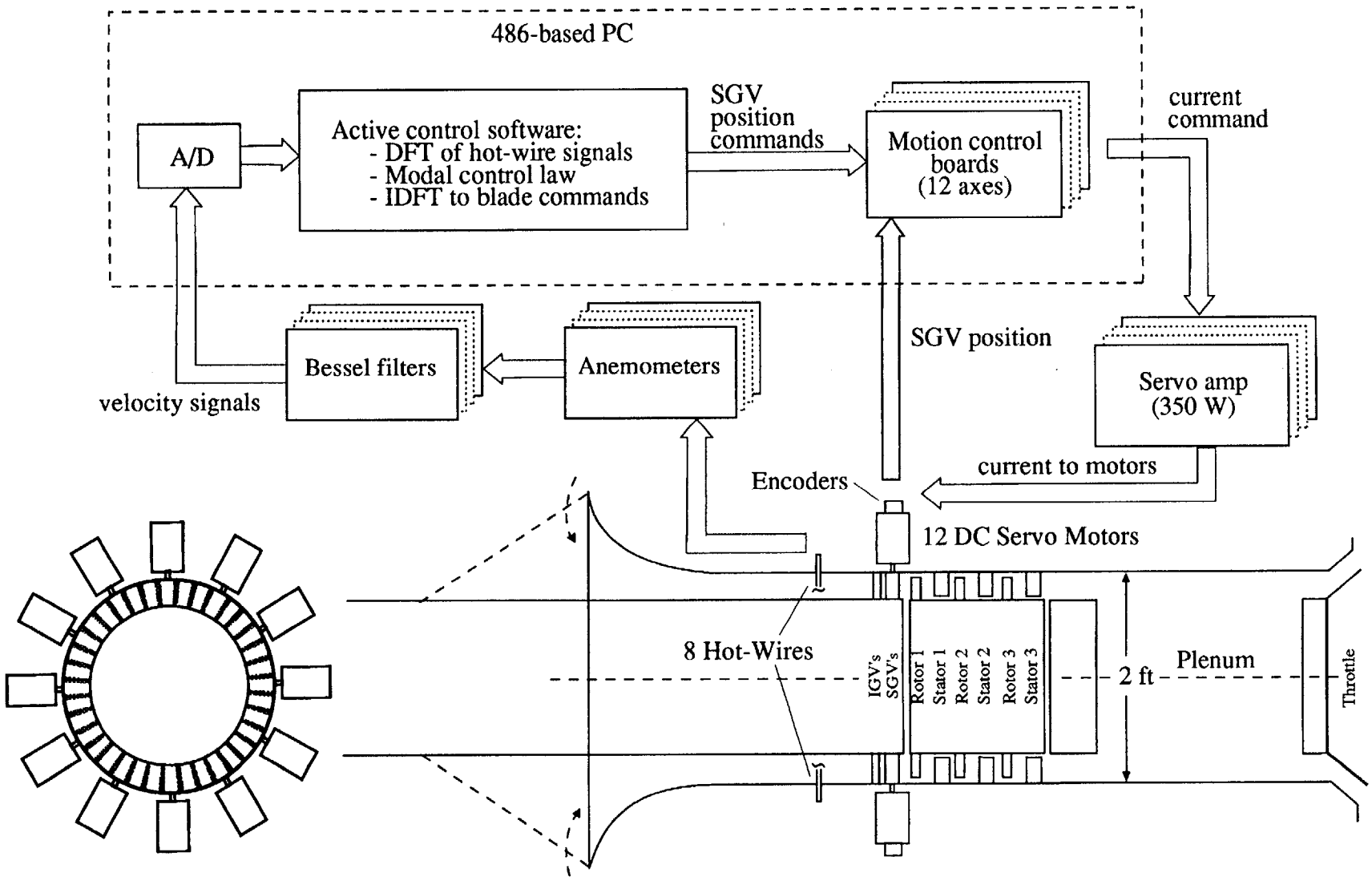

Figure 2.9: Closed-Loop Control Feedback Path

CHAPTER 3

Modeling Higher Spatial Mode Dynamics in a Compressor with Active Modal Stabilization

This chapter highlights the basic compressor model and various modifications to it and presents the models for components in the feedback path. The Moore-Greitzer compressor model is the foundation in this analysis for modeling the higher-mode dynamics in the compressor. Zeroth mode dynamics, i.e. surge dynamics, are considered in the original theory, but only the special case of pure rotating stall is used in this study.

3.1 Compressor Model

3.1.1 Assumptions

The compressor model is based on a simplified representation of an actual compressor. The simplifying assumptions and approximations that were made in developing the partial differential equations describing rotating stall will be discussed here. Figure 3.1 illustrates the compressor which will be modeled, pertinent axes, and the axial stations used in the model.

- 2-D flow field upstream, downstream, and through the compressor - This means radial variations in velocity and pressure are not considered. A constant cross-sectional area high hub-to-tip ratio compressor comes the closest to satisfying this condition; although its blades may still be designed to handle radial flow differences, the blade shape is modeled based on its midspan characteristics. A constant area inlet duct following an initial inlet contraction and a constant area exit duct are also needed to satisfy this condition, although different geometries could be accounted for in a more

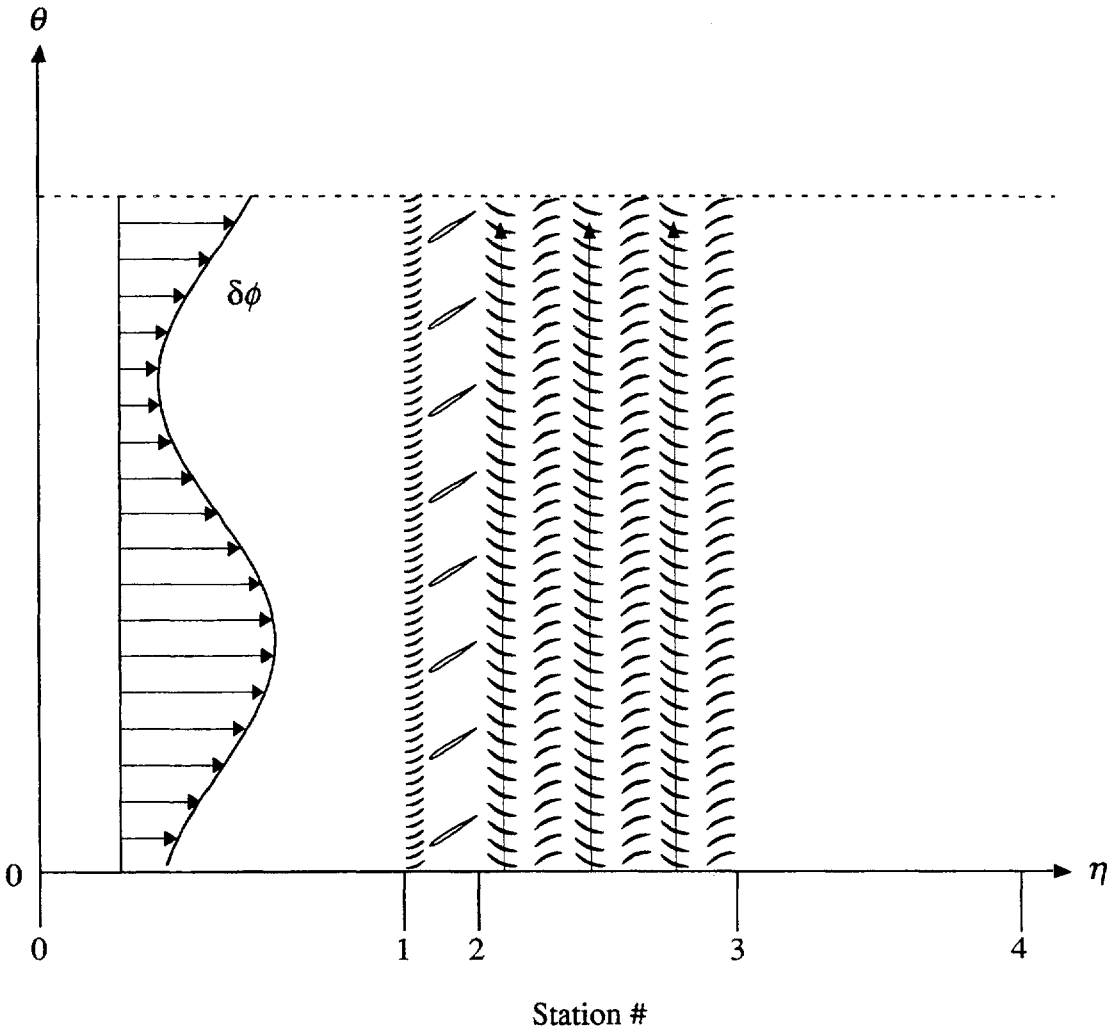

Figure 3.1: Stations in a 2-D Axial Compressor Model

general model. The experimental compressor used in this research has a hub-to-tip ratio of 0.88 and constant area ducting downstream of the initial inlet contraction, both of which help it to conform to the 2-D description.

- Inviscid flow everywhere outside of the compressor blade rows - This assumption simplifies the analysis of the flow through the inlet and exit ducts. It is appropriate to use this assumption outside of the boundary layers of the ducts when inertial effects dominate viscous effects; this occurs in high Reynolds number flows. In these experiments the Reynolds number seen by a spatial mode n was on the order of $6.27 \times 10^5/n$ which indicates that the modes of greatest influence in a modal stall inception (i.e. n=1,2,3) are clearly dominated by inertial effects.

- Incompressible flow - This assumption limits this model to low speed compressors in which the flow Mach number is small (Ma < 0.3). In this study the mean blade Mach number U/a was 0.21, guaranteeing that compressibility effects were small. A closer evaluation of the effects of incompressibility on modal disturbances can be made from the speed of the modal waves themselves. The Mach number of the modal waves was calculated to be less than .1 for each of the first three modes. Current research is focusing on modifying the model to accurately account for the effects of compressibility in a high-speed compressor.

- Uniform and irrotational inlet flow conditions far upstream - This limits the model to inlet flows without distortion and without vorticity. However, recent and ongoing research has been focused on developing an accurate model that accounts for these conditions as well [24, 25, 26]. Based on this and the inviscid flow assumption, the flow in the inlet can be modeled as a potential flow coming from a uniform total pressure reservoir upstream.

- Negligible surge effects - This assumption allows the use of the special case of the Moore-Greitzer model which describes pure rotating stall. The implications are that the plenum pressure and the annulus-averaged axial flow maintain steady-state values. This assumption can be physically realized by designing the compression system to have a small B parameter [33]. For the experimental compressor the B parameter was estimated to be between 0.16 and 0.21; so surge dynamics can be neglected.

- Compressor performance conforms to the semi-actuator disk model - This is the most significant simplifying assumption because it allows the compressor to be modeled without focusing on the details of the flow inside the compressor. An actuator disk representation of the compressor reduces the entire compressor to a disk of infinitesimal thickness which produces a pressure rise in the flow as specified by the steady-state compressor characteristic. An actuator disk representation does not account for blade-to-blade variations in the flow field; this approximation in effect treats each blade row as if it had an infinite number of identical blades. Although this model greatly simplifies the compressor representation, it is only appropriate when the effects of unsteady flow are negligible. The semi-actuator disk representation of the compressor modifies this model by accounting for the effects of unsteady flow in the compressor blade rows. Effectively, the semi-actuator disk model accounts for the inertia of the flow in the blade passages and its effects on local pressure rise when blade passages see an unsteady flow field. This model is appropriate for modeling the effects on pressure rise of long scale (compared to the spacing between blades) annular flow disturbances. Long scale modal disturbances had previously been observed in the experimental compressor used for

these experiments; so the model is appropriate at least for describing these disturbances.

- Time invariant compressor exit flow angle - This assumption is valid if the flow deviation from the last stator row is neglected. Since deviation effects on the last stator row are small in this compressor, this is a valid assumption.

- Inlet and exit ducts are long enough to allow annular pressure disturbances to die out - This assumption makes for the pressure matching between the nonaxisymmetric pressure field at the compressor and the atmospheric and plenum pressure reservoirs mathematically possible. The Moore-Greitzer model can account for shorter exit duct lengths as well, but in this case it is assumed that the exit duct of the experimental compressor is long enough [7]. The upstream duct of this high hub-to-tip ratio machine is .58 mean compressor radii in length, and the downstream duct is 1.42 mean radii.

- Annular static pressure disturbances in the exit duct are small compared with the plenum static pressure - This assumption needs to be made in order to linearize the Euler equation describing the downstream pressure flow field. Small amplitude higher-mode disturbances conform to this condition. Hence, the prestall waves occurring when the compressor is operating near the stall point will not violate this condition as long as their amplitude remains small.

- No loss of total pressure across the IGV's & SGV's - The flow turning by the guide vanes is relatively small and the incidence angle is not large; therefore, separation should not be a problem. The solidity of the IGV's is 1.39 and 0.53 for the SGV's; since these solidities are not large, pressure

losses originating in the boundary layers of the guide vanes will be of little effect relative to the pressure rise through the compressor.

- IGV's and SGV's function as a single IGV blade row - The IGV's provide an initial swirl to the flow; this reduces the losses and amount of turning that must be performed by the zero-camber SGV's. The SGV's were modeled with an initial nonzero stagger angle by Longley [27], and the fixed IGV's only help to reduce the flow deviation and improve the accuracy of that model. The unimportance of mean flow turning on SGV disturbance generation was also shown experimentally by Silkowski [20]. Therefore, the model only needs to consider the effects of periodic SGV stagger angle perturbations.

- IGV's and SGV's have an infinitesimal axial chord and are immediately upstream of the actuator disk - This assumption simplifies the model by discounting the decay in perturbations as they travel between the compressor and the guide vanes. This assumption is more accurate for the first mode than it is for the higher modes. The accuracy of this assumption and ways of overcoming its limitations are discussed in Section 3.1.4.

- SGV perturbations during control are small - The behavior of the flow in the SGV's is modeled for small changes in stagger angle between adjacent blades. Additionally, the fluid inertia parameter for the flow through the SGV's is based on stagger angle and is assumed to be a constant. Since the actual changes in SGV stagger angle during active control were only $\pm 4°$, this was an accurate assumption.

- Velocity perturbations are small - This assumption is necessary if the perturbations are to be modeled and controlled using linear methods.

Modal disturbances were at most $\pm$ 1.5 m/sec during stable active control when the mean flow velocity was greater than 31 m/sec. From these quantities, it seems that the perturbations are small enough (less than 5%) to be treated as linear.

3.1.2 Notation

3.1.2.1 Nondimensionalization

To express the compressor equations and parameters in a general form, all variables were nondimensionalized. The parameters used in nondimensionalization are as follows:

R - The mean of the hub and tip compressor radius was used to nondimensionalize length. (length)/R

U - The mean rotor blade velocity, equal to $2\pi\omega R$, was applied to quantities of speed. (speed)/U

ρ - The air density under standard operating conditions was used in conjunction with the other variables to nondimensionalize pressure. (pressure)/ρ U^2

These variables were used to nondimensionalize time as well, (time)·U/R.

3.1.2.2 Independent Variables

The compressor model shown in Figure 3.1 has two spatial degrees of freedom and one degree of freedom in time. The notation used to describe these independent variables is:

η - nondimensional axial position in the compressor. At station 0, the front face of the IGV's, η=0.

θ - annular position in radians measured from top dead center of the annulus.

$\bar{t}$ - nondimensional quantification of time. Time zero can be any fixed reference time.

3.1.2.3 Dependent Variables

Five quantities describing the flow field are used in the model. These quantities are, in general, variable in both time and space.

$P_s(\eta,\theta,\bar{t})$ - local static pressure, (static pressure)/ρU^2

$P_t(\eta,\theta,\bar{t})$ - local total pressure, (total pressure)/ρU^2

$\Phi(\eta,\theta,\bar{t})$ - local flow potential, (flow potential)/UR

$\phi(\eta,\theta,\bar{t})$ - local flow coefficient, (axial velocity)/U. This quantity is related to flow potential by $\phi = \partial\Phi/\partial\eta$

$\gamma(\theta,\bar{t})$ - local SGV stagger and exit flow angle as would be produced by a continuum of SGV blades

3.1.2.4 Parameters Characterizing the Compressor

The semi-actuator disk model of the compressor requires several parameters describing the compressor's performance and geometry. These parameters and the parameter describing the velocity feedback location are

$\psi(\phi,\gamma)$ - steady-state total-to-static pressure rise across the compressor, $(P_{s,3}-P_{t,1})/(\rho U^2)$

$\psi_T(\phi,\gamma)$ - ideal isentropic total-to-static steady-state compressor pressure rise which follows from the torque work done on the air. It is determined from the torque characteristic in the following way:

$$\psi_T(\phi,\gamma) = \frac{T}{\phi} - \frac{\phi^2}{2}\left(1+\tan^2\alpha_{S3}\right). \tag{3.1}$$

$\psi_i(\phi,\gamma)$ - ideal total-to-static steady-state compressor pressure rise. This is calculated using the Euler equation for pressure rise across a blade row. For the three-stage compressor it has the form

$$\psi_i(\phi,\gamma) = 3 - \phi\left[\tan\gamma + \left[\sum\tan\alpha\right] - \tan\alpha_{S3}\right] - \frac{\phi^2}{2}\left(1+\tan^2\alpha_{S3}\right) \tag{3.2}$$

where α is consecutively the rotor and stator flow exit angle of each stage, γ is the flow exit angle of the SGV's, and α_{S3} is the flow exit angle of the last stator stage which determines exit swirl.

λ - rotor fluid inertia. This parameter quantifies the inertial path length through the compressor's rotors. It is defined to be:

$$\lambda = \sum \frac{b_R}{\cos(\gamma_R)} \tag{3.3}$$

where b_R is the nondimensional mid-span blade chord for each set of rotor blades and γ_R is the mid-span stagger angle for the blades of each rotor. Table 2.1 provides the pertinent data for calculating λ.

μ_C - compressor fluid inertia (excluding SGV's). This parameter accounts for the fluid inertia in the stator passages as well as in the rotor passages. It is defined as:

$$\mu_C = \lambda + \Sigma[\, b_S/\cos(\gamma_S)\,] \tag{3.4}$$

where b_S is the nondimensional mid-span blade chord for each set of stator blades and γ_S is the mid-span stagger angle for the blades of each stator. Table 2.1 contains the data needed to make this calculation.

μ_{SGV} - SGV inertia. This parameter accounts for the inertial effects of the flow accelerating/decelerating through the nozzle/diffuser passages created by the SGV's. It is defined as

$$\mu_{SGV} = b_{SGV}/\cos(\bar{\gamma}) \tag{3.5}$$

where b_{SGV} is the nondimensional blade chord of the SGV's and $\bar{\gamma}$ is the nominal stagger angle of the blades. Table 2.1 has the pertinent data for calculating this.

μ - total fluid inertia in the compressor including SGV's:

$$\mu = \mu_{SGV} + \mu_C. \tag{3.6}$$

η_{HW} - nondimensional axial position for axial velocity measurements. This parameter is important for determining the relationship between the measured upstream flow perturbations and the flow perturbations in the compressor.

3.1.2.5 Parameter Perturbations

The compressor model takes the unsteady variations of various dependent variables and expresses their relationship to each other. When disturbances are small,

they can be described in a linearized form. The general form of a perturbed parameter X is

$$X = X_{ss} + \delta X$$

where X_{ss} is the steady-state and annulus-averaged value of X and δX is the magnitude of the perturbation. When the perturbation of an independent variable I is small, the following linear approximation applies to the dependent variable:

$$X(I) = X_{ss}(I) + \frac{\partial X}{\partial I}\,\delta X$$

These definitions are implicit in the equations describing the compressor.

3.1.2.6 Spatial Fourier Coefficients (SFC's)

In general, perturbations δX which vary in the θ direction have an implicit periodicity around the compressor annulus. These perturbations are given a Fourier series modal description in the final form of the solution to the compressor equations. A unique method of performing the Fourier decomposition is used so that the coefficients are physically meaningful. The formula for determining the n^{th} spatial Fourier coefficient (SFC) $\tilde{X}_n$ is

$$\tilde{X}_n = \frac{2}{\pi}\int X(\theta)e^{in\theta}d\theta$$

and the true form of the perturbation is recomposed by the formula

$$X(\theta) = \sum_{n>0} Re[\tilde{X}_n^* e^{in\theta}].$$

The asterisk * indicates the complex conjugate. These formulas differ from the standard Fourier series definition by the sign of the exponents. This definition for the transformation makes $|\tilde{X}_n|$ the amplitude of the measured disturbance at its peak, and $\angle\tilde{X}_n$ corresponds to the physical orientation in θ of the peak.

3.1.3 Compressor Model Equations and their Solution, Model 1

The form of the compressor model presented in this section is the same as the model used by Paduano [16]. The simplest form of the linearized compressor model was first given by Moore [7] and later modified by Moore & Greitzer [8]. Epstein et al [15]

introduced the concept of wave launchers to damp the compressor, and Longley [27] modeled SGV actuators with the compression system, giving the model the form that it has here. The linearized partial differential equations describing the SGV actuated compression system as developed by Paduano are

Upstream:

$$\nabla^2(\delta\Phi) = 0 \tag{3.7}$$

$$\delta\phi_1 = \frac{\partial(\delta\Phi_1)}{\partial\eta} \tag{3.8}$$

Compressor:

$$\begin{aligned} 0 = & -\frac{\partial(\delta\Phi_1)}{\partial\bar{t}} - \mu_{SGV}\frac{\partial(\delta\phi_2)}{\partial\bar{t}} - \frac{\bar{\phi}}{2}\cdot\mu_{SGV}^2\frac{\partial^2(\delta\gamma)}{\partial\theta\partial\bar{t}} + \frac{\partial\psi}{\partial\phi}\delta\phi_2 \\ & + \frac{\partial\psi}{\partial\gamma}\delta\gamma - \mu_C\frac{\partial(\delta\phi_2)}{\partial\bar{t}} - \lambda\frac{\partial(\delta\phi_2)}{\partial\theta} - \delta P_{s,3} \end{aligned} \tag{3.9}$$

$$\delta\phi_2 = \delta\phi_1 - \bar{\phi}\cdot\mu_{SGV}\frac{\partial(\delta\gamma)}{\partial\theta} \tag{3.10}$$

Downstream:

$$\frac{\partial(\delta P_{s,3})}{\partial\eta} = -\frac{\partial(\delta\phi_2)}{\partial\bar{t}} \tag{3.11}$$

$$\nabla^2(\delta P_s) = 0 \tag{3.12}$$

By applying the boundary conditions that Φ and δP_s are periodic in θ and decay to zero far upstream and far downstream respectively, their solutions can be written in the form

$$\delta\Phi = \sum_{n>0}\mathrm{Re}\left\{A_n^*(\bar{t})\cdot e^{n\eta}\cdot e^{in\theta}\right\} \tag{3.13}$$

$$\delta P_s(\text{downstream}) = \sum_{n>0}\mathrm{Re}\left\{\delta\tilde{P}_{s,3,n}^*(\bar{t})\cdot e^{-n\eta}\cdot e^{in\theta}\right\}. \tag{3.14}$$

Equations 3.7 to 3.12 can be transformed to match the modal form of these solutions by decomposing the perturbation variables into their SFC's using the method described in Section 3.1.2.6. The perturbations $\delta\phi_2$ and $\delta\gamma$ are decomposed in this way, but to make the final equation useful for modeling experiments, $\delta\phi_1$ is decomposed in terms of the upstream flow coefficient at the hot-wire flow measurement station as follows:

$$\delta\phi_1 = \sum_{n>0}\mathrm{Re}\left\{\tilde{\phi}_n^*(\bar{t})\cdot e^{-n\eta_{HW}}\cdot e^{in\theta}\right\} \tag{3.15}$$

Here $\tilde{\phi}_n$ is the SFC at the hot-wire measurement station. From these solutions and definitions, the following description of the unsteady compressor behavior is obtained:

$$A_n = \frac{e^{-n\eta_{HW}}}{n} \cdot \tilde{\phi}_n \tag{3.16}$$

$$0 = \sum_{n>0} \mathrm{Re}\left\{\left[-\dot{A}_n - \mu_{SGV}\dot{\tilde{\phi}}_{2,n} + in\cdot\frac{\bar{\phi}}{2}\cdot\mu_{SGV}^2\cdot\dot{\tilde{\gamma}}_n + \frac{\partial\psi}{\partial\phi}\tilde{\phi}_{2,n} + \frac{\partial\psi}{\partial\gamma}\tilde{\gamma}_n - \mu_C\dot{\tilde{\phi}}_{2,n} + in\cdot\lambda\cdot\tilde{\phi}_{2,n} - \delta\tilde{P}_{s,3,n}\right]^*\cdot e^{in\theta}\right\} \tag{3.17}$$

$$\tilde{\phi}_{2,n} = e^{-n\eta_{HW}}\cdot\tilde{\phi}_n + in\cdot\bar{\phi}\cdot\mu_{SGV}\cdot\tilde{\gamma}_n \tag{3.18}$$

In deriving this form of the model the assumption that $\eta_1 = \eta_2 = 0$ was used. This modal description of the compressor can be further simplified by means of a straightforward substitution. Due to linearity each of the modal solutions is independent of the others; this allows a general expression describing the dynamics of any mode n to be written as:

$$e^{-n\eta_{HW}}\cdot\left[\frac{2}{n}+\mu\right]\dot{\tilde{\phi}}_n = e^{-n\eta_{HW}}\cdot\left[\frac{\partial\psi}{\partial\phi}+in\cdot\lambda\right]\tilde{\phi}_n + \left[\left(\frac{\partial\psi}{\partial\gamma}-n^2\bar{\phi}\lambda\mu_{IGV}\right)+in\bar{\phi}\mu_{IGV}\frac{\partial\psi}{\partial\phi}\right]\tilde{\gamma}_n - in\bar{\phi}\mu_{IGV}\left[\frac{1}{n}+\mu-\frac{\mu_{IGV}}{2}\right]\dot{\tilde{\gamma}}_n \tag{3.19}$$

From this expression, "Model 1" predictions of open-loop dynamics were calculated. A physically more meaningful form of the expression is

$$\dot{\tilde{\phi}}_n = \frac{1}{\frac{2}{n}+\mu}\left\{\left[\frac{\partial\psi}{\partial\phi}+in\cdot\lambda\right]\tilde{\phi}_n + e^{n\eta_{HW}}\cdot\left[\left(\frac{\partial\psi}{\partial\gamma}-n^2\bar{\phi}\lambda\mu_{SGV}\right)+in\bar{\phi}\mu_{SGV}\frac{\partial\psi}{\partial\phi}\right]\tilde{\gamma}_n - in\bar{\phi}\mu_{SGV}e^{n\eta_{HW}}\cdot\left[\frac{1}{n}+\mu-\frac{\mu_{SGV}}{2}\right]\dot{\tilde{\gamma}}_n\right\} \tag{3.20}$$

The imaginary part of the coefficient for $\tilde{\phi}_n$ is the open-loop frequency of the n^{th} mode predicted by the model, and the real part of the coefficient for $\tilde{\phi}_n$ indicates whether the

mode will grow (positive) or decay (negative) in an open-loop situation. To simplify the discussion of the model, the coefficients in Equation 20 will be reduced to

$$\dot{\tilde{\phi}}_n = (\sigma_n + i\cdot\omega_n)\tilde{\phi}_n + (b_{r,n} + i\cdot b_{i,n})\tilde{\gamma}_n + i\cdot g_{i,n}\cdot\dot{\tilde{\gamma}}_n \qquad (3.21)$$

This form indicates more clearly that ω_n is the frequency of the mode and σ_n is the growth rate. In even more general discussions the model may be described in the form

$$\dot{\tilde{\phi}}_n = A\tilde{\phi}_n + B\tilde{\gamma}_n + G\dot{\tilde{\gamma}}_n. \qquad (3.22)$$

The transfer function of the compressor can then be written as

$$G_n(s) = \frac{B+Gs}{s-A}. \qquad (3.23)$$

3.1.4 Evaluation of Parameters

Equation 3.20 shows that only six fundamental parameters, besides the mode number n and mean flow coefficient $\overline{\phi}$, are needed to characterize the dynamics of any mode. In this analysis, these parameters (λ, μ_{SGV}, μ, η_{HW}, $\frac{\partial\psi}{\partial\phi}$, $\frac{\partial\psi}{\partial\gamma}$) were evaluated to represent the MIT three-stage axial research compressor. Some of these parameters (λ, μ_{SGV}, μ) are derived solely from the compressor geometry. These are calculated by the method described in Section 3.1.2.4 using the data in Table 2.1, although there have been other methods of evaluation suggested that take into account the inter-blade-row gaps [7]. These three parameters are easily calculated for any compressor, but the other three are harder to assess accurately without using measurements of the flow in the compressor during operation.

The axial distance η_{HW} from the hot-wire measurement station to the compressor was evaluated as the distance to the face of the first rotor (η_{HW} = -.60). From the purely theoretical standpoint, the front face of the IGV's should be considered to be the front of the compressor from which modal disturbances begin their upstream decay; this would set $(\eta_{HW})_{IGV\,face}$ = -.19. However, substitution of experimental measurements of first mode strength (Figure 5.5) into the theoretical expression for their decay outside the compressor indicates that modal disturbances actually decay between

the first rotor and the IGV face. Section 5.1.2 discusses these measurements in greater detail. The decay of the first mode differs from the theoretical decay by a distance that can be accounted for by the IGV-SGV and SGV-R1 inter-blade-row gaps, $(\eta_{HW})_{IGV\,face\,\&\,gaps}$ = -.25. However, the decay of the second mode disturbances was calculated from flow measurements to occur over a distance $(\eta_{HW})_{Mode\,2}$ = -.64 which is most accurately modeled by the distance from the hot-wires to the face of the first rotor. This phenomenon can be explained in part by the relatively small solidity of the SGV's which allows them to be less "visible" to higher modes. It is concluded that if only one value of η_{HW} is to be used for all modes, the distance to the face of the first rotor is the best approximation for modes n>1.

Determining the pressure rise as a function of ϕ or γ can be approached in a theoretical manner, but the accuracy of such methods in modeling a multistage compressor is still rather limited. In order to test the actual reliability of the compressor model and not the reliability of these relatively crude theoretical approximations of the term ψ, a function for ψ derived from experimental measurements was used. The function for ψ needs to be most accurate for flow coefficients near the stall point. It is the slope of ψ in this region that is of greatest significance to the compressor model, so only data around this point were used in determining a parabolic approximation of ϕ. Pressure rise data from the uncontrolled compressor continue beyond the peak value of ψ and can give a function for ψ that is fairly accurate for flow coefficients below the stall point. However, to insure optimum accuracy and decrease the range over which data are obtained by extrapolation, data from operating points which are stable during closed-loop control but lie below the stall point of the uncontrolled compressor were included in determining the ψ function. Figure 3.2 illustrates this extended pressure rise characteristic fitted with a parabolic curve to match the curvature of the high pressure rise region. Figure 3.3 shows the slope of this parabolic fit to the compressor characteristic. For comparison, the slope of the parabolic fit to the unextended

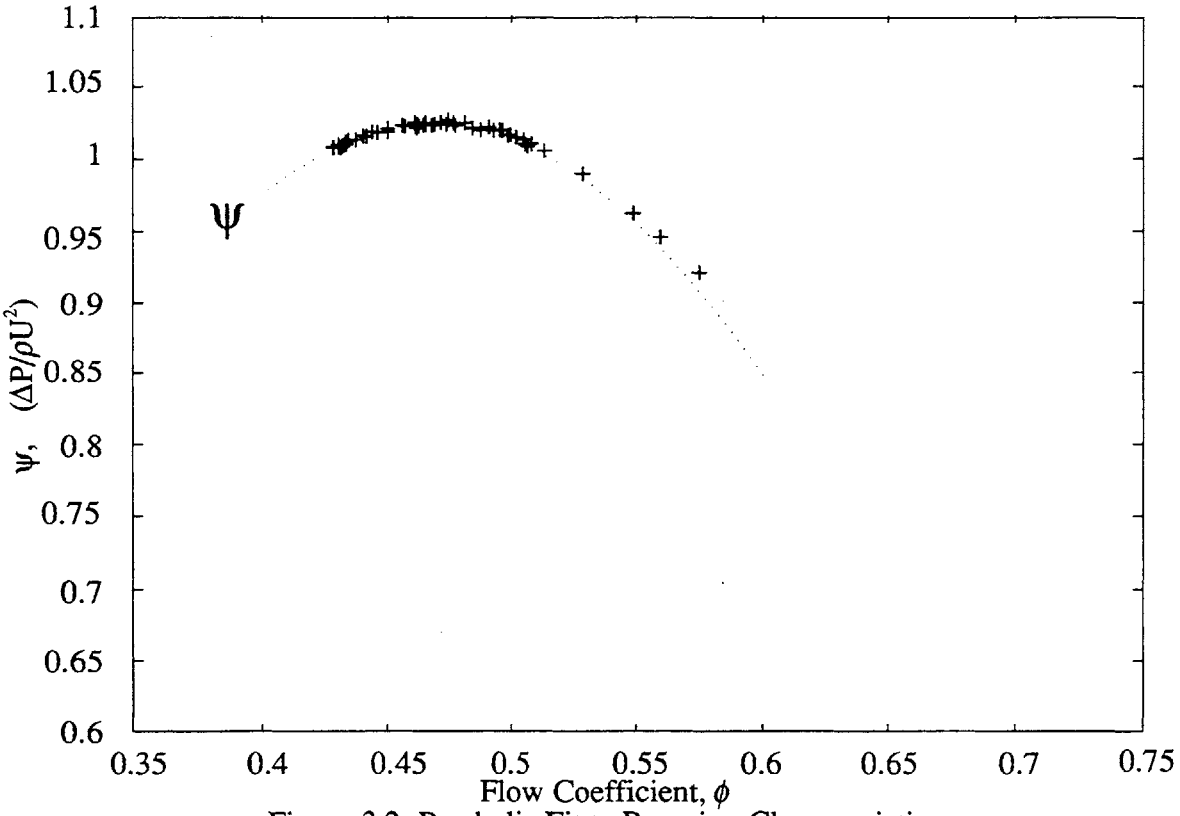

Figure 3.2: Parabolic Fit to Pumping Characteristic

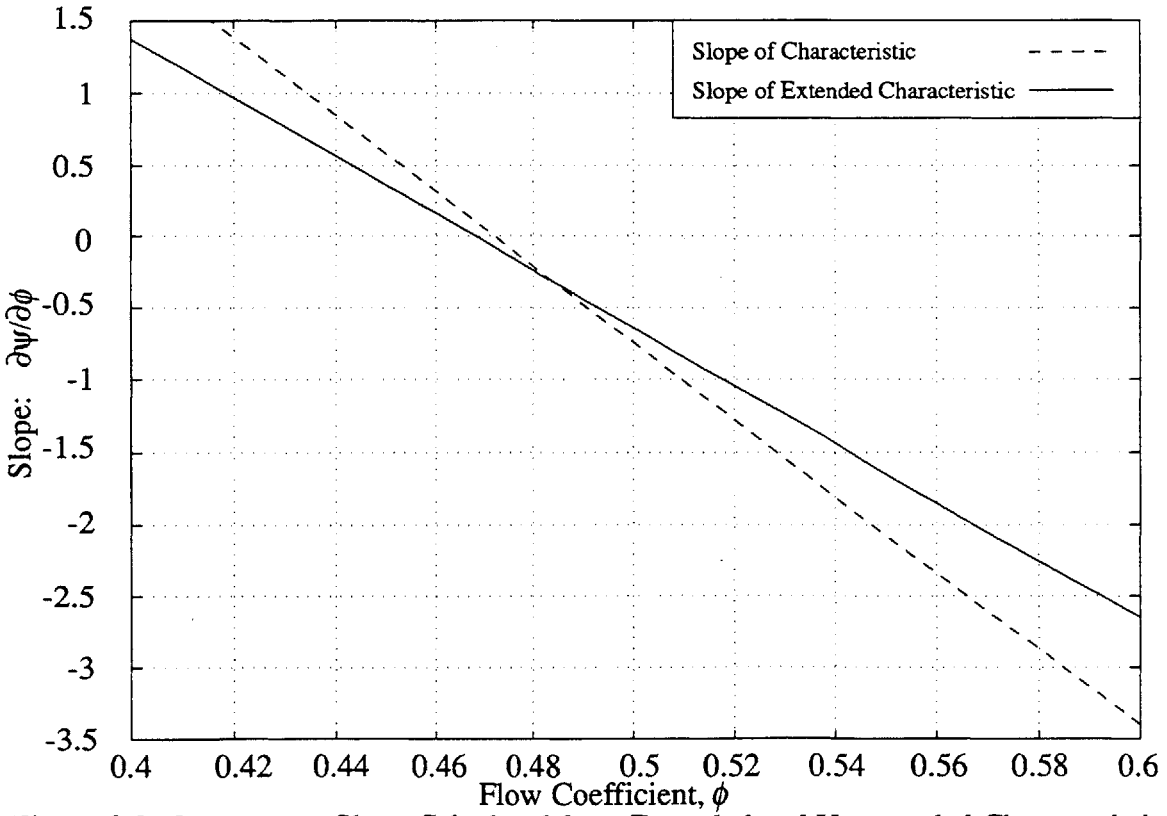

Figure 3.3: Compressor Slope Calculated from Extended and Unextended Characteristics

compressor characteristic is also shown. More typically, this would be the type of data that would be available for developing a model.

The $\frac{\partial\psi}{\partial\gamma}$ parameter was evaluated experimentally using the data from several extended compressor characteristics that differed only by their IGV stagger angle. A parabolic fit was made to the low flow portion of the pressure rise characteristics with -1.9°, 3.1°, 8.1°, 13.1°, and 18.1° SGV stagger angles (Figure 3.4), and by means of a least squares method the best expression for $\frac{\partial\psi}{\partial\gamma}$ was determined. Figure 3.5 plots the functional form of $\frac{\partial\psi}{\partial\gamma}$ determined from experimental measurements. The figure also shows the functional form of $\frac{\partial\psi}{\partial\gamma}$ that would be obtained from data for unextended compressor characteristics. A summary of the mathematical expressions and numerical values for each of the model's parameters is given in Table 3.1.

3.1.5 Discretization

The modes in the compressor are spatially continuous around the annulus, but the sensors and actuators are spatially discrete. This implies that the measured signals and the disturbances created by the actuators will be to some degree only approximations of spatially continuous modes. In each case the accuracy of these approximations is best for the first mode and decreases for higher modes.

Eight evenly spaced hot-wires were used for sensing modal velocity disturbances in the flow. The array of eight hot-wires positioned around the upstream annulus could resolve a maximum of three modes according to the definition of the discrete Fourier transformation (DFT):

$$\tilde{\phi}_n(\eta,\bar{t}) \equiv \frac{2}{K}\sum_{k=0}^{K-1}\delta\phi(\eta_{HW},\theta_k,\bar{t})\cdot e^{jn\theta_k} \tag{3.24}$$

where

$$\theta_k = \frac{2\pi k}{K}, \quad k = 1, 2, \ldots K,$$

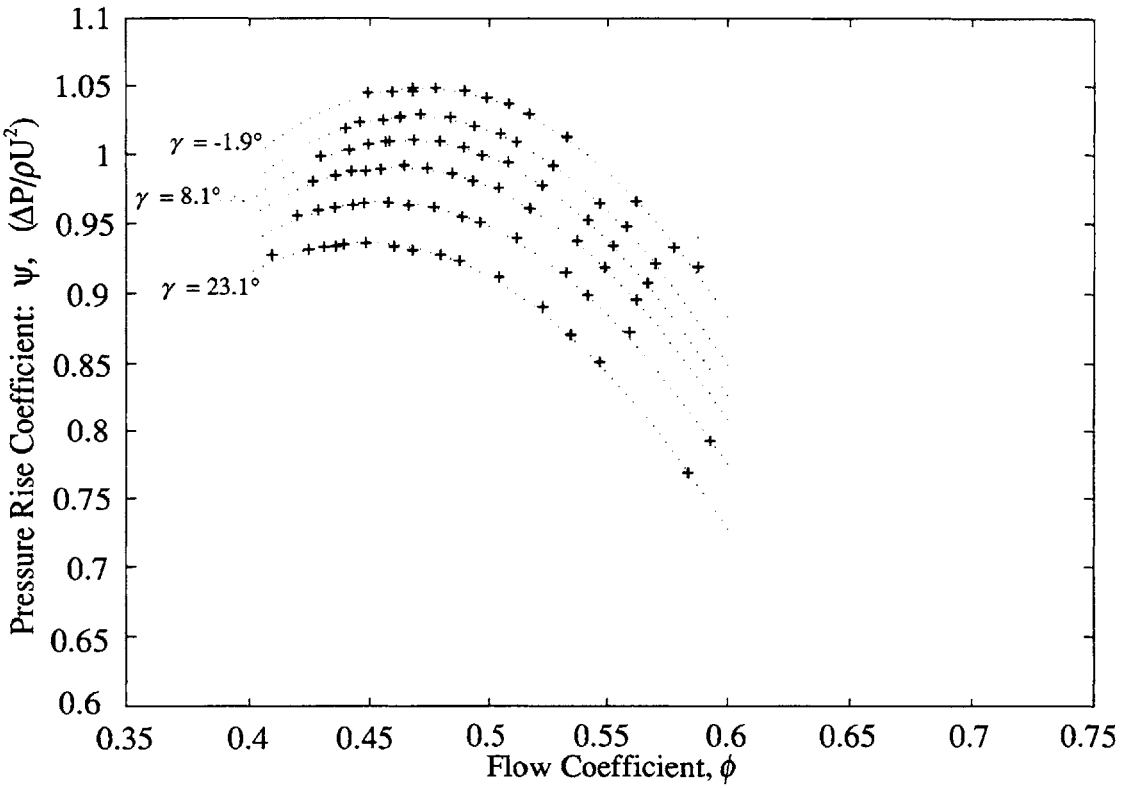

Figure 3.4: ψ vs ϕ for $-1.9° < \gamma < 23.1°$ in 5° intervals

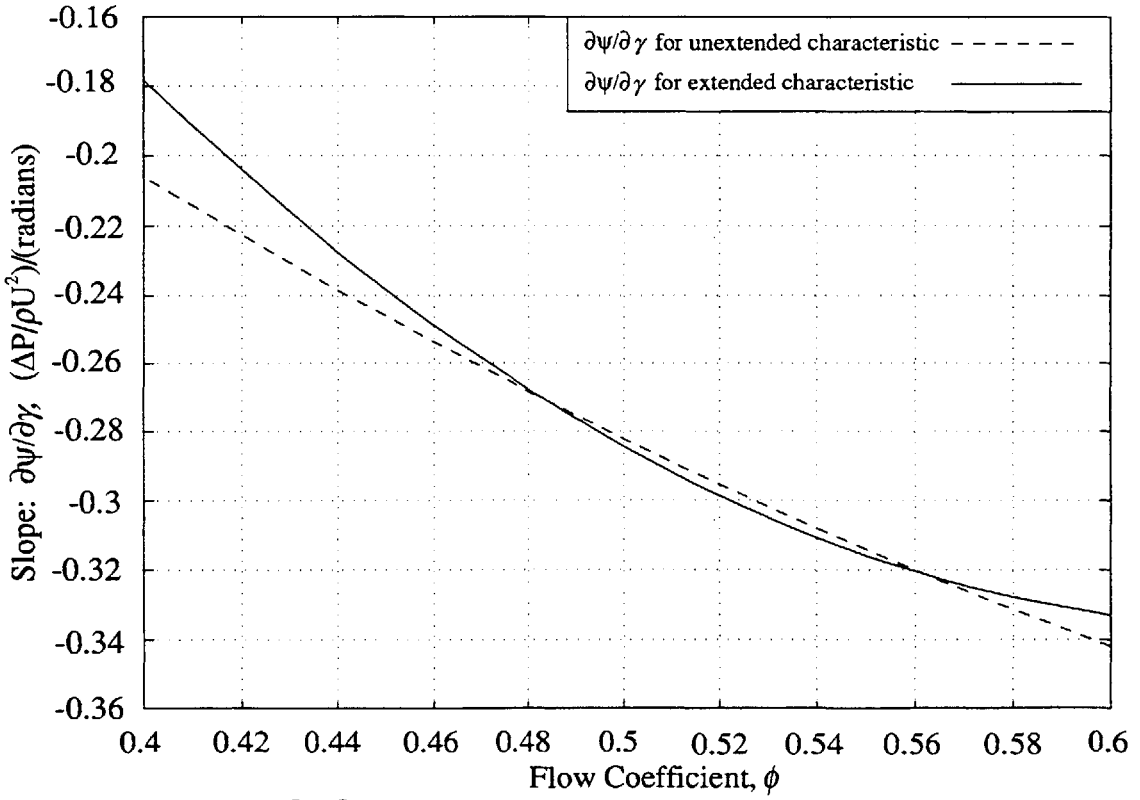

Figure 3.5: $\partial\psi/\partial\gamma$ Calculated from Extended and Unextended Characterisics

and K=8 is the number of hot-wires. Cross-coupling in the measurement of modal disturbances could not occur between the first three modes because the disturbances are truly periodic around the annulus and the hot-wires were evenly spaced. These conditions guarantee the precision of the DFT for signals with only first, second, and third mode content. Aliasing of modes numbered higher than the fourth (n>K/2) does degrade the DFT, but modal disturbances of this order are attenuated because of their distance from the compressor face. Using $\eta_{HW} = -.60$ as was determined above, fifth mode (n=5) disturbances are calculated to decay by a factor of $e^{-n\eta_{HW}} = 0.049$; this is less than a third of the strength of any of the first three modes, which by the time they reach the hot-wire measurement station will have decayed by factors of 0.547, 0.299, and 0.164 respectively. Noise in the signal also contributes to decreased modal resolution when performing a DFT. The largest recorded signal-to-noise ratios before stall were 46 dB, 29 dB, and 23 dB for the first three modes respectively. The cumulative effect on modal resolution is that third mode resolution is degraded the most. Problems with controlling higher-mode disturbances are also compounded by the decreasing capability of the actuators to generate perturbations of increasing mode number.

Twelve evenly spaced SGV's were used for feedback control. Their angular displacements were determined by applying the specified control law to the measured modal disturbances and summing the discretized contribution of each mode for each SGV. This calculation is expressed mathematically as

$$\delta\gamma(\theta_m,\tilde{t}) = \sum_{n=-5}^{6} \mathrm{Re}\left\{\tilde{\gamma}_n^*(\tilde{t})\cdot e^{in\theta_m}\right\} \tag{3.25}$$

where

$$\theta_m = \frac{2\pi m}{12},\ m = 0, 1, 2, ..., 11.$$

Theoretically, the SGV's could produce disturbances for the first five modes, but in reality the discrete nature of the SGV's limits them to merely creating an approximation of a truly sinusoidal flow disturbance even for the first mode. Calculations by Silkowski

[22] revealed that the array of 12 SGV's could produce first mode disturbances with very little excitation of the other modes. The most significant coupling was with the 12th mode, but these disturbances decay very rapidly because of their high mode number. Attenuation of the desired SGV modal disturbances was also shown by Silkowski to be significant when the solidity of the SGV's is not infinite.

3.2 Additional Dynamic Considerations

When modeling the behavior of the actively controlled compressor, the dynamics of the components in the feedback path were accounted for to improve the accuracy of the closed-loop predictions. The discretization of the compressor flow field required that feedback signals be transferred through separate channels, but the dynamics of each channel were kept essentially the same. Paduano [16] showed that the transfer function for similar components in separate channels is the same as the transfer function acting on each SFC in the feedback loop. Because of this, the development of the transfer function for the SFC feedback dynamics focuses on the dynamics of individual components.

Figure 3.6 illustrates the component models that were used in the feedback loop. The compressor dynamics for each mode are designated $G_n(s)$, and the general form of the control law for each SFC is shown. As will be discussed, several things contribute to the feedback time delay designated D(s). The zero order hold (ZOH) sampling of the filtered hot-wire signals by the A/D is also modeled. The dynamics of the IGV actuators are represented by the transfer function A(s). Together these models account for the dynamics of all components outside of the compressor itself.

3.2.1 Time Lags in the Feedback Path

Time lags in the feedback are inevitable because of limitations on sensing and the finite bandwidth of the physical devices. Increasing either the time lag or the disturbance's forcing frequency degrades the closed-loop stability of a system with response lag. The feedback system was designed to be fast enough to handle the

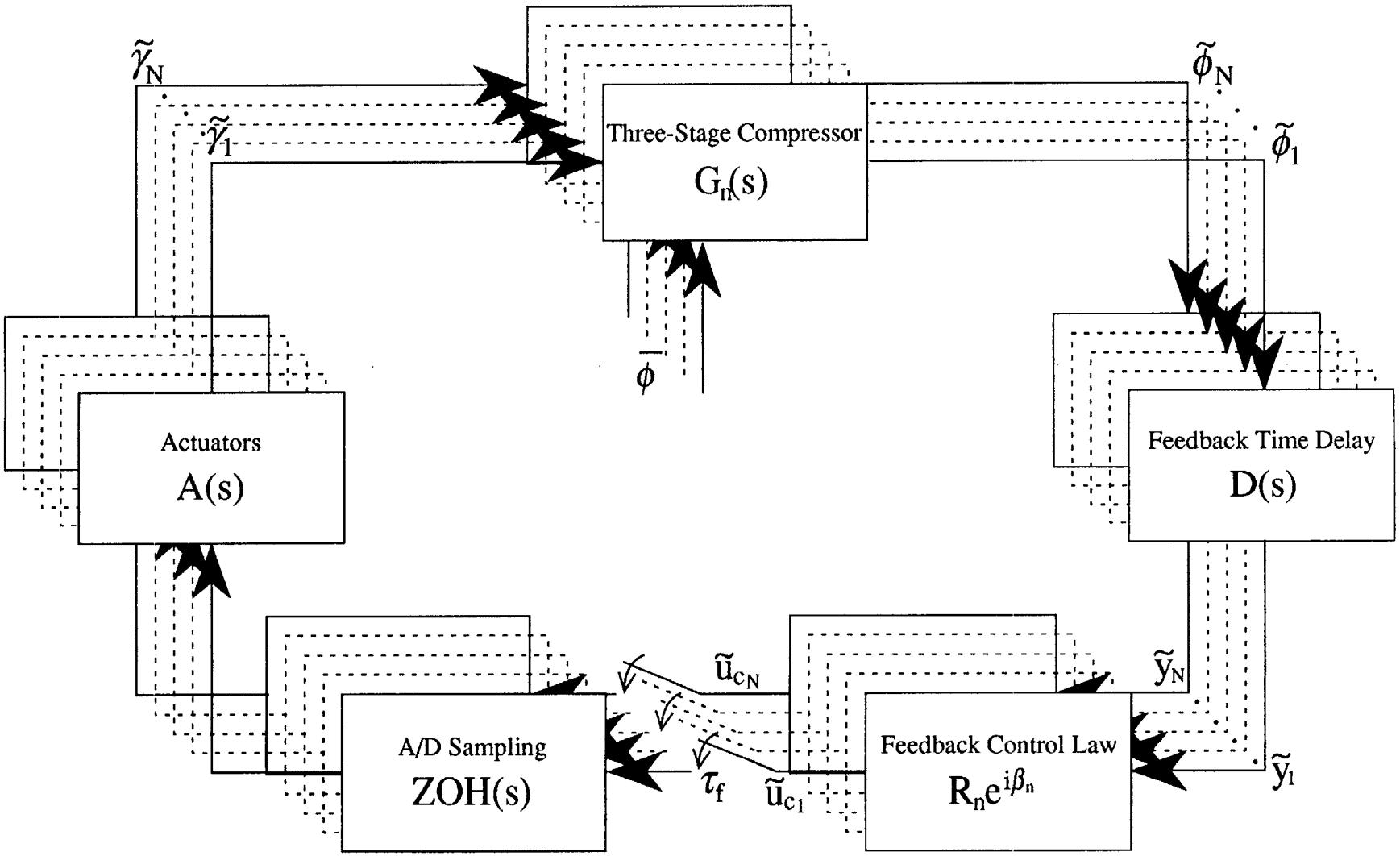

Figure 3.6: Model of Closed-Loop Dynamics

disturbance frequencies of the first few modes, but this also required minimizing the time lag in the feedback path. The first source of lag in the feedback path is in the sensing of the compressor state. The compressor flow field is assumed to be uniform, but there exists a lag time for the signal to travel upstream to the hot-wires. The modeled distance from the hot-wires to the compressor was discussed in Section 3.1.4, and it is assumed that the flow disturbances travel this distance at the speed of sound. From this, the time for the compressor disturbance to reach the hot-wires is calculated to be 0.498 msec ($\tau_{t,1}$=0.125).

The second source of delay is associated with the sensors and signal filters. The hot-wire anemometers were set to a bandwidth of 50 kHz. With such a rapid response it is reasonable to ignore any time lag between the sensed flow velocity and the voltage signal produced by the anemometer. The hot wire signal filters, on the other hand, did introduce a time lag. One of property of Bessel filters is that the time lag associated with each frequency, up to the cutoff frequency, can be considered to be the same. For this reason, modeling the Bessel filter dynamics as a pure delay is justifiable. With the cutoff frequency set to 1000 Hz, the filters introduced a .34 msec ($\tau_{t,2}$=.085) time delay in the signal being sent to the A/D.

Accompanying the implementation of the control law by the computer is a time delay. The computer reads the signals on the A/D, computes their SFC's, calculates the feedback SFC's based on the control law, constructs the discrete servo commands from the calculated feedback SFC's, and commands the motion control boards to position the servos. This whole process was performed by the computer in an average time of 0.75 msec ($\tau_{t,3}$=0.19); the model uses this delay as the lag time between acquiring hot-wire data and sending the signal to the servos, i.e. the computational delay.

The servo control system was complex, but its transfer function was easily reproduced by two equivalent second order systems in series (Section 3.2.3), a zero order hold, and a pure delay. The time delay between issuing a displacement command to an

SGV and having it actually go to the desired position was 0.75 msec ($\tau_{t,4}$=0.19) according to the servo model. This time delay is believed to be created primarily by the signal amplifier, and it is lumped with the other delays when modeling the closed-loop system.

Outside of the compressor, there are no other pure delays to be modeled. Lags in the fluid response in the compressor can actually help stabilize it, unlike a pure time delay in the feedback loop. This will be seen in the alternative forms of the model.

The transfer function of the total time delay in the feedback loop can be represented by the Laplace transform of a pure time delay. It is written in the form

$$D(s) = e^{-\tau_t s}. \tag{3.26}$$

This expression determines the time induced phase shift for signals of any frequency. Because of its exponential form, it can be shown that any time delay introduces an infinite number of poles to the closed-loop dynamics. This complicates the modeling of the closed-loop dynamics, but only one pole is significant if disturbance frequencies are low. Because the modal frequencies being considered are associated with small phase shifts, the following linear approximation of the delay time was used in the feedback model:

$$D(s) = \frac{1 - \frac{\tau_t}{2}s}{1 + \frac{\tau_t}{2}s} \tag{3.27}$$

This linear approximation accurately models the unity gain and for low frequencies the complex phase as well. The cumulative delay was 2.33 msec which when nondimensionalized sets τ_t=0.587. The linearized approximation of time delay has a positive bias, but it is only 5% for phase shifts of $\pi/4$ which, according to the calculated delay, corresponds to 54 Hz signals. This means the time delay phase shift approximation has an error of approximately 5% for third mode disturbances and an even smaller error for the second and first modes.

3.2.2 Zero Order Hold (ZOH) Feedback

The sample and hold dynamics introduced in a discrete-time control system can be given a continuous time representation. The sample and hold is modeled as the difference between a unit step and a delayed unit step normalized by the delay time [31]:

$$\mathrm{ZOH}(s) = \frac{1}{\tau_f s}(1 - e^{-s\tau_f}) \tag{3.28}$$

In this expression τ_f is the period of the discrete-time control loop which in this case was 2.00 msec or $\tau_f = 0.503$ in nondimensional form. Because the exponential form of this expression would introduce an infinite number of poles to the continuous representation of the controlled system, it too was linearized. The linearized form of this expression which was used in modeling the feedback dynamics is:

$$\mathrm{ZOH}(s) = \frac{1}{1 + \frac{\tau_f}{2}s} \tag{3.29}$$

This introduces an additional lag in the feedback and attenuation of high frequency signals. In this case, the linear expression has at most a positive bias of only 2.4% for phase shifts of $\pi/4$ which, according to the calculated delay, corresponds to 63 Hz signals (i.e. for the first three modes).

3.2.3 Closed-Loop Actuator Dynamics

The servo motor dynamics were also included in the model of the feedback path dynamics. The servo motor closed-loop transfer function was determined while operating the compressor near the stall point by exciting one mode of the spatial array of motors with a pseudo-random binary signal (PRBS) having a minimum pulse width of 100 Hz and by simultaneously reading the blade positions given by the optical encoders. Figure 3.7 shows the Bode plot of the servo motor responses. The spikes in the calculated response are due to the bandwidth limitations of the input signal [16]. Imbedded in the servo response are a time lag, ZOH effects, and the actual actuator dynamics A(s). Two equivalent second order systems in series reproduced the actuator

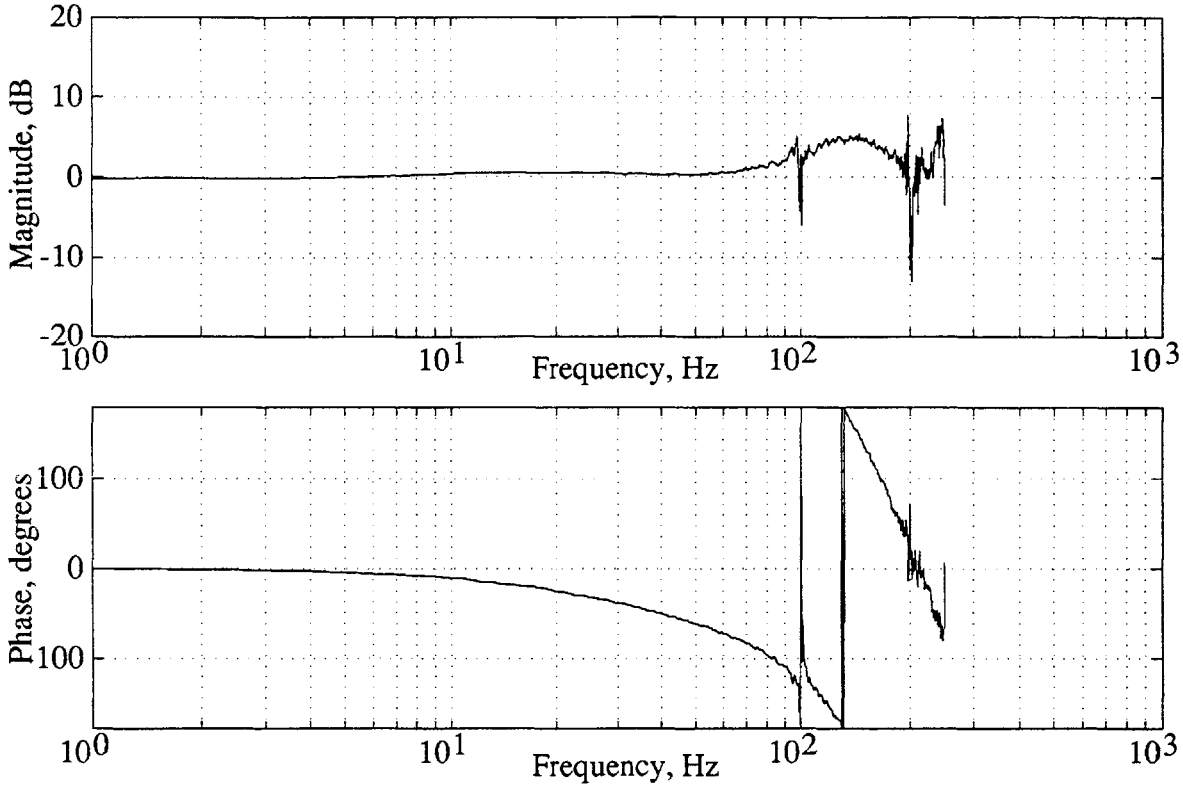

Figure 3.7: Servo Motor Closed-Loop Transfer Function

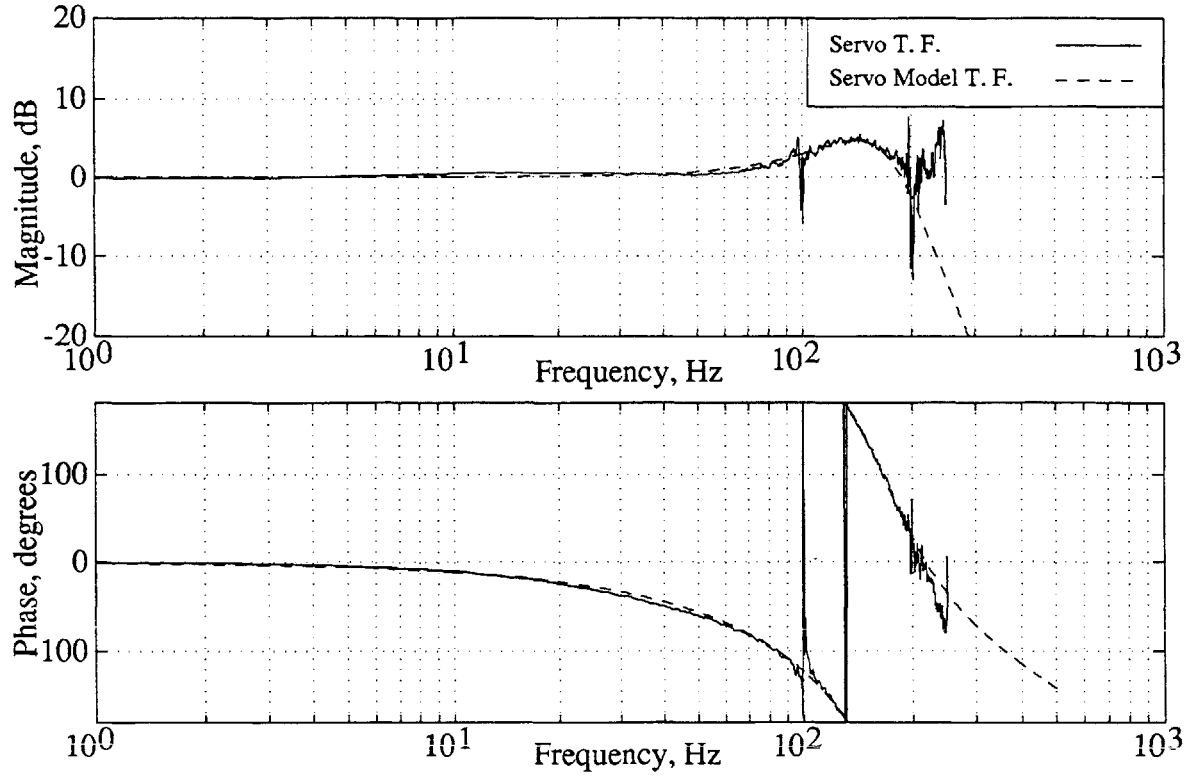

Figure 3.8: SGV Actuator Model Compared with Measured Transfer Function

dynamics very accurately. The fourth order model has the following form:

$$A(s) = \left[\frac{\omega_N^2}{s^2 + 2\omega_N \zeta s + \omega_N^2} \right]^2 . \tag{3.30}$$

This representation limits the model of the actuator dynamics to two parameters. The servo motor transfer function was best matched by choosing a natural frequency of ω_N=170 Hz and a damping ratio of ζ=.35. The actuator dynamics A(s) modeled together with the ZOH and the servo time lag $\tau_{t,4}$ fit the actual transfer function of the servos quite well as is illustrated in Figure 3.8.

3.3 Modeling Unsteady Losses in the Compressor, Model 2

3.3.1 Model Development

Because of its complex behavior, the compressor is clearly the most poorly modeled component of the system, and for this reason any improvements in further modeling of closed-loop dynamics should focus on the compressor model. The compressor model described in Section 3.1.3 ("Model 1") does not account for the fluid dynamic lag in changes in pressure rise across a blade row when there is a flow disturbance. Model 1 treats the compressor's response as instantaneous; by implication the compressor is treated as if it were always in a steady state and matched the steady-state characteristic. This assumption will be increasingly inaccurate with increasing mode number because the higher modes "see" more rapid flow unsteadiness.

A more accurate model of the blade response will account for the hysteresis in the blades' pressure rise response to flow unsteadiness. This hysteresis was recognized early on by Emmons [1]. A first-order lag model of the pressure rise has been shown to match experimental data in research performed by Nagano et al [28], Mazzawy [29], and others. A first-order lag will be adopted here in a second version of the compressor model ("Model 2"). A similar form of this model was also used by Hendricks [30]. It should be noted that the model lumps together the time lag for the rotor rows into one term τ_R and lumps together the time lag for the stator rows into the term τ_S. The time

lag for both the rotors and stators is computed to be proportional to the nondimensional flow-through time across the average rotor, $\bar{t}_R$, or stator, $\bar{t}_S$. This is expressed mathematically as

$$\frac{\tau_R}{\bar{t}_R} = \frac{\tau_S}{\bar{t}_S} = \tau_u. \tag{3.31}$$

The proportionality constant τ_u is a general characterization of the time lag through any blade row nondimensionalized with respect to its flow-through time. The instantaneous pressure rise across the compressor after a flow disturbance is assumed to be equal to the isentropic pressure rise ψ_T. This is chosen because at the time of the flow disturbance no viscous losses associated with the new flow coefficient have yet developed in the blade passage and the compressor performance without viscous losses is described by the isentropic pressure rise characteristic. The rotors and stators have different dynamic characteristics in unsteady flow, and the proportion of the contribution of each was determined by the reaction of the compressor blading. The notation used for the loss of pressure across the compressor in an unsteady flow is

$$\begin{aligned} L_{u,ss} &= \psi_T - \psi \\ L_{uR} &= r\left(L_{u,ss} + \delta L_u\right) = L_{uR,ss} + \delta L_{uR} \quad \text{Rotors} \\ L_{uS} &= (1-r)\left(L_{u,ss} + \delta L_u\right) = L_{uS,ss} + \delta L_{uS} \quad \text{Stators} \end{aligned} \tag{3.32}$$

where r is the reaction of the compressor blading. Using these definitions the Model 2 equations are developed.

This model introduces two new equations for describing the lag in the compressor's pressure rise response in addition to making a few changes in the compressor equation (Equation 3.9). The description of the compressor in Model 2 uses equations 3.7, 3.8, 3.10, 3.11, and 3.12 as before. The expression for the total-to-static pressure balance across the compressor changes the term for the slope of the characteristic $\frac{\partial \psi}{\partial \phi}$ to be the slope of the isentropic characteristic $\frac{\partial \psi_T}{\partial \phi}$ and introduces two

new terms for the lag in the pressure rise response across the rotors δL_{uR} and the stators δL_{uS}

$$0 = -\frac{\partial(\delta\Phi_1)}{\partial\bar{t}} - \mu_{SGV}\frac{\partial(\delta\phi_2)}{\partial\bar{t}} - \frac{\bar{\phi}}{2}\cdot\mu_{SGV}^2\frac{\partial^2(\delta\gamma)}{\partial\theta\partial\bar{t}} + \frac{\partial\psi_T}{\partial\phi}\delta\phi_2$$
$$-\delta L_{uR} - \delta L_{uS} + \frac{\partial\psi}{\partial\gamma}\delta\gamma - \mu_C\frac{\partial(\delta\phi_2)}{\partial\bar{t}} - \lambda\frac{\partial(\delta\phi_2)}{\partial\theta} - \delta P_{s,3}. \quad (3.33)$$

To describe the flow seen by the rotor blade rows the time lag in pressure rise must be written in the rotating reference frame of the rotor:

$$\tau_R\left(\frac{\partial(\delta L_{uR})}{\partial\bar{t}} + \frac{\partial(\delta L_{uR})}{\partial\theta}\right) = \frac{\partial L_{uR,ss}}{\partial\phi}\delta\phi_2 - \delta L_{uR}. \quad (3.34)$$

The time lag in pressure rise across the stators is calculated in a stationary reference frame to be

$$\tau_S\frac{\partial(\delta L_{uS})}{\partial\bar{t}} = \frac{\partial L_{uS,ss}}{\partial\phi}\delta\phi_2 - \delta L_{uS}. \quad (3.35)$$

The first-order lag equations are given in this form by Hendricks [30]. Again, by applying the boundary conditions, putting the solution in modal form, and solving, the following expression for the compressor dynamics is obtained:

$$\dot{\tilde{\phi}}_n = \frac{1}{\frac{2}{n}+\mu}\left[\left(\frac{\partial\psi_T}{\partial\phi} + in\cdot\lambda\right)\tilde{\phi}_n - \tilde{L}_{uR,n} - \tilde{L}_{uS,n}\right.$$
$$+e^{n\eta_{HW}}\left[\left(\frac{\partial\psi}{\partial\gamma} - n^2\bar{\phi}\lambda\mu_{SGV}\right) + in\bar{\phi}\mu_{SGV}\frac{\partial\psi_T}{\partial\phi}\right]\tilde{\gamma}_n \quad (3.36)$$
$$\left.-in\bar{\phi}\mu_{SGV}e^{n\eta_{HW}}\left[\frac{1}{n}+\mu-\frac{\mu_{SGV}}{2}\right]\dot{\tilde{\gamma}}_n\right]$$

and the first-order lag across the rotor and stator are described in modal form by

$$\tau_R\dot{\tilde{L}}_{uR,n} = \frac{\partial L_{uR,ss}}{\partial\phi}\tilde{\phi}_n + in\bar{\phi}\mu_{SGV}e^{n\eta_{HW}}\frac{\partial L_{uR,ss}}{\partial\phi}\tilde{\gamma}_n - (1-in\tau_R)\tilde{L}_{uR,n} \quad (3.37)$$

$$\tau_S\dot{\tilde{L}}_{uS,n} = \frac{\partial L_{uS,ss}}{\partial\phi}\tilde{\phi}_n + in\bar{\phi}\mu_{SGV}e^{n\eta_{HW}}\frac{\partial L_{uS,ss}}{\partial\phi}\tilde{\gamma}_n - \tilde{L}_{uS,n}. \quad (3.38)$$

To simplify further discussion of Model 2, the following reduced description of

Equations 3.36 to 3.38 will be used:

$$\dot{\tilde{\phi}}_n = A'\tilde{\phi}_n - C'\tilde{L}_{uR,n} - C'\tilde{L}_{uS,n} + B'\tilde{\gamma}_n + G\dot{\tilde{\gamma}}_n \tag{3.39}$$

$$\tau_R\dot{\tilde{L}}_{uR,n} = L_{uR\phi}\,\tilde{\phi}_n + L_{uR\gamma}\,\tilde{\gamma}_n - (1 - in\tau_R)\tilde{L}_{uR,n} \tag{3.40}$$

$$\tau_S\dot{\tilde{L}}_{uS,n} = L_{uS\phi}\,\tilde{\phi}_n + L_{uS\gamma}\,\tilde{\gamma}_n - \tilde{L}_{uS,n}. \tag{3.41}$$

It is convenient to write the transfer function of the compressor $G_n(s)$ using this notation. The third order transfer function has the form

$$G_n(s) = \frac{\tilde{\phi}_n}{\tilde{\gamma}_n} = \frac{B' + Gs - \dfrac{C'L_{uR\gamma}}{1 - in\tau_R + \tau_R s} - \dfrac{C'L_{uS\gamma}}{1 + \tau_S s}}{s - A' + \dfrac{C'L_{uR\phi}}{1 - in\tau_R + \tau_R s} + \dfrac{C'L_{uS\phi}}{1 + \tau_S s}} \tag{3.42}$$

3.3.2 Discussion and Evaluation of Parameters, Model 2

Model 2 is functionally different from Model 1 for only one reason: Model 2 is based on the assumption that pressure rise changes in time following a flow perturbation $\delta\phi$. It initially changes according to the slope of the isentropic pressure rise characteristic $\frac{\partial\psi_T}{\partial\phi}$ and then decays in time to match the slope of the steady-state compressor characteristic $\frac{\partial\psi}{\partial\phi}$. The addition of the unsteady losses introduces two additional poles and two additional zeros in the compressor transfer function.

The new compressor equation requires the introduction of the rotor and stator flow response lag time τ_R and τ_S which are based on the generalized blade row lag time τ_u. The numerical value of τ_u was chosen so as to allow Model 2 to reproduce as accurately as possible the measured open-loop dynamics of the compressor (see Section 4.2.2). This value of τ_u determined from the compressor dynamics fell within a range of values that have been found experimentally by other investigators. Nagano et al [28] observed that the first-order time lag τ_u was between 1.0 and 1.5 times the flow-through time of a blade row depending on the blade row stagger and flow conditions. A value of 1.5 for the nondimensional first-order lag τ_u was used in Model 2 because it enabled the model to make the best prediction of the measured open-loop dynamics. This comparison can be seen in Section 4.2.2.

Besides τ_R and τ_S, the only new terms in this model are r and $\frac{\partial \psi_T}{\partial \phi}$ which is derived from the isentropic pressure rise characteristic ψ_T. Figure 3.9 illustrates the relation of the isentropic compressor characteristic to the steady-state compressor characteristic ψ. Figure 3.9 also illustrates the importance of obtaining an accurate ψ_T characteristic in the low flow range. The polynomial description of ψ_T , developed using the unstabilized compressor data set, deviates to a notable extent in the low flow region from the other, developed using the extended characteristic which comes from the use of active control. Figure 3.9 also shows the shape of $L_{u,ss}$, the net pressure loss caused by viscous losses. It should be noted that the derivation of τ_u is very sensitive to the shape of ψ_T. The value of τ_u derived from the data can change by 50% depending on which characteristic is used. The values of the new parameters introduced in Model 2 are shown in Figure 3.10 for the compressor modeled here. Since the slope of $\frac{\partial \psi_T}{\partial \phi}$ is more negative than that of $\frac{\partial \psi}{\partial \phi}$, the model predicts that the compressor is most stable immediately after the occurrence of a perturbation. Without periodic perturbations however, the compressor would return to the steady-state performance described by $\frac{\partial \psi}{\partial \phi}$. The periodic nature of the modal disturbances decreases the effective slope of the characteristic seen by the compressor and increases the stability as predicted by the model. Higher modes "see" higher frequency disturbances and are predicted to have a lower effective slope and greater stability. This phenomenon is important because it greatly simplifies the problem of mode stabilization.

3.4 Modeling Compressor Flow Deviation & Blockage Effects, Model 3

3.4.1 Model Development

The second compressor model, Model 2, adds additional dynamics to represent the compressor's response to unsteady flow; however, it is not all-inclusive. The effects of short lived deviations from the expected flow angle and unsteady blockage in the

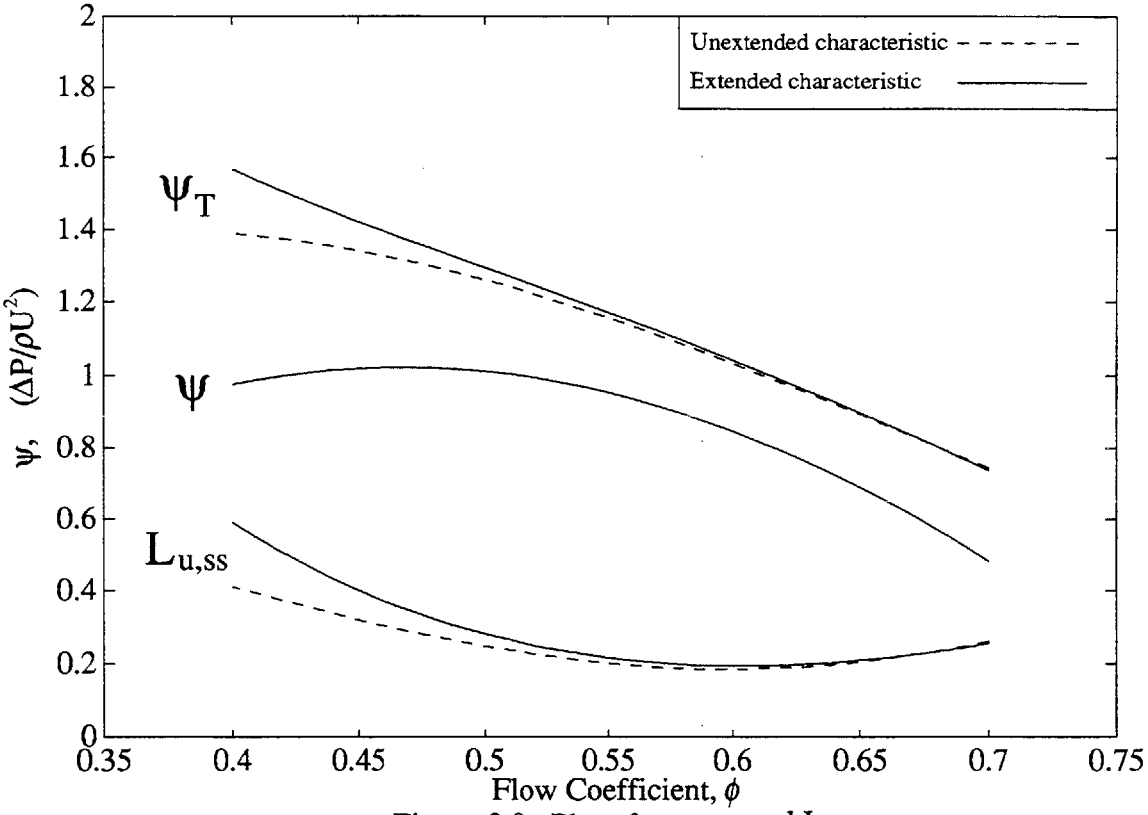

Figure 3.9: Plot of ψ, ψ_T, and $L_{u,ss}$

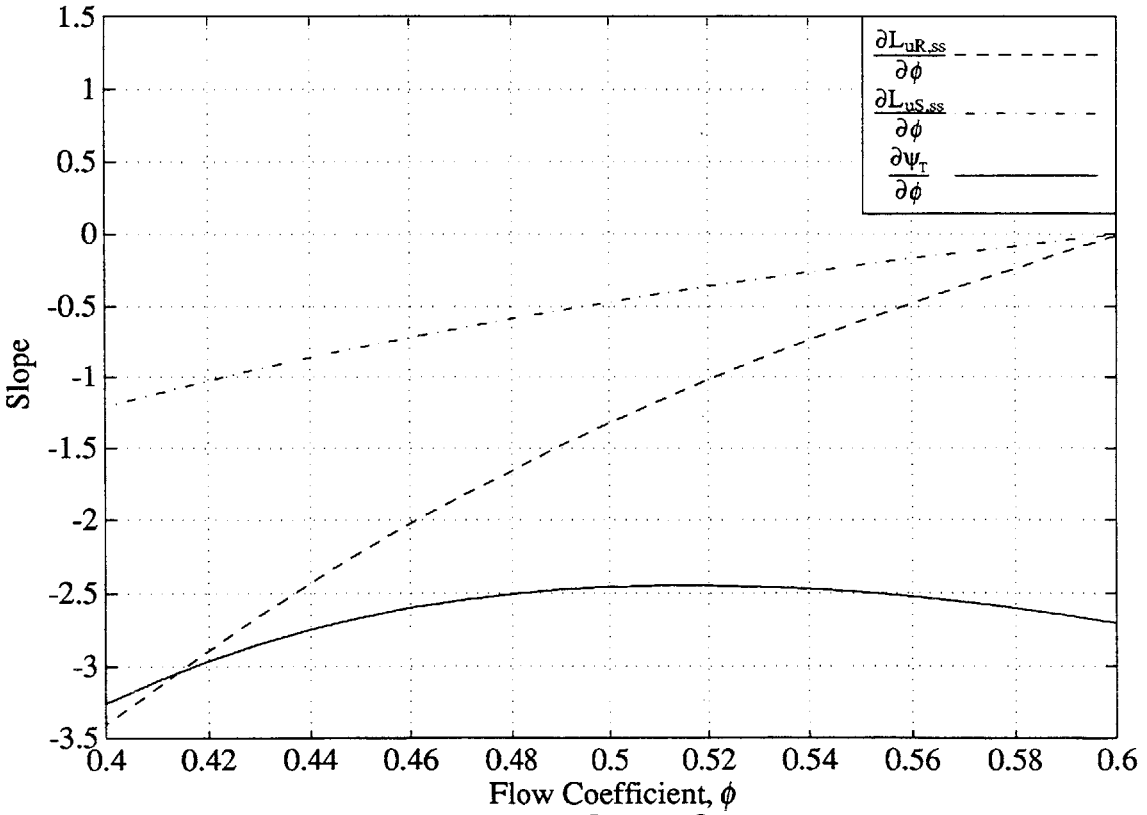

Figure 3.10: Plot of Parameters $\partial L_{uR,ss}/\partial\phi$, $\partial L_{uS,ss}/\partial\phi$, and $\partial\psi_T/\partial\phi$

compressor duct have not yet been modeled. The significance of these effects varies between compressors and is still an important area of research.

In an attempt to improve the modeling of the unsteady flow dynamics, Model 2 was expanded to include these effects. The analysis in Appendix C of the instantaneous pressure rise across an ideal blade row subjected to a $\delta\phi$ flow perturbation indicates that the instantaneous pressure rise changed in accordance with the slope of the ideal pressure rise characteristic (Equation 3.2) calculated using the Euler compressor equation. The ideal blade row model neglects not only the actual losses that occur in the passages but also the nonideal flow characteristics which develop in the compressor. By making the assumption that these nonideal effects are not instantaneous but develop in accordance with a first-order lag, the instantaneous compressor response can be described by the slope of the ideal characteristic $\frac{\partial \psi_i}{\partial \phi}$. As the nonideal effects adjust following a flow disturbance $\delta\phi$, the compressor behavior will move toward the steady state described by $\psi(\phi)$. In reality, the instantaneous behavior across the compressor will fall short of the slope $\frac{\partial \psi_i}{\partial \phi}$ and the various flow phenomena may not be best described by a first-order lag. For simplicity in the model development, it was assumed that all of the nonideal flow phenomena develop over the same time scale τ_d. Additionally, it was assumed that the nonideal flow phenomena develop over the same time scale as the losses through the blade rows so that $\tau_d = \tau_u$. Without data clearly indicating otherwise, this seemed to be the most reasonable approximation. To account for the differences between the pressure loss across the rotors and the stators, the reaction of the compressor blading was used to determine the way pressure losses are distributed between the two as was done in Model 2. This version of the first-order lag model was suggested by Hendricks and applied for the first time to the study of closed-loop control in this thesis.

Additional notation is required in Model 3 to describe the effects of flow deviation and blockage. The loss of pressure caused by these phenomena when

operating in the steady state or during flow perturbations will be expressed respectively as:

$$\begin{aligned} L_{d,ss} &= \psi_i - \psi_T \\ L_{dR} &= r\left(L_{d,ss} + \delta L_d\right) = L_{dR,ss} + \delta L_{dR} \qquad \text{Rotors} \\ L_{dS} &= (1-r)\left(L_{d,ss} + \delta L_d\right) = L_{dS,ss} + \delta L_{dS} \qquad \text{Stators.} \end{aligned} \tag{3.43}$$

As before, r is the reaction of the compressor blading. Although these definitions are used in the new equation set, some equations that characterize the flow are unaltered. Equations 3.7, 3.8, 3.10, 3.11, 3.12, 3.34, and 3.35 are still used in Model 3 to describe the compressor flow field. The equation describing the flow dynamics inside the compressor is altered to include the new dynamic contributions of the additional flow phenomena. The equation has the form

$$\begin{aligned} 0= \quad & -\frac{\partial(\delta\Phi_1)}{\partial\bar{t}} - \mu_{SGV}\frac{\partial(\delta\phi_2)}{\partial\bar{t}} - \frac{\bar{\phi}}{2}\cdot\mu_{SGV}^2\frac{\partial^2(\delta\gamma)}{\partial\theta\partial\bar{t}} + \frac{\partial\psi_i}{\partial\phi}\delta\phi_2 - \delta L_{uR} \\ & -\delta L_{uS} - \delta L_{dR} - \delta L_{dS} + \frac{\partial\psi}{\partial\gamma}\delta\gamma - \mu_C\frac{\partial(\delta\phi_2)}{\partial\bar{t}} - \lambda\frac{\partial(\delta\phi_2)}{\partial\theta} - \delta P_{s,3}. \end{aligned} \tag{3.44}$$

In addition to these, two new expressions are needed to describe the time lag associated with the flow phenomena being added to the model. The first-order lag in the flow across the rotors and stators respectively is described by

$$\tau_R\left(\frac{\partial(\delta L_{dR})}{\partial\bar{t}} + \frac{\partial(\delta L_{dR})}{\partial\theta}\right) = \frac{\partial L_{dR,ss}}{\partial\phi}\delta\phi_2 - \delta L_{dR} \tag{3.45}$$

$$\tau_S\frac{\partial(\delta L_{dS})}{\partial\bar{t}} = \frac{\partial L_{dS,ss}}{\partial\phi}\delta\phi_2 - \delta L_{dS}. \tag{3.46}$$

This system of 10 equations can be reduced by applying the upstream and downstream boundary equations as was done for Model 1. Expressing the solution in modal form,

the modal dynamics of the compressor are described by

$$\dot{\tilde{\phi}}_n = \frac{1}{\frac{2}{n}+\mu}\left[\left(\frac{\partial \psi_i}{\partial \phi} + in\cdot\lambda\right)\tilde{\phi}_n - \tilde{L}_{uR,n} - \tilde{L}_{uS,n} - \tilde{L}_{dR,n} - \tilde{L}_{dS,n}\right.$$
$$+e^{n\eta_{HW}}\left[\left(\frac{\partial \psi}{\partial \gamma} - n^2\bar{\phi}\lambda\mu_{SGV}\right) + in\bar{\phi}\mu_{SGV}\frac{\partial \psi_i}{\partial \phi}\right]\tilde{\gamma}_n$$
$$\left.-in\bar{\phi}\mu_{SGV}e^{n\eta_{HW}}\left[\frac{1}{n}+\mu-\frac{\mu_{SGV}}{2}\right]\dot{\tilde{\gamma}}_n\right], \qquad (3.47)$$

and the flow lag dynamics are described by equations 3.37, 3.38, and the following:

$$\tau_R\dot{\tilde{L}}_{dR,n} = \frac{\partial L_{dR,ss}}{\partial \phi}\tilde{\phi}_n + in\bar{\phi}\mu_{SGV}e^{n\eta_{HW}}\frac{\partial L_{dR,ss}}{\partial \phi}\tilde{\gamma}_n - (1-in\tau_R)\tilde{L}_{dR,n} \qquad (3.48)$$

$$\tau_S\dot{\tilde{L}}_{dS,n} = \frac{\partial L_{dS,ss}}{\partial \phi}\tilde{\phi}_n + in\bar{\phi}\mu_{SGV}e^{n\eta_{HW}}\frac{\partial L_{dS,ss}}{\partial \phi}\tilde{\gamma}_n - \tilde{L}_{dS,n} \qquad (3.49)$$

for the rotor and stator respectively. Since it is assumed that $\tau_d = \tau_u$, it is possible to further simplify the equations.

To abbreviate the equations above the coefficients of the independent variables are lumped into one parameter. Equation 3.47 is abbreviated by the expression

$$\dot{\tilde{\phi}}_n = A''\tilde{\phi}_n - C'\left(\tilde{L}_{uR,n} + \tilde{L}_{dR,n}\right) - C'\left(\tilde{L}_{uS,n} + \tilde{L}_{dS,n}\right) + B''\tilde{\gamma}_n + G\dot{\tilde{\gamma}}_n. \qquad (3.50)$$

The reduced notation used in Model 2 to describe the time lag of the viscous losses in the rotor and stator blade passages is retained (Equations 3.40 and 3.41), and a reduced notation for the new lag dynamics is adopted. The expression for the rotor will be reduced to

$$\tau_R\dot{\tilde{L}}_{dR,n} = L_{dR\phi}\tilde{\phi}_n + L_{dR\gamma}\tilde{\gamma}_n - (1-in\tau_R)\tilde{L}_{dR,n} \qquad (3.51)$$

and the expression for the stator reduced to the form

$$\tau_S\dot{\tilde{L}}_{dS,n} = L_{dS\phi}\tilde{\phi}_n + L_{dS\gamma}\tilde{\gamma}_n - \tilde{L}_{dS,n}. \qquad (3.52)$$

The reduced notation aids in understanding the contribution of the various dynamic equations to the compressor transfer function. By performing a Laplace transformation

on the dynamic equations, the transfer function can be written as

$$G_n(s) = \frac{\tilde{\phi}_n}{\tilde{\gamma}_n} = \frac{B'' + Gs - \dfrac{C'\left(L_{uR\gamma} + L_{dR\gamma}\right)}{1 - in\tau_R + \tau_R s} - \dfrac{C'\left(L_{uS\gamma} + L_{dS\gamma}\right)}{1 + \tau_S s}}{s - A'' + \dfrac{C'\left(L_{uR\phi} + L_{dR\phi}\right)}{1 - in\tau_R + \tau_R s} + \dfrac{C'\left(L_{uS\phi} + L_{dS\phi}\right)}{1 + \tau_S s}}. \qquad (3.53)$$

3.4.2 Discussion and Evaluation of Parameters, Model 3

The transfer function reveals that this version of the compressor model, Model 3, is dynamically very similar to Model 2. Like Model 2 this one has three poles and three zeros, and the rotor and stator lag terms are represented in the same way. If the nonideal flow phenomena developed over a different time scale (i.e. if $\tau_d \neq \tau_u$) then the compressor model would have five poles and five zeros.

The plot of the compressor characteristics (Figure 3.11) reveals that losses in the blade rows have a more significant effect on the unsteady-compressor model than deviation and blockage. The difference between the ideal characteristic and the isentropic characteristic $L_d = (\psi_i - \psi_t)$ is nearly constant over the flow range, which indicates that deviation and blockage – which account for this difference – change little with flow coefficient. Figure 3.12 reveals that the slopes $\frac{\partial L_{dR,ss}}{\partial \phi}$ and $\frac{\partial L_{dS,ss}}{\partial \phi}$ are small in magnitude relative to $\frac{\partial L_{uR,ss}}{\partial \phi}$ and $\frac{\partial L_{uS,ss}}{\partial \phi}$ which are shown in Figure 3.10, and Figure 3.12 shows that the slope of the ideal characteristic is nearly constant. Thus the compressor response predicted by this model will differ only slightly from Model 2, because the additional effects that are modeled are small. This means the poles and zeros are relatively close to the poles and zeros of Model 2. It is also important to note that Model 4 does not require knowledge of $\frac{\partial \psi_T}{\partial \phi}$. This can be seen by writing equation 3.53 in its expanded form; the addition of the unsteady loss terms $L_{u,ss}$ with the unsteady deviation and blockage terms $L_{d,ss}$ results in a cancellation of all $\frac{\partial \psi_T}{\partial \phi}$ terms. This means that this model gives the same result as the unsteady loss without needing to know the isentropic pressure rise characteristic which can only be determined accurately

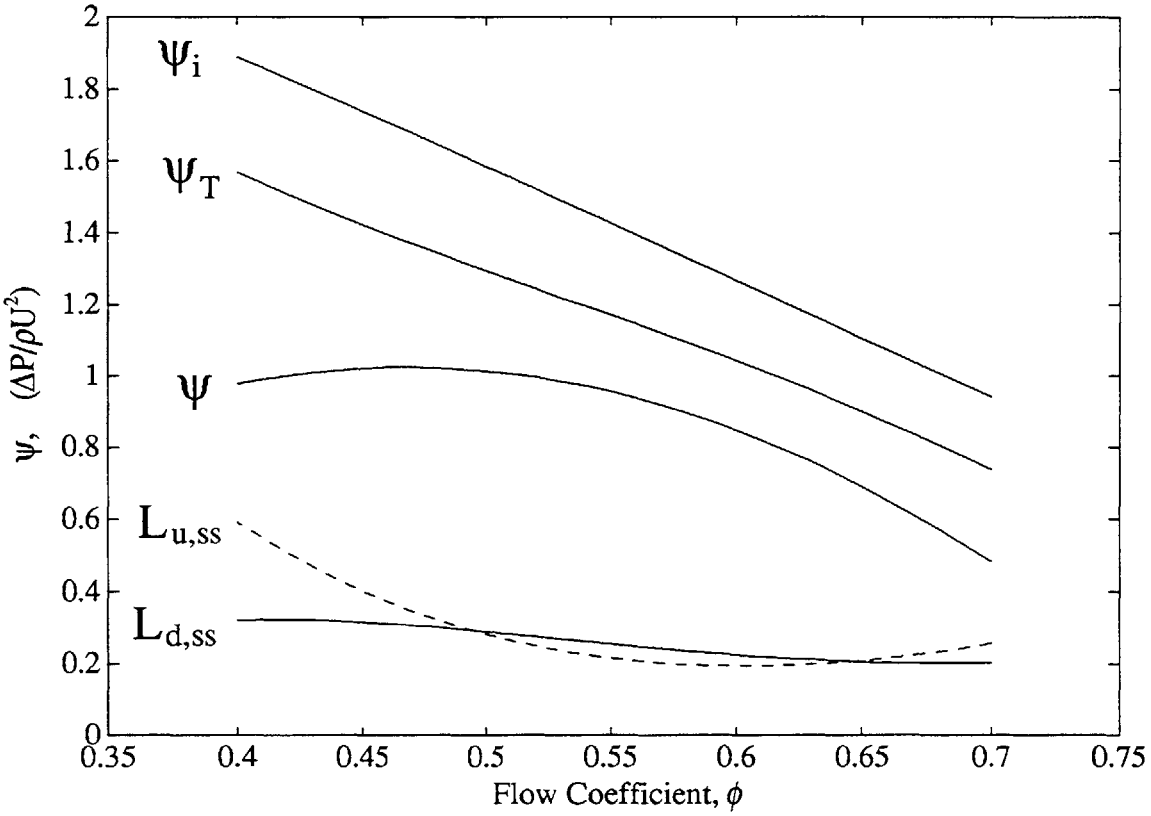

Figure 3.11: Plot of ψ, ψ_T, ψ_i, $L_{d,ss}$ and $L_{u,ss}$

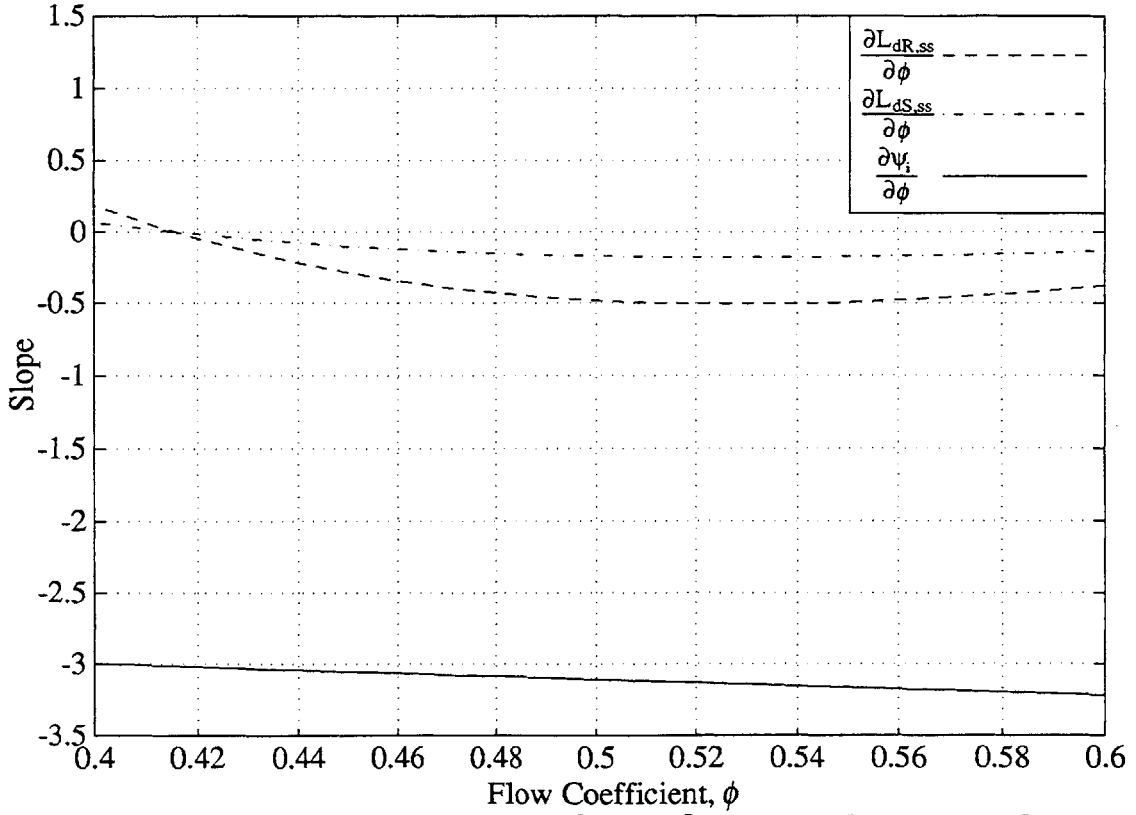

Figure 3.12: Plot of Parameters $\partial L_{dR,ss}/\partial\phi$, $\partial L_{dS,ss}/\partial\phi$, and $\partial\psi_i/\partial\phi$

with an actively stabilized compressor. So Model 3 only requires an accurate evaluation of $\psi(\phi,\gamma)$ and an appropriate value for τ_u. This model is an improvement over Model 2 in that it requires less empirical information.

3.5 Modeling Lag in Pressure Rise Due to Changes in Flow Angle, Model 4

3.5.1 Model Development

It may seem that the lumped parameters of Model 3 accounted for all of the nonideal flow characteristics in the compressor, but in fact there is another aspect to the unsteady dynamics in the compressor. When developing the model for the compressor dynamics, the steady-state compressor pressure rise was attributed to two independent parameters. Model 3 accounted for the effects associated with perturbations in flow coefficient $\delta\phi$; however, the compressor models developed so far have not dealt with unsteady effects in regard to perturbations in SGV stagger angle $\delta\gamma$, the other independent parameter. Model 4 is developed with the intent of capturing these effects.

Changes in SGV stagger angle are a unique attribute of the SGV actuation system, and an understanding of the physical mechanism connecting their unsteady behavior to ψ is required in order to develop an accurate model. The most basic level of analysis is to examine the SGV's influence on rotor blade incidence angle. Increases in SGV stagger angle cause decreases in the angle of attack on the first rotor (Figure 3.13). This reduces the adverse pressure gradient on the suction surface of the blade making separation less likely. The flow exit angle from the first rotor can be considered to be independent of γ if it is assumed that changes in deviation are negligible and that any amount of separation remains unchanged. Neglecting changes in flow exit angle allows this modification to the model to focus on interactions between the SGV's and first stage rotor alone. In an ideal system in which there are no losses or flow deviations from the blade angle, the total pressure rise across the first rotor is described by the Euler expression for a single rotor. By taking the derivative of this expression (or the

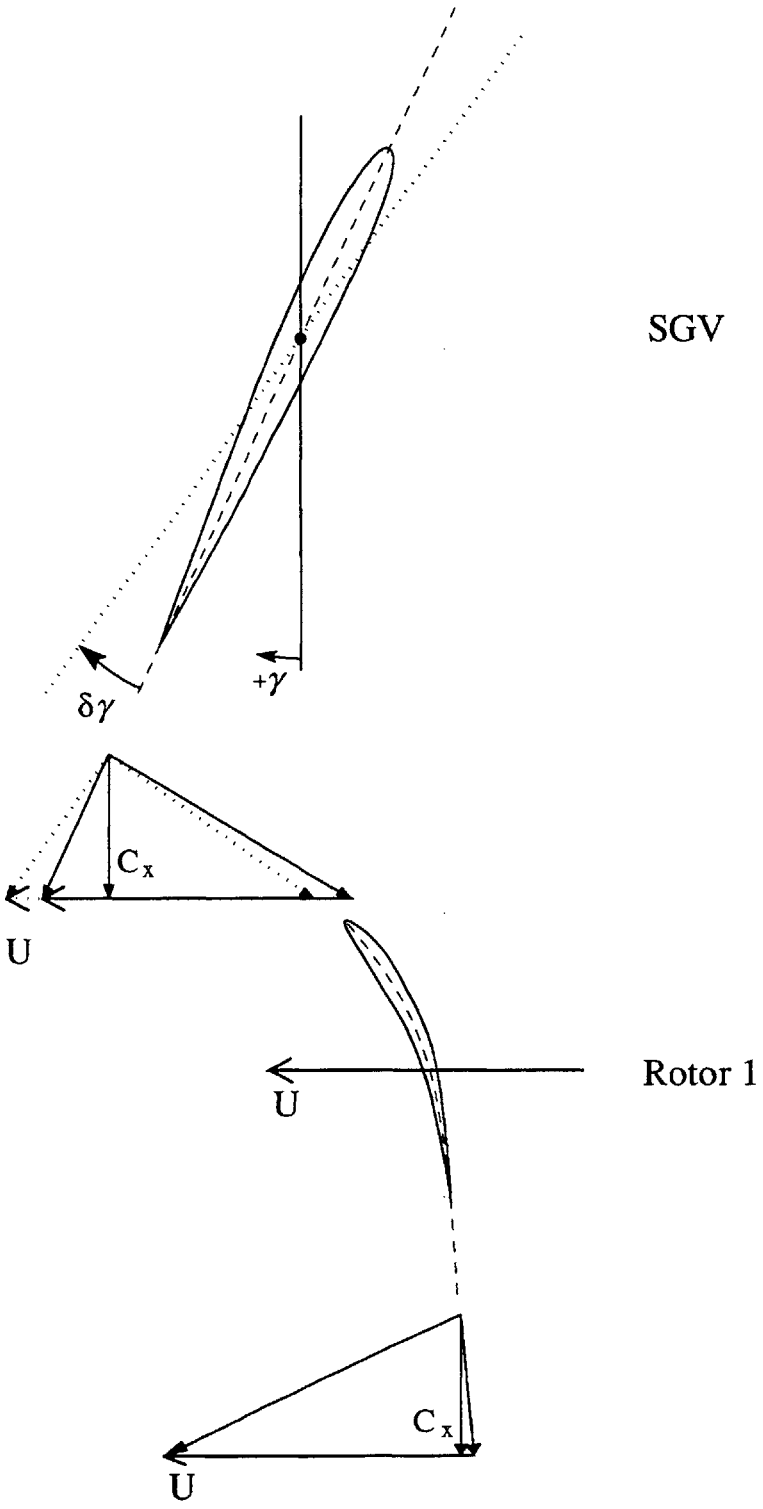

Figure 3.13 Effect of SGV Unsteadiness on Flow into First Blade Row

derivative of Equation 3.2) with respect to γ, the influence of γ on pressure rise in the ideal compressor is determined. It is written as

$$\frac{\partial \psi_i}{\partial \gamma} = -\phi \sec^2(\gamma)\delta\gamma. \tag{3.54}$$

In reality there are pressure losses in the blade row due to the viscous nature of the fluid, flow blockage, and deviations in flow angle from the ideal. These effects that cause the flow to deviate from the ideal description are the same ones as listed before, but in this case unsteady changes in these nonideal phenomena are associated with perturbations in SGV stagger angle. In developing the model for the unsteady SGV stagger angle effects, it was assumed that these nonideal flow phenomena all require a finite amount of time to adjust to the perturbations in stagger angle. The instantaneous effect of $\delta\gamma$ will therefore match the description in equation 3.54, and after a short lag the flow will readjust to match the steady state. This is the basis for the lumped parameter description of the compressor response to unsteady SGV stagger angle. The lag in the nonideal flow response was modeled as a first-order time lag, as was done previously. The time lag parameter used to characterize the development of the nonideal flow phenomena associated with $\delta\gamma$ is given the notation τ_m and is set equal to the other time delays so that

$$\frac{\tau_R}{\bar{t}_R} = \frac{\tau_S}{\bar{t}_S} = \tau_m = \tau_u = \tau_d. \tag{3.55}$$

This is a reasonable first-order assumption since the same nonideal flow phenomena are being described. Here it was also assumed that the axial chord of the first rotor is the same as the average axial rotor chord for the compressor. The notation adopted to describe the decrease in pressure from the ideal after perturbations in γ is

$$L_{SGV,ss} = \psi_i - \psi,$$
$$L_{SGV} = L_{SGV,ss} + \delta L_{SGV}. \tag{3.56}$$

Using this notation and all of the notation defined for the previous models, a complete description of the compressor can be given which accounts for the first-order lag in the

compressor response to $\delta\gamma$. The fluid dynamic description of the compressor flow retains Equations 3.7, 3.8, 3.10, 3.11, 3.12, 3.34, 3.35, 3.45, and 3.46. The expression which accounts for the fluid inertia and flow response lags in the compressor is now

$$\begin{aligned} 0 \;=\; & -\frac{\partial(\delta\Phi_1)}{\partial\bar{t}} - \mu_{SGV}\frac{\partial(\delta\phi_2)}{\partial\bar{t}} - \frac{\bar{\phi}}{2}\cdot\mu_{SGV}^2\frac{\partial^2(\delta\gamma)}{\partial\theta\partial\bar{t}} + \frac{\partial\psi_i}{\partial\phi}\delta\phi_2 - \delta L_{uR} - \delta L_{uS} \\ & -\delta L_{dR} - \delta L_{dS} + \frac{\partial\psi_i}{\partial\gamma}\delta\gamma - \delta L_{SGV} - \mu_C\frac{\partial(\delta\phi_2)}{\partial\bar{t}} - \lambda\frac{\partial(\delta\phi_2)}{\partial\theta} - \delta P_{s,3} \end{aligned} \tag{3.57}$$

and the new expression which is added to describe the lag in the nonideal flow across the first rotor is

$$\tau_R\left(\frac{\partial(\delta L_{SGV})}{\partial\bar{t}} + \frac{\partial(\delta L_{SGV})}{\partial\theta}\right) = \frac{\partial L_{SGV,ss}}{\partial\gamma}\delta\gamma - \delta L_{SGV}. \tag{3.58}$$

This system of equations constitutes a semi-actuator disk model of the compressor with flow response lags resulting from perturbations $\delta\phi$ and $\delta\gamma$ accounted for. By applying the upstream and downstream boundary conditions, the system of equations can be reduced and conveniently changed into a modal form. Having solved for the boundary conditions, the dynamics of each mode can be expressed as

$$\begin{aligned} \dot{\tilde{\phi}}_n = \frac{1}{\frac{2}{n}+\mu}\Bigg[& \left(\frac{\partial\psi_i}{\partial\phi} + in\cdot\lambda\right)\tilde{\phi}_n - \tilde{L}_{uR,n} - \tilde{L}_{uS,n} - \tilde{L}_{dR,n} - \tilde{L}_{dS,n} \\ & + e^{n\eta_{HW}}\left[\left(\frac{\partial\psi_i}{\partial\gamma} - n^2\bar{\phi}\lambda\mu_{SGV}\right) + in\bar{\phi}\mu_{SGV}\frac{\partial\psi_i}{\partial\phi}\right]\tilde{\gamma}_n \\ & - \tilde{L}_{SGV} - in\bar{\phi}\mu_{SGV}e^{n\eta_{HW}}\left[\frac{1}{n} + \mu - \frac{\mu_{SGV}}{2}\right]\dot{\tilde{\gamma}}_n\Bigg] \end{aligned} \tag{3.59}$$

with the lag dynamics described by Equations 3.37, 3.38, 3.48, 3.49, and one new equation for the lag associated with the unsteady SGV movement:

$$\tau_R\dot{\tilde{L}}_{SGV,n} = \frac{\partial L_{SGV,ss}}{\partial\gamma}\tilde{\gamma}_n - (1 - in\tau_R)\tilde{L}_{SGV,n}. \tag{3.60}$$

The terms in Model 4 can be given a simpler representation by lumping the coefficients of the independent variables into single terms. Equations 3.59 and 3.60

respectively are put in a reduced form in the following way:

$$\dot{\tilde{\phi}}_n = A''\tilde{\phi}_n - C'\left(\tilde{L}_{uR,n} + \tilde{L}_{dR,n}\right) - C'\left(\tilde{L}_{uS,n} + \tilde{L}_{dS,n}\right) + B'''\tilde{\gamma}_n - C'\tilde{L}_{SGV} + G\dot{\tilde{\gamma}}_n \quad (3.61)$$

and

$$\tau_R \dot{\tilde{L}}_{SGV,n} = L_{SGV\gamma}\,\tilde{\gamma}_n - (1 - in\tau_R)\tilde{L}_{SGV,n}. \quad (3.62)$$

From the dynamic equations, the transfer function for the compressor dynamics in Model 4 can be written in the following way:

$$G_n(s) = \frac{\tilde{\phi}_n}{\tilde{\gamma}_n} = \frac{B''' + Gs - \dfrac{C'\left(L_{uR\gamma} + L_{dR\gamma} + L_{SGV\gamma}\right)}{1 - in\tau_R + \tau_R s} - \dfrac{C'\left(L_{uS\gamma} + L_{dS\gamma}\right)}{1 + \tau_S s}}{s - A'' + \dfrac{C'\left(L_{uR\phi} + L_{dR\phi}\right)}{1 - in\tau_R + \tau_R s} + \dfrac{C'\left(L_{uS\phi} + L_{dS\phi}\right)}{1 + \tau_S s}} \quad (3.63)$$

3.5.2 Discussion and Evaluation of Parameters, Model 4

The assumptions that are built into this model are limited approximations to the actual fluid dynamics. Treating the instantaneous compressor response as ideal is only an initial estimate of the actual instantaneous response, and high-response pressure measurements are needed to evaluate the accuracy of this approximation. The response time for the nonideal effects could also be evaluated in this way. The assumption that changes in blade exit angle remain constant is usually reasonable for small perturbations in stagger angle. The research compressor used in this work exhibited SGV perturbations of only $\pm 4°$ during active control, and because the changes in exit angle should be a small percentage of this, changes in exit flow angle were assumed to be negligible. This assumption will not hold however when the blade is on the verge of exhibiting separation. For the same research compressor, the assumption that the first rotor's axial chord is equal to the mean axial rotor chord of the compressor is accurate to 2.3%.

The parameters of Model 4 that are identical to the parameters used in previous models are evaluated in the same way as before. The two new parameters in this model are $\frac{\partial \psi_i}{\partial \gamma}$ and L_{SGV}. Figure 3.14 graphs the values of these parameters and allows a

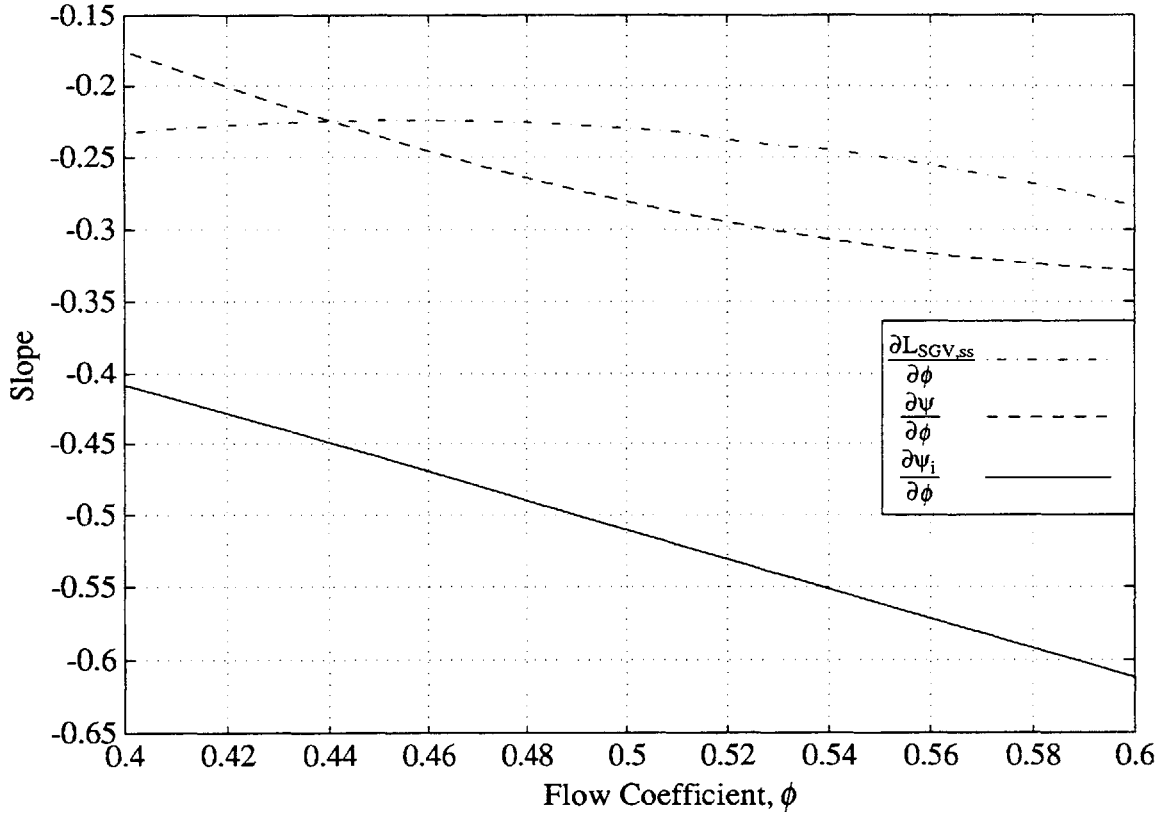

Figure 3.14: Plot of Parameters $\partial\psi_i / \partial\phi$, $\partial\psi / \partial\phi$, and $\partial L_{SGV,ss} / \partial\phi$

comparison with $\frac{\partial \psi}{\partial \gamma}$. As can be seen in the figure, the change in ideal pressure rise with stagger angle is about twice the steady-state value $\frac{\partial \psi}{\partial \gamma}$.

The compressor transfer function for Model 4 has the same open-loop poles as Model 3. The effect of modeling the lag in the compressor response to SGV perturbations is to introduce a shift in the open-loop zeros of the compressor. Since the slope $\frac{\partial \psi_i}{\partial \gamma}$ is more negative than $\frac{\partial \psi}{\partial \gamma}$, it is expected that the closed-loop zeros will shift to the left and closed-loop stability will increase. Experimental data for the open-loop poles and zeros of each mode are compared with the various compressor models' predictions and experimental data in the next chapter. Closed-loop comparisons are made in Chapter 5 which demonstrate the accuracy of each model.

$$\lambda = 0.6787$$

$$\mu_{SGV} = 0.2818$$

$$\mu = 1.2937$$

$$\eta_{HW} = -0.6034$$

$$\psi = 1.023 - 10.07\,(\phi - 0.46825)^2 \qquad \text{(for } .42 < \phi < .6\text{)}$$

$$\frac{\partial \psi}{\partial \gamma} = 2.888\,\phi^2 - 3.655\phi + 0.8251 \qquad \text{(for } .42 < \phi < .6\text{)}$$

$$\psi_T = -7.4985\phi^2 + 8.9947\phi - 3.3741 + \frac{1.0114}{\phi} \qquad \text{(for } .42 < \phi < .6\text{)}$$

$$\psi_i = -0.5467\phi^2 - 2.559\phi + 3 \qquad \text{(for all } \phi\text{)}$$

$$\frac{\partial \psi_i}{\partial \gamma} = -1.020\phi \qquad \text{(for all } \phi\text{)}$$

$$\frac{\partial \psi_T}{\partial \gamma} = -6.079\phi^2 + 5.552\phi + 1.547 \qquad \text{(for } .42 < \phi < .6\text{)}$$

Table 3.1: Parameter Values & Expressions which Characterize the High Reaction Build of the MIT Three-Stage Axial Compressor and were Used in the Compressor Models

CHAPTER 4

Open-Loop Compressor Characterization

The actual dynamic behavior of the compressor is more complicated than any of the models given in the previous chapter; however, as will be shown in this chapter, the compressor's response to small amplitude actuated modal disturbances can be accurately characterized by a first-order dynamic representation. The parameters used in this dynamic representation characterize the open-loop compressor behavior. Section 4.1 discusses the methods by which the compressor's transfer function and its approximation by open-loop parameters were determined. The parameters characterizing the dynamics of the first three modes of the compressor are listed and described as well. Section 4.2 relates the experimentally determined parameters to the parameters predicted by the various models.

4.1 Characterization of Open-Loop Spatial Mode Dynamics

4.1.1 Identification Methodology

The goal of this identification proceedure is to determine the relationship between SGV perturbations and the resulting flow field response. The transfer functions expressing this relationship are determined independently for each *spatial* mode because only small amplitude disturbances are being considered, and this means the modes behave in a learly independant manner. Transfer functions are also unique for each steady-state flow coefficient of the compressor because the compressor dynamics change with ϕ. The identification techniques used to determine the compressor transfer functions and their reduced description by open-loop parameters were developed by

Paduano [16]. This section summarizes the details of these techniques and discusses the effect of increasing the complexity of the compressor model on the parameter determination process.

4.1.1.1 Spatial Mode Transfer Function Identification

The transfer function is calculated using sampled data of the SGV position $\gamma_{\theta,m}$ and the simultaneous flow field description $\phi_{\theta,k}$. Because sampled data are being used, only a discrete time approximation of the transfer function can be calculated:

$$G_n(s)\big|_{s=j\omega} \cong G_n(z)\big|_{z=e^{j\omega\tau_f}} \tag{4.1}$$

Since the sampling time τ_f is several times faster than the dominant frequencies in the response, this approximation can still provide a good resolution of the dominant frequencies. At any frequency $j\omega$=s, the transfer function of each spatial mode response is characterized by the change in the gain $|G(s)|$ and phase $\angle G(s)$ between the input signal $\tilde{\gamma}_n$ and the compressor response $\tilde{\phi}_n$. This can be expressed as:

$$\frac{\tilde{\phi}_n(j\omega)}{\tilde{\gamma}_n(j\omega)} = G_n(j\omega,\phi) = |G_n(j\omega,\phi)|e^{j(\angle G_n(j\omega,\phi))} \tag{4.2}$$

It is uniquely determined for each mode and flow coefficient ϕ.

Rather than measuring the system's response to a range of distinct input frequencies, a pseudo-random binary signal (PRBS) with broad band characteristics was used, making identification faster and easier. A 50 Hz bandwidth signal that alternates about the equilibrium position by an amount $\pm$ K at random time intervals greater than or equal to .01 sec was used as the compressor excitation input signal. The frequency of the alternations set the bandwidth of the signal. The amplitude of the commanded SGV displacement, K, was usually 5° but was reduced in some cases to as low as 2° when identification was for a ϕ close to the stall point. The input signal could be applied to the compressor as a spatially fixed cosine disturbance, sine disturbance, or as a combination of the two. In some cases one method provided better resolution of the compressor's spatial mode dynamics than the others. The command to excite spatial mode n of the

SGV array can be represented quite simply in the form of a complex number $\tilde{u}_{c,n}$ shown in Figure 3.6 whose magnitude corresponds to the maximum possible deflection of an SGV and whose phase corresponds to the location of the peak of the commanded spatial mode. Using this definition for $\tilde{u}_{c,n}$ a spatially fixed cosine wave with random oscilliations in magnitude can be described by

$$\begin{aligned} \text{real}\left(\tilde{u}_{c,n}\right) &= \text{PRBS} \\ \text{imag}\left(\tilde{u}_{c,n}\right) &= 0 \end{aligned} \tag{4.3}$$

a spatially fixed sine wave

$$\begin{aligned} \text{real}\left(\tilde{u}_{c,n}\right) &= 0 \\ \text{imag}\left(\tilde{u}_{c,n}\right) &= \text{PRBS} \end{aligned} \tag{4.4}$$

or a combination of two PRBSs

$$\begin{aligned} \text{real}\left(\tilde{u}_{c,n}\right) &= \text{PRBS}_1 \\ \text{imag}\left(\tilde{u}_{c,n}\right) &= \text{PRBS}_2 \end{aligned} \tag{4.5}$$

From the monitored SGV position data $\gamma_{\theta,m}$ and the measured response $\phi_{\theta,k}$ an estimate of the mode dynamics was calculated by means of a spectral method. As an example, the spectral estimate of the dynamics of the first spatial mode at ϕ =.49 (6% above the stalling flow coefficient) is shown in Figure 4.1. The spectral estimate of the spatial mode's response is best resolved for frequencies below the 50 Hz bandwidth of the input signal (i.e. below the normalized frequency ωR/U = 1.25). At frequencies above the signal bandwidth, the determination of the transfer function parameters is less precise because resolution will vary widely at frequencies above the Nyquist frequency. This will cause scattering in the parameters describing the higher mode dynamics with poles and zeros at or above the 50 Hz bandwidth of the input signal.

4.1.1.2 Parametric Estimation of Spatial Mode Transfer Functions

Even though spatial mode transfer functions can be determined from data, it is desirable for them to be expressed in a reduced form that clarifies the dynamics of a

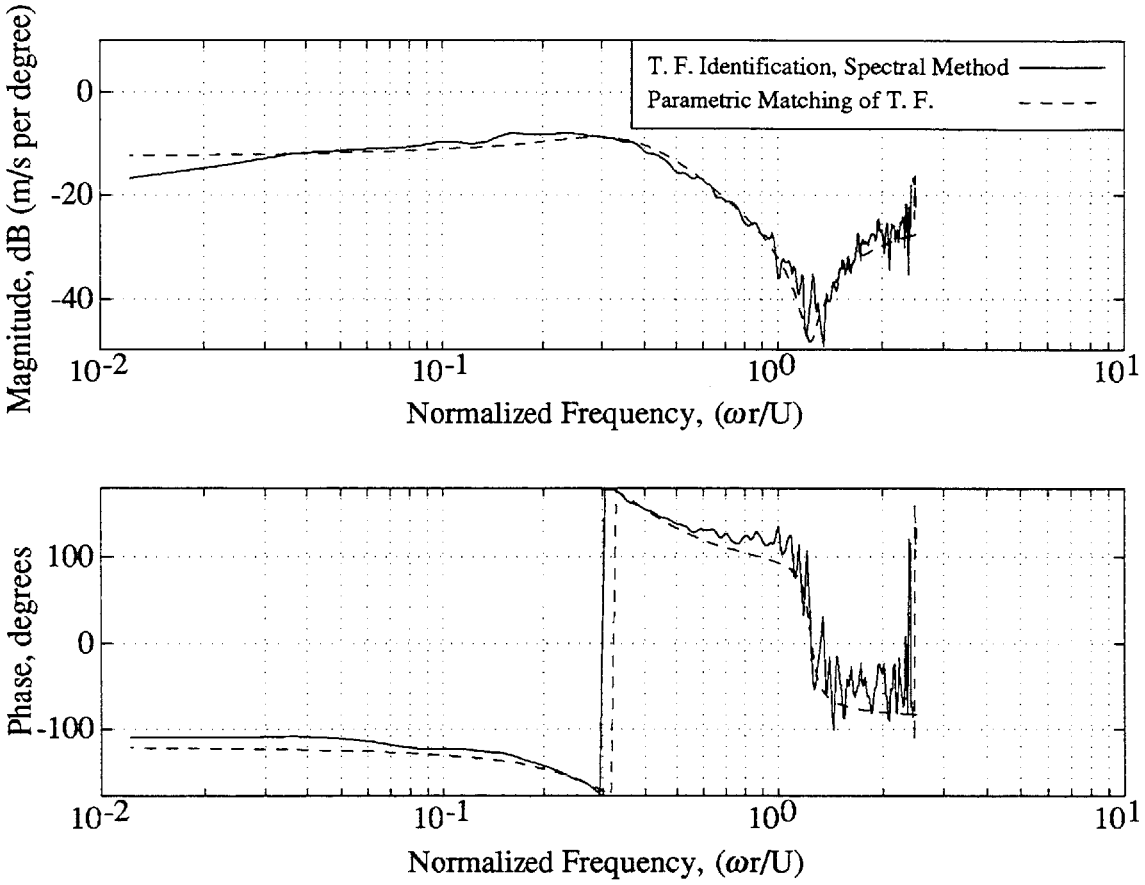

Figure 4.1: Estimate of Compressor Transfer Function for Mode 1 at $\phi = .49$ (6% above the stalling flow coefficient)

$$\hat{\Theta}_1(.49) = [\ -.184 \quad .329 \quad -.0709 \quad .00280 \quad -.0573\ ]$$

$$= [\ \sigma_{n,1} \quad \omega_{n,1} \quad b_{r,1} \quad b_{i,1} \quad g_{i,1}\ ]$$

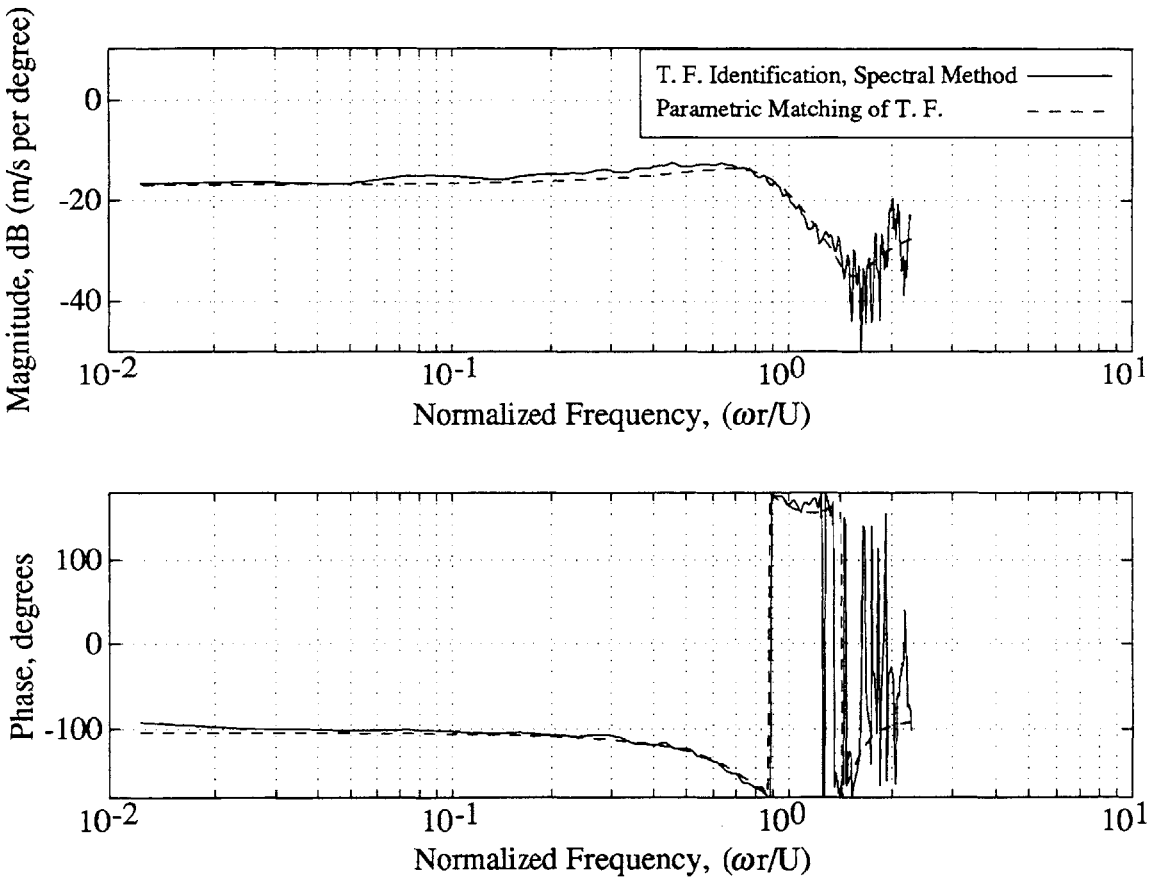

Figure 4.2: Estimate of Compressor Transfer Function for Mode 2 at $\phi = .49$ (6% above the stalling flow coefficient)

$$\hat{\Theta}_2(.49) = [\ -.298 \quad .794 \quad -.0950 \quad -.0113 \quad -.0631\ ]$$

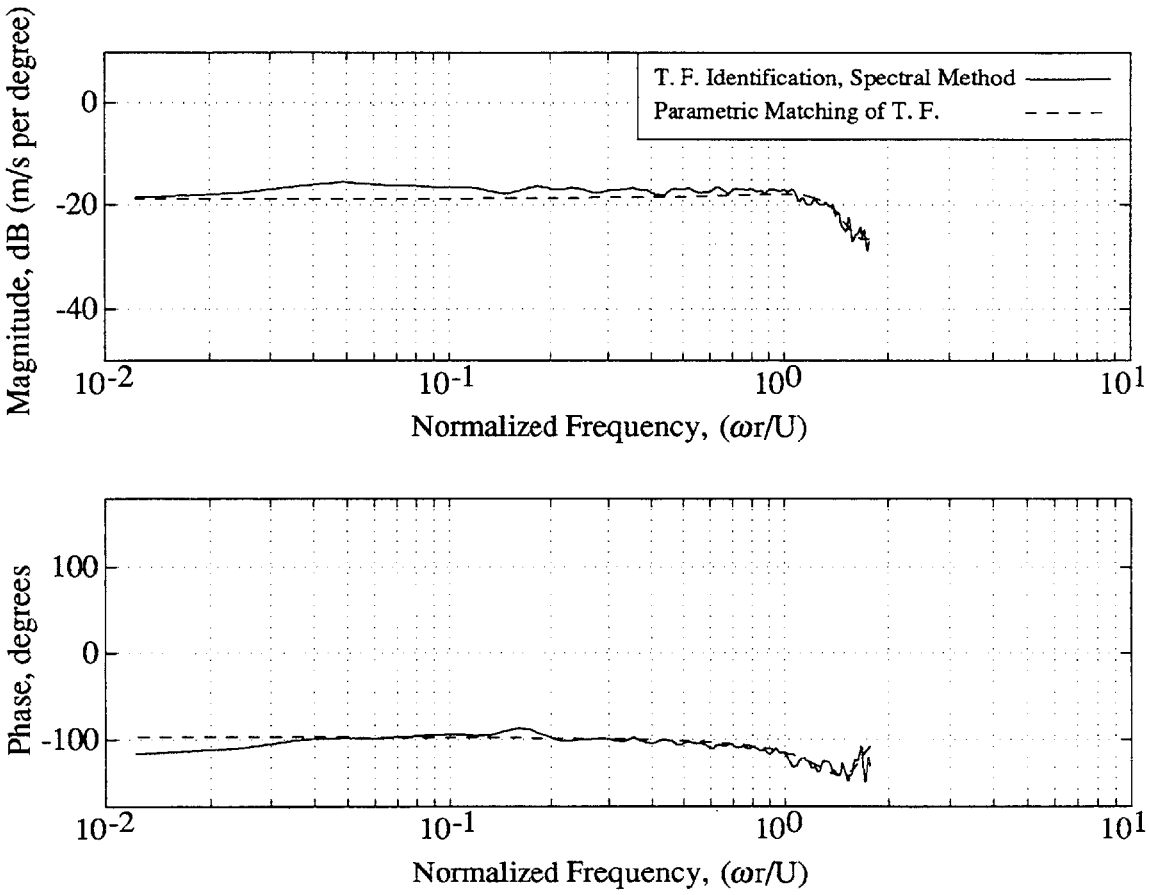

Figure 4.3: Estimate of Compressor Transfer Function for Mode 3 at $\phi = .49$ (6% above the stalling flow coefficient)

$$\hat{\Theta}_3(.49) = [\,-.364 \quad 1.37 \quad -.129 \quad -.0176 \quad -.0787\,]$$

existence of a complex conjugate pair of poles, followed by a complex conjugate pair of zeros. These are the same dynamic characteristics that are described in Model 1. The complex coefficients in this model (Equation 3.22) are actually a unique way of representing a complex conjugate pair of poles and zeros in an annular duct. Having recognized this, the structure of Model 1 was used in the process of transfer function reduction. The five real-valued coefficients of Model 1 (Equation 3.21) were evaluated based on experimental data. The parameters are written together in vector form in the following way:

$$\hat{\Theta}_n(\phi) = \begin{bmatrix} \sigma_n \\ \omega_n \\ b_{r,n} \\ b_{i,n} \\ g_{i,n} \end{bmatrix} \tag{4.6}$$

These parameters were evaluated using one of two methods.

4.1.1.2.1 Transfer Function Fitting

This section discusses the method used to evaluate the Model 1 coefficients which best describe the transfer function when the mode being identified is not under closed-loop control. The spectral method can be used for transfer function evaluation when the spatial mode being identified is not closed-loop controlled although other modes may be. This can be done because there is no significant spatial cross talk between the spatial modes that can be excited by the SGV actuators (i.e. the first five). In the cases in which the spectral method was used, the experimentally determined transfer function was fitted using a regression technique developed by Lamaire [32] which treats the transfer function fitting problem as a weighted least squares problem.

The details of applying this method to compressor parameter identification are given by Paduano [16].

In most cases the fit to the transfer function had a high degree of agreement with the spectral estimate. Figures 4.1, 4.2, and 4.3 together demonstrate that the transfer function behavior of each of the first three modes can be characterized using only the five parameters. In most cases it was necessary to limit the range of spectral estimate frequencies to which the fit was made so that the poor resolution of the higher frequency response data would not distort the fit. For the third mode parameter identification, this sometimes meant that the high frequency contributions of the zero in the transfer function were only partially resolved. However, this problem was addressed by only considering fits to the third mode transfer function that properly resolved the phase change caused by the zero. Figure 4.3 is an example of this type of fit. Appendix B shows the fits to the spectral method estimates of the transfer function at several flow coefficients for each of the first three modes.

4.1.1.2.2 Instrumental-Variable Method

To determine the open-loop dynamics of a spatial mode while it is under closed-loop control, an instrumental-variable method was employed. A noise free simulation of the instruments was used in Young's Refined Instrumental Variable - Approximate Maximum Likelihood (NF/RIV-AML) technique in order to determine the parameters describing the open-loop dynamics during closed-loop operation. The details of how the NF/RIV-AML technique was applied for the determination of compressor dynamics is given by Paduano [16].

Accurate modeling of the actuators and delays in the closed-loop system enabled an accurate noise free simulation of the SFC velocity perturbations and SFC SGV perturbations to be generated and helped bring about the success of this technique. The accuracy of the simulation was checked in each case to assure the accuracy of the

prediction of the compressor dynamics. The accuracy of the predicted parameters is further validated by the fact that they were consistent with their previous trends at higher flow coefficients.

The NF/RIV-AML technique gave a prediction of the open-loop compressor response based upon the closed-loop data. Figure 4.4 is an example of a prediction of the compressor's spatial mode dynamics; in this case the first mode open-loop response is illustrated. Like the previous Bode plots, it shows the distinct characteristics of a complex conjugate pair of poles and zeros. The more pronounced peak in this transfer function is indicative of the fact that the first mode is near the mode's neutral stability flow coefficient (ϕ_{stall} in this case). Documentation of transfer function predictions resulting from this method at other flow coefficients and for other modes is given in Appendix B.

4.1.1.2.3 Influence of Additional Poles and Zeros on Parameter Identification

At the beginning of Section 4.1.1.2 it was stated that the Model 1 parameters were able to describe the general dynamic characteristics of the compressor, and this has been demonstrated in the last two sections. However, the significance of the additional poles and zeros introduced by the third order models (i.e. Models 2,3, and 4) needs to be considered before comparisons are made between these models and the experimentally predicted parameters. Specifically, the influence of the additional poles and zeros on the estimated transfer function must be determined. Figure 4.5 illustrates the frequency response associated with the additional first mode poles and zeros of Model 2 for $\phi = 0.46$. Over the range of frequencies where the complex pole and zero of Model 1 had the greatest influence, the dynamic contribution of the additional poles and zeros is negligible. Below 80 Hz the change in gain is at most 2.3 dB and the change in phase is at most -2.2°. The frequency response of the second and of the third mode of Model 1 and of each of the three modes of the other models for flow coefficients near the stall point was found to be similar. The influence of the additional poles and zeros on

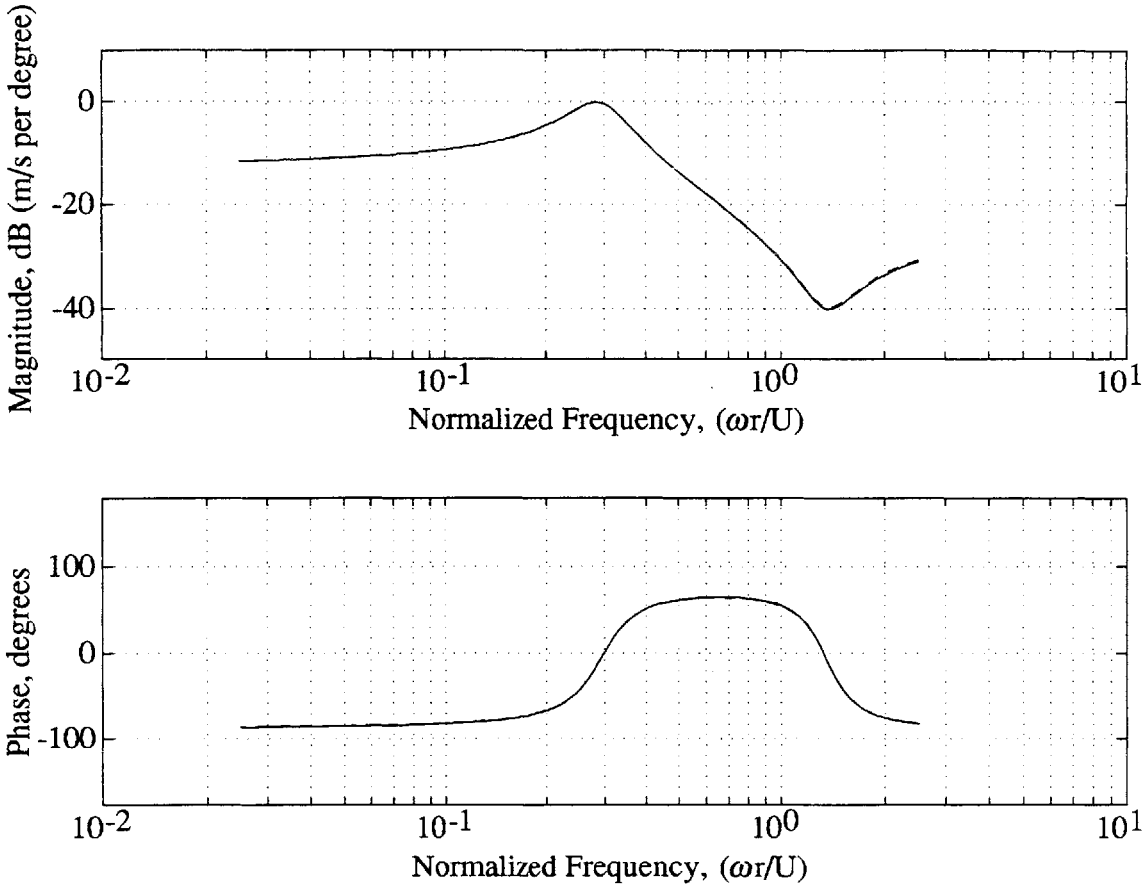

Figure 4.4: Estimate of Compressor Transfer Function for Mode 1 at $\phi = .45$ (2% below the stalling flow coefficient)

$$\hat{\Theta}_1(.45) = [\ .0576 \quad .286 \quad -.0565 \quad .00844 \quad -.0421\ ]$$

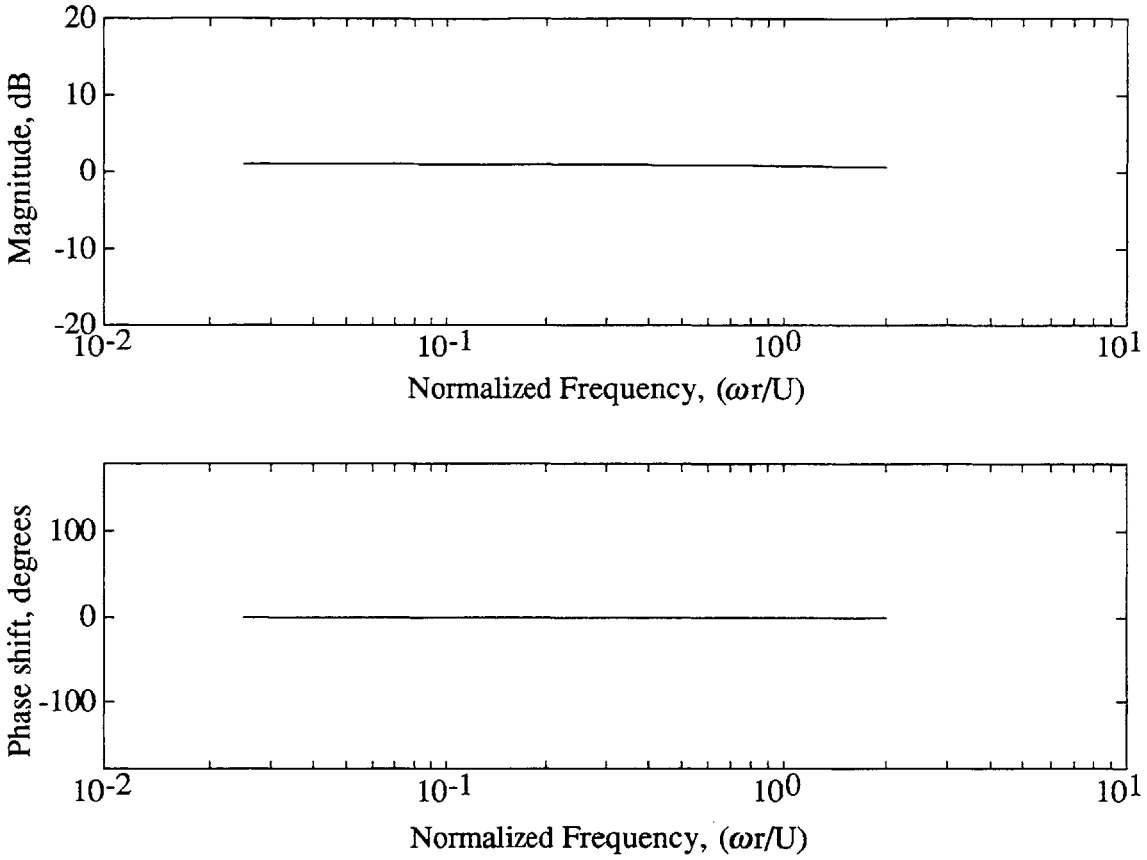

Figure 4.5: Frequency Response Associated with the Poles and Zeros of Model 2 that are Not Represented in Model 1 (ϕ = .46 in this case)

predicted parameters was small. If their dynamic contribution was removed from the dynamic response, the predicted poles shifted by less than 3% and the zeros shifted by less than 7% in most cases. These findings justify making comparisons between the experimentally determined poles and zeros and the dominant poles and zeros of the third order models. Since the additional poles and zeros have been shown to contribute little to the dynamic response, the five parameter description of the measured response is adequate for describing the compressor dynamics in either case.

4.1.2 Identification Results

The parameters describing the compressor dynamics were determined for each of the first three modes over a range of flow coefficients in the experimental three-stage axial compressor. The parameter identification data and related information are presented in Table 4.1. The results reveal many things about the behavior of the modal disturbances and are helpful in determining the control law parameters for closed-loop control.

The first parameter, σ_n, is the real part of the pole in the compressor transfer function and indicates the growth/decay rate of the modal disturbances. Negative values indicate that disturbances of this mode number n at the specified flow coefficient are damped and decay in time, and positive values indicate that the mode is unstable at that point. Figure 4.6 presents the experimental values of σ_n for the three-stage compressor over a range of flow coefficients. Important characteristics are the movement toward instability with decreasing flow coefficient and the sequential transition of the modes into the unstable range starting with the first. The intervals between the modes on the line $\sigma = 0$ reflect the extension in the flow range that can be achieved by sequentially stabilizing the modes starting with the first. No unstable data were obtained for the third mode because of the limitations in compressor stabilization.

The parameter ω_n is the imaginary part of the compressor pole and indicates the rate at which modal disturbances travel in the mode space around the compressor

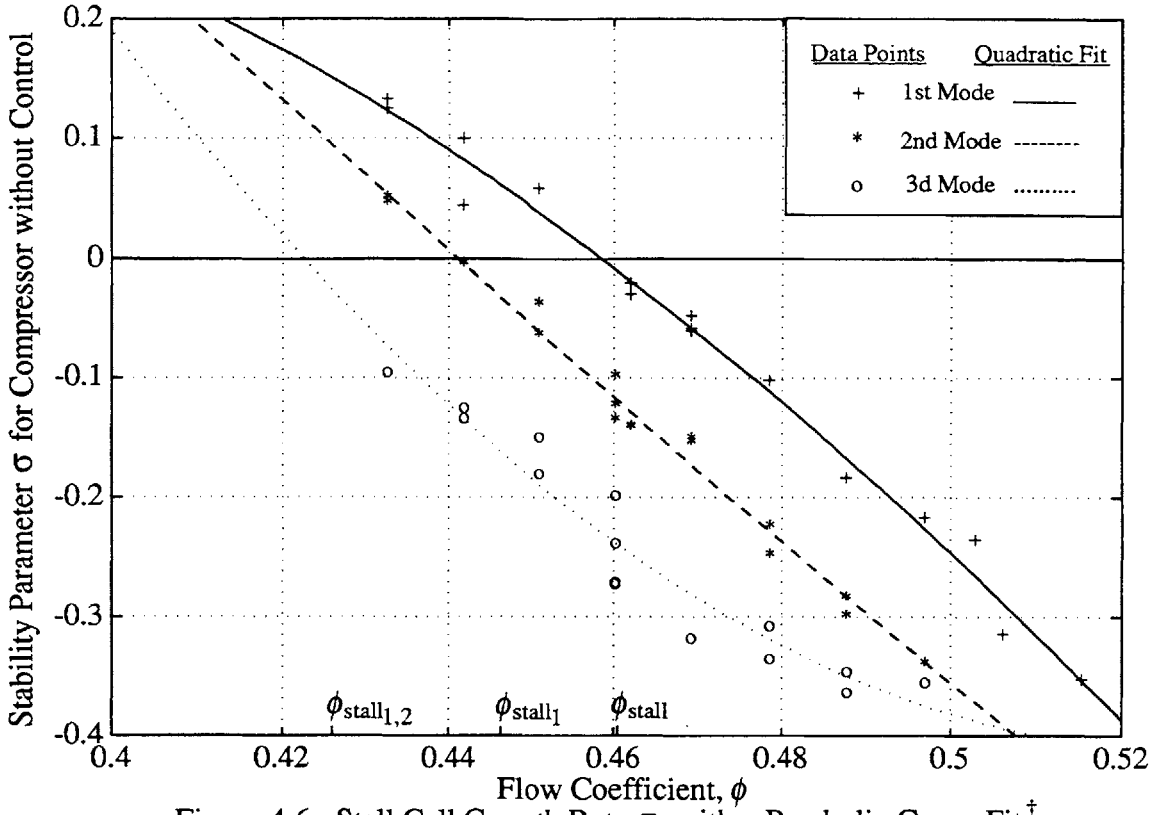

Figure 4.6: Stall Cell Growth Rate σ_n with a Parabolic Curve Fit †

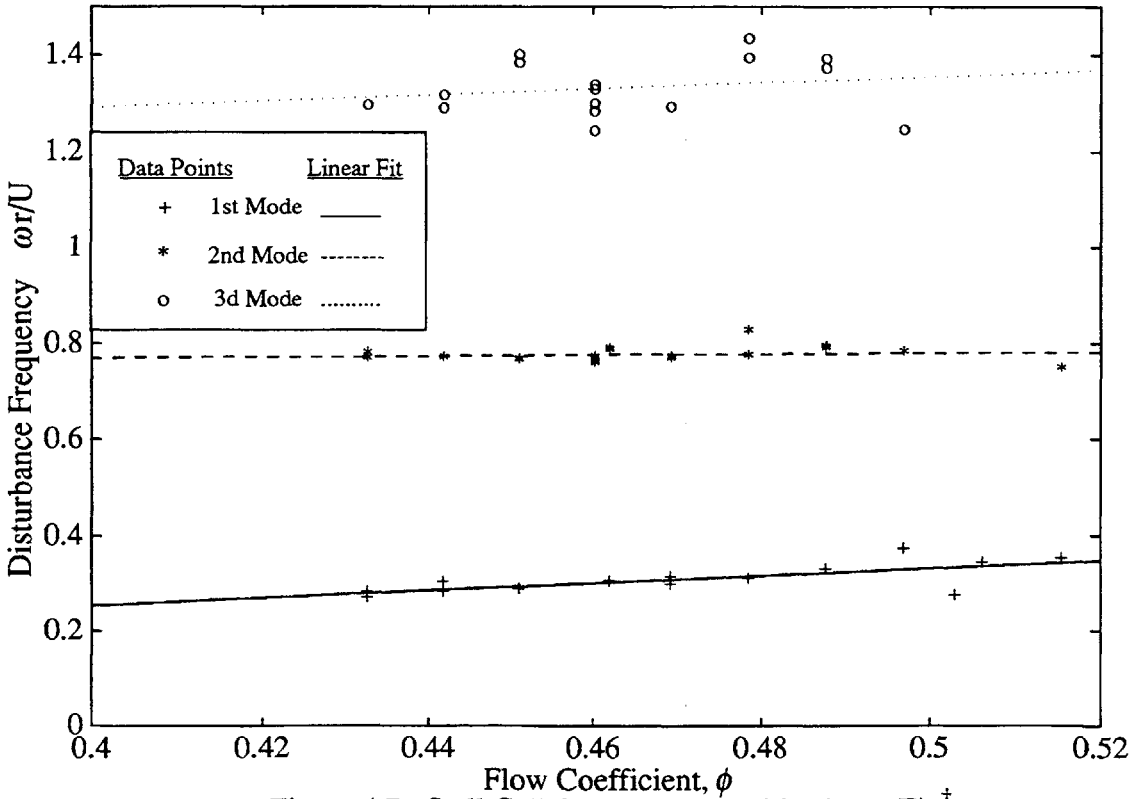

Figure 4.7: Stall Cell Frequency ω_n with Linear Fit.†

†Data points were determined from parameter identification experiments.

annulus. The experimental results shown in Figure 4.7 indicate that the frequency of each of the modal waves tends to decrease by small amounts with decreasing ϕ. The spacing of the modal frequencies is greater than it would be if the modes traveled at the same speed around the compressor annulus in a flow pattern which did not change as it rotated. This indicates the occurrence of a beating phenomenon in the flow in which the higher numbered modes travel more quickly around the annulus than the lower numbered modes and the two are periodically aligned at a frequency determined by the difference in their propagation speeds around the annulus. This phenomenon was also observed by Paduano [16] In regard to the precision of the measurements, it should be noted that the normalized frequency of ω_3 is greater than 1.25, the bandwidth of the input signal. This causes the increased scattering in the third mode data as a whole in comparison with the other modal data.

The real part of the zero in the transfer function is equal to $Z_{r,n} = b_{i,n}/g_{i,n}$, and the imaginary part of the zero is $Z_{i,n} = - b_{r,n}/g_{i,n}$. The zero effects the transient response of the compressor, but has no effect on steady-state performance except under closed-loop conditions. Closed-loop compressor performance is discussed in the next chapter. However, the location of the open-loop zeros during closed-loop control is still treated here. Figures 4.8, 4.9, and 4.10 illustrate the open-loop poles and zeros of the first, second, and third modes respectively in the complex plane. A unique value of ϕ corresponds to each pole and zero. In the diagrams the arrows indicate the direction of migration of the open-loop poles and zeros as ϕ is reduced from 8% above ϕ_{stall}, the stalling flow coefficient, to 6% below ϕ_{stall} in even increments. A nonminimum phase condition exists when either the open-loop pole or zero is in the right hand plane. Figure 4.8 shows that the first mode is nonminimum phase, and Figure 4.9 shows that the second mode becomes nonminimum phase at the lower flow coefficients. The locations of the poles in each diagram correspond to the values for σ_n (real axis) and ω_n (imaginary axis).

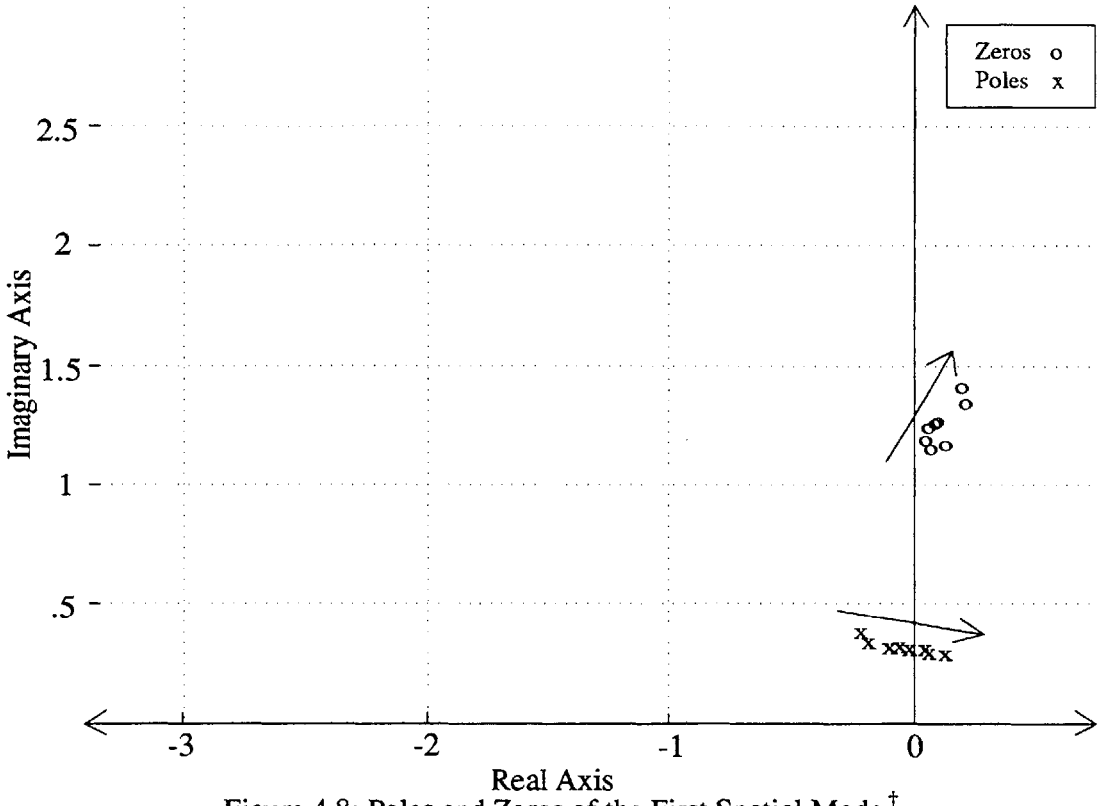

Figure 4.8: Poles and Zeros of the First Spatial Mode †

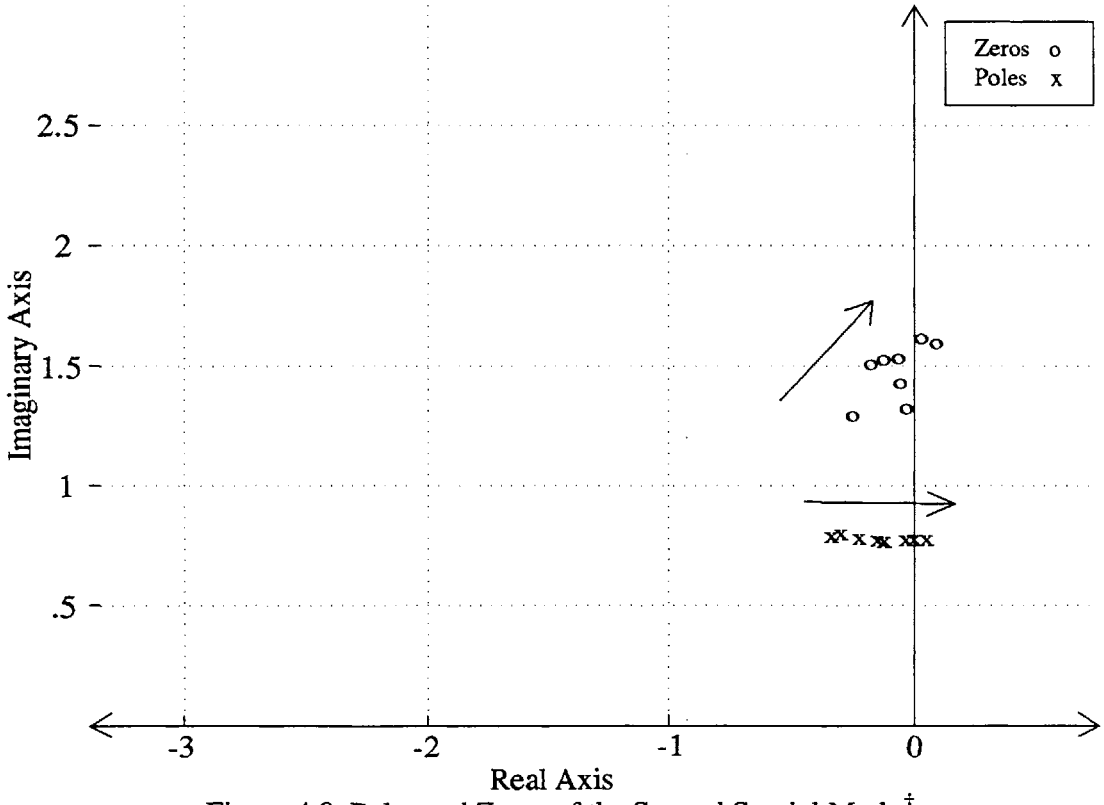

Figure 4.9: Poles and Zeros of the Second Spatial Mode †

† Arrows are in the direction of decreasing ϕ; data were determined from parameter identification experiments.

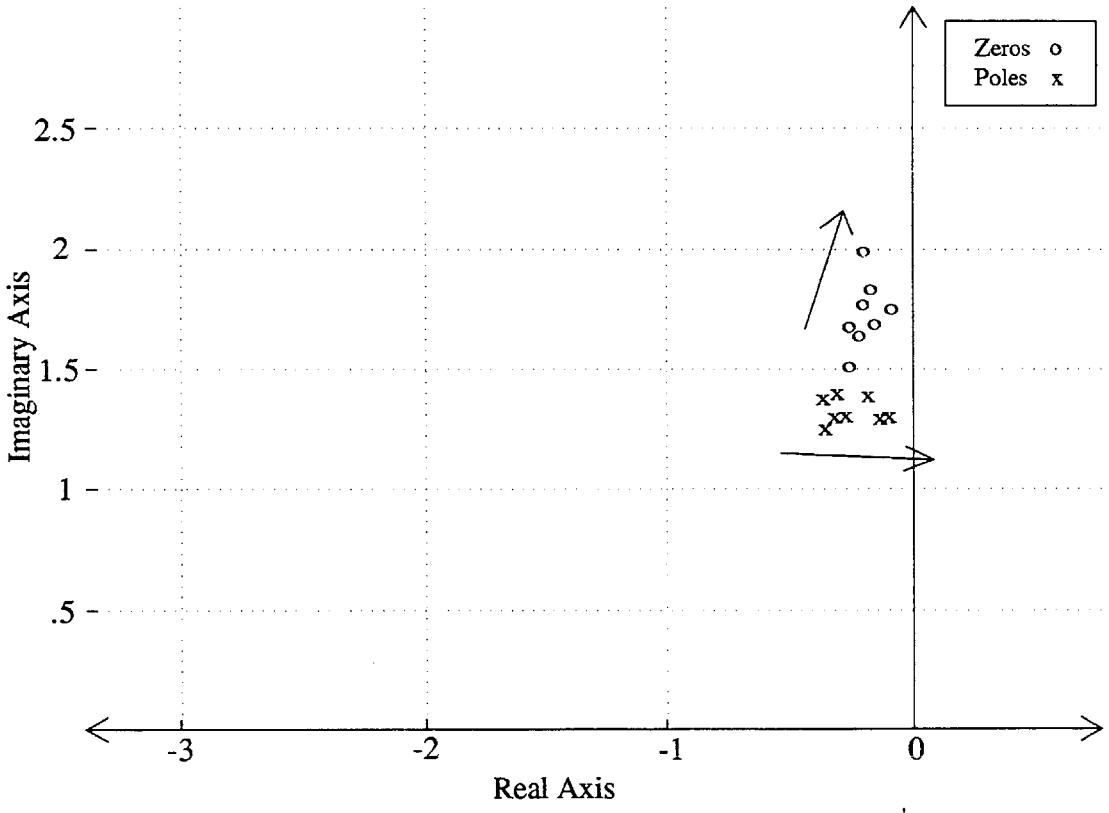

Figure 4.10: Poles and Zeros of the Third Spatial Mode†

† Arrows are in the direction of decreasing ϕ; data were determined from parameter identification experiments.

In addition to the complex poles and zeros, the compressor transfer function has associated with it a gain which is characterized by the parameter g_i. Table 4.1 shows that this parameter is in all cases small and negative. The small value of g_i is necessary to scale changes in γ to changes in flow coefficient. The magnitude of this term is related to the control effectiveness of the SGVs. The sign of g_i indicates an inverse relationship between $\delta\phi$ and $\delta\gamma$. This is related to the fact that the SGV passages resemble diffusers in the annular regions that exhibit positive increments in stagger angle as the annulus is traversed in the positive direction.

4.2 Prediction of Open-loop Dynamics

4.2.1 Model 1

The simplest form of the compressor model gives rough estimates of the open-loop compressor dynamics. The modal stability σ_n predicted by this model is directly proportional to the slope of the compressor characteristic $\frac{\partial\psi}{\partial\phi}$; Figure 3.5 plots the value of the slope which was used in the model. In comparison with the measured stability data, this approximation is shown to be accurate only for the first mode (Figure 4.11). This is due to the fact that the spatial modes having n>1 are more stable than the first and go unstable at flow coefficients further below the steady-state compressor peak. The prediction that all of the modes go unstable at the same flow coefficient is one of the major shortcomings of this model.

Model 1 is capable of making rough estimates of the stall cell speed solely from compressor geometry. Figure 4.12 shows that the predictions of ω made using this model have an accuracy of about 25% for ϕ below ϕ_{stall}. Because the geometry is fixed, the predicted modal frequency is a constant for all flow coefficients, unlike the actual ω. However, the model does predict beating between spatial modes because the modal spacings are not calculated to be directly proportional to n. As was found experimentally, the disturbances of higher mode number are predicted to travel more quickly around the annulus.

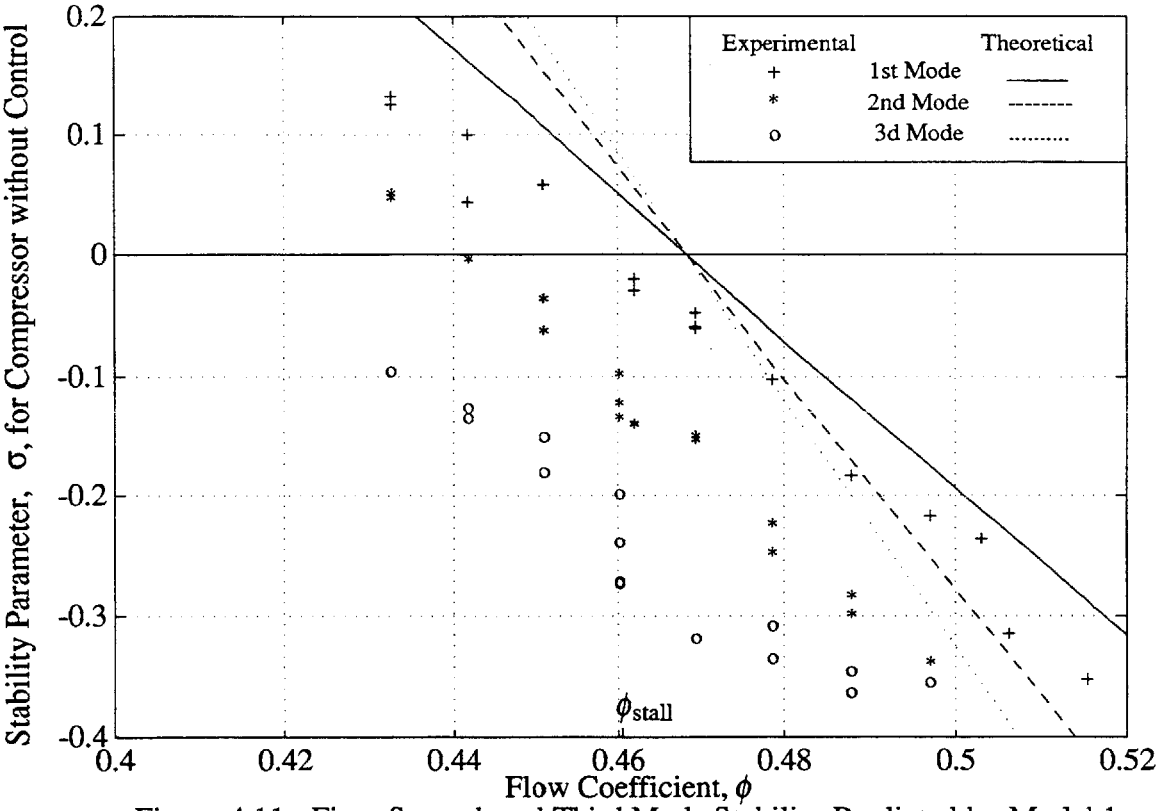

Figure 4.11: First, Second, and Third Mode Stability Predicted by Model 1 Compared with Experimental Data

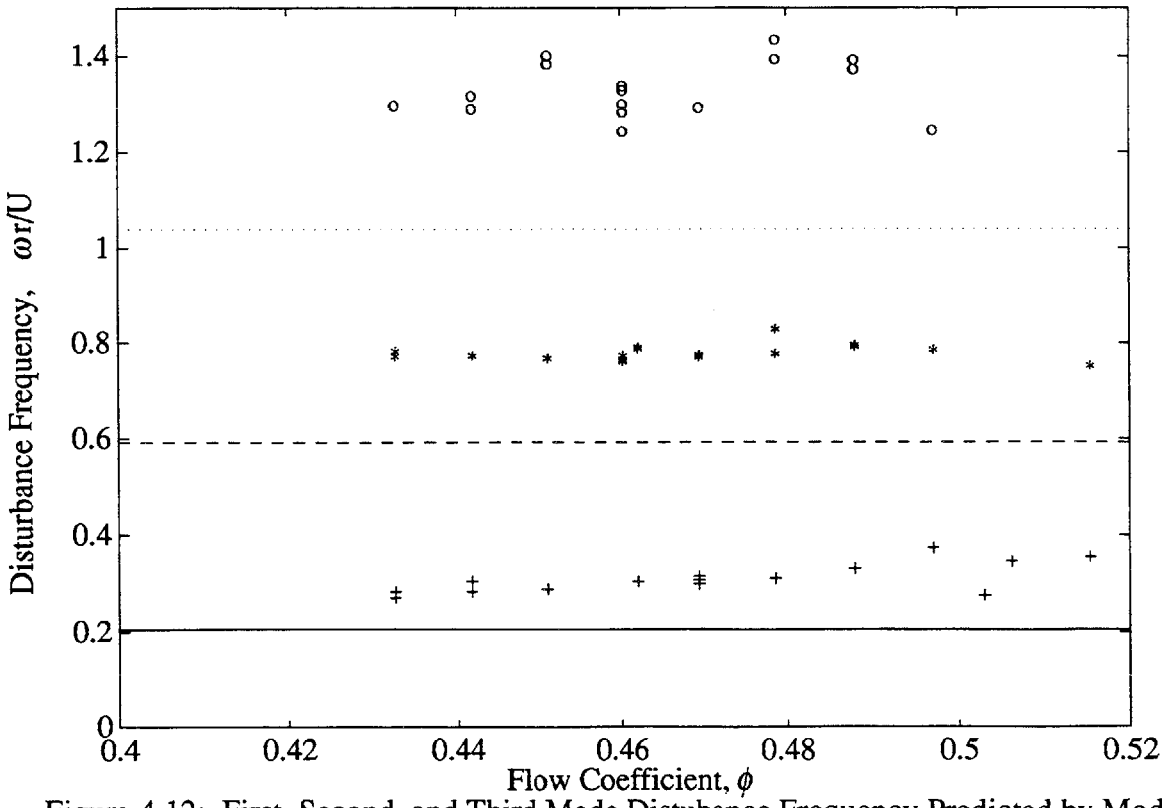

Figure 4.12: First, Second, and Third Mode Distubance Frequency Predicted by Model 1 Compared with Experimental Data (Legend as in Figure 4.11)

Figure 4.17 shows the migration of the poles and zeros of the first three modes with changing ϕ. The model predicts that the zeros, like the poles, move into the right hand plane when $\frac{\partial \psi}{\partial \phi}$ becomes positive. This is not consistent with the experimental data however. As can be seen in the figure, the model predicts that the shift in open-loop poles and zeros is proportional to changes in ϕ, hence the even spacing is associated with the even increments in ϕ. This is only a rough approximation, however, of the measured trends.

4.2.2 Model 2 - Unsteady Losses

The significance of modeling the compressor in greater detail is that it brings about a shift in the dominant poles and zeros so that the model is better able to predict the measured modal dynamics. An unavoidable result of introducing additional dynamics to the model is that the system is characterized by additional poles and zeros; however, in Section 4.1.1.2.3 it was shown that the additional poles and zeros actually have little influence on the transfer function in the frequency range of interest. This means that the frequency response is determined by the dominant poles and zeros and can be characterized by the same parameters as before.

The only additional parameter needed to describe the system is τ_u, the parameter characterizing the time lag through a blade row. Equation 3.42 characterizes how the time lag is able to influence all three complex poles and zeros. The roots of the numerator and denominator are clearly influenced by each of the terms in the original polynomial. Model 1 corresponds to the case in which $\tau_u = 0$. Because the actual value of τ_u was not known accurately, a value was chosen that enabled the model to best match the experimentally measured complex poles ($\sigma_n + i\omega_n$) over a range of flow coefficients near the stall point. Figures 4.13 and 4.14 illustrate the best fit case in which τ_u=1.5. The fact that the predicted values of σ_n and ω_n for all three modes can be made to agree with the measured values simply by choosing τ_u indicates that the model captures the important dynamic characteristics that determine the change in open-loop

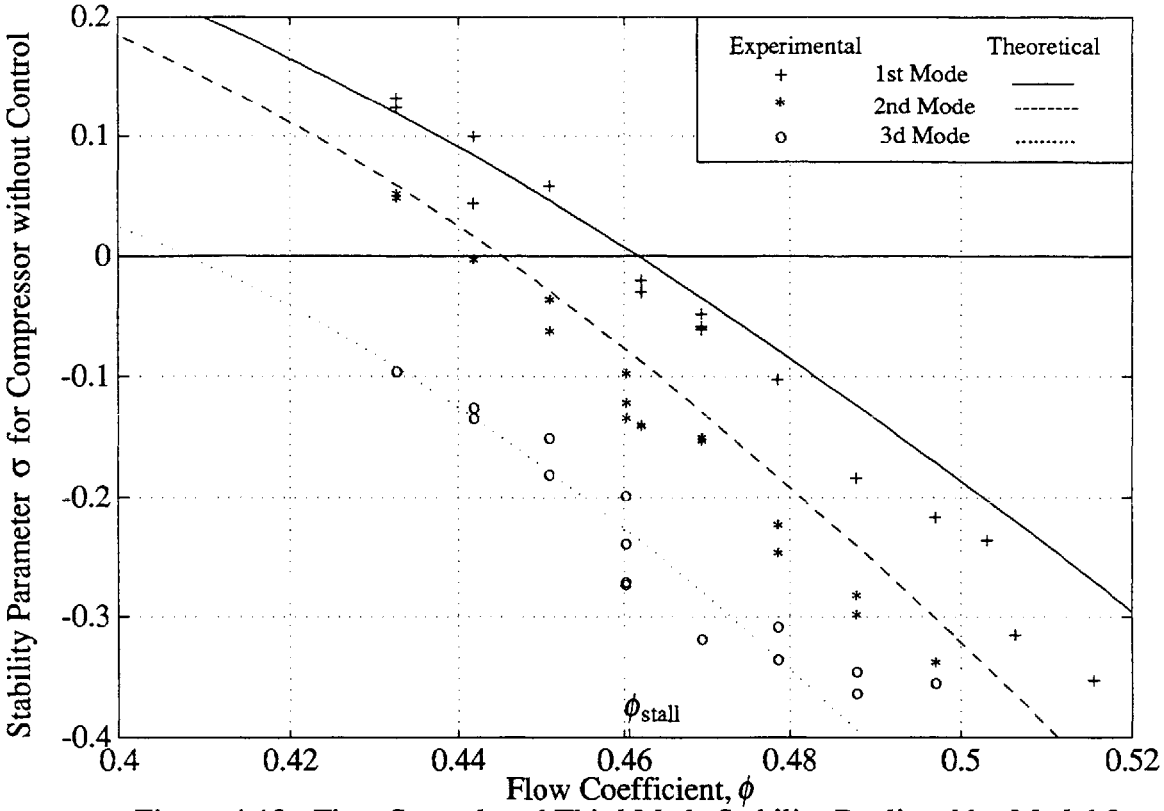

Figure 4.13: First, Second, and Third Mode Stability Predicted by Model 2 Compared with Experimental Data

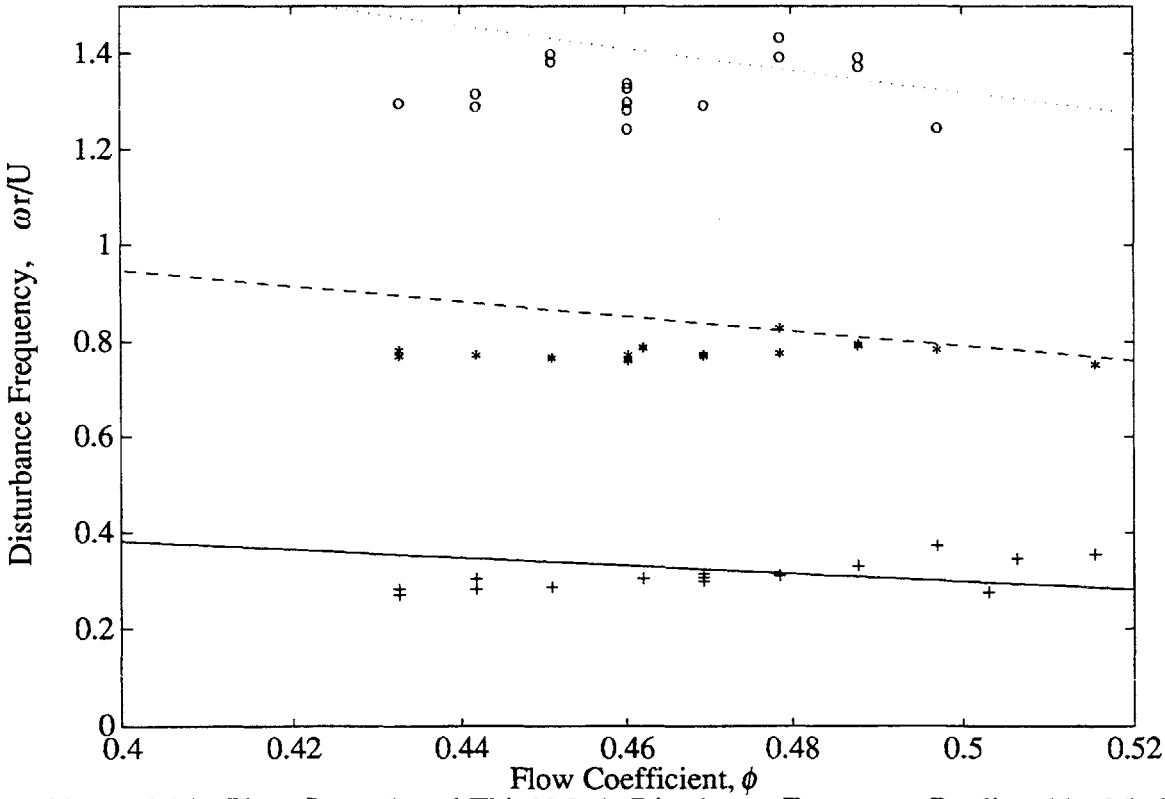

Figure 4.14: First, Second, and Third Mode Distubance Frequency Predicted by Model 2 Compared with Experimental Data (Legend as in Figure 4.13)

dynamics with mode number and the relationship between the complex and real part of the pole. Although τ_u was not measured experimentally in this case, experiments by Nagano et al [28] show that values for τ_u can fall between 1.0 and 1.5 depending on the blade row stagger and flow conditions. The fact that the optimal τ_u is within this range is an encouraging result that seems to support the validity of the model. Designing an experiment to independantly determine the actual τ_u for the compressor was considered, but the existing instrumentation and SGV actuators were determined to be insufficient for the task.

As a point of interest, the location of the additional poles and zeros relative to the dominant poles and zeros is discussed here. Figure 4.17 illustrates the position of all three complex poles and zeros in Model 2 for the first three modes over a range of flow coefficients. The arrows indicate the direction in which they move as ϕ is decreased. The dominant poles and zeros are closest to the imaginary axis. As was determined previously, the poles have very good agreement with the experimental data, but the zeros do not agree as well with the data. The first mode zeros are not predicted to always be nonminimum phase as the data indicate; however, the trend of dominant zeros shifting to the left with increasing mode number is captured. The change in the compressor dynamics over the 14% change in ϕ being illustrated is significant, but the large scale used in the plots conceals this. The large scale real axis emphasizes the fact that the additional poles and zeros are very far from the imaginary axis and can have little effect on the compressor dynamics. Although movement of the poles and zeros is evident, there is no indication that the additional poles and zeros will become dominant without very large decreases in ϕ. Changes in the poles and zeros of the third order compressor model which result from modeling the compressor differently are discussed in the next two sections.

4.2.3 Model 3 - Unsteady Losses & Other Flow Response Lags

The compressor dynamics of Model 3 are determined by the effects of both unsteady losses and the pressure rise response lag associated with other nonideal flow characteristics. As was mentioned in Section 3.4, allowing the nonideal flow phenomena to develop over the same time scale as the unsteady losses makes this a third order model instead of a fifth order one. The additional terms in the compressor's transfer function (Equation 3.53) result in changes in both the poles and zeros of the model. As with Model 2, the flow response lag parameter, $\tau_u = \tau_d$, was chosen so that the predicted open-loop poles best matched the ones measured experimentally, and the best value, $\tau_u = \tau_d = 1.5$, was identical to the one used in Model 2. This is not surprising, because the pressure rise associated with both the flow blockage and deviation and other nonideal phenomena were found not to be a strong function of ϕ (Figure 3.11) and hence changed very little due to axial flow disturbances $\delta\phi$. Nevertheless, the good agreement between the predicted and experimental open-loop poles ($\sigma+i\omega$), which is shown in Figures 4.15 and 4.16, and the fact that τ_u and τ_d fall within the range of values found experimentally strongly support the appropriateness of this model.

The dynamic contributions of Model 3 can be understood more completely by looking at the predicted locations of the poles and zeros. Figure 4.17 illustrates the three complex poles and zeros of the model for the first three modes. In comparison with Model 2 the dominant open-loop poles and zeros are nearly identical. The additional poles and zeros are located somewhat differently than they were in Model 2, but their influence on the compressors dynamic response is still negligible.

4.2.4 Model 4 - Flow Response Lags to $\delta\phi$ and $\delta\gamma$

Like Models 2 and 3, Model 4 is a third order representation of the compressor dynamics. By modeling the flow response lags associated with perturbations in SGV stagger angle the zeros of the compressor model are changed. This result is obtained by assuming that pressure rise perturbations associated with $\delta\gamma$ develop over the same time

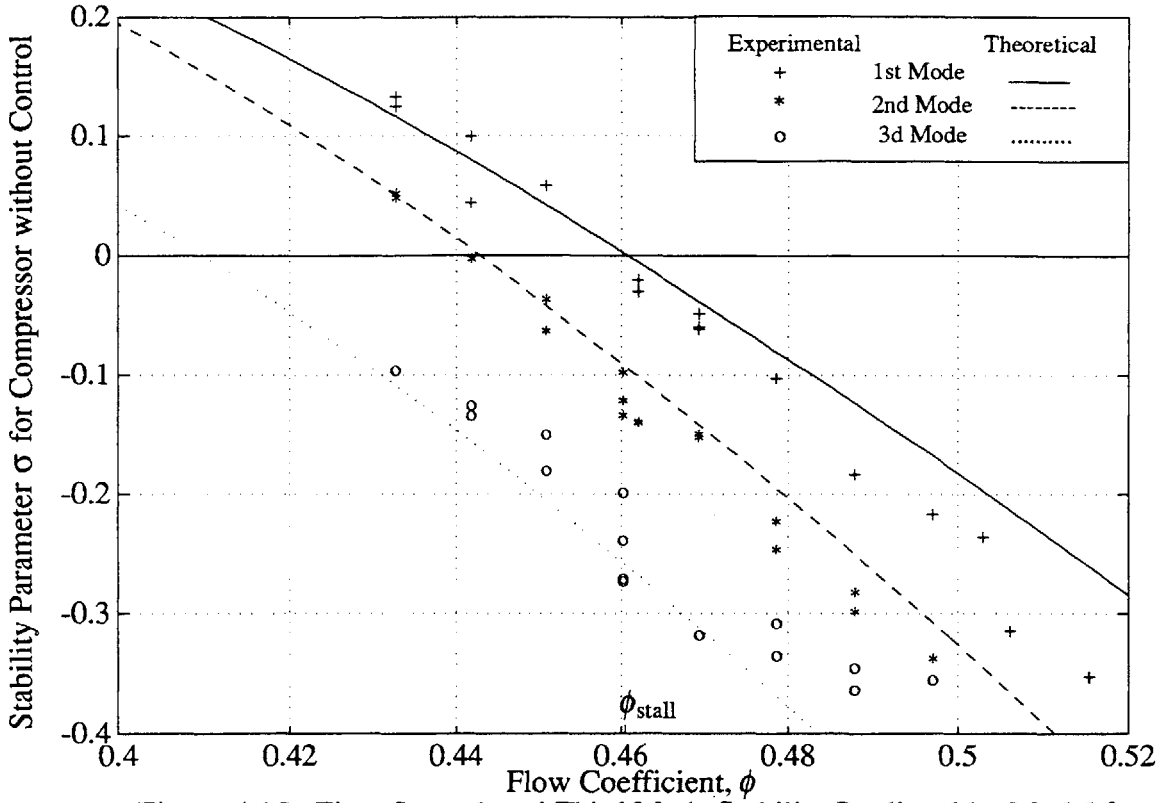

Figure 4.15: First, Second, and Third Mode Stability Predicted by Model 3 Compared with Experimental Data

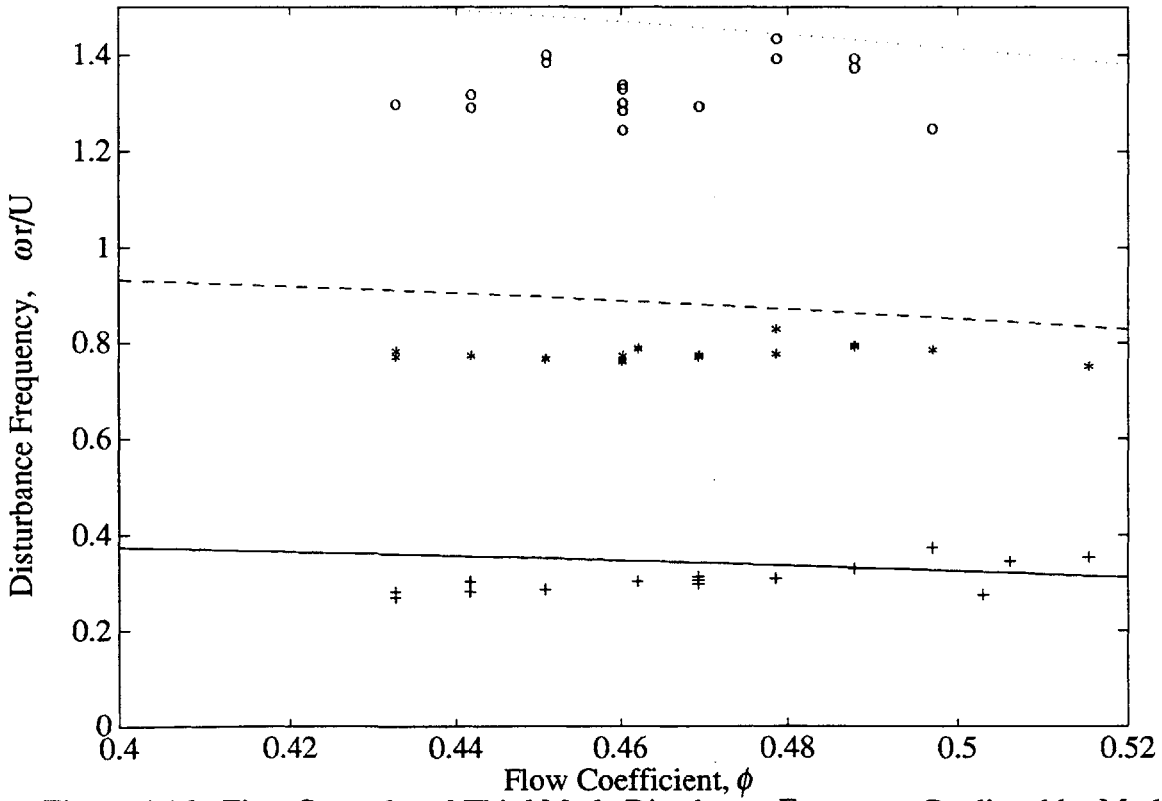

Figure 4.16: First, Second, and Third Mode Distubance Frequency Predicted by Model 3 Compared with Experimental Data (Legend as in Figure 4.15)

scale as those associated with $\delta\phi$ (i.e. $\tau_m = \tau_u = \tau_d$). A comparison of Equations 3.53 and 3.63 shows that Models 3 and 4 have identical poles. Since this is the case, the value of τ used in Model 4 to match the compressor dynamics will be the same as it was for Model 3 – which is also the same as the value used in Model 2. It also follows from this fact that Figures 4.15 and 4.16 are descriptive of both Model 3 and Model 4.

Figure 4.17 shows the similarities and differences between Models 3 and 4 most clearly. The three poles of Model 3 are identical to those of Model 4. The high frequency poles move as ϕ is decreased but will have negligible influence on the compressor's open-loop frequency response. All three complex zeros, however, are repositioned due to the new lag term in the compressor transfer function. The dominant zeros exhibit small shifts toward the right hand plane.

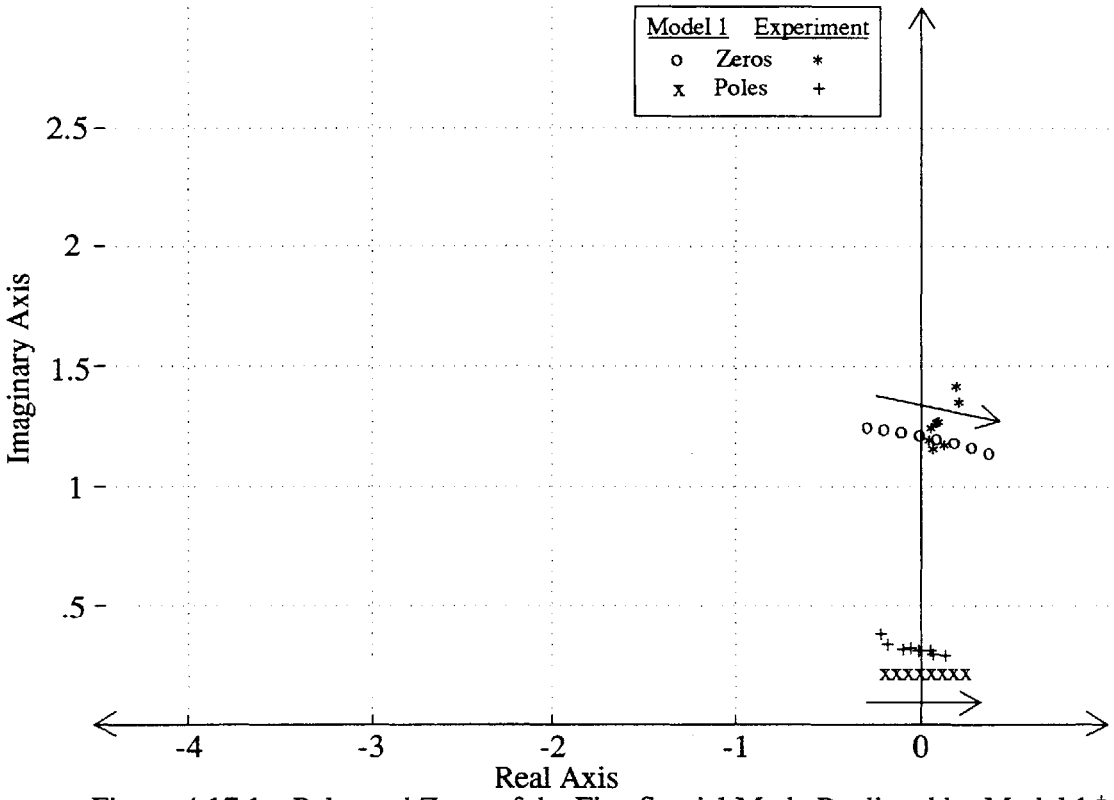

Figure 4.17.1a: Poles and Zeros of the First Spatial Mode Predicted by Model 1 †

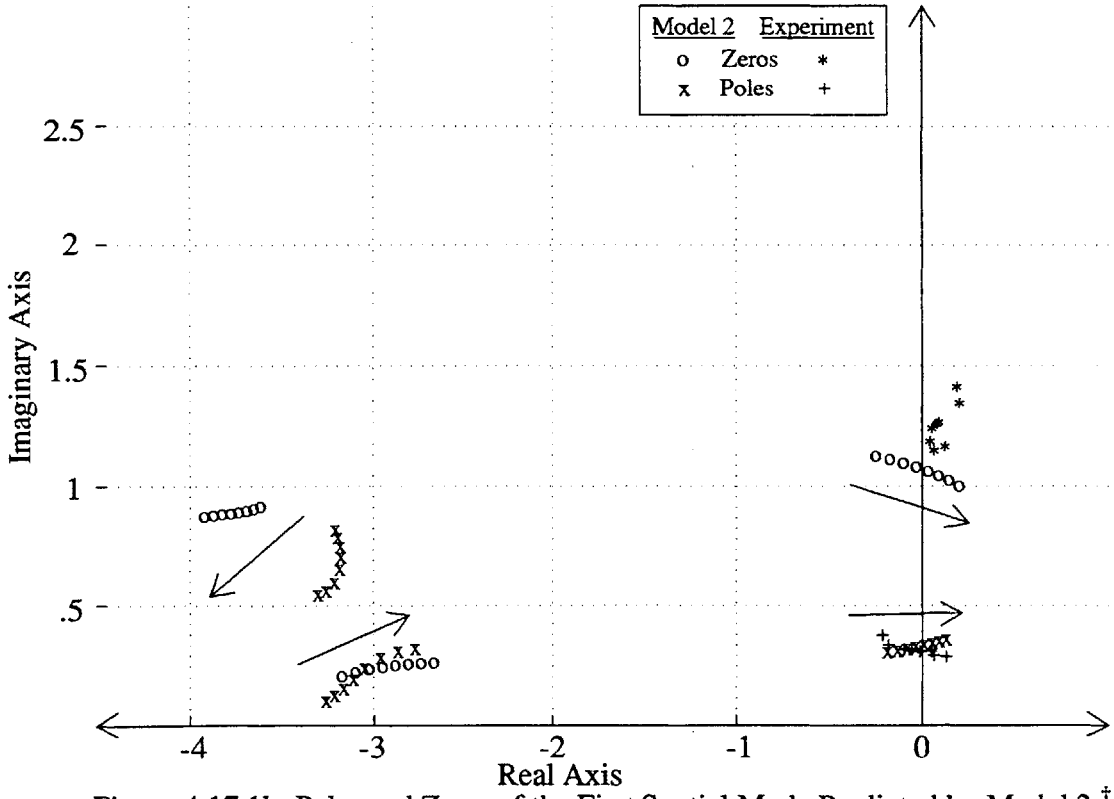

Figure 4.17.1b: Poles and Zeros of the First Spatial Mode Predicted by Model 2 †

† Arrows are in the direction of decreasing ϕ.

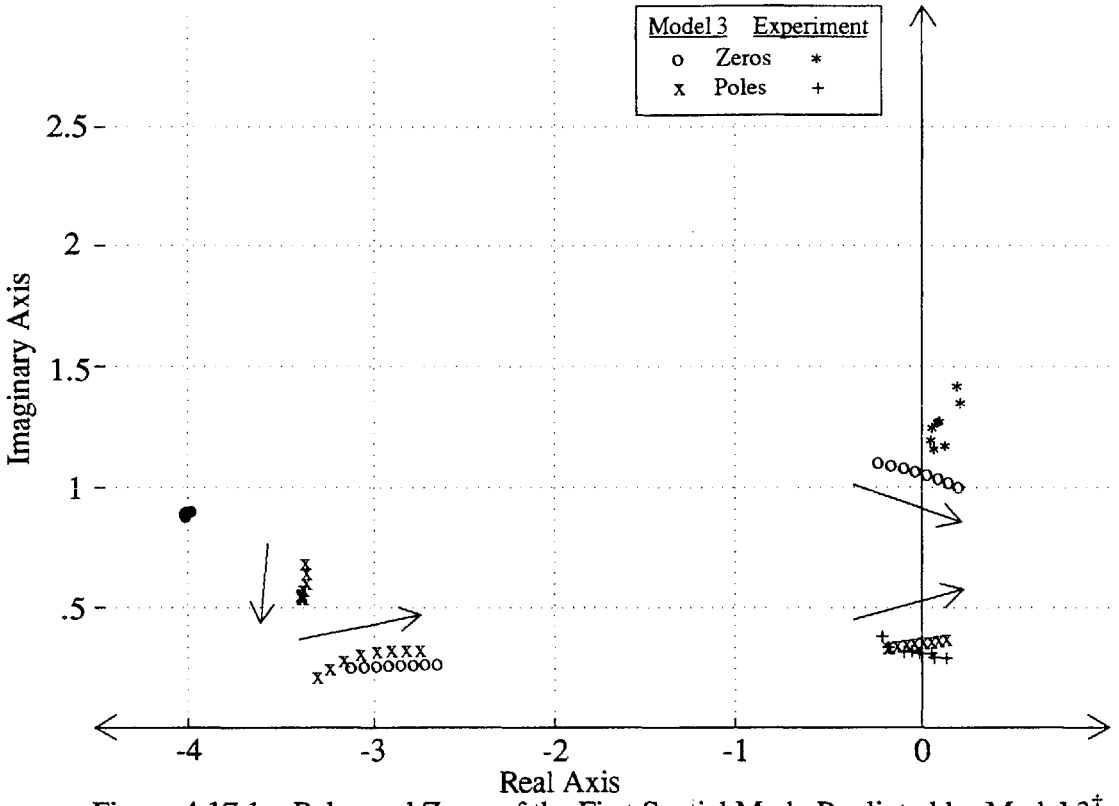

Figure 4.17.1c: Poles and Zeros of the First Spatial Mode Predicted by Model 3†

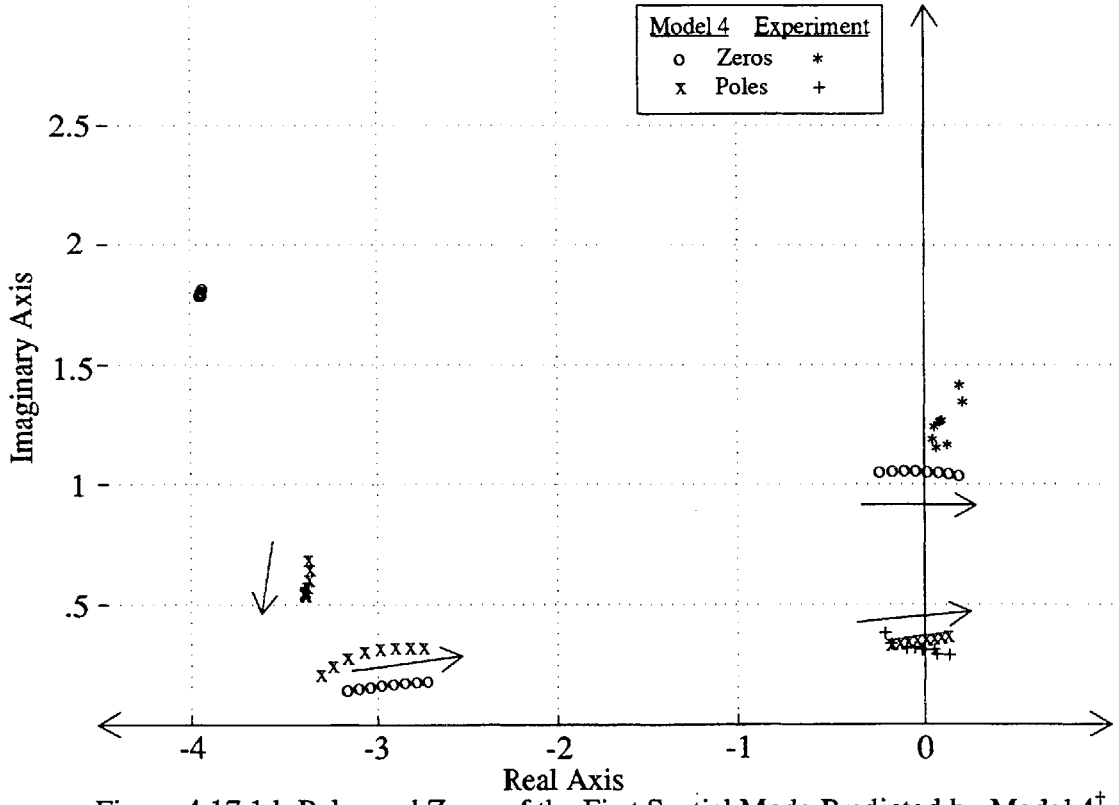

Figure 4.17.1d: Poles and Zeros of the First Spatial Mode Predicted by Model 4†

† Arrows are in the direction of decreasing ϕ.

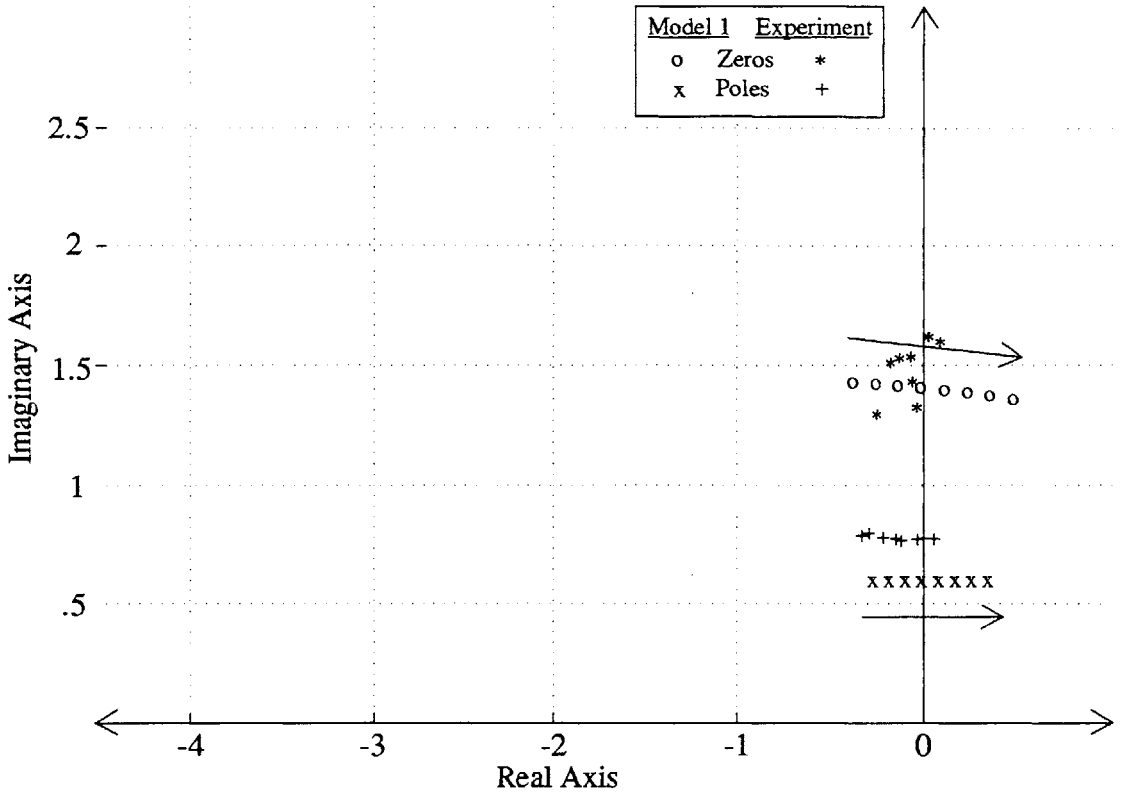

Figure 4.17.2a: Poles and Zeros of the Second Spatial Mode Predicted by Model 1†

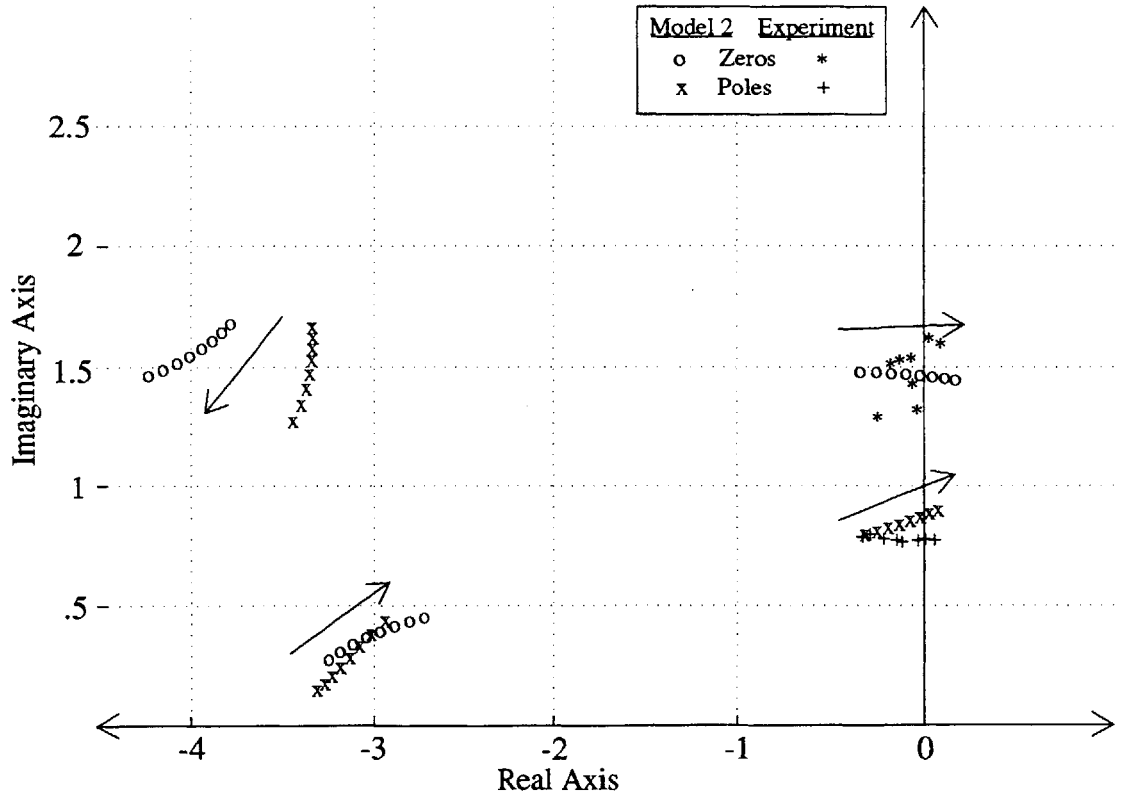

Figure 4.17.2b: Poles and Zeros of the Second Spatial Mode Predicted by Model 2†

† Arrows are in the direction of decreasing ϕ.

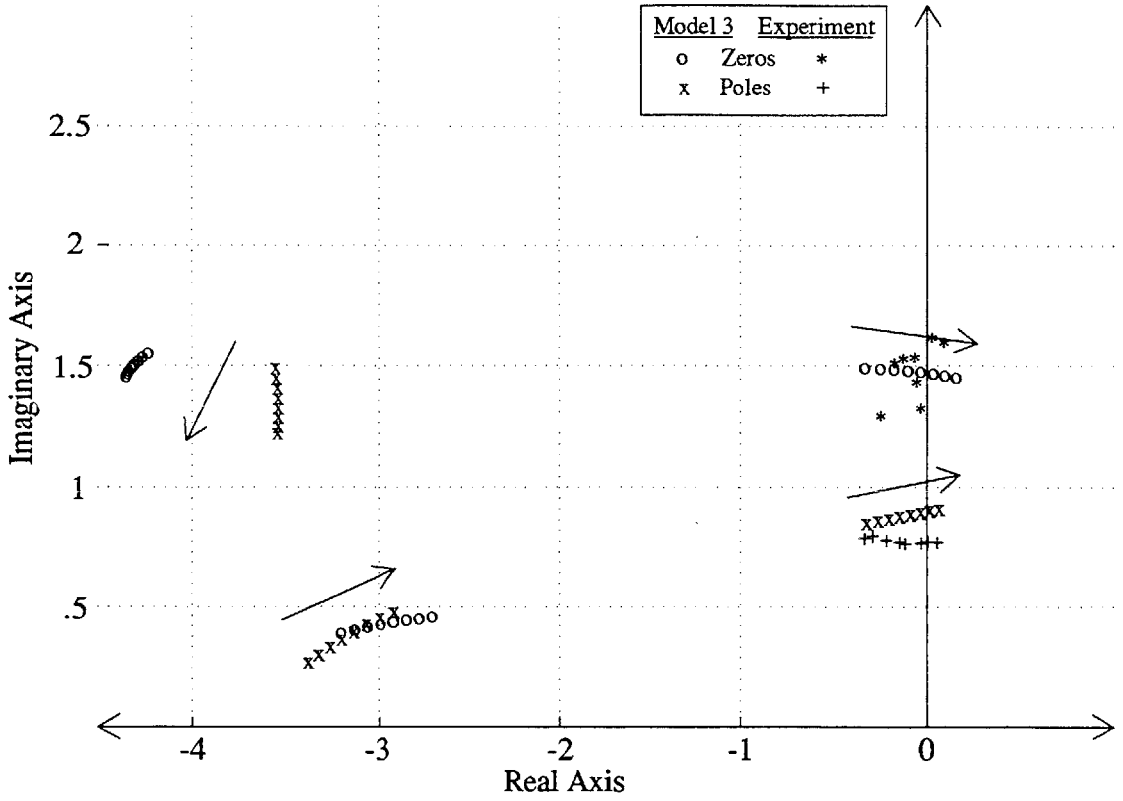

Figure 4.17.2c: Poles and Zeros of the Second Spatial Mode Predicted by Model 3†

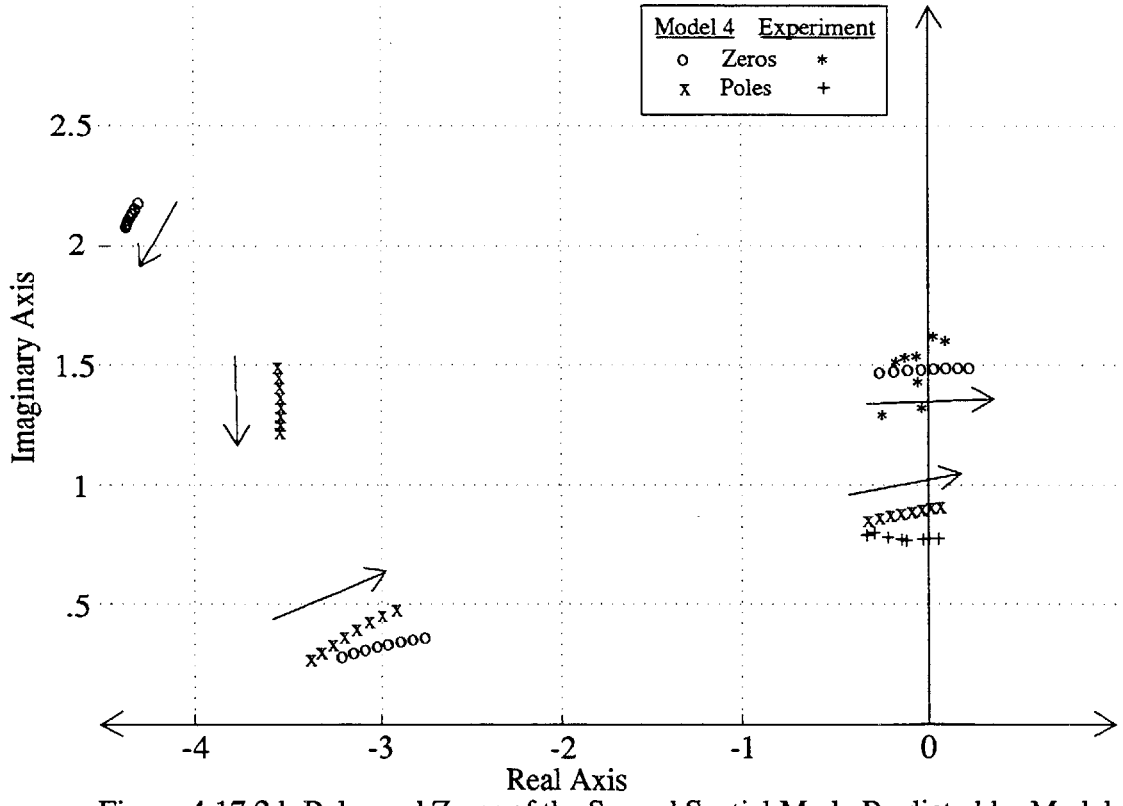

Figure 4.17.2d: Poles and Zeros of the Second Spatial Mode Predicted by Model 4†

† Arrows are in the direction of decreasing ϕ.

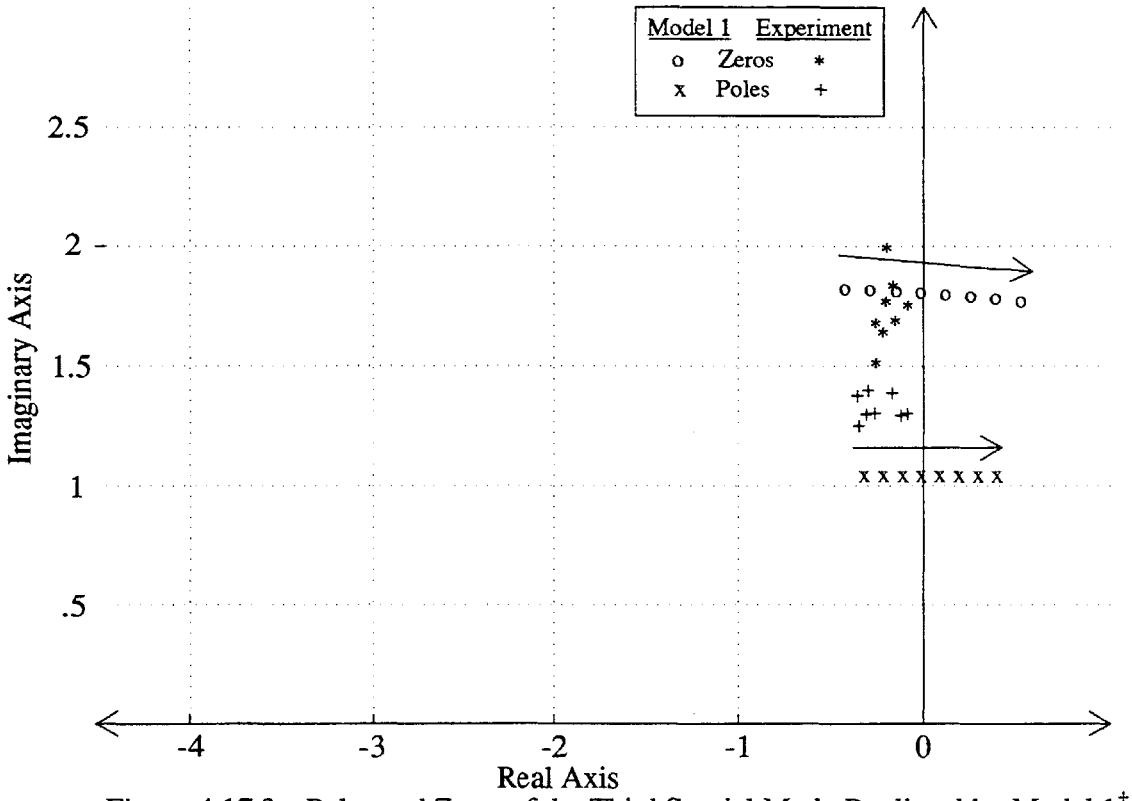

Figure 4.17.3a: Poles and Zeros of the Third Spatial Mode Predicted by Model 1†

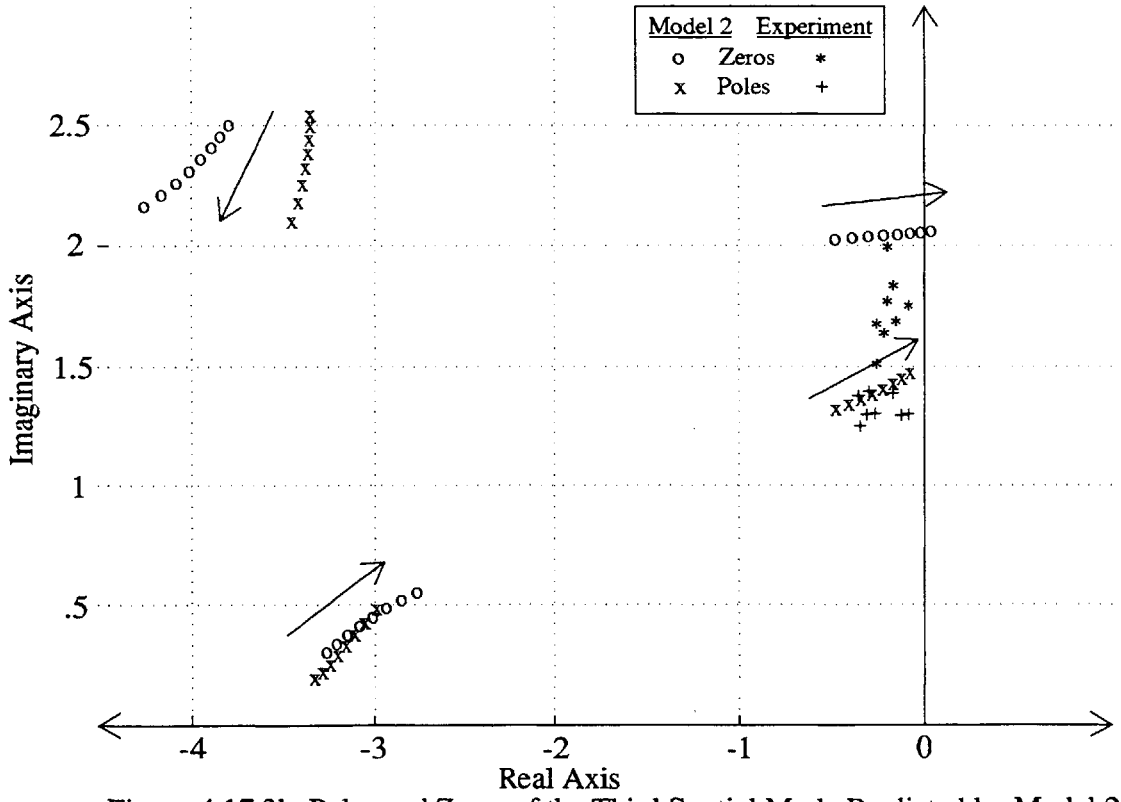

Figure 4.17.3b: Poles and Zeros of the Third Spatial Mode Predicted by Model 2 †

† Arrows are in the direction of decreasing ϕ.

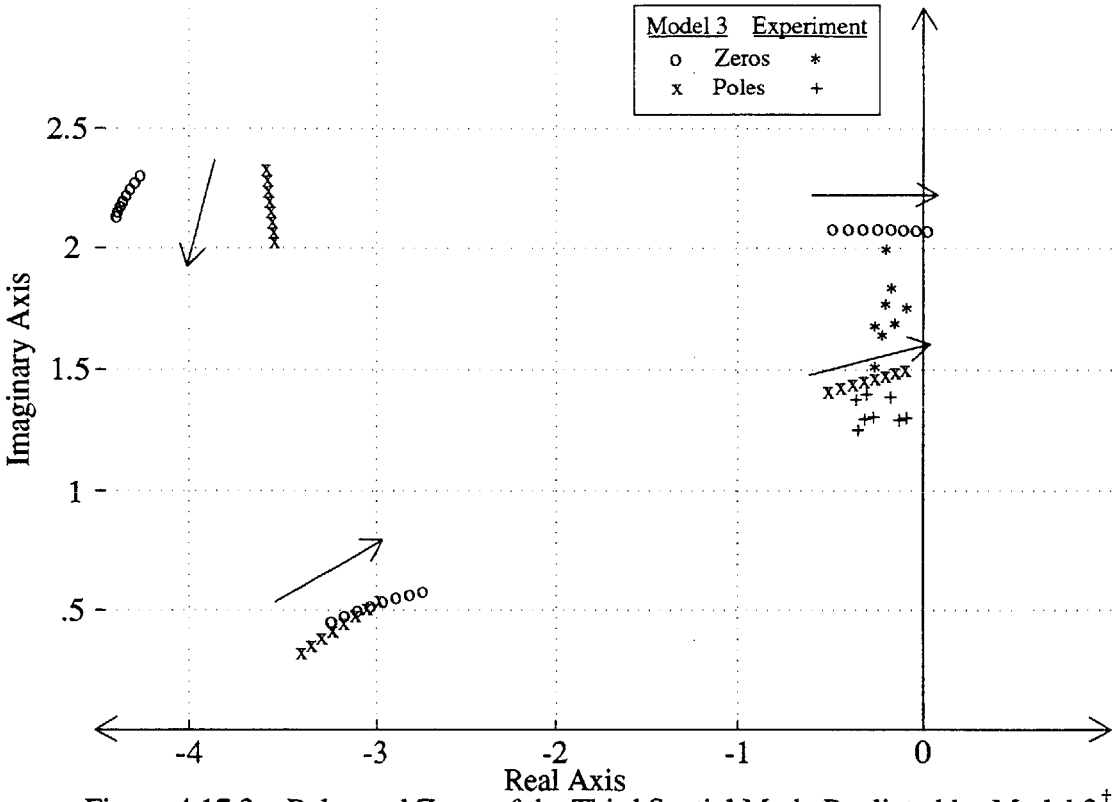

Figure 4.17.3c: Poles and Zeros of the Third Spatial Mode Predicted by Model 3†

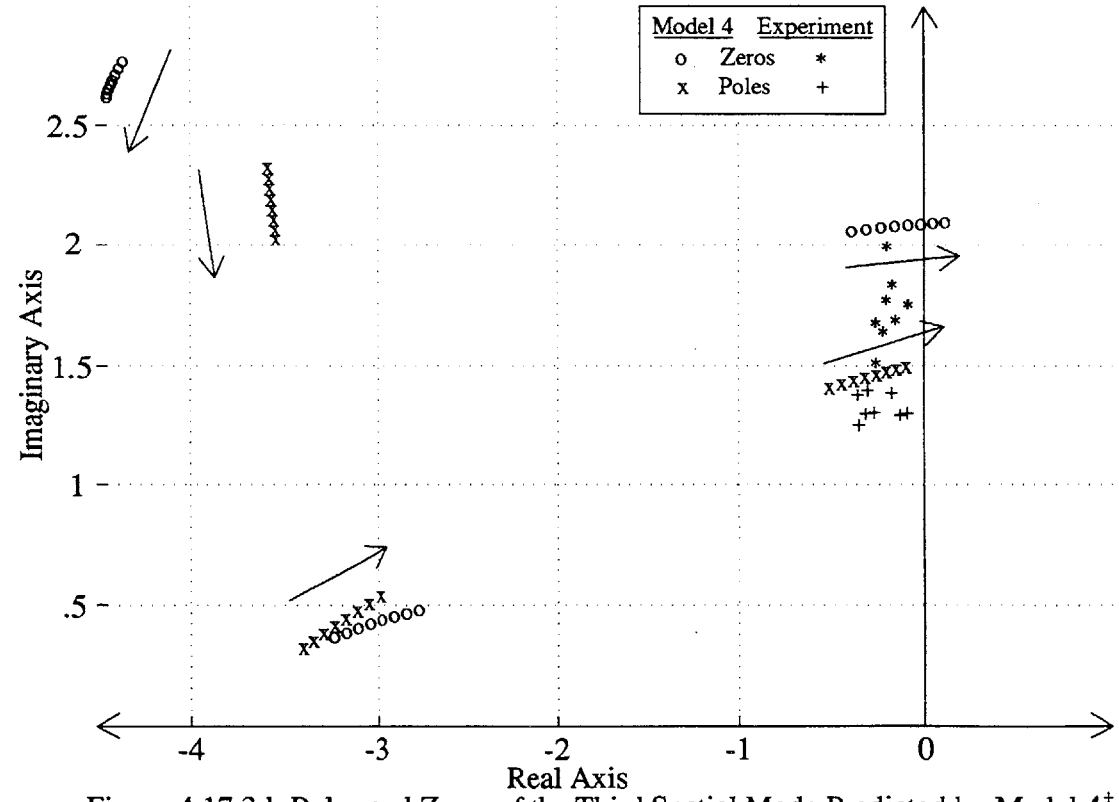

Figure 4.17.3d: Poles and Zeros of the Third Spatial Mode Predicted by Model 4†

† Arrows are in the direction of decreasing ϕ.

ϕ	Percent Difference from ϕ_{stall}	Actuation/ ID Method	σ_1	ω_1	$b_{r,1}$	$b_{i,1}$	$g_{i,1}$	Open-Loop Zeros $Z_{r,1}=\frac{b_{i,1}}{g_{i,1}}$	Open-Loop Zeros $Z_{i,1}=\frac{b_{r,1}}{g_{i,1}}$
0.515	12.0	5°cos/SM-TFF	-0.3531	0.354	-0.0761	-0.01189	-0.0608	-0.1957	1.252
0.506	10.0	5°cos/SM-TFF	-0.3151	0.344	-0.0791	-0.00815	-0.0645	-0.1263	1.227
0.503	9.3	5°cos/SM-TFF	-0.2361	0.275	-0.0768	-0.02215	-0.0636	-0.3483	1.207
0.497	8.0	5°cos/SM-TFF	-0.2173	0.373	-0.0729	0.00383	-0.0635	0.0603	1.149
0.488	6.0	5°cos/SM-TFF	-0.1839	0.329	-0.0709	0.00280	-0.0573	0.0489	1.238
0.479	4.0	5°cos/SM-TFF	-0.1030	0.310	-0.0639	0.00449	-0.0506	0.0887	1.264
0.469	2.0	3°cos/SM-TFF	-0.0484	0.298	-0.0574	0.00250	-0.0420	0.0597	1.367
0.469	2.0	3°cos/SM-TFF	-0.0594	0.306	-0.0628	0.00295	-0.0472	0.0625	1.330
0.469	2.0	3°sin/SM-TFF	-0.0613	0.313	-0.0600	0.00203	-0.0506	0.0402	1.186
0.462	0.4	5°both/NF	-0.0206	0.303	-0.0652	0.00409	-0.0518	0.0788	1.258
0.462	0.4	5°both/NF	-0.0303	0.304	-0.0650	0.00375	-0.0515	0.0728	1.262
0.451	-2.0	5°cos/NF	0.0576	0.286	-0.0565	0.00844	-0.0421	0.2007	1.343
0.442	-4.0	4°sin/NF	0.0431	0.303	-0.0519	0.00542	-0.0446	0.1215	1.163
0.442	-4.0	4°cos/NF	0.0992	0.282	-0.0522	0.00663	-0.0362	0.1830	1.439
0.432	-6.0	2°cos/NF	0.1244	0.282	-0.0475	0.00625	-0.0337	0.1854	1.410
0.432	-6.0	2°cos/NF	0.1320	0.270	-0.0463	0.00943	-0.0329	0.2865	1.406

Table 4.1a: First Mode Parameter Identification Data

ϕ	Percent Difference from ϕ_{stall}	Actuation/ ID Method	σ_2	ω_2	$b_{r,2}$	$b_{i,2}$	$g_{i,2}$	Open-Loop Zeros $Z_{r,2} = \frac{b_{i,2}}{g_{i,2}}$	Open-Loop Zeros $Z_{i,2} = \frac{b_{r,2}}{g_{i,2}}$
0.515	12.0	5°sin/SM-TFF	-0.4369	0.750	-0.1155	-0.03575	-0.0934	-0.3826	1.237
0.497	8.0	5°sin/SM-TFF	-0.3382	0.783	-0.1163	-0.02282	-0.0902	-0.2529	1.289
0.488	6.0	5°both/SM-TFF	-0.2984	0.794	-0.0950	-0.01128	-0.0631	-0.1788	1.507
0.488	6.0	5°sin/SM-TFF	-0.2829	0.790	-0.1119	-0.01525	-0.0872	-0.1749	1.283
0.479	4.0	5°both/SM-TFF	-0.2233	0.775	-0.0868	-0.00736	-0.0569	-0.1293	1.524
0.479	4.0	5°sin/SM-TFF	-0.2471	0.827	-0.1242	-0.00903	-0.0951	-0.0950	1.306
0.469	2.0	5°sin/SM-TFF	-0.1533	0.772	-0.0968	-0.00719	-0.0711	-0.1011	1.361
0.469	2.0	5°both/SM-TFF	-0.1502	0.768	-0.0806	-0.00364	-0.0526	-0.0691	1.530
0.462	0.4	5°both/NF	-0.1409	0.788	-0.1018	-0.00147	-0.0728	-0.0202	1.398
0.462	0.4	5°both/NF	-0.1402	0.786	-0.1003	-0.00167	-0.0710	-0.0235	1.413
0.460	0.0	5°cos/NF	-0.1343	0.759	-0.0835	-0.00229	-0.0521	-0.0440	1.604
0.460	0.0	5°sin/NF	-0.0979	0.772	-0.1151	-0.00790	-0.0875	-0.0902	1.315
0.460	0.0	5°both/NF	-0.1223	0.762	-0.1032	-0.00446	-0.0724	-0.0616	1.426
0.451	-2.0	5°cos/NF	-0.0630	0.765	-0.0798	0.00182	-0.0497	0.0366	1.607
0.451	-2.0	5°sin/NF	-0.0366	0.766	-0.1087	-0.00319	-0.0824	-0.0387	1.320
0.442	-4.0	5°cos/NF	-0.0039	0.771	-0.0789	0.00107	-0.0489	0.0219	1.613
0.432	-6.0	2°cos/NF	0.0471	0.769	-0.0644	0.00339	-0.0404	0.0838	1.593
0.432	-6.0	2°cos/NF	0.0510	0.781	-0.0684	0.00345	-0.0431	0.0799	1.587

Table 4.1b: Second Mode Parameter Identification Data

ϕ	Percent Difference from ϕ_{stall}	Actuation/ ID Method	σ_3	ω_3	$b_{r,3}$	$b_{i,3}$	$g_{i,3}$	Open-Loop Zeros $Z_{r,3} = \frac{b_{i,3}}{g_{i,3}}$	Open-Loop Zeros $Z_{i,3} = \frac{b_{r,3}}{g_{i,3}}$
0.497	8.0	5°both/SM-TFF	-0.3551	1.246	-0.1202	-0.02095	-0.0799	-0.2624	1.506
0.488	6.0	5°sin/SM-TFF	-0.3458	1.392	-0.1049	-0.01259	-0.0611	-0.2061	1.718
0.488	6.0	5°both/SM-TFF	-0.3636	1.372	-0.1287	-0.01755	-0.0787	-0.2230	1.635
0.479	4.0	5°sin/SM-TFF	-0.3353	1.433	-0.1106	-0.01037	-0.0631	-0.1642	1.752
0.479	4.0	5°both/SM-TFF	-0.3081	1.393	-0.1176	-0.01105	-0.0699	-0.1581	1.682
0.469	2.0	5°both/SM-TFF	-0.3186	1.292	-0.1226	-0.01919	-0.0733	-0.2617	1.673
0.460	0.0	5°cos/SM-TFF	-0.2387	1.243	-0.1220	-0.02405	-0.0731	-0.3292	1.670
0.460	0.0	5°sin/SM-TFF	-0.1990	1.283	-0.1465	-0.02048	-0.0909	-0.2255	1.612
0.460	0.0	5°cos/SM-TFF	-0.1990	1.338	-0.1103	-0.00973	-0.0681	-0.1429	1.620
0.460	0.0	5°both/SM-TFF	-0.2729	1.299	-0.1106	-0.01300	-0.0627	-0.2072	1.764
0.460	0.0	5°sin/SM-TFF	-0.2712	1.328	-0.1219	-0.01008	-0.0714	-0.1413	1.708
0.451	-2.0	5°cos/SM-TFF	-0.1506	1.399	-0.0911	-0.00538	-0.0528	-0.1020	1.725
0.451	-2.0	5°sin/SM-TFF	-0.1807	1.383	-0.1019	-0.00529	-0.0583	-0.0908	1.747
0.442	-4.0	5°cos/SM-TFF	-0.1260	1.316	-0.0907	-0.00656	-0.0526	-0.1248	1.725
0.442	-4.0	5°sin/SM-TFF	-0.1346	1.289	-0.0889	-0.00841	-0.0486	-0.1732	1.830
0.432	-6.0	3°cos/SM-TFF	-0.0960	1.296	-0.0651	-0.00668	-0.0327	-0.2041	1.989

Table 4.1c: Third Mode Parameter Identification Data

CHAPTER 5

Active Stabilization of a Three-Stage Low Speed Compressor

The previous chapter described the dynamics of the compressor flow field when the compressor is allowed to operate without feedback from the flow field, i.e. the open-loop dynamics. This chapter discusses the flow field dynamics exhibited in the compressor while the flow field is forcibly perturbed in a manner related to the measured flow field conditions, i.e. the closed-loop dynamics. If the perturbations being fed back into the compressor counteract the flow phenomena that cause the compressor flow field to become unstable, stable closed-loop operation can be maintained at operating points that would otherwise be unstable.

In Chapter 4 a first-order dynamic model with complex coefficients was shown to accurately describe the small-disturbance frequency response of the compressor over a wide range of operating points for disturbance frequencies below twice the rotor frequency. If stall inception is triggered by small amplitude flow disturbances, then the model describes the dynamics of the precursors to rotating stall, and a closed-loop control system can be designed using this information to stabilize these disturbances and prevent fully developed stall from occurring. Section 5.1 describes the flow field of the compressor just before and during the transition into rotating stall. Measurements show a connection between stall inception and spatially continuous small amplitude disturbances which precede the stall. The measurements also demonstrate the linear independence of the spatial modes in the presence of small amplitude disturbances.

The modal independence predicted in the small disturbance model for uniform inlet flow provides a convenient basis for designing a closed-loop control system. The

concept adopted is that spatial modes can be controlled independently if they behave independently. This is not true when the inlet flow field is asymmetric, as in the case of inlet distortion; however, only uniform inlet flow is being considered here. Mathematically the number of spatial modes around the compressor annulus can be infinite, but they do not become unstable simultaneously because each has a different degree of damping. Figure 4.6 presented the experimental findings that the spatial modes become unstable at lower flow coefficients with increasing mode number. This simplifies greatly the task of active control since all modes need not be stabilized to realize a benefit. Stabilization of only the first mode should decrease the stall point to the flow coefficient where the second mode goes unstable. Simultaneous stabilization of the first and second modes is expected to decrease the stall point to the flow coefficient where the third mode goes unstable. Figure 4.6 suggests that this is the case because the stalling flow coefficient during first mode stabilization $\phi_{stall,1}$ is close to the flow coefficient at which the second mode goes unstable, and the stalling flow coefficient during first and second mode stabilization $\phi_{stall,1,2}$ nearly matches the flow coefficient at which the third mode goes unstable. It should be noted that this model does not accurately describe compressor behavior in the presence of large magnitude disturbances because under such conditions the system's behavior is nonlinear.

A proportional control system is one of the simplest methods of obtaining mode stabilization. More sophisticated feedback methods which compensate for dynamic characteristics that are related to the feedback but aren't stabilized by simply using proportional control could be used, but only proportional control was used in this research. More sophisticated feedback methods would prove to be no better if the critical modes of the compressor are not dealt with by the controller. The information presented here on open- and closed-loop compressor dynamics should be useful in the design of more sophisticated controllers.

A phasor representation of each spatial mode around the compressor annulus is useful for describing complex-coefficient proportional control. The magnitude of the phasor corresponds to the magnitude at the mode peak, and the phase of the phasor is proportional to the spatial orientation of the mode around the compressor annulus by a factor of 1/n. Because the flow field and the SGV perturbations can each be described independently by phasors, it is convenient to implement proportional feedback by relating the flow field phasor to the SGV perturbation phasor by a complex coefficient. A real-valued proportional feedback would change the magnitude of the SGV phasor in relation to the flow field phasor without changing the spatial orientation. The aim of closed-loop control is to damp the flow field; stability is only going to be achieved when the feedback is spatially out of phase with the measured disturbance. A complex feedback coefficient rotates the SGV phasor in relation to the flow field phasor in addition to changing the magnitude. These two effects are separated mathematically by writing the complex feedback coefficient as $R_n e^{i\beta_n}$. In this section β_n is given in degrees, and the relationship between the magnitudes of modal velocity perturbations measured upstream of the IGV's and the magnitudes of the SGV perturbations R_n is expressed in units of degrees/(m/s).

Although the ideal control system would relate the modes of the SGV deflections directly to the flow field modes using a complex feedback coefficient, the a real control system must introduce feedback dynamics in the closed-loop path which influence the relationship between the two. Figure 3.6 illustrates the feedback dynamics that were considered in the models of the closed-loop system. The diagram shows that γ_n is not related to ϕ_n directly by the control law, but rather the sampled modes of the flow field $\tilde{y}_n$ are related to the commanded SGV modal deflections $\tilde{u}_{c,n}$ by the complex-coefficient proportional control law. This is written as

$$\tilde{u}_{c,n} = \left(R_n e^{i\beta_n}\right)\tilde{y}_n . \tag{6.1}$$

If the feedback dynamics are modeled accurately, they will describe the relation between the SGV and velocity state variables of each spatial mode of the compressor during closed-loop control in the form

$$\tilde{\gamma}_n = \left(R_n e^{i\beta_n}\right) A(s)\, ZOH(s)\, D(s) \tilde{\phi}_n. \tag{6.2}$$

The actuator dynamics, the discrete time control, and the lags in the data acquisition system all contribute to the dynamics in the feedback path. If the feedback dynamics limit the level of stability that can be obtained, the feedback dynamics need to be changed or a more sophisticated controller needs to be implemented. In this research, stability problems associated with the actuator dynamics were encountered, but some of these were corrected simply by giving the actuators a more strongly damped response.

In this chapter a vector notation is adopted to communicate the values of the parameters describing the complex coefficient proportional feedback for each mode. The vector is

$$\hat{Z} = [\, R_1 \quad \beta_1 \quad R_2 \quad \beta_2 \quad R_3 \quad \beta_3 \,]. \tag{6.3}$$

Detection of the modes n>4 was never attempted, so $R_n = 0$ and $\beta_n = 0$ for n>4.

5.1 Stall Inception in the Uncontrolled Compressor

A direct connection between stall inception and small prestall modal flow disturbances needs to be shown experimentally to justify the use of modal feedback control and demonstrate the accuracy of the linearized compressor model in describing the performance of this compressor. The dynamic description of the compressor is based on a linear approximation of its response; this requires perturbations to the system to be small in order for the approximation to be accurate. This section analyzes the velocity flow field around the compressor annulus at the point of transition into rotating stall. An examination of the hot-wire anemometer velocity measurements around the compressor annulus at stall inception, the Fourier decomposition of those measurements into spatial modes, and the power spectral density (PSD) of each mode's Fourier coefficients before stall will demonstrate that small modal disturbances grow directly into fully developed

stall cells and that the spatial modes are decoupled before stall. This section also looks at the effects of uniform IGV restaggering as an alternative to modal feedback control.

5.1.1 Axial Velocity Flow Field at Stall Inception

Small amplitude first mode disturbances were observed to grow into a fully developed stall cell. Figure 5.1 illustrates the inlet flow field velocity measurements made upstream of the IGV's at the midspan of the compressor duct during the transition into rotating stall. In these measurements the mean flow velocity around the annulus $\overline{\phi}$ was nearly constant over the time shown; because of this the perturbation magnitudes could be computed by subtracting a weighted average velocity from each trace. The rotor rotates in the positive Θ direction, and the disturbances in the flow field are observed to rotate in the same direction. A distinctive but small-amplitude rotating prestall disturbance $\delta\phi/\overline{\phi}$ = .065 performs five rotations around the annulus in the time of 16 rotor revolutions before growing into a fully developed stall cell. The two dashed lines trace the location of one part of the velocity perturbation wave as it travels around the annulus. The phase measurements show that the wave's motion is not discontinuous through space, and its shape and speed simply change during the transition into a fully developed stall cell. This is a good indicator that the small amplitude prestall waves are a precursor of stall cell formation in this compressor.

Analyzing the velocity field by its modal components helps distinguish the dominant spatial harmonics that govern the transition into rotating stall and illustrates the continuity between small magnitude flow disturbances and large ones. Section 3.1.5 described how the array of eight anemometer probes, evenly spaced around the compressor annulus, could be used to resolve the first three spatial Fourier coefficients (SFC's), $\tilde{\phi}_1$, $\tilde{\phi}_2$, $\tilde{\phi}_3$, by performing a DFT of the velocity data. In Figure 5.2 the magnitude of the SFC's ($|\tilde{\phi}_1|$, $|\tilde{\phi}_2|$,...) and the phase of these complex numbers ($\angle\tilde{\phi}_1$, $\angle\tilde{\phi}_2$,...) are plotted. It should be noted that the plotted phase is normalized by the mode

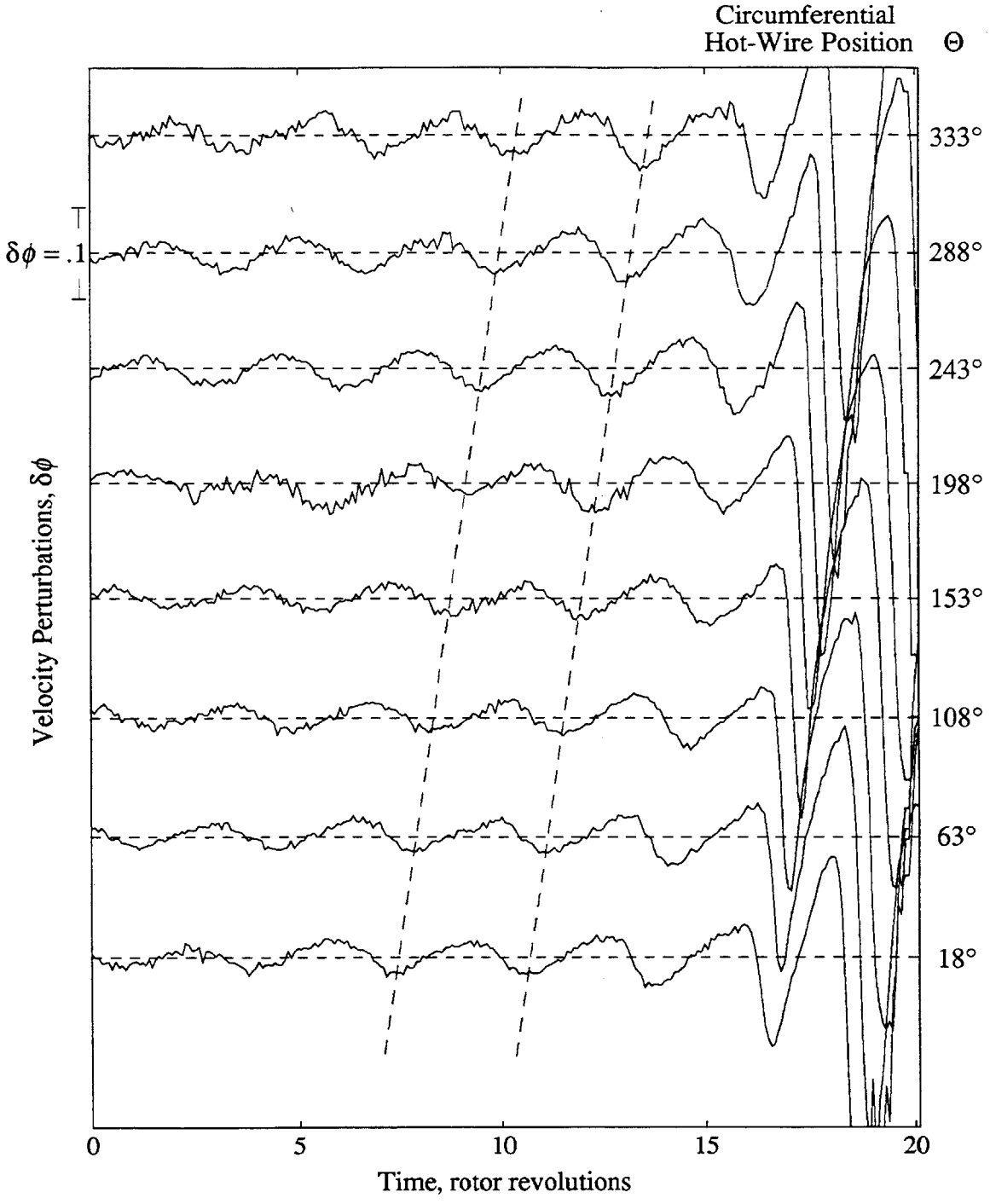

Figure 5.1: Stall Inception Flow Field around Compressor Annulus at Midspan Measured Upstream of the IGV's when $\overline{\phi} = .46$

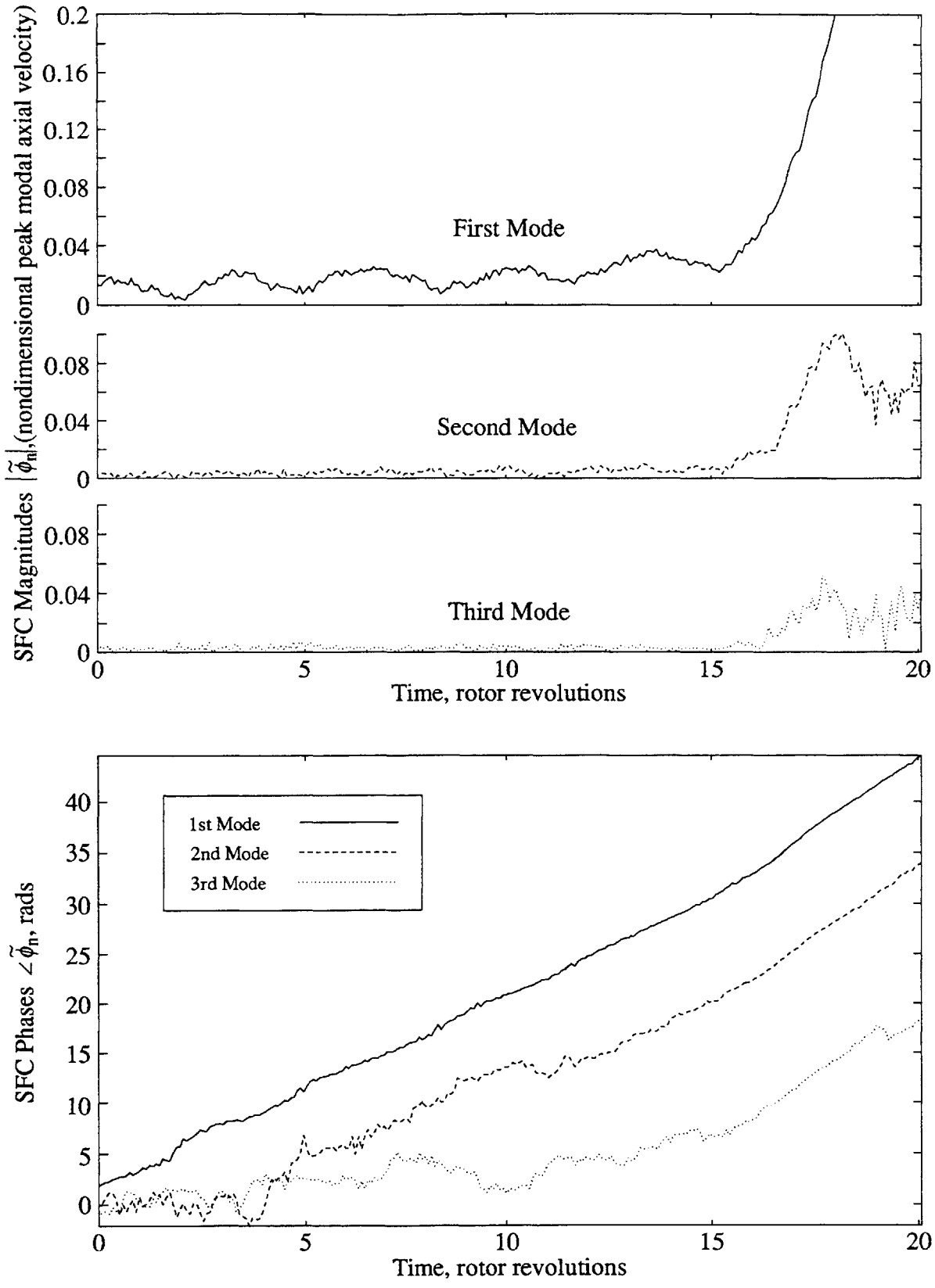

Figure 5.2: Magnitude and Phases of the First Three Spatial Fourier Coefficients Calculated from the Stall Inception Flow Field at Midspan (Data in Figure 5.1)

number (i.e. multiplied by 1/n) so that different modal disturbances that travel at the same speed through space will be represented by parallel traces.

The magnitude plots in the figure indicate that the first mode $|\tilde{\phi}_1|$ is the dominant component of the prestall disturbance. A careful examination of Figure 5.1 reveals the same thing because it shows that the disturbance only traverses the annulus once. The first mode grows in magnitude gradually at first and then quite rapidly during the transition into fully developed stall. The fact that this change takes place in a continuous manner supports the argument that it is the large magnitude of the modal disturbance that initiates the process of stall cell formation. $|\tilde{\phi}_2|$ makes significant contributions to the disturbance shape only at the point at which the first mode begins its rapid growth. One period earlier the second mode magnitude seems to make only a weak contribution to the prestall disturbance. One peculiarity of the magnitude traces is that a nearly fixed frequency oscillation is superimposed on the growth of $|\tilde{\phi}_1|$. Comparison with Figure 5.1 shows that the oscillation is nearly in phase with the velocity trace at 108°. This seems to indicate that $|\tilde{\phi}_1|$ goes through periodic changes corresponding to the mode's position in the annulus and that the peak amplitude occurs at 108°. When the second mode obtains a noticeable magnitude, it demonstrates this behavior too. Another cause of this might be an improper calibration of the disturbances measured by the hot-wires.

The phase traces in Figure 5.2 indicate the position of each mode over time. A trace that is accurately approximated by a straight line is indicative of a modal disturbance that travels at a fixed speed, which is proportional to its slope on the plot. Throughout the time period plotted, $|\tilde{\phi}_1|$ maintains a nonzero value; this may be related to the fact that the first mode moves in a nearly continuous manner through space as shown in the plot of $\angle\tilde{\phi}_1$. Before stall, the slope of the first mode phase corresponds to a speed that is 30% of the rotor speed. This matches the rotational speed identified for first mode dynamics near the stall point as shown in Table 4.1a. The fully developed stall cell forms after the sixteenth rotor revolution on the plot, and at this time the slope

of the first mode phase trace increases to represent a speed that is 46% of the rotor speed. This is the speed of the fully developed stall cell, and the second and third spatial modes travel at the same speed at this point. While $|\tilde{\phi}_2|$ and $|\tilde{\phi}_3|$ fluctuate about a zero value, these modes appear around the annulus in a random fashion, but as $|\tilde{\phi}_2|$ begins to demonstrate consistently a nonzero value, the second mode phase tends to rotate in the positive direction.

The flow measurements discussed above give strong indications that first mode disturbances are crucial to the stall inception process of this compressor; however, to be more certain, the flow field was examined near the hub and tip as well. In Figures B.15 to B.20 (Appendix B) flow field measurements taken in different experiments at 20%, 50%, and 80% of the span of the duct are presented in the same format as in this section. The data show that the flow behaves in a very similar fashion although at stall inception $|\tilde{\phi}_1|$ is smaller at 20% and 80% span than at 50%. This is probably due to the influence of the boundary layer at these points. The duration of the prestall waves was different in each case, but this is thought to be related to the manner in which the throttle was closed.

5.1.2 Power Spectral Density (PSD) of the Prestall Flow Field

An analysis of the change over time in the Fourier coefficient of each spatial mode of the flow field at a constant $\bar{\phi}$ can be used to show which modes resonate the loudest before the compressor stalls and demonstrate the decoupled behavior of the spatial modes. To carry out this analysis measurements of the velocity field around the compressor annulus are used to compute the SFC's $\tilde{\phi}_n$ in the manner described in Section 3.1.2.6; using a time resolved sequence of these measurements, the power spectral density (PSD) of each SFC can be computed for the corresponding mode. Because the SFC's are complex numbers, each PSD will contain both a positive and a negative frequency component. When at some frequency one component is dominant in magnitude, the PSD can be interpreted physically to represent a disturbance of the designated spatial mode rotating at the corresponding frequency. When both the positive

and negative frequency components have the same magnitude, the PSD describes a standing wave oscillating at the corresponding frequency. To simplify the comparison between positive and negative frequency values, the sign of the negative frequencies was changed so that they could be superimposed on the positive values. The magnitude of the PSD is indicative of the average wave strength of the mode, and it is proportional to the square of the velocity.

5.1.2.1 Upstream PSD Measurements

The PSD's of the first three spatial modes around the compressor annulus were used to examine modal disturbances before stall. Velocity measurements were taken upstream of the IGV's at the duct's midspan while the compressor was held at a fixed operating point which was stable but close to the stall point. Figure 5.3 illustrates the PSD's of the measured modes and shows that the first mode resonates when the compressor operates near the stall point. The frequency corresponding to the first mode peak is the same as the frequency that was calculated from the first mode phase in Figure 5.2 for small disturbances before stall, i.e. 30% of the rotor speed. The PSD's give verification that periodic disturbances are significantly stronger in the first mode at this operating point than in the other modes. PSD measurements at operating points closer to the stall point show that the magnitude of the first mode disturbances increases with decreasing ϕ. Because of this, it is inferred that first mode disturbances are of primary importance to the mechanism of stall cell formation in the flow field.

The fact that the PSD's of the second and third modes contain no disturbances of significant magnitude demonstrates the decoupled behavior of the modes before stall. Because all three PSD's were computed from the same set of velocity measurements, the spatial modes are demonstrated to act as independent dynamic components of the compressor under these conditions. The second and third modes do contain small increases in magnitude corresponding to the frequency of the first mode disturbance, but they are significantly attenuated in comparison with the magnitude of the first mode

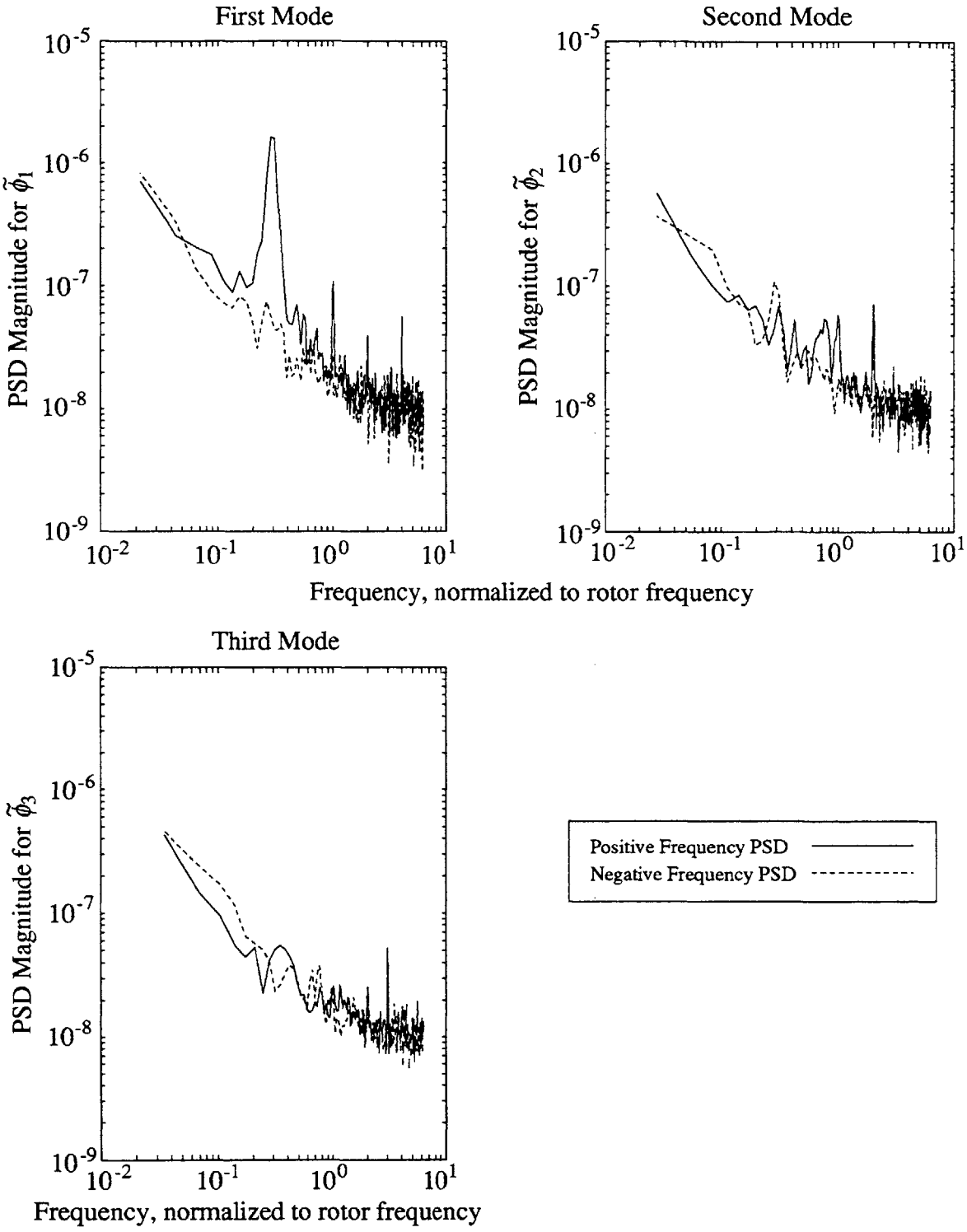

Figure 5.3: PSD of the First, Second, and Third Mode Measured Upstream of the IGV's during Operation near ϕ_{stall} in the Absence of Active Control

disturbance. As the magnitude of the first mode grows, nonlinear coupling between the modes is expected to increase. However, as long as first mode disturbances are small or are forced to remain small, the modes can be treated in a decoupled manner. This further supports independent treatment of the modes in the control system design.

5.1.2.2 Variations in Mode Strength within the Compressor

The ability of a PSD to distinguish and quantify a modal disturbance makes it a useful tool for making quantitative comparisons of mode strength between different axial and radial locations in the compressor flow field. The 2-D compressor model treats the compressor as if there are no radial flow variations in the system and as if each blade row sees the same flow field. An experimental investigation of the magnitude of modal disturbances at various radial and axial positions demonstrates the limitations of this approximation in even a high hub-to-tip ratio machine, but it also gives insight into the selection of the sensing location for closed-loop modal control and the description of this location η_{HW} in the compressor models.

Disturbance magnitudes are compared on the basis of the area under the dominant peak in the PSD. This was done to account for variations in the bandwidth of the measured signal and the errors which could stem from the discrete description of the frequency spectrum. The area was calculated using a trapezoidal rule on the distance between the positive and negative frequency traces over range of frequencies centered about 30% of the rotor speed. Two data sets were obtained for each measurement to check for steadiness in ϕ and check the repeatability of the measurements.

Figure 5.4 illustrates the axial and radial variations in mode strength upstream and through the compressor. Measurements were made simultaneously at one radial position for each set of data points. The data indicate that upstream the first mode is the strongest at midspan. During closed-loop control flow measurements were made at the same locations, and, according to the data, the midspan position gives the best resolution of the second and third modes as well. Figure 5.5 illustrates the radially averaged

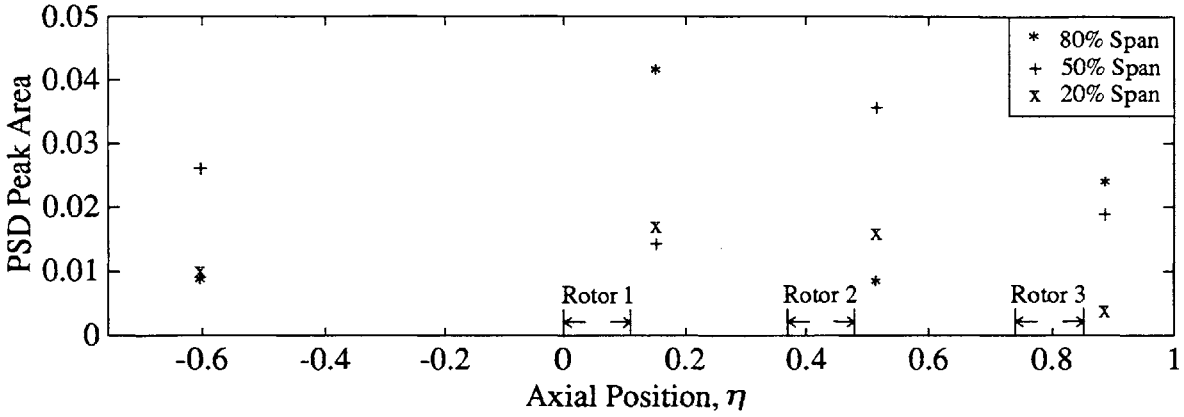

Figure 5.4: Axial Variation in 1st Mode Strength Measured at 3 Radial Positions

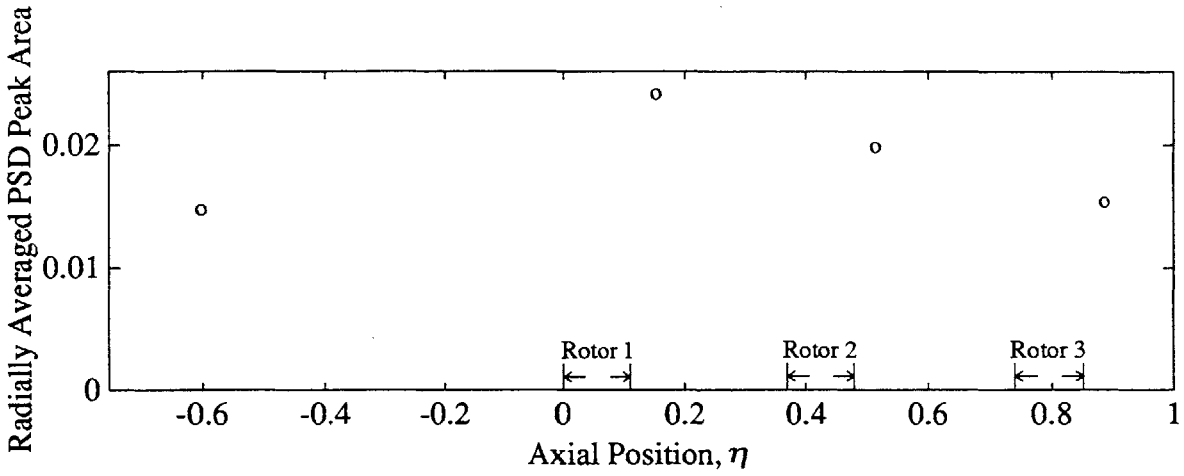

Figure 5.5: Radially Averaged 1st Mode Strength Upstream and Inside the Compressor

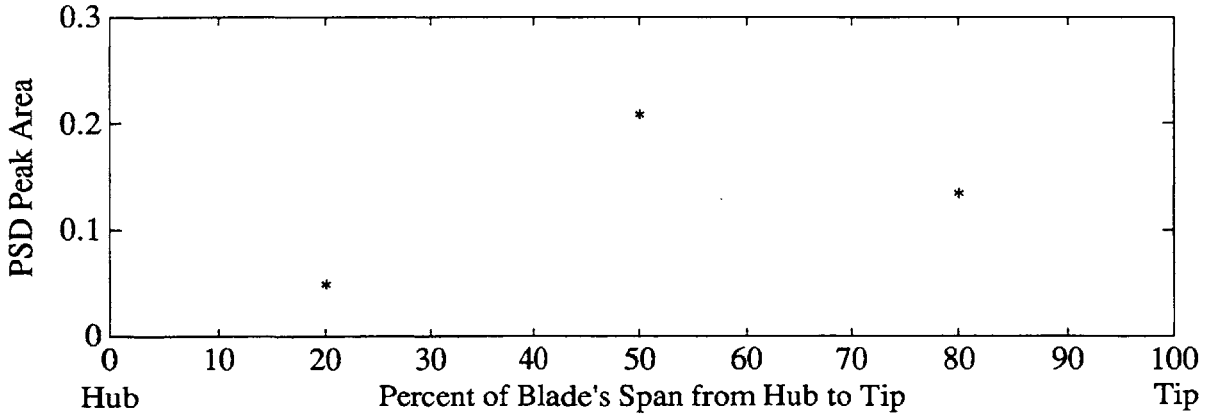

Figure 5.6: Radial Variation in 1st Mode Strength,
Measured Downstream of the Second Rotor ($\eta = .51$)

strength of the first mode at different axial positions. Assuming that the modes decay upstream as in a potential flow, η_{HW} can be estimated from this data. To decay from the value measured behind rotor 1 to the value measured upstream, an axial distance of η_{HW} = -.25 is required. As was discussed in Section 3.1.4, this value is consistent with considering modal decay only upstream and in the blade row gaps associated with the IGV's and SGV's which due to their solidity can prevent decay of at least the first mode. Measurements of second mode strength were also used to estimate η_{HW}. The estimated axial distance for second mode decay was η_{HW} = -.64 which nearly matches the physical distance between the first rotor and the upstream measurement station. This seems to indicate that IGV's and SGV's did not inhibit the decay of this mode, and this would be increasingly accurate for the third and higher modes. For this reason the physical distance between the first rotor and the hot-wires η_{HW} = -.60 was used in the modeling.

An experimental investigation focusing on obtaining a more accurate evaluation of the radial variation in first mode strength was also conducted. The PSD peak area was computed in the same way as before, but measurements were made behind the second rotor simultaneously at two different radial positions. The difference in mode strength between midspan and 20% of the duct's span was measured, and after moving the sensors, the difference between midspan and 80% of the duct's span was also measured. Figure 5.6 displays the averaged results which show that the first mode is stronger at midspan in either case. The results at 20% and 80% span appear to contradict the results shown in Figure 5.4 for mode strength behind the second rotor. One possible explanation is that small changes in ϕ caused detectable changes in mode strength and increased the scattering in the data.

5.1.3 IGV Restaggering

Before presenting the results of closed-loop control using feedback of the spatial modes, an alternative method of changing the stalling flow coefficient is examined. The

axial compressor equipped with SGV's can change the pressure rise characteristic simply by changing the nominal SGV stagger angle γ. Changing the inlet flow swirl encountered by the first rotor effectively changes the system so that it behaves as if it were a different compressor. This is illustrated in Figure 5.7 for the three-stage axial compressor operating over a wide range of SGV stagger angles. When γ is large the SGV's are certainly stalled, and ϕ_{stall} is no longer sensitive to γ. In the other extreme when γ is negative and the inlet flow swirl greatly reduced, the blades on the first rotor are stalled, and again ϕ_{stall} is no longer sensitive to γ. Between these two extremes ϕ_{stall} appears to decrease steadily with increasing γ. However, it should be noted that the stall point follows a nearly constant throttle line. The data for each characteristic were taken using a consistent group of throttle settings, and the alignment of the data points between different characteristics is indicative of different throttle lines. Because the stall points follow a nearly constant throttle line, the benefits of restaggering are limited. A control system could be implemented that restaggers the blades when the compressor operates near the stall line so that ϕ_{stall} is decreased, but this would prove to be useless unless the throttle setting were opened as well. It will be shown in the next few sections that SGV restaggering is inferior to active control of the spatial modes because active control not only reduces the stalling flow coefficient but also reduces the effective throttle setting at which the compressor stalls.

5.2 Experimental Optimization of the Closed-Loop Controller

Successful stabilization of stall in the compressor is dependent not only on identifying the dynamics which are underdamped but also on the proper selection of parameters for the closed-loop control scheme. These parameters can be predicted using the model, or they can be determined experimentally. This section describes a systematic experimental procedure for controller optimization. Following the identification of open-loop compressor dynamics near the stall point, an estimate of the optimal controller parameters can be made. This estimate can help narrow the range of

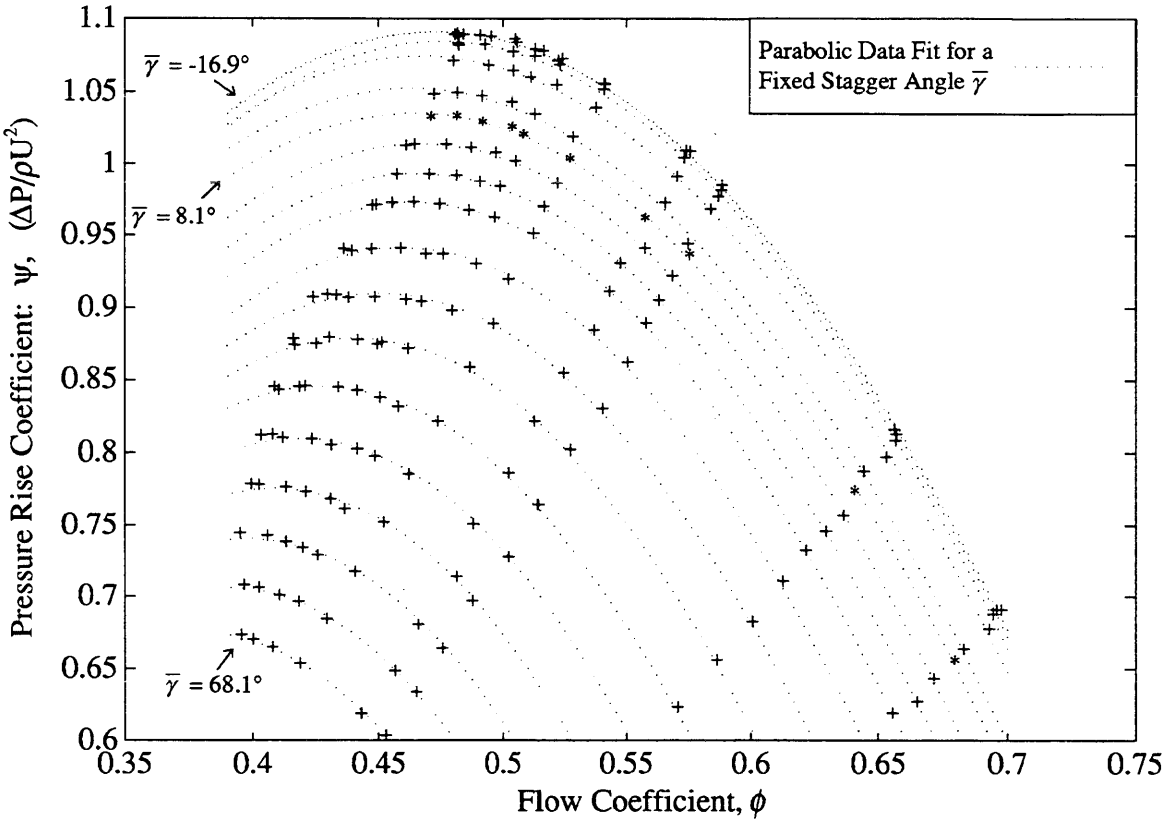

Figure 5.7: Unstalled Steady-State Compressor Performance
for SGV Stagger Angles Ranging from -16.9° to 68.1° in 5° Intervals

control parameters that need to be examined experimentally. The optimal controller parameters can be determined exactly by performing the tests described in Sections 5.2.2 and 5.2.3. Both tests should be repeated whenever β_n or R_n are changed significantly so that nonlinearities in the system will be detected and compensated for.

5.2.1 Controller Parameter Estimates

The parameters R_n and β_n used in the controller can be estimated from the experimental data describing the open-loop dynamics near the stall point $\hat{\Theta}_n(\phi)$. The estimate shown here is made without consideration of the feedback dynamics. Using the same method as Paduano [16], a minimum gain value $R_{n\,min}$ can be calculated which would theoretically double the decay rate of the mode

$$R_{n\,min} = \frac{\sigma_n}{\sqrt{b_{r,n}^2 + b_{i,n}^2}}. \tag{6.4}$$

This gain should have a noticeable effect on the system, but the optimal value will be somewhat greater than this. The optimal phase shift $\beta_{n\,opt}$ is the one that gives the most stable closed-loop pole. The location of the closed-loop pole of the compressor is calculated using

$$s_{CL\,pole} = \frac{A + R_n e^{i\beta_n} B}{1 - R_n e^{i\beta_n} G}. \tag{6.5}$$

The coefficients A, B, and G in this expression are the same as those described in Equation 3.22, and they are determined from the elements of $\hat{\Theta}_n(\phi)$. Keeping R_n constant and varying β_n generates a constant magnitude root locus from which $\beta_{n\,opt}$ can be determined. Figures 5.8, 5.9, and 5.10 show graphically the estimate of optimal phase $\beta_{n\,opt}$ for the first three modes. The estimate of $\beta_{1\,opt}$ is accurate, but the estimates for the other modes fall increasingly below the measured value as mode number is increased. The reason for this is that feedback dynamics (i.e. time lags, etc.) are increasingly significant in the determination of $\beta_{n\,opt}$ as mode number is increased.

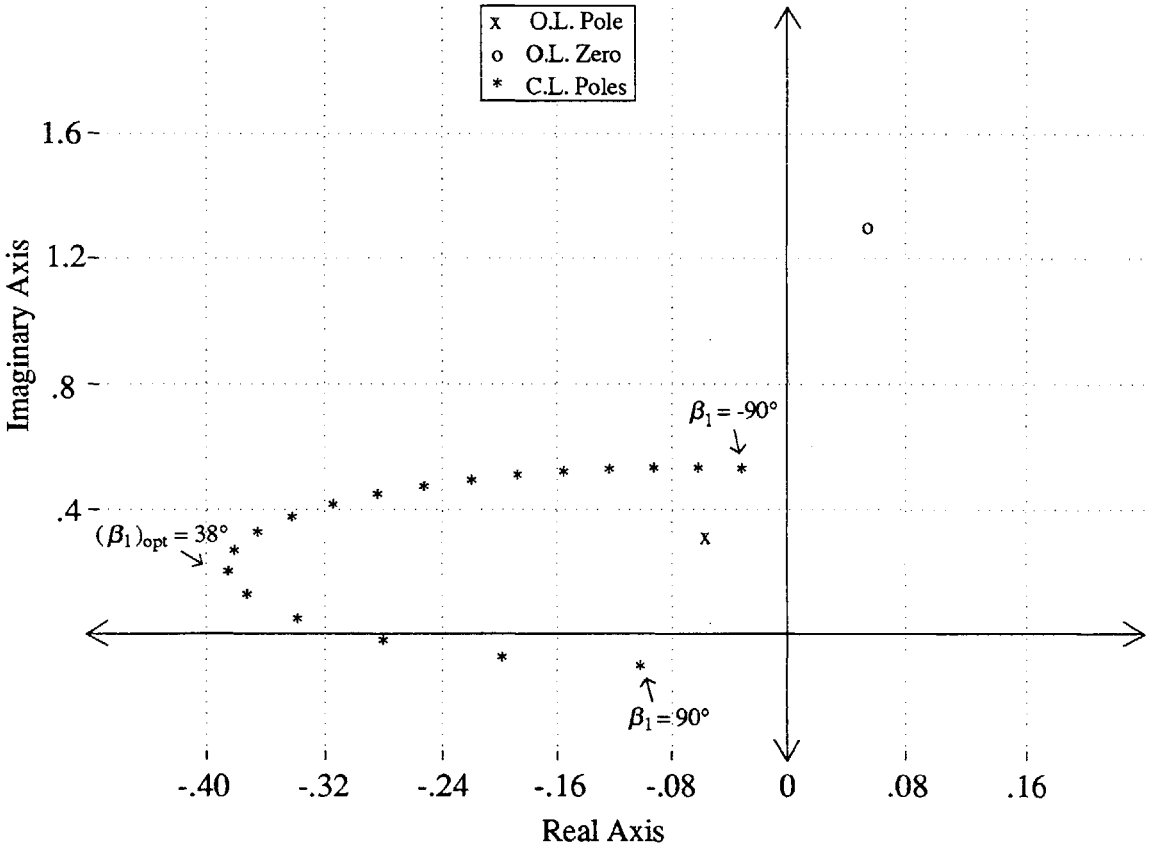

Figure 5.8: Constant R_1 Root Locus Representing 1st Mode Compressor Dynamics at 2% above ϕ_{stall} for Variable Closed-Loop Phase β_1 ($R_1 = 5.0$)

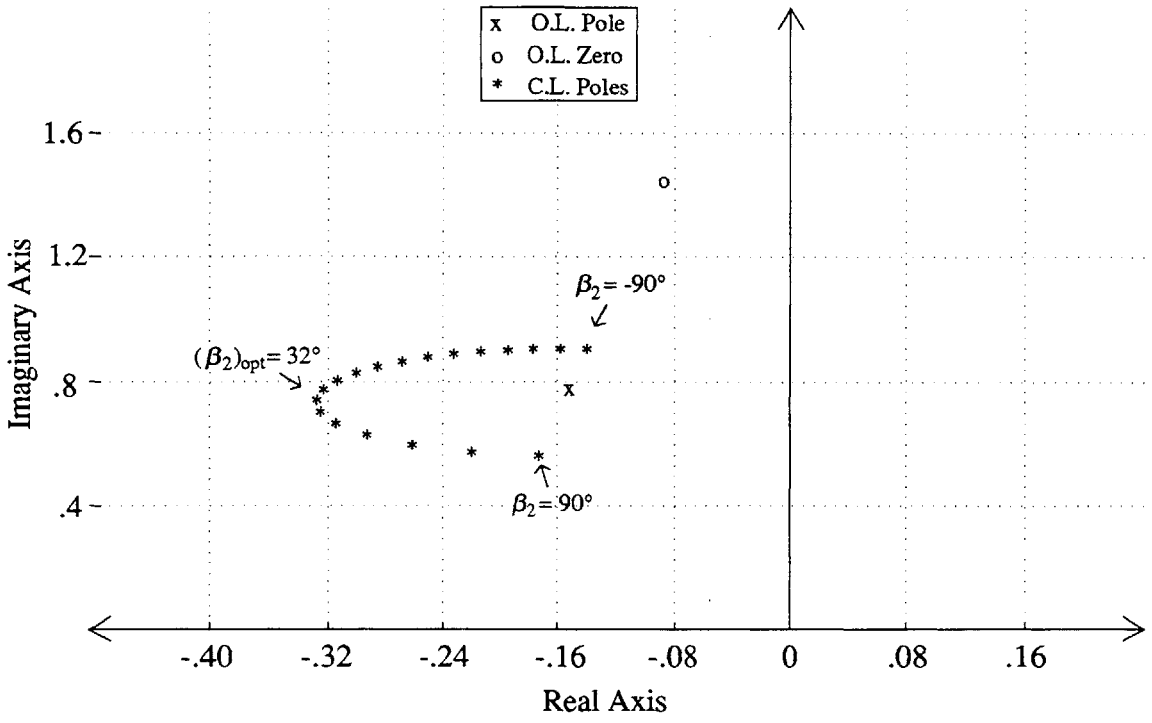

Figure 5.9: Constant R_2 Root Locus Representing 2nd Mode Compressor Dynamics at 2% above ϕ_{stall} for Variable Closed-Loop Phase β_2 (R_2 = 3.1)

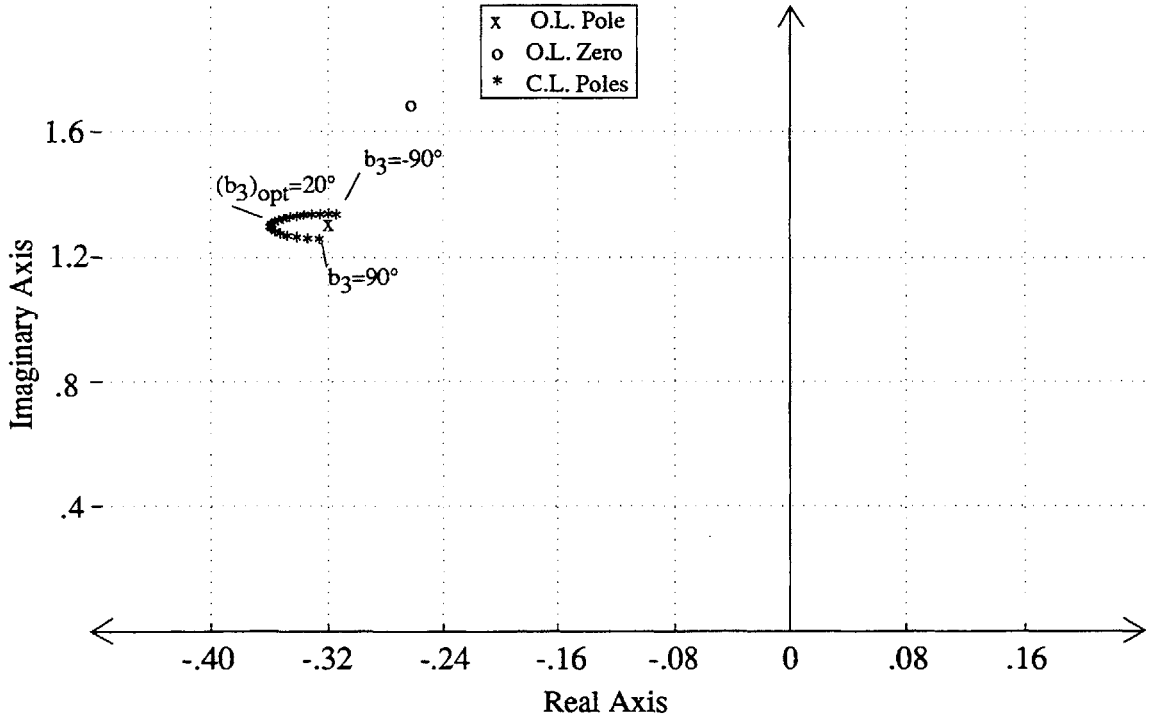

Figure 5.10: Constant R_3 Root Locus Representing 3rd Mode Compressor Dynamics at 2% above ϕ_{stall} for Variable Closed-Loop Phase β_3 (R_3= 1.1)

5.2.2 Experimental Optimization of Gain

The optimal value of the feedback gain $R_{n\,opt}$ is that value which enables the corresponding mode to be stabilized down to the lowest flow coefficient ϕ and has the least destabilizing influence on the other modes. The compressor is not very sensitive to changes in R_n that are less than the estimated minimum. On the other extreme, the controller will quickly become saturated at large gains (e.g. $25\,R_{n\,min}$), and its nonlinear behavior can cause compressor destabilization. Having estimated a set of control parameters $\hat{Z}$, the gain for mode n can be optimized with respect to the other values in $\hat{Z}$ by running the compressor with control at a steady-state operating point near the controlled compressor's stall point and obtaining flow field measurements for several values of R_n. PSD's of this data will indicate the manner in which mode strengths change with respect to R_n at operating points near the current minimum ϕ. Figures 5.11, 5.12, and 5.13 show the change in mode strengths with changes in R_1, R_2 and R_3 respectively. Increasing R_1 had a clear stabilizing effect on the first mode, but as the gain was increased above 5, nonlinearities in the system caused a decrease in the stability of the second mode. Increasing R_2 decreased the stability of the second mode, but in hindsight this is known to be caused by a poor choice of β_2 in this case. Figure 5.13 not only shows $R_{3\,opt}$ for this $\hat{Z}$ but also indicates that the second mode resonates the strongest of the three modes; therefore, attempts should be made to further improve $\hat{Z}$.

5.2.3 Experimental Optimization of Phase

The phase β_n used by the controller for mode n was optimized experimentally by determining which β_n could decrease the neutral stability flow coefficient ϕ_{neut} the most. In the controlled compressor, ϕ_{neut} is sensitive to β_n; by testing a range of values for β_n while holding the other control parameters constant, $\beta_{n\,opt}$ for the specified $\hat{Z}$ could be determined experimentally. If the phases of the other modes or the gains in $\hat{Z}$ to be optimized were changed significantly, $\beta_{n\,opt}$ was reevaluated to check against coupled behavior although it was not expected. Figures 5.14, 5.15, and 5.16 show the

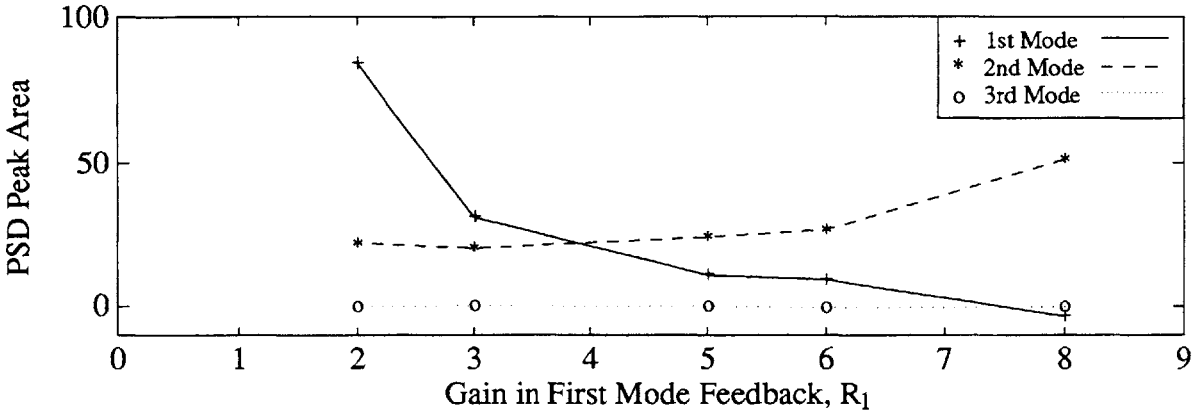

Figure 5.11: Variation in Mode Strength near Stall with First Mode Gain during 1st and 2nd Mode Active Control

$\hat{Z}$ = [x, -2, 1.1, -4, 0, 0]

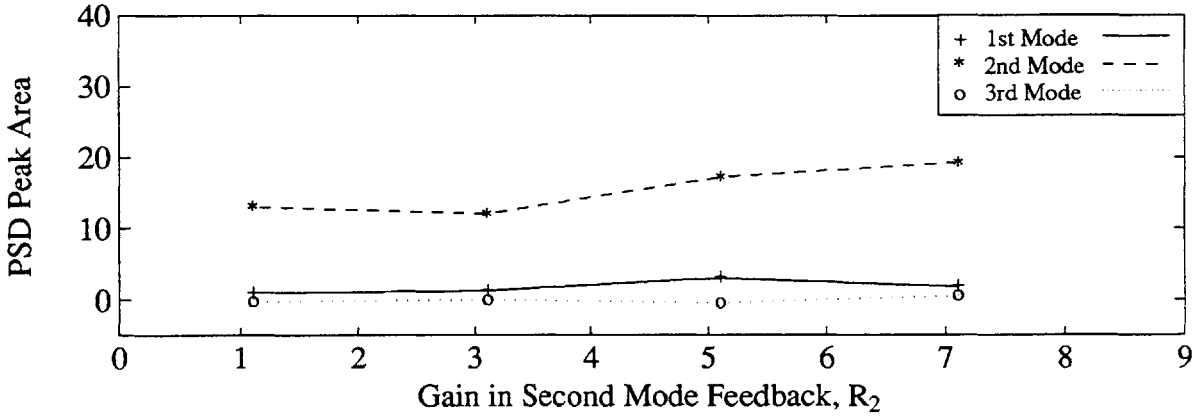

Figure 5.12: Variation in Mode Strength near Stall with Second Mode Gain during 1st and 2nd Mode Active Control

$\hat{Z}$ = [5, -2, x, -4, 0, 0]

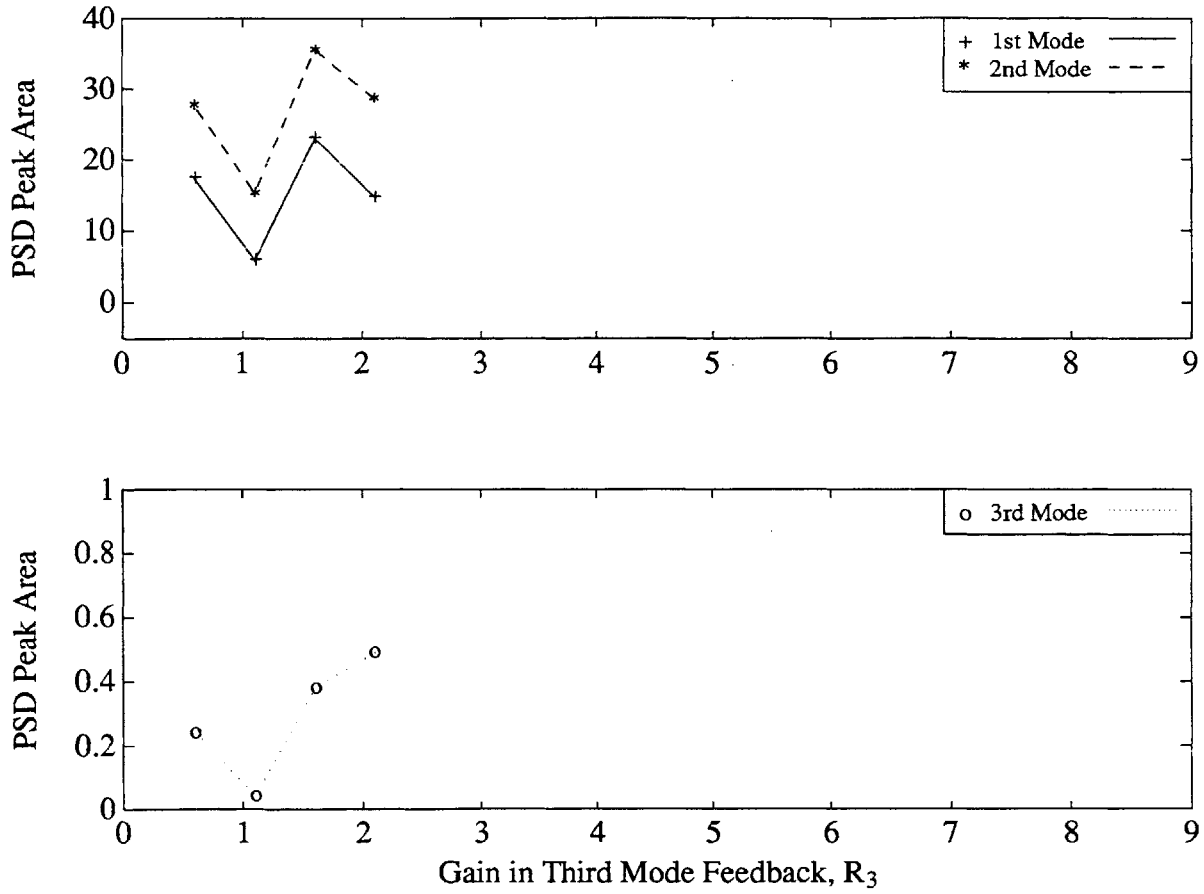

Figure 5.13: Variation in Mode Strength near Stall with Third Mode Gain during 1st, 2nd, and 3rd Mode Active Control

$\hat{Z}$ = [5, 36, 3.1, 91, x, 110]

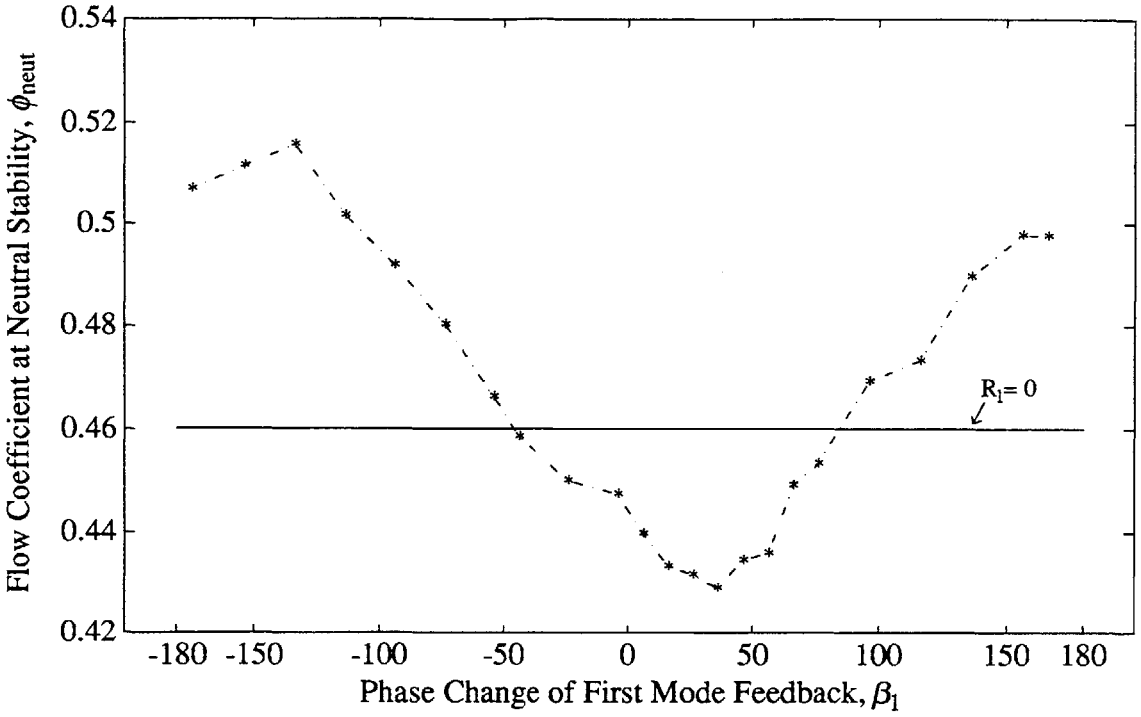

Figure 5.14: Experimental Determination of Optimal First Mode Phase $\beta_{1\,opt}$

$\hat{Z}_{opt}$ = [5, x, 4.1, 91, 2.1, 110]

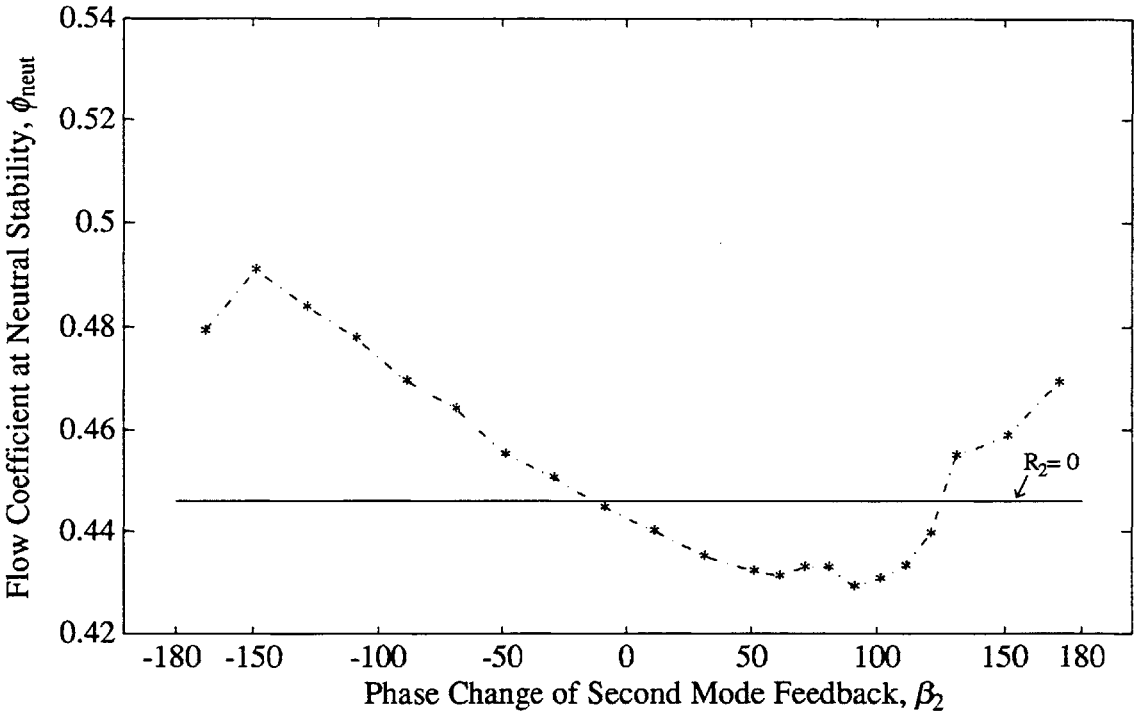

Figure 5.15: Experimental Determination of Optimal Second Mode Phase $\beta_{2\,opt}$

$\hat{Z}_{opt}$ = [5, 36, 4.1, x, 2.1, 110]

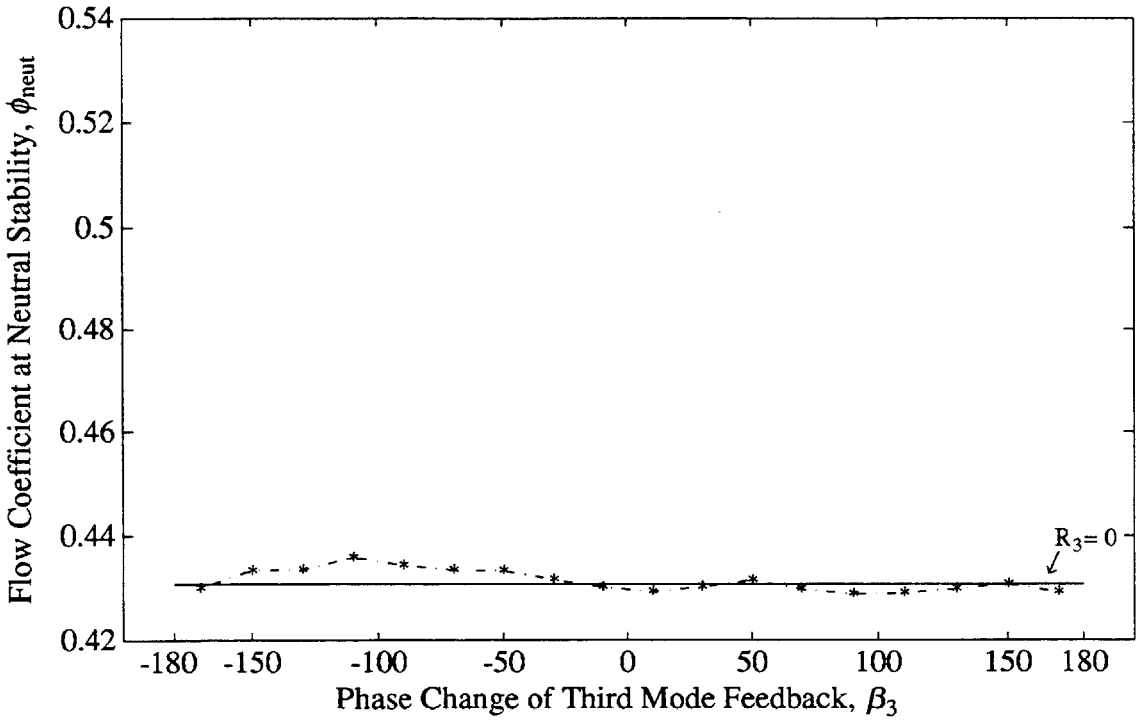

Figure 5.16: Experimental Determination of Optimal Third Mode Phase, $\beta_{3\ opt}$

$\hat{Z}_{opt}$ = [5, 36, 4.1, 91, 2.1, x]

change in ϕ_{neut} over the full range of β_n for $\hat{Z}_{opt}$. The full range of β_n does not need to be examined to determine $\beta_{n\,opt}$ if optimal phase can either be predicted accurately or is known approximately from previous experiments. It should be noted that in these three figures the optimal phase shown in one diagram was then used in the other two. This provides a check against nonlinear effects once $\beta_{n\,opt}$ is determined for mode n. The process of determining $\beta_{n\,opt}$ for a specific $\hat{Z}$ is repeated iteratively with the gain optimization process until $\hat{Z}_{opt}$ is known. Because the modes were largely decoupled this iteration only needed to be performed once.

5.2.4 Limitations on Stabilization

From what is known about the dynamics of the compressor modes, a nonzero lower limit on ϕ_{neut} is expected. However, there are several additional factors associated with the controlled compressor that raise the expected lower limit for ϕ_{neut}. The actuators can trigger stall inception if they are underdamped or respond too slowly, and time lags anywhere in the feedback loop will degrade the controller's ability to stabilize high frequency modes. The frequency of the discrete time control loop should be several times the frequency of the modes being stabilized so that the modal perturbations are not allowed to become nonlinear when the modal growth rates are large as is the case with low values of ϕ. In regard to the control parameters, the optimal choice of $\hat{Z}$ may for some reason still leave a mode underdamped due to a low feedback gain. In the other extreme, $\hat{Z}_{opt}$ may have been determined by the saturation limit of the actuators being approached due to a large value of R_n (i.e. the control power limit is reached). Signal noise and spatial aliasing can also raise the lower limit on ϕ_{neut} because they degrade the control system's ability to resolve the position and magnitude of the mode and hence its ability to give proper feedback. In addition to these, the actuators have a limited ability to control a spatially continuous system because they are discrete components (see Section 3.1.5). The actual limit on ϕ_{neut} is determined by

tradeoffs between several of these factors. With this understanding, the iterative process described above can be seen as an experimental method for making design tradeoffs until an optimal performance is achieved with the system at hand.

5.3 Optimal Closed-Loop Compressor Performance

Rotating stall inception has been successfully delayed to lower flow coefficients using closed-loop control of modal disturbances. Measurements of open-loop modal dynamics indicated that the growth rate of a mode n becomes positive at a higher flow coefficient in comparison with modes of higher mode number. This was confirmed by compressor models 2,3, and 4 and by flow measurements showing that the first mode dominated the stall inception of the uncontrolled compressor. To confront this problem, optimal control parameters for only first mode feedback were determined using the procedure described in the previous section. Optimal closed-loop control of only the first mode was applied to the compressor to dampen first mode disturbances while it operated near ϕ_{stall}. Figure 5.17 shows that stall inception was delayed to $\phi_{stall,1} = .446$ under the influence of only first mode feedback. This corresponds to a characteristic slope of $\frac{\partial \psi}{\partial \phi} = .45$ and a 3.1% decrease in ϕ_{stall}. The decrease in the stalling flow coefficient proves that first mode disturbances played a crucial role in the stall inception mechanism in the uncontrolled compressor because their stabilization prevented stall inception from occurring at ϕ_{stall}. The success of first mode control also demonstrates the validity of the linear model and the decoupled behavior of the modes.

Maintaining the stability of the first spatial mode of the flow into the compressor prevented stall inception until the second spatial mode went unstable at $\phi_{stall,1}$. Stabilizing the second spatial mode further decreased the stalling flow coefficient. Figure 5.18 illustrates the stall inception flow field at $\phi_{stall,1}$; the second mode perturbations in the flow were evident for several rotor revolutions before the transition into fully developed stall. The SFC's of this flow field are shown in Figure 5.19, and

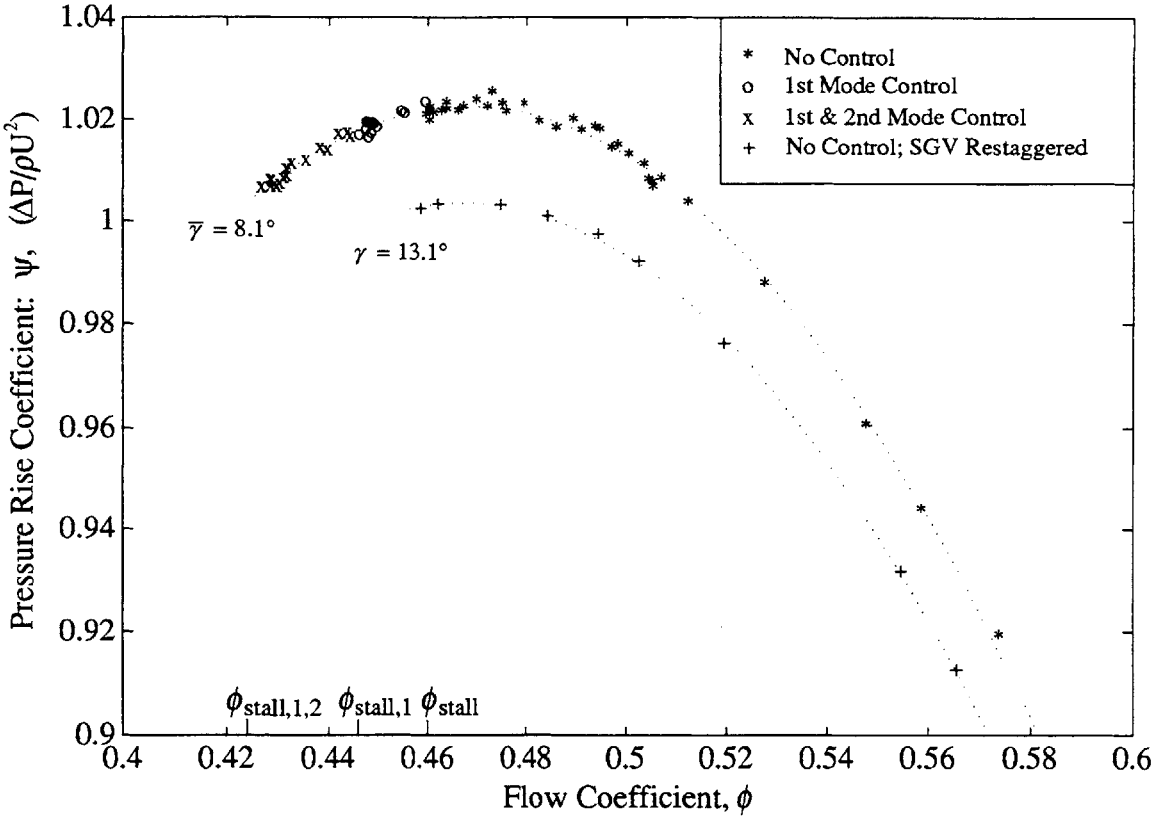

Figure 5.17: Compressor Speedline with Extended Flow Range due to Active Control Compared with Zeroth Mode Restagger of SGVs by 5°

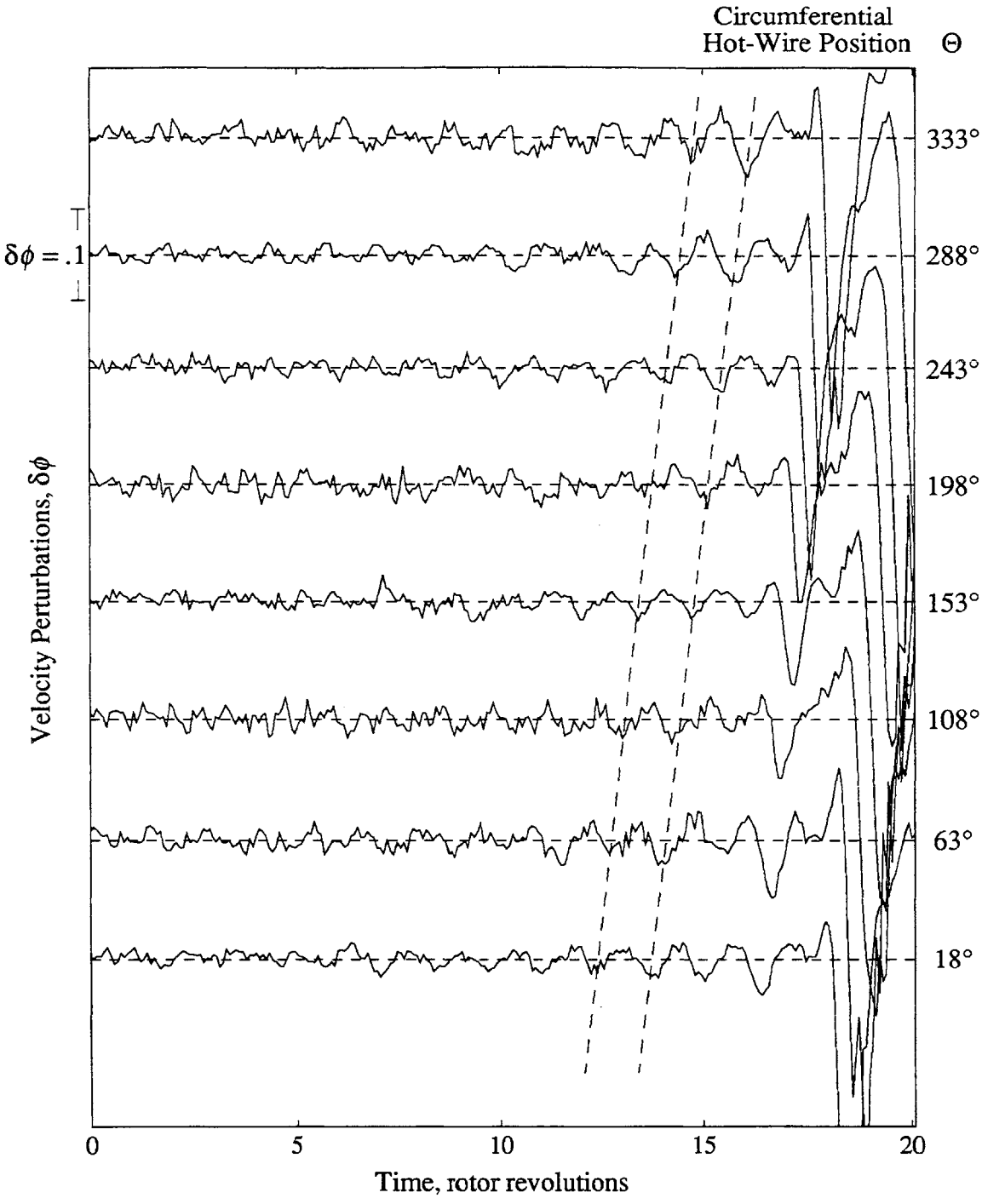

Figure 5.18: Stall Inception Flow Field around Compressor Annulus at Midspan during 1st Mode Control Measured Upstream of the IGV's when $\overline{\phi} = .45$

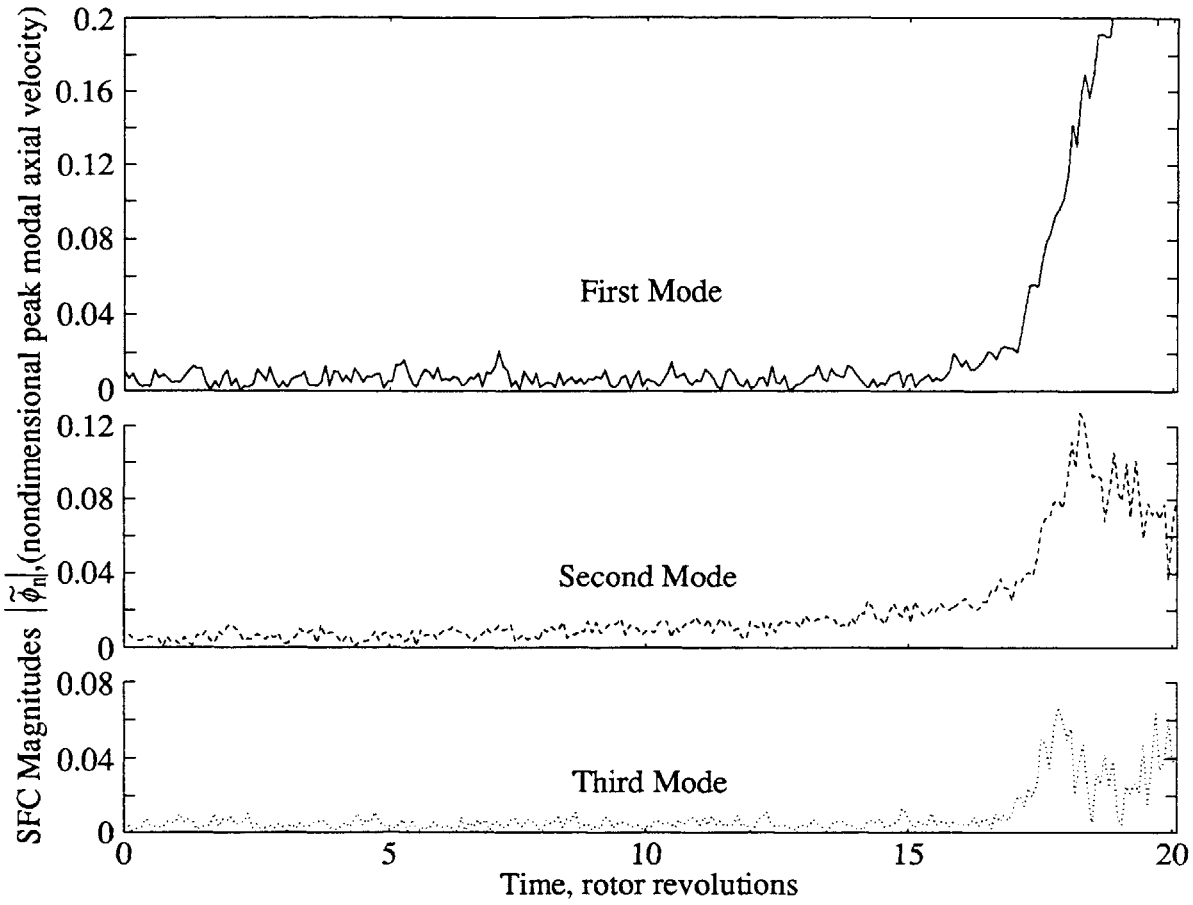

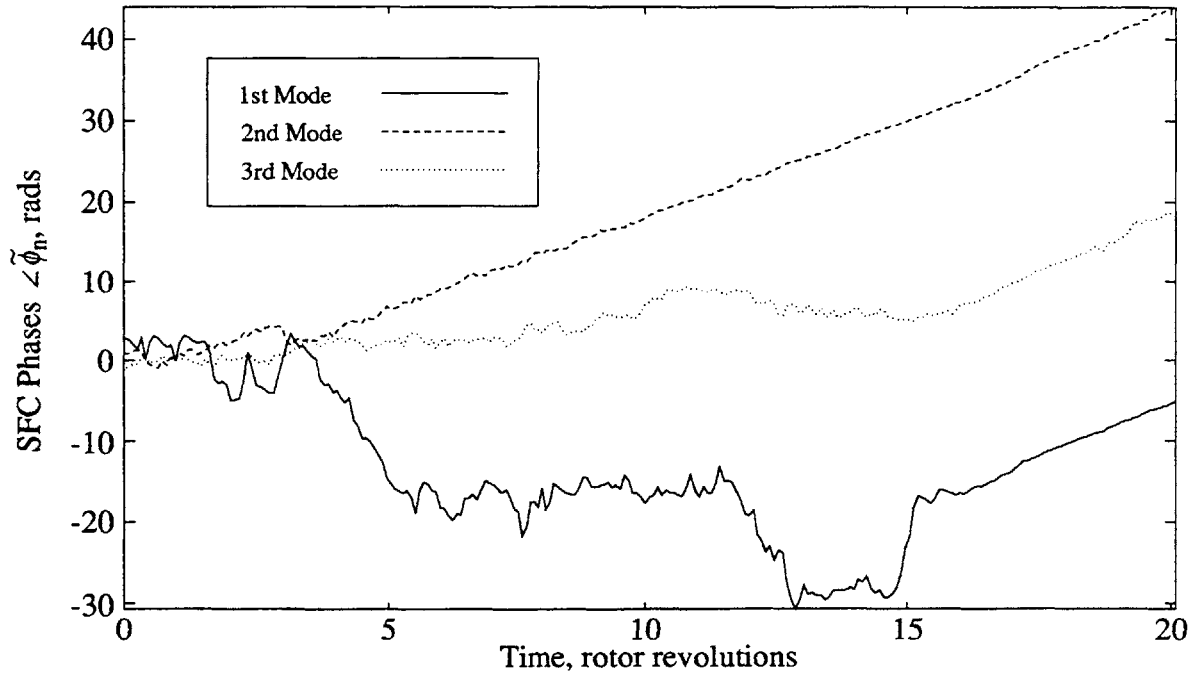

Figure 5.19: Magnitude and Phases of the First Three Spatial Fourier Coefficients Calculated from the Stall Inception Flow Field at Midspan during 1st Mode Control (Data in Figure 5.18)

they reveal that the second mode grows steadily in magnitude until it triggers stall inception. The phase plot of the SFC's shows that the second mode rotates around the compressor annulus in a continuous fashion during the time of 12 rotor revolutions before stall. These measurements all point to the fact that growth of second mode is crucial to the stall inception mechanism at this point.

Implementation of optimal second mode control decreases the compressor's stalling flow coefficient to $\phi_{stall,1,2} = .424$. This is a 7.8% decrease in ϕ_{stall}, and the slope of the characteristic is $\frac{\partial \psi}{\partial \phi} = .89$ at this operating point. The large slope is related to the large growth rate $\sigma_1 = .27$ of the first mode at this point calculated using Model 1. This result indicates a superior performance of the controller at stabilizing high growth rate disturbances on the three stage compressor in comparison to the single-stage stabilization experiments of Paduano [16] in which $\sigma_1 = .02$ at the lowest operating point. As with the first mode, the decrease in the stalling flow coefficient as a result of second mode stabilization proves that second mode disturbances were crucial to the stall inception process at $\phi_{stall,1}$.

One or more of the performance limiting criteria mentioned in Section 5.2.4 restricts the success of optimal first and second mode control. Small amplitude first mode disturbances can be seen in the flow field before stall inception in Figure 5.20 during first and second mode control at $\phi_{stall,1,2}$; however, the flow perturbation which grows into the stall cell has an initial wavelength resembling a second mode perturbation. The speed of this modal perturbation is 54% of the rotor speed until its nadir reaches $\Theta = 198°$ and $\delta\phi > .1$ at which point it becomes nonlinear. The SFC's of the flow field are shown in Figure 5.21 and provide further evidence that the second mode may still be problematic during optimal first and second mode control. The phase measurements indicate that the second mode develops before the third and first develop and at least 5 rotor revolutions before the transition into stall. In the previous figures of stall inception SFC's, a mode forming and rotating continuously through space before

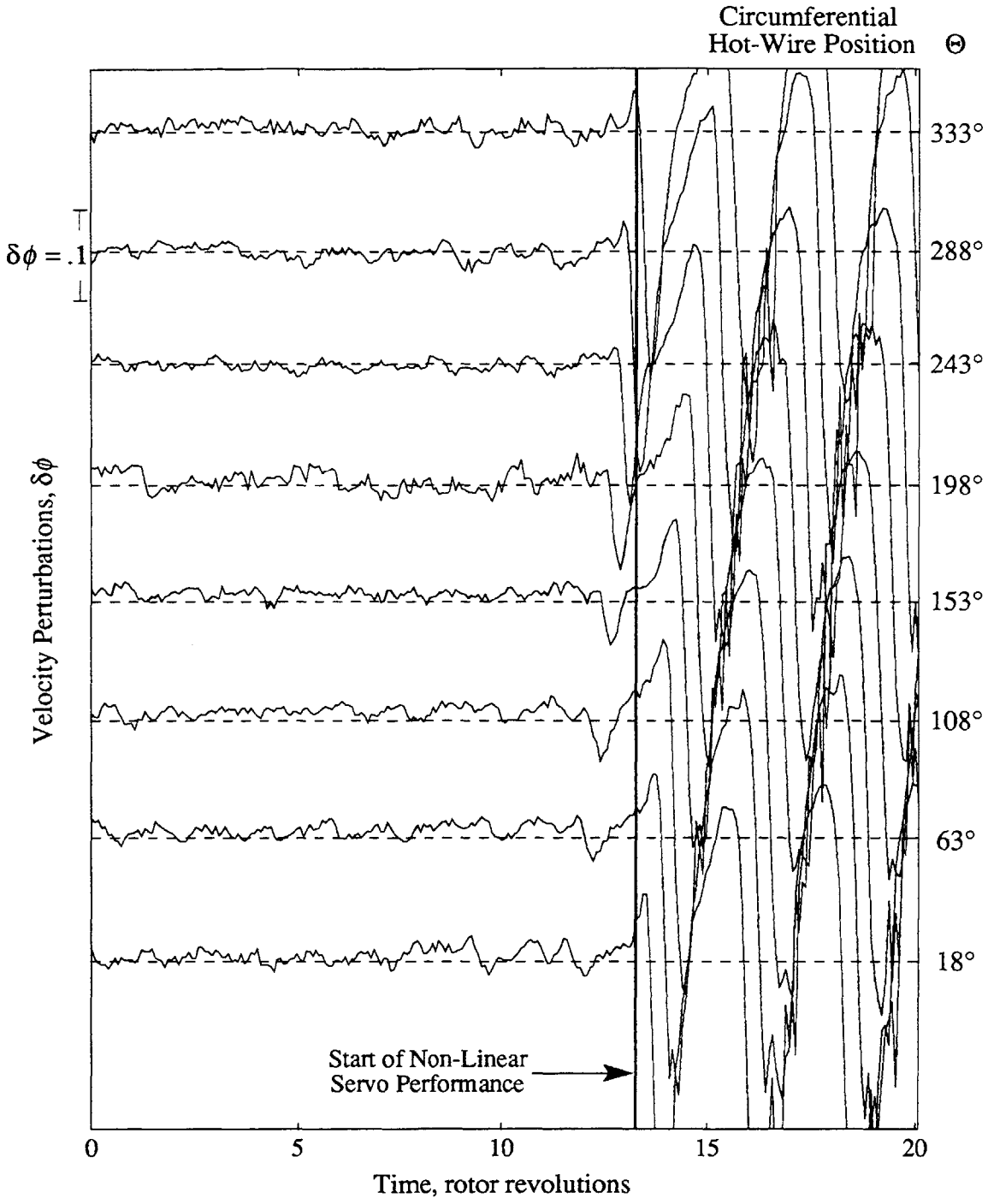

Figure 5.20: Stall Inception Flow Field around Compressor Annulus during Optimal 1st and 2nd Mode Control Measured Upstream of the IGV's when $\overline{\phi} = .43$

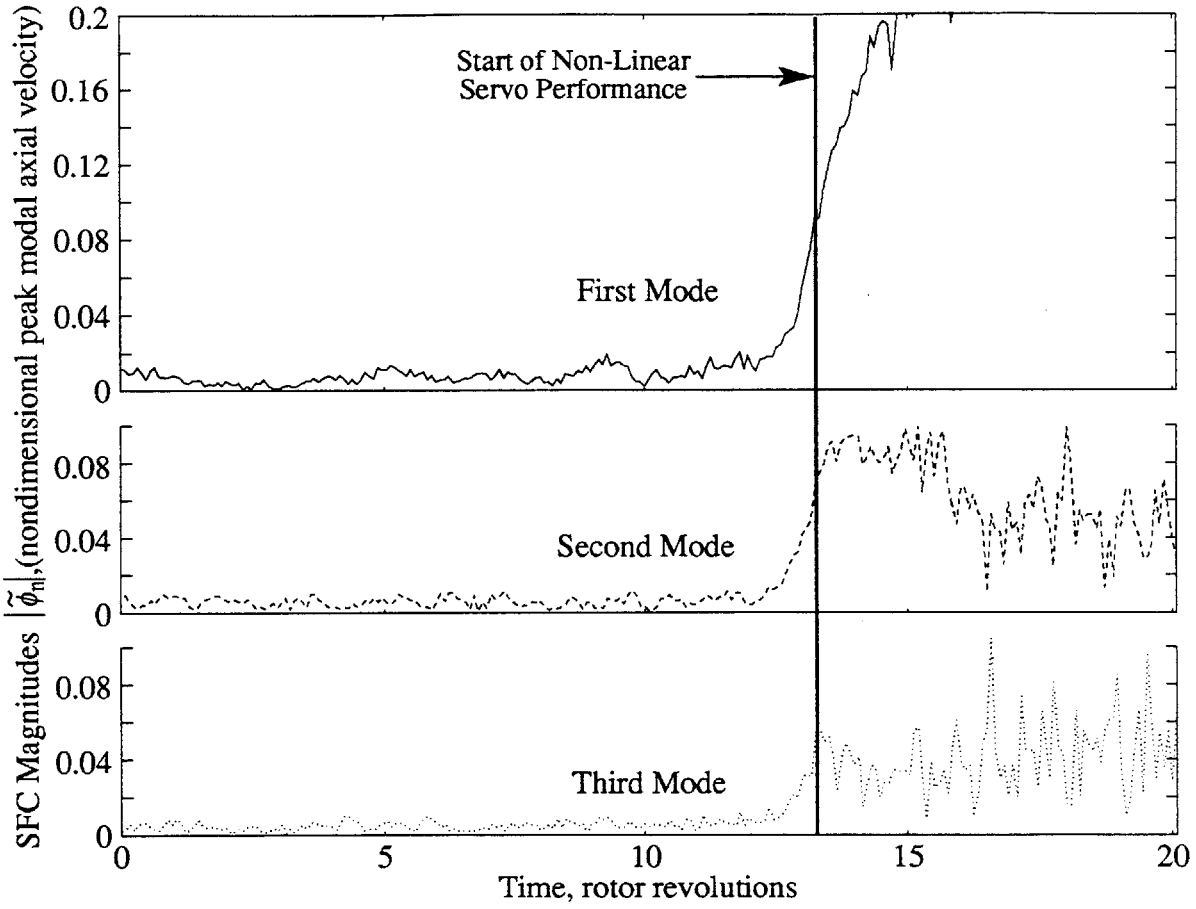

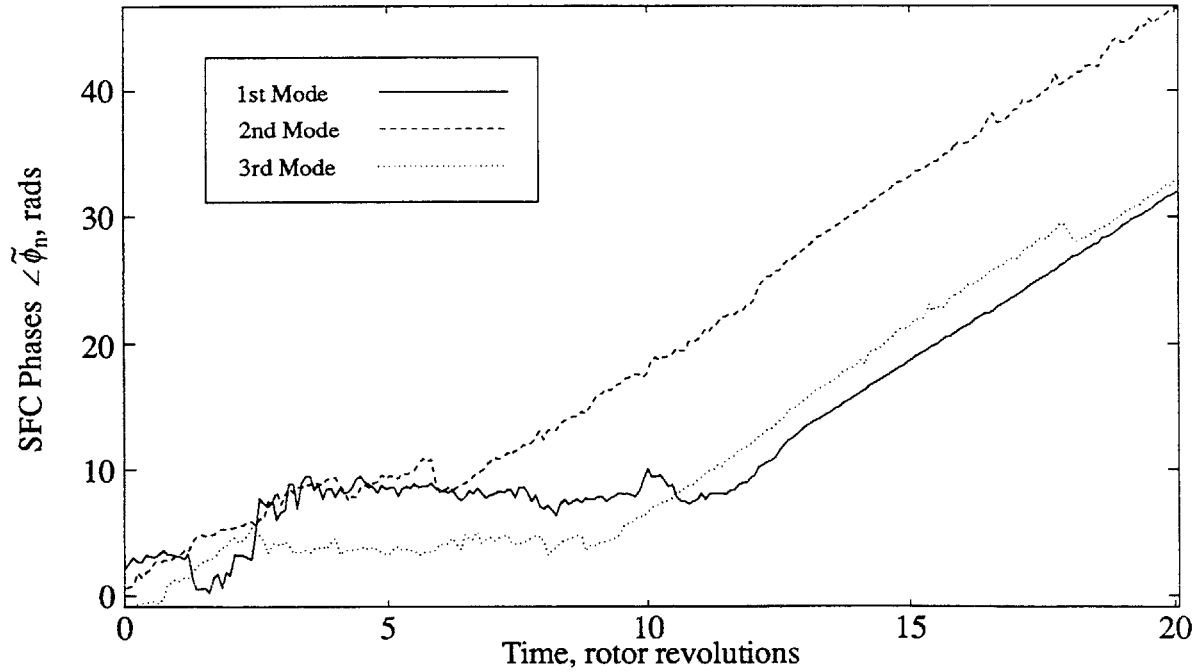

Figure 5.21: Magnitude and Phases of the First Three Spatial Fourier Coefficients Calculated from the Stall Inception Flow Field at Midspan during Optimal 1st and 2nd Mode Control (Data in Figure 5.20)

stall was the earliest indicator that it was the culprit for triggering stall inception. This is reason to believe that the second mode was underdamped even when using optimal proportional control. Figures B.21 to B.26 (Appendix B) give radial resolution of the stall inception flow field and SFC's during optimal first and second mode control and support the conclusion of an underdamped second mode. Investigation of the reasons for this only revealed that the actuators were not saturated or underdamped before stall inception, so other limitations created by the feedback system were suspected.

PSD's of the flow field near $\phi_{stall,1,2}$ showed that the third mode resonated when operating near $\phi_{stall,1,2}$ indicating that it was near the point at which it goes unstable. Its amplitude was still small; nevertheless, optimal third mode control was implemented to test the possibility that third mode disturbances were triggering stall inception at $\phi_{stall,1,2}$. The search for $\beta_{3,opt}$ (Figure 5.16) showed that the controller with third mode feedback was capable of destabilizing the compressor at a larger ϕ but was not very successful at lowering the stalling flow coefficient below $\phi_{stall,1,2}$. For this reason, third mode disturbances are not considered to be crucial to stall inception at $\phi_{stall,1,2}$. The stall inception flow field of the compressor with optimal first, second, and third mode control is shown in Figure 5.22. The flow perturbation which grows into the stall cell seems to develop from a first mode flow perturbation. The SFC's of the flow field in Figure 5.23 also provide some evidence that the first mode may be growing along with the second mode before stall inception. Since the third mode is apparently not dominant in this modal stall inception at this operating point, the limitation on compressor stabilization is attributed to the dynamics in the feedback loop and limits on modal sensing and actuation inherent to the design of the controller.

5.4 Modeling Closed-Loop Compressor Performance

The development of an accurate model of the actively stabilized compression system can simplify the determination of $\hat{Z}_{opt}$, help developers evaluate how much ϕ_{stall} can be reduced in another compressor with modal stall inception, and broaden

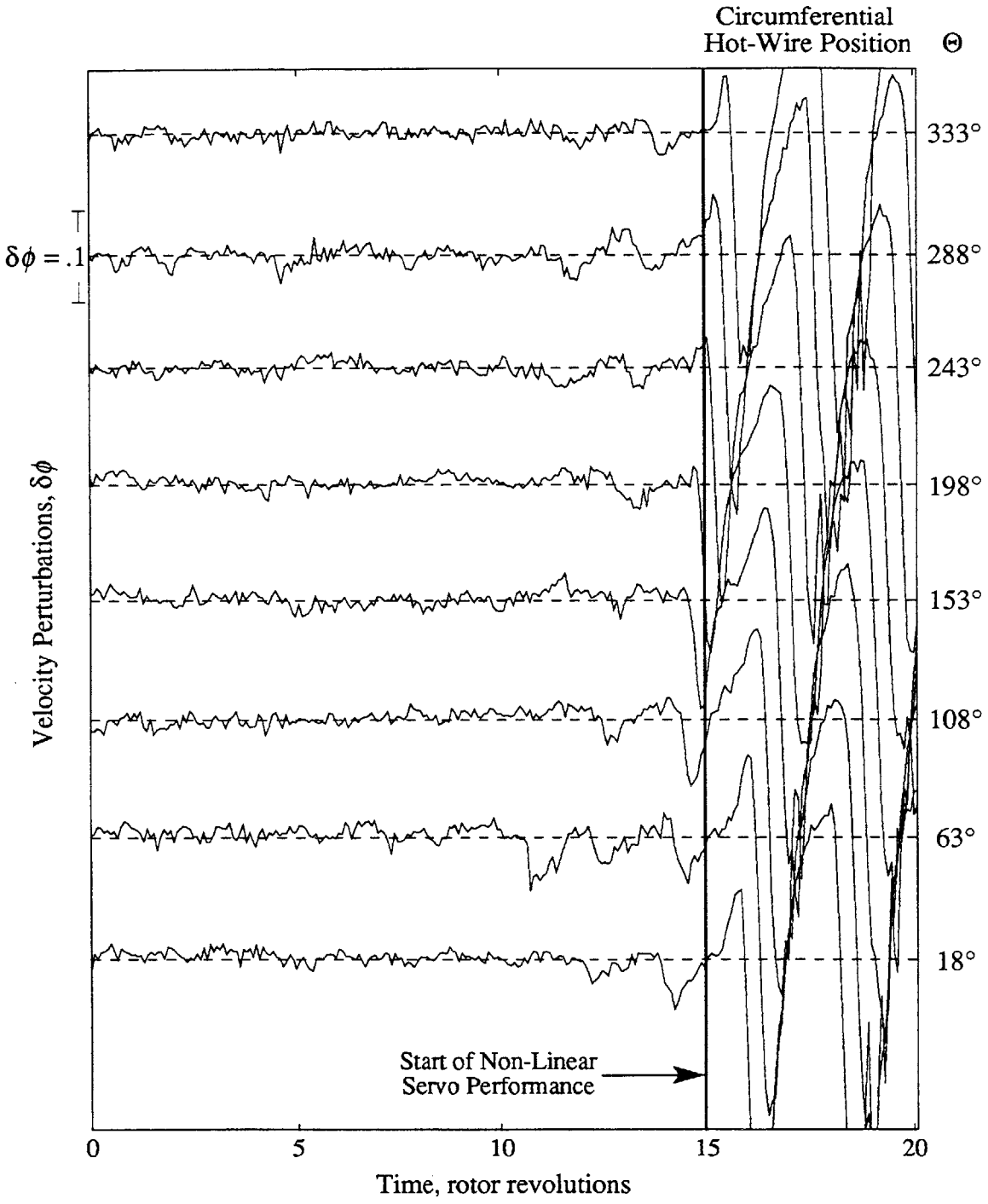

Figure 5.22: Stall Inception Flow Field around Compressor Annulus during Optimal 1st, 2nd, and 3rd Mode Control Measured Upstream of the IGV's when $\overline{\phi}$ = .43

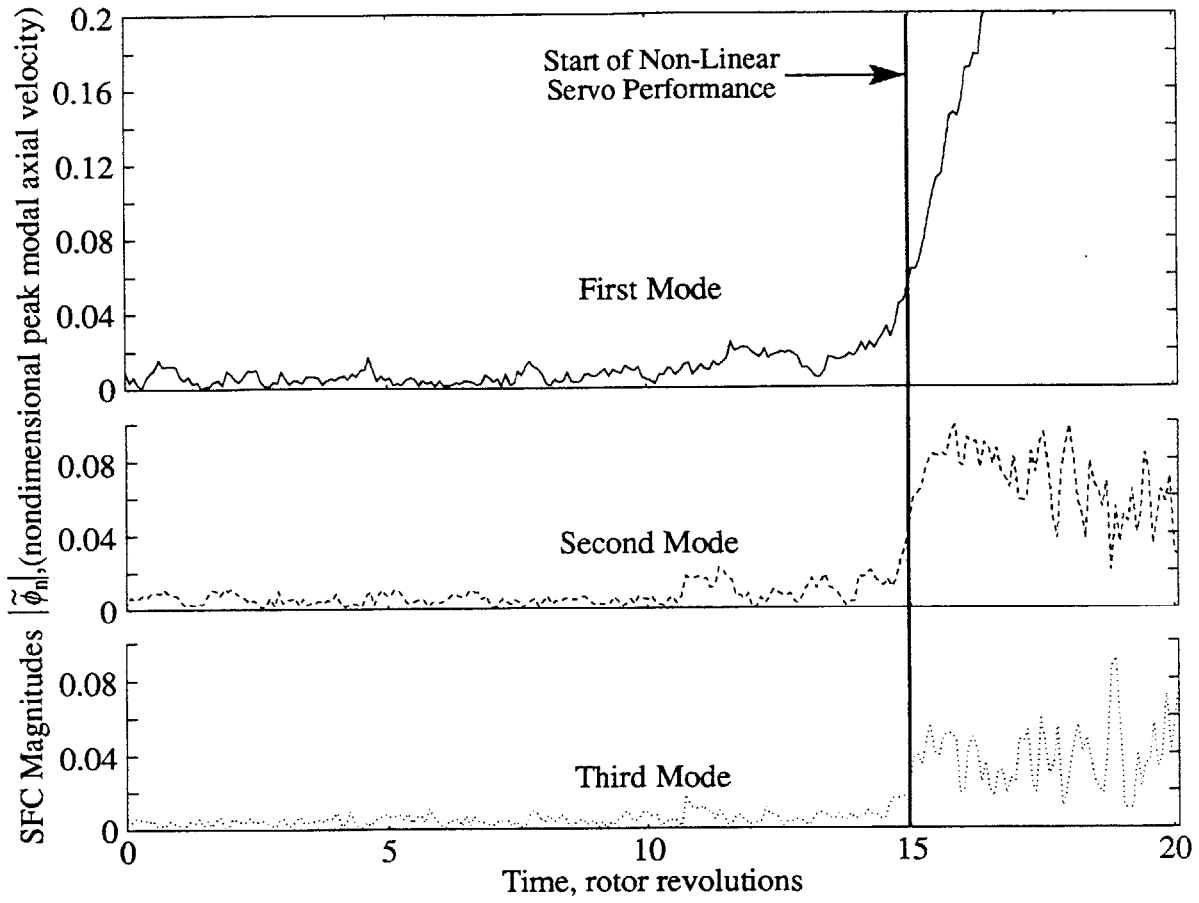

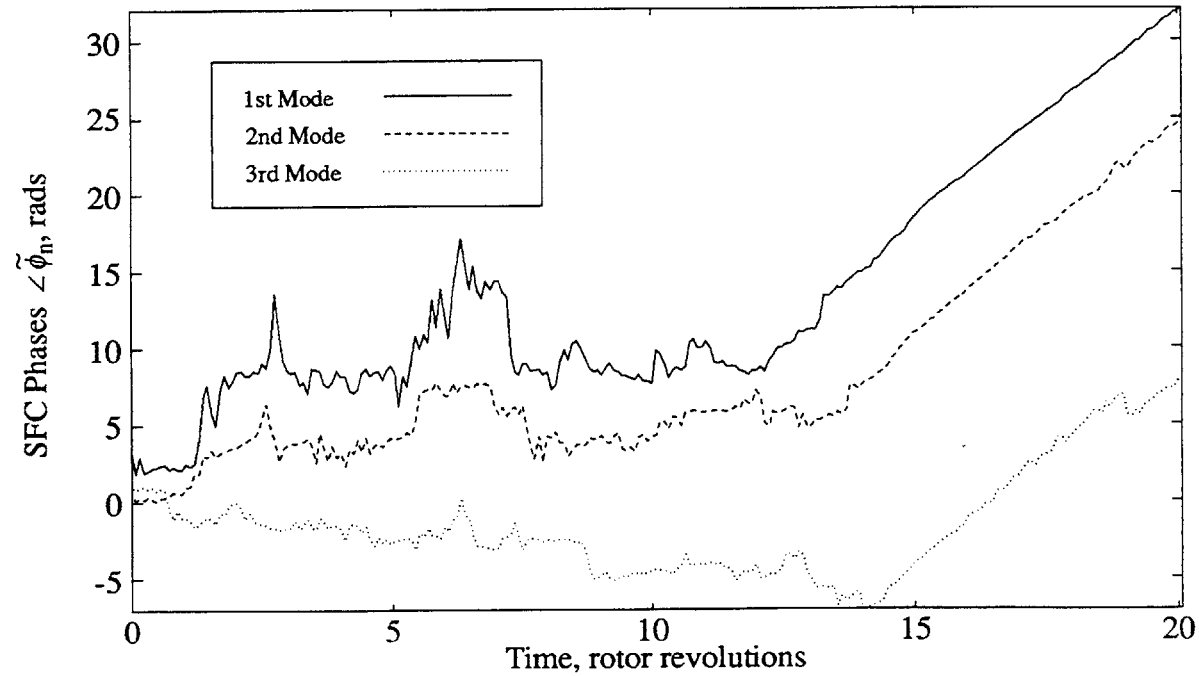

Figure 5.23: Magnitude and Phases of the First Three Spatial Fourier Coefficients Calculated from the Stall Inception Flow Field at Midspan during Optimal 1st, 2nd, and 3rd Mode Control (Data in Figure 5.22)

understanding of the closed-loop compressor dynamics. Chapter 3 put forward four different models to describe the compressor dynamics and also models for the components in the feedback path. In this section closed-loop compressor performance is predicted using each of the compressor models together with models for feedback dynamics. By comparing the predictions of each closed-loop model with experimental results, the model which best describes the compressor performance can be identified.

Before examining the capability of the compressor models to predict $\hat{Z}_{opt}$, the accuracy of the models' prediction of ϕ_{neut} for various control parameters will be examined. The closed-loop compressor model is in each case given the same control parameters $\hat{Z}$ as were used in gathering the experimental data. Since the models consider each mode independently, $\hat{Z}$ was at first chosen so that in the experiments only mode n would cause destabilization of the compressor as β_n was varied; this was accomplished by significantly decreasing the gain for mode n while keeping the other control parameters at their optimal value. Figures 5.24 through 5.31 show the degree of accuracy that Models 1 to 4 have in predicting the stability of the first and second modes over the full range of phase. The inability of Model 1 to accurately predict the stability of modes n>1 is evident. Model 2 gives the most accurate predictions of all the models even though it does not account for several fluid dynamic effects. The new fluid dynamic phenomena described in Models 3 and 4 cause them to predict greater stability for the modes than actually existed and a positive shift in phase from the actual phase. Considered together, Models 2, 3, and 4 each demonstrate the ability to accurately predict modal stability if they are given correct information on the feedback gain R_n and have accurate models of the feedback dynamics. Figures 5.32 to 5.34 show the model predictions under more complicated conditions. In these cases, the optimal gain $R_{n,opt}$ for mode n was input to each model. In Figures 5.32 and 5.33 model predictions differ from the experimental data at some points. This could result either from the limitations on the controller at high gains not being modeled accurately or from a mode other than

the one considered triggering the stall inception. Figure 5.34 provides some confirmation of the accuracy of Models 2, 3, and 4 in predicting third mode stability by showing that the decrease in compressor stability over the range $-150 < \beta_3 < -50$ is aligned with the predictions of the models. In the experiments the compressor presumably did not have its first two modes stabilized well enough to resolve the rest of the third-mode neutral stability points.

The previous figures demonstrate that the models can in some cases accurately predict the compressor stability at a given phase if they are first given the correct value of gain. In designing a compressor stabilization system the feedback gain will not be known ahead of time and will have to be chosen based on the predictions given by the model. Figures 5.35 to 5.38 show the changes in ϕ_{neut} at $\beta_{n,opt}$ as R_n is incremented by 1 degree/(m/s) from 0 to the value at which the mode is predicted by the model to either become truly unstable or decreasingly stable with increases in gain. The optimum gains predicted using Model 2 were the closest to the values used in $\hat{Z}_{opt}$. Predictions by the other models tended to estimate $R_{n,opt}$ to be higher than it actually was. All of the models predicted the lowest attainable ϕ_{neut} to be lower than it was in reality. This is partially caused by the model not accounting for the limits on stabilization described in Section 5.2.4. Although the compressor models lacking a more accurate feedback model have limited usefulness in predicting the optimal gains, they are still very useful for describing the optimal feedback phase because it shifts by only a small amount over the range of stable gains.

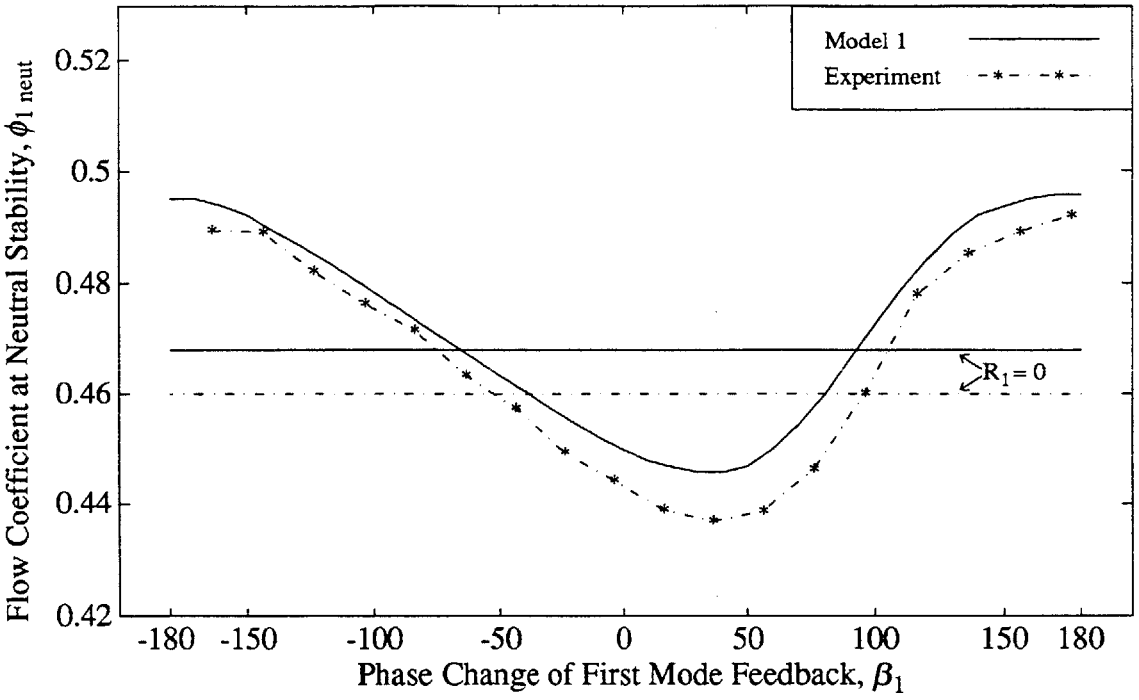

Figure 5.24: Comparison of Model 1 Prediction and Experimental Measurement of $\phi_{1\ neut}$ for Mode 1 during Active Control with Reduced First Mode Gain, $R_1 = 2.5$

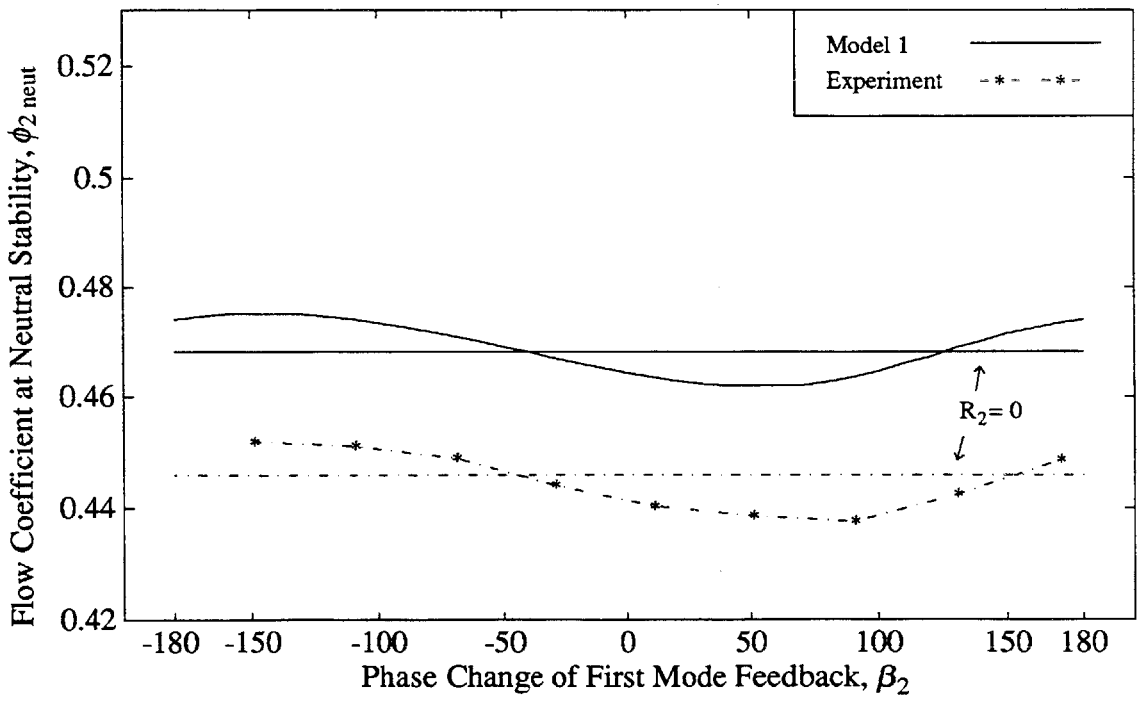

Figure 5.25: Comparison of Model 1 Prediction and Experimental Measurement of $\phi_{2\ neut}$ for Mode 2 during Active Control with Reduced Second Mode Gain, $R_2 = 1.0$

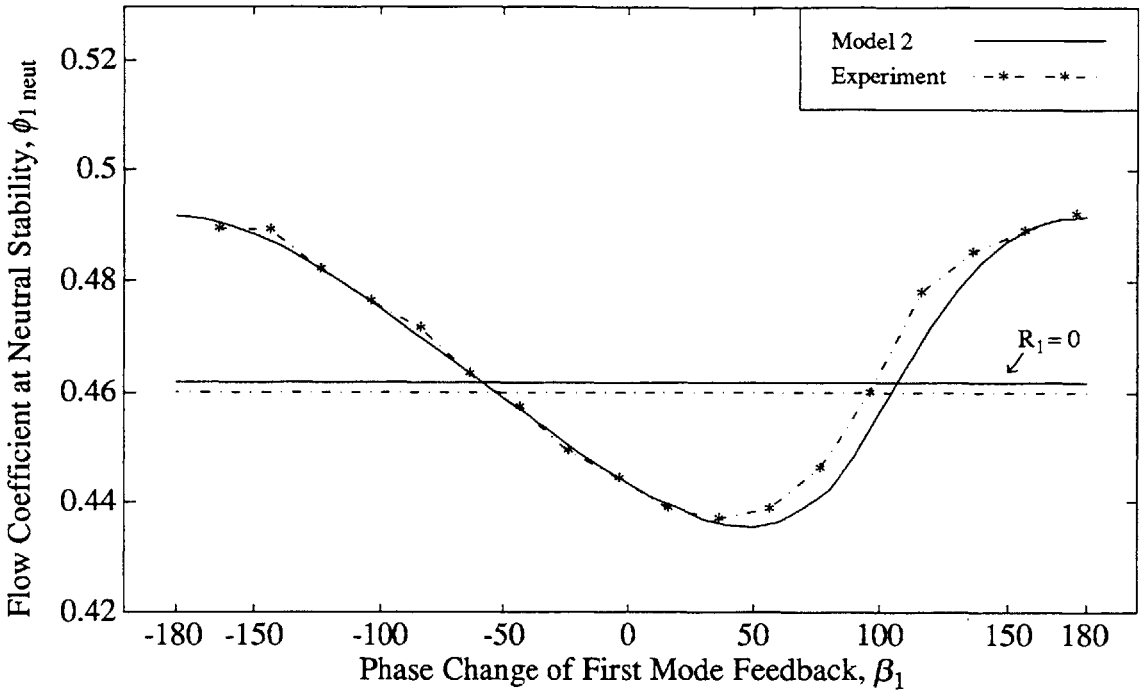

Figure 5.26: Comparison of Model 2 Prediction and Experimental Measurement of $\phi_{1\,neut}$ for Mode 1 during Active Control with Reduced First Mode Gain, $R_1 = 2.5$

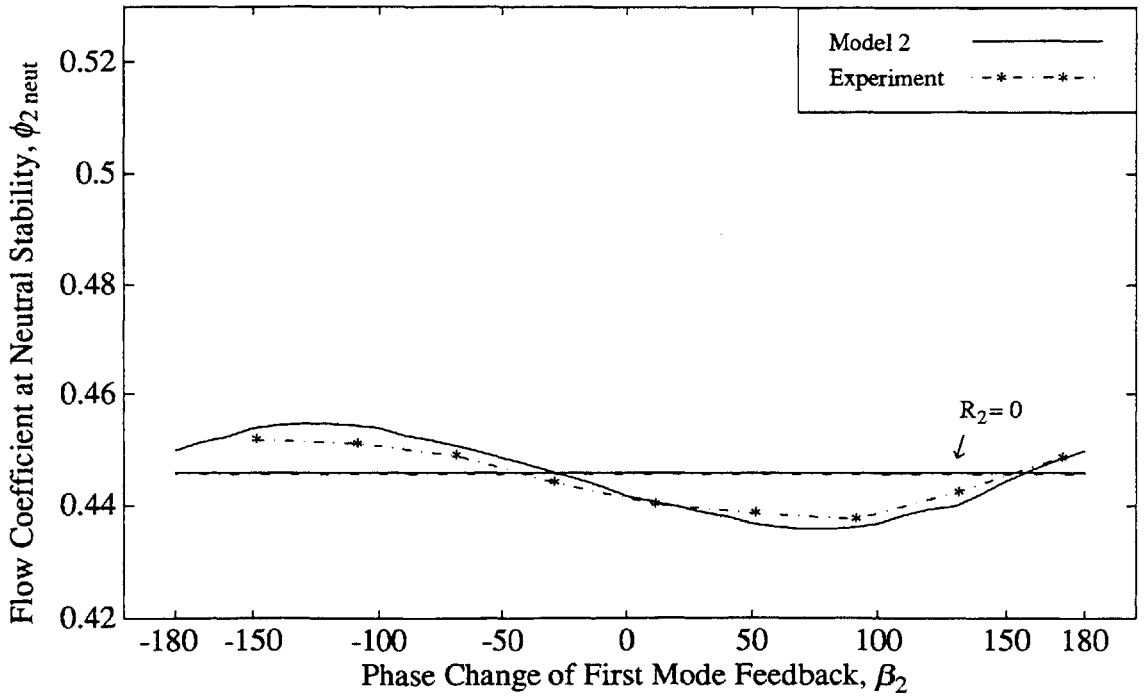

Figure 5.27: Comparison of Model 2 Prediction and Experimental Measurement of $\phi_{2\,neut}$ for Mode 2 during Active Control with Reduced Second Mode Gain, $R_2 = 1.0$

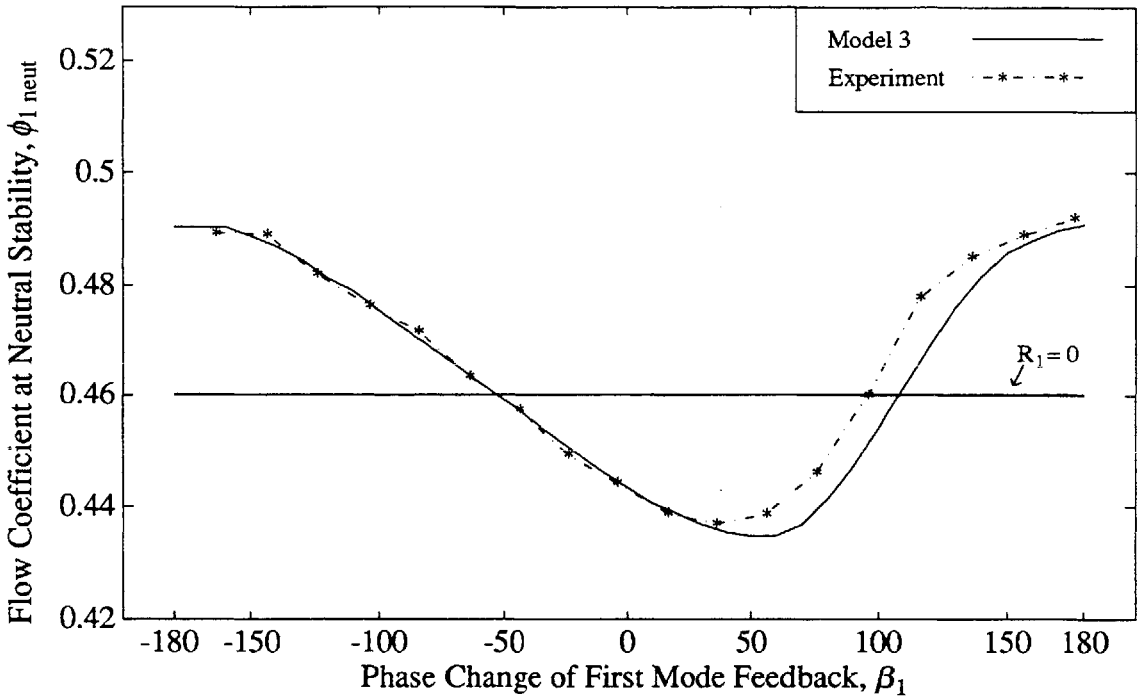

Figure 5.28: Comparison of Model 3 Prediction and Experimental Measurement of $\phi_{1\ neut}$ for Mode 1 during Active Control with Reduced First Mode Gain, $R_1 = 2.5$

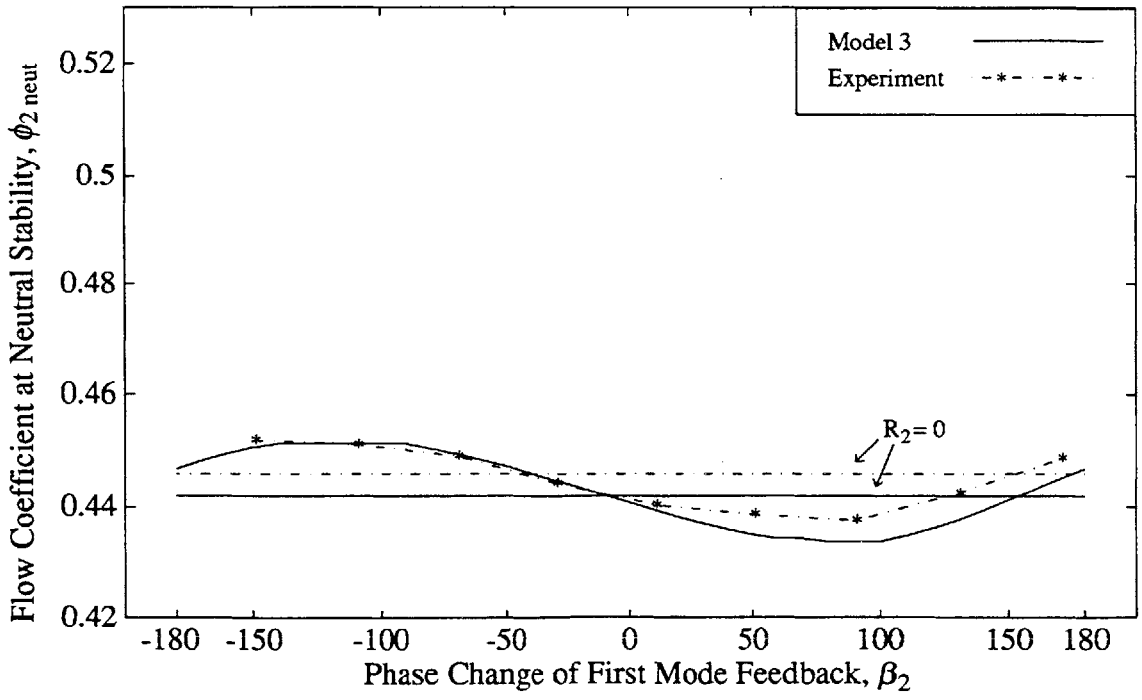

Figure 5.29: Comparison of Model 3 Prediction and Experimental Measurement of $\phi_{2\ neut}$ for Mode 2 during Active Control with Reduced Second Mode Gain, $R_2 = 1.0$

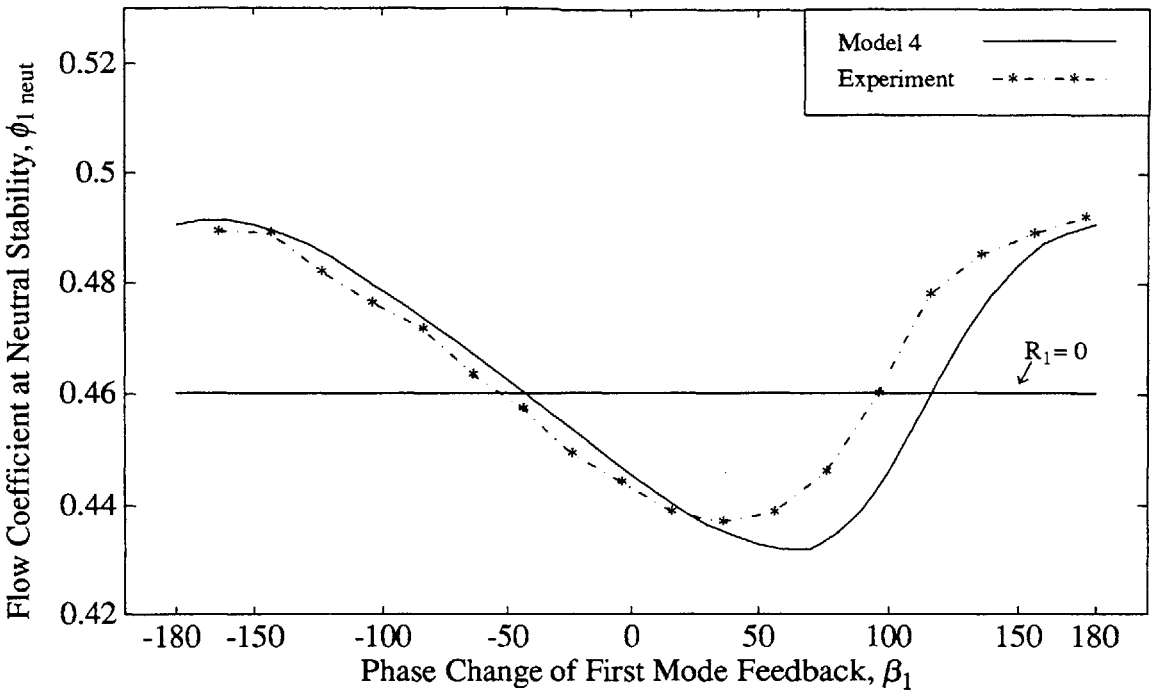

Figure 5.30: Comparison of Model 4 Prediction and Experimental Measurement of $\phi_{1\ neut}$ for Mode 1 during Active Control with Reduced First Mode Gain, $R_1 = 2.5$

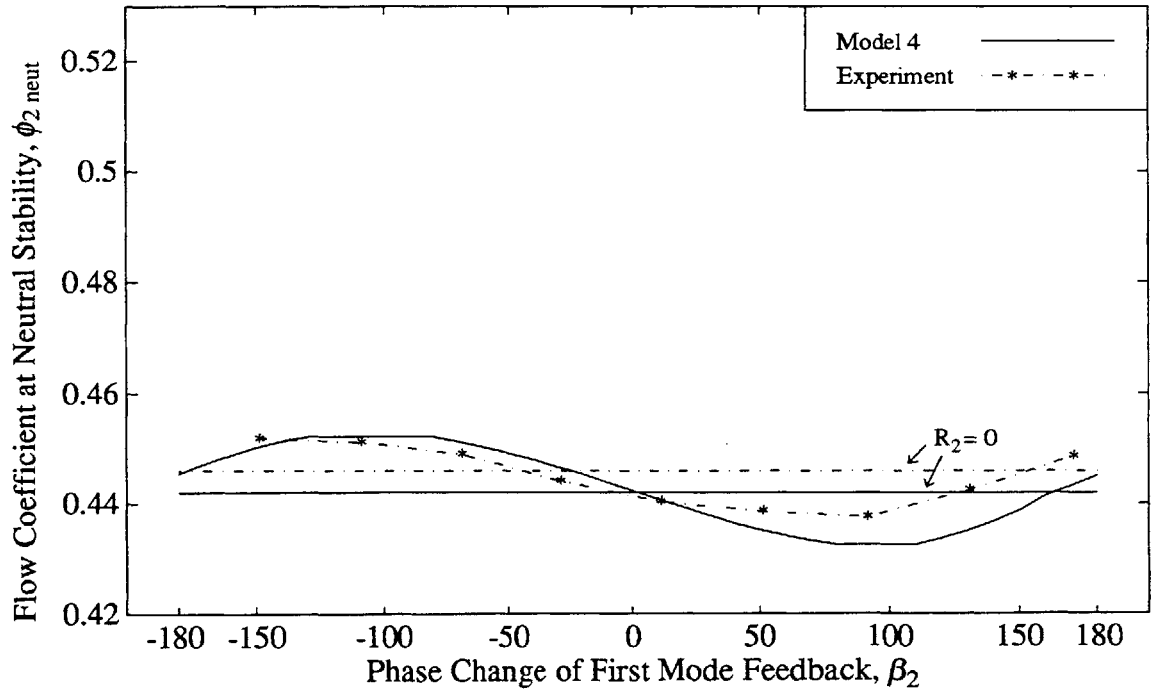

Figure 5.31: Comparison of Model 4 Prediction and Experimental Measurement of $\phi_{2\ neut}$ for Mode 2 during Active Control with Reduced Second Mode Gain, $R_2 = 1.0$

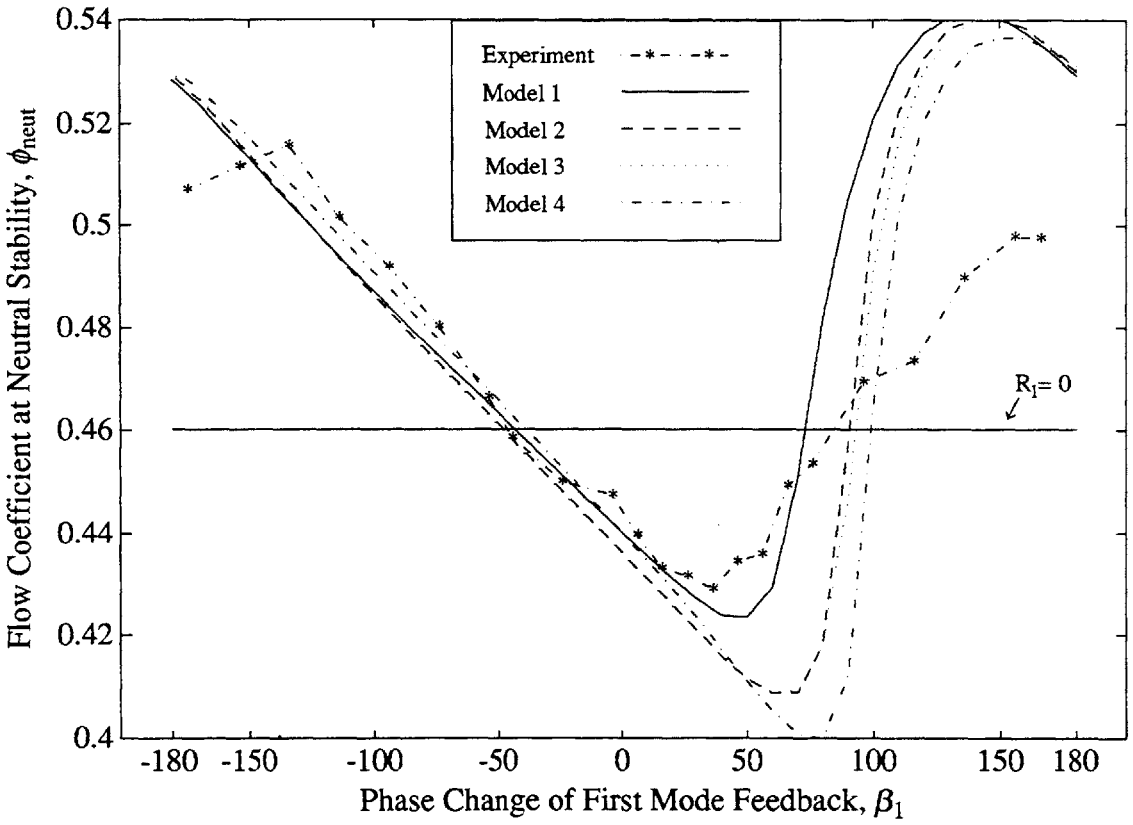

Figure 5.32: Comparison of Model Predictions of $\phi_{1\ neut}$ with Experimental Measurements of ϕ_{neut}

Optimal control parameters $\hat{Z}_{opt}$ were used with the exception of β_1,which was variable.

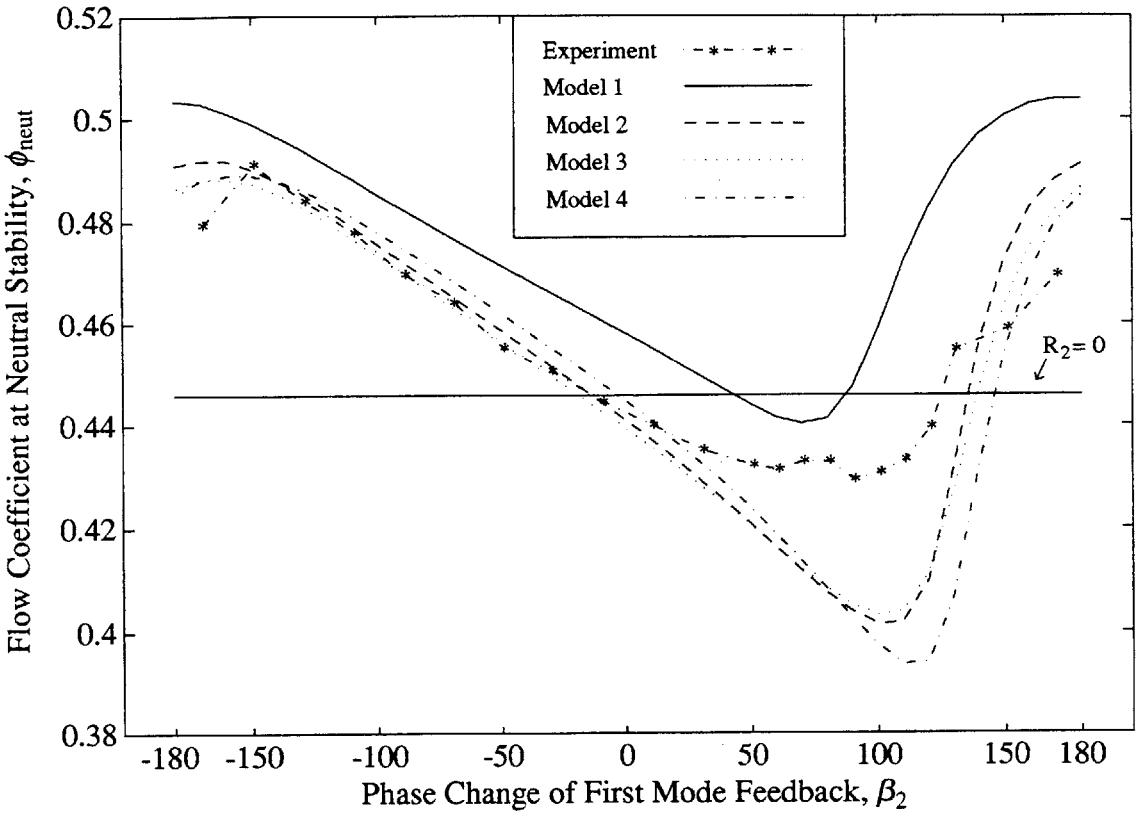

Figure 5.33: Comparison of Model Predictions of $\phi_{2\,neut}$ with Experimental Measurements of ϕ_{neut}

Optimal control parameters $\hat{Z}_{opt}$ were used with the exception of β_2,which was variable.

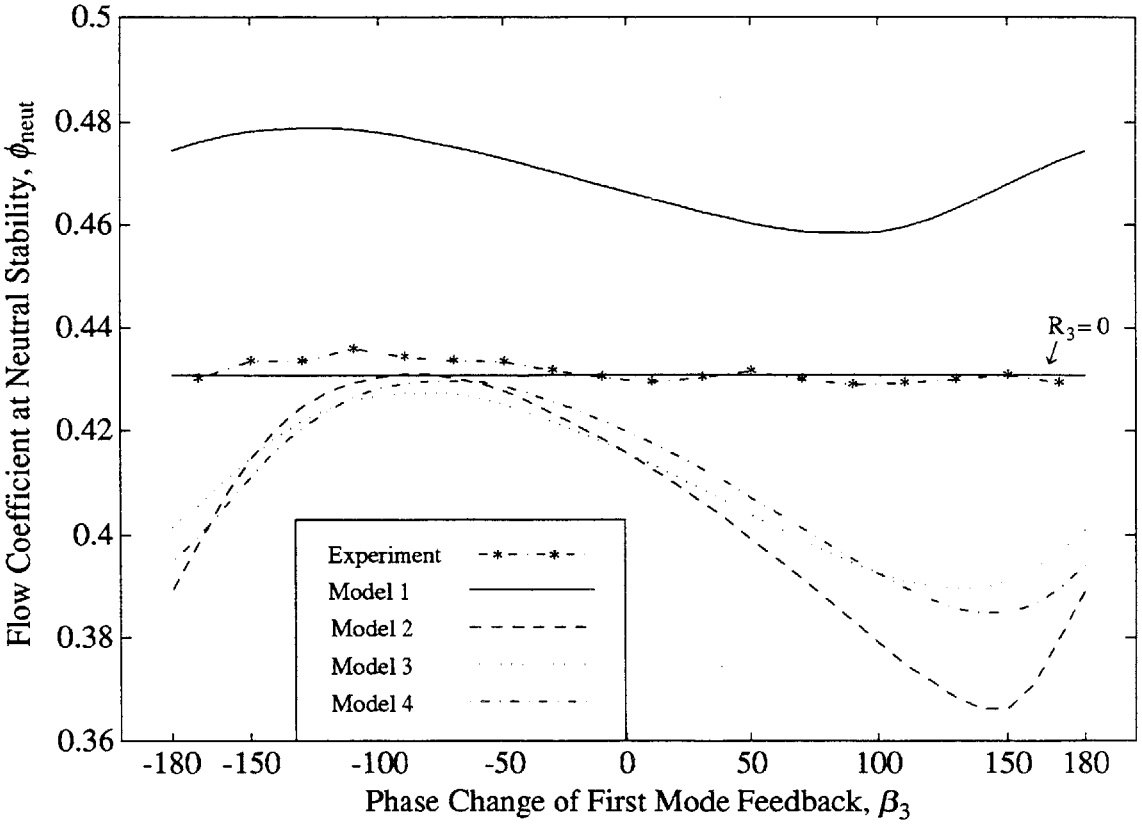

Figure 5.34: Comparison of Model Predictions of $\phi_{3\ neut}$ with Experimental Measurements of ϕ_{neut}

Optimal control parameters $\hat{Z}_{opt}$ were used with the exception of β_3,which was variable.

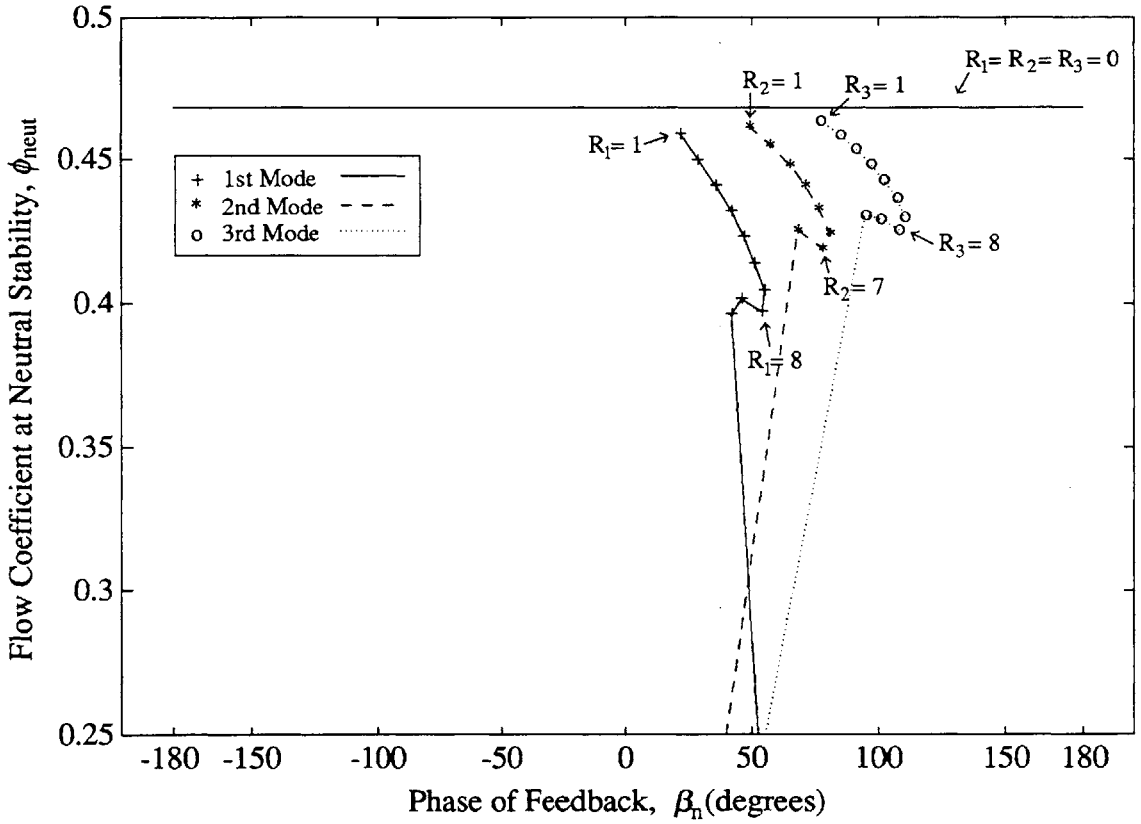

Figure 5.35: Flow Coefficient at Neutral Stability Predicted by Model 1 for Modes 1, 2, and 3 using Optimal Closed-Loop Phase for Values of Gain Incremented from $R_n = 0$ to the Maximum Stable Value

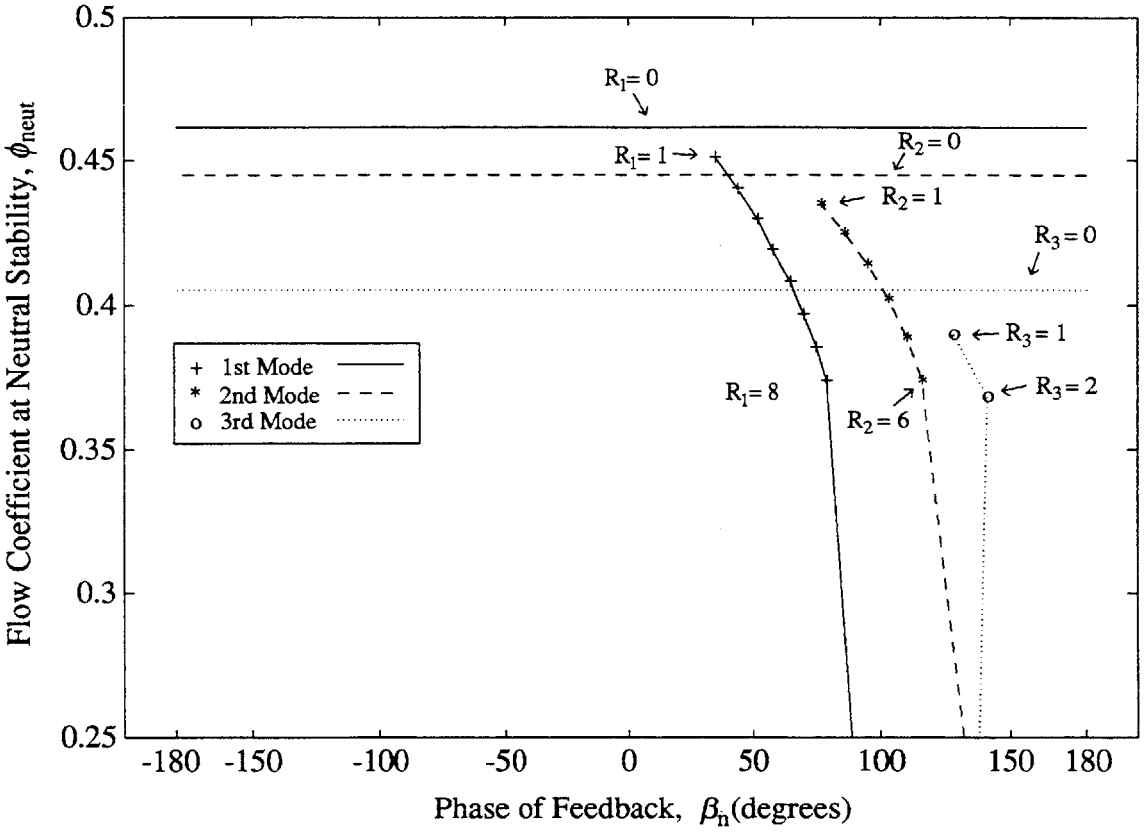

Figure 5.36: Flow Coefficient at Neutral Stability Predicted by Model 2 for Modes 1, 2, and 3 using Optimal Closed-Loop Phase for Values of Gain Incremented from $R_n = 0$ to the Maximum Stable Value

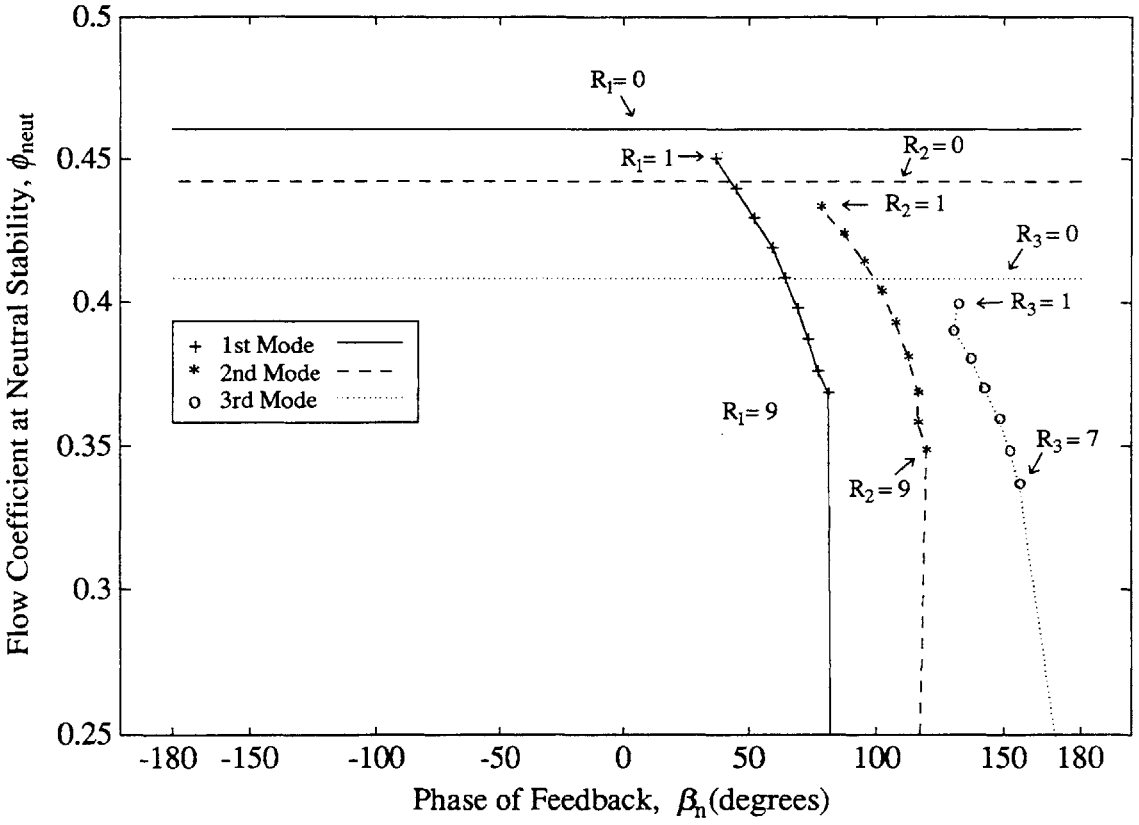

Figure 5.37: Flow Coefficient at Neutral Stability Predicted by Model 3 for Modes 1, 2, and 3 using Optimal Closed-Loop Phase for Values of Gain Incremented from $R_n = 0$ to the Maximum Stable Value

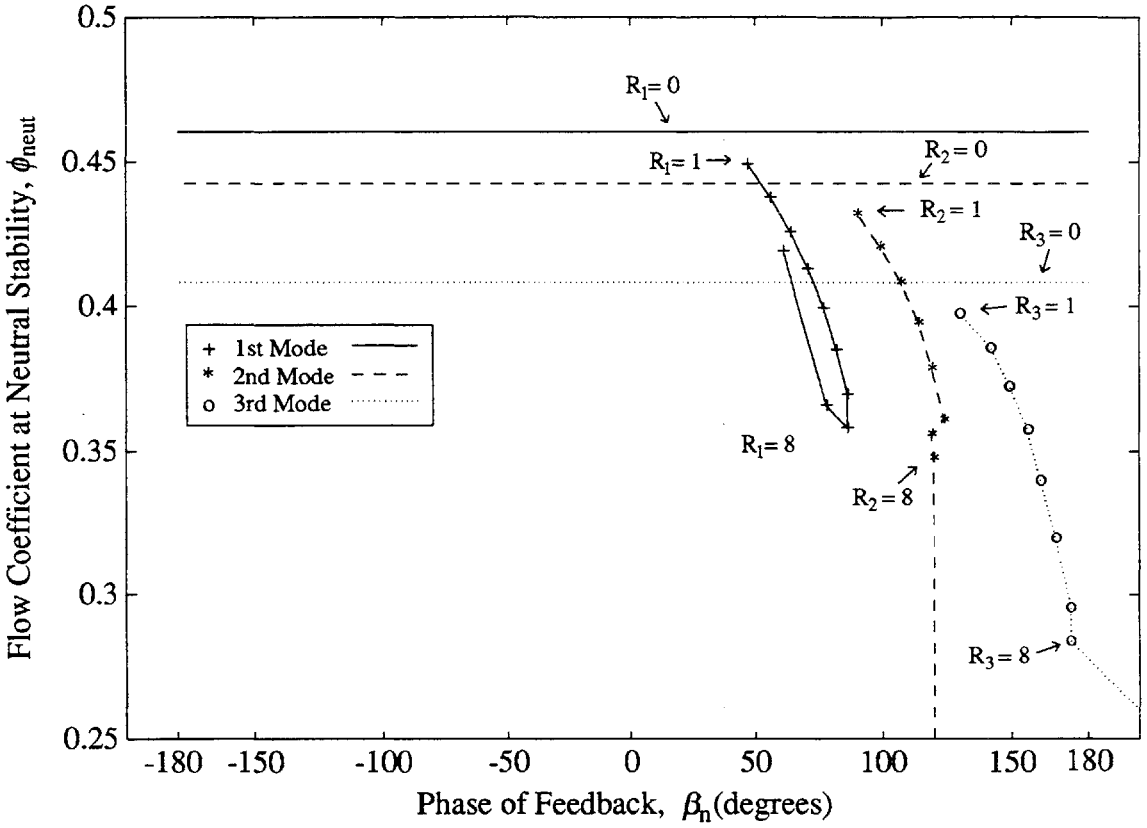

Figure 5.38: Flow Coefficient at Neutral Stability Predicted by Model 4 for Modes 1, 2, and 3 using Optimal Closed-Loop Phase for Values of Gain Incremented from $R_n = 0$ to the Maximum Stable Value

CHAPTER 6

Summary, Conclusions, and Recommendations

6.1 Summary

Stall inception has been sufficiently suppressed in a three-stage axial compressor to enable in a 7.8% extension of the flow range. This was accomplished using feeding back of measured flow field disturbances to an array of 12 individually actuated guide vanes which created flow disturbances upstream of the compressor. Control system design and identification of flow disturbance dynamics were greatly influenced by a model of the compressor founded upon principles of linearized fluid mechanics and linear control theory.

Chapter 3 presented four variations of a model describing the response of the compressor to flow field perturbations introduced by servo-controlled guide vanes (SGV's). The models describe the compressor response dynamics with varying degrees of accuracy and complexity. Model 1 is the simplest description of the compressor dynamics and is constructed from information on the compressor's geometry and steady-state pressure rise characteristic. Model 2 introduces a first order description of the pressure rise response lag and assumes that the initial response of a blade row is described by the slope of the isentropic pressure rise characteristic. Model 3 also contains a first order description of the pressure rise response lag but describes the initial response of the compressor to axial flow perturbations using an analytic expression for the ideal pressure rise. This avoids the problem of obtaining data for the isentropic pressure rise across the compressor if steady-state data of the torque characteristic are not available. Model 4 incorporates the first order lag model used in Model 3 but modifies it

to include a first order lag in pressure rise associated with the perturbations in SGV stagger angle.

The compressor and other equipment that were used in the active control experiments are described in Chapter 2. Details of the servo-controlled guide vanes which were uniquely designed for active control experiments were given in this chapter. The models which represent the flow sensing, discrete time control, and actuator feedback were presented in Chapter 3.

The open-loop performance of the compressor was described in Chapter 4. The SGV's were used to excite the spatial modes of the flow into the compressor and determine their dynamic characteristics. The mode dynamics were predicted using the compressor models; Models 2, 3, and 4 gave the most accurate predictions of the open-loop mode dynamics. Chapter 5 examined the effects of proportional control on mode stability. Flow field measurements were presented which indicate that spatial mode instabilities were crucial to the stall inception process, and then a methodology for determining the control parameters which give the best improvement in flow range was described. The stall inception flow field which exists at the point of neutral stability is examined under conditions of 1st; 1st & 2nd; and 1st, 2nd, & 3rd mode stabilization. Also in this chapter predictions of the closed loop stability are compared with experimental results to show the level of accuracy and usefulness of each model.

6.2 Conclusions

The rotating stall suppression experiments performed using the low speed three-stage axial compressor gave many valuable insights into the problem of stall inception and the implementation of an active control system for its stabilization over a range of operating points. Conclusions can be drawn which explain the performance of the control system which was applied to this compressor, and these conclusions can be generalized to any compressor which has the same characteristic stall inception features. In Chapters 4 and 5 many conclusions were drawn which explain the behavior of the

compression system. This section highlights the answers to the principle hypotheses which guided this research. They are as follows:

1) Small amplitude spatial mode flow field perturbations are crucial to the stall inception process in all observed cases in this compressor. The short length scale disturbances described by Day were not observed, and this is reason to expect that there is a class of compressors which only experience stall inception via the destabilization of the spatial modes of the flow field.

2) A circumferential array of high-response servo-controlled guide vanes upstream of a low speed three-stage compressor can be used to actuate sinusoidal axial flow perturbations in the compressor and stabilize the flow across multiple stages. This demonstrates that the flow field through the compressor maintains a degree of continuity that allows the lower stages to experience the flow field perturbations created several blade rows upstream.

3) Identification of the open-loop dynamics of small amplitude spatial modal disturbances in the flow field indicates that individual modes do not become unstable at the same flow coefficient, but instead they go unstable sequentially with decreasing flow coefficient starting with the first. For the control system, this means the spatial modes of the flow field can be stabilized one at a time, and their damping will yield a noticeable increase in the stable flow range each time. On the three-stage compressor first mode stabilization could decrease the stalling flow coefficient at most by 3.1% before the second mode became unstable. First and second mode stabilization decreased the stalling flow coefficient by at most 7.8%.

4) Successful compressor stabilization by independent treatment of the spatial modes demonstrates that linear theory is applicable to the treatment of prestall flow disturbances. The description of the modal dynamics resulting from a linearized treatment of the compressor is found to approximate the rotation rate of the prestall disturbance quite well.

5) A compressor model which accounts for the lag in the pressure rise response associated with a flow perturbation can be used to accurately predict the rotation rate and growth rate of prestall disturbances. The closed-loop performance can then be predicted accurately by modeling the feedback dynamics as well. In this compressor the flow range extension resulting from closed-loop mode stabilization was predicted with better than 1.5% accuracy.

6.3 Recommendations for Future Work

There are two principal areas that need to be investigated further. Some questions still remain concerning the flow behavior surrounding stall inception in low speed compressors, and additional questions center around the application of the

principles demonstrated here to higher speed compressors and eventually to a gas turbine engine. Both areas are of importance to the future utility of this research. Specific questions for future investigation are:

1) What design factors and prestall flow field phenomena cause stall inception to occur due to short length scale disturbances instead of mode destabilization? Knowing these factors will clarify which compressors can be accurately described by linear theory. To accomplish this higher response instrumentation just upstream of the first rotor is needed for more accurate documentation of the flow field associated with short length scale disturbances.

2) How can the transient pressure rise response of the compressor to flow disturbances be characterized more accurately and predicted? A first-order description of the delay in the pressure rise response introduced a lag parameter to the model. Being able to predict the lag parameter for a compressor would be useful. Finding ways to determine the magnitude of the transient pressure response associated with a disturbance in the flow would improve the usefulness of the model as well.

3) How can the feedback dynamics be improved so that they contribute less to the loss of control? Determining this would provide more detailed guidelines for the design of the controller and supplement the current understanding as to which qualities are performance limiting.

4) How can the compressor be stabilized in the presence of non-uniform inlet boundary conditions such as inlet distortion? Understanding this will broaden the range of conditions over which active stabilization can be successfully implemented. Research in this area is ongoing.

5) Do different actuation schemes stabilize the compressor more effectively, and if so, by how much do they extend the flow range? The IGV actuators were simple to implement, but more sophisticated actuators should be analyzed and tested.

6) In what ways does the analysis of low speed machines need to be modified to extend the application of the stall inception model to a high-speed gas turbine engine? Accounting for the effects of flow compressibility and developing high speed actuators and a robust control system are presumably the main challenges of this research.

References

1. Emmons, H.W., Pearson, C.E., and Grant, H.P., "Compressor Surge and Stall Propagation", Transactions of the ASME , Vol. 79, pp. 455-469, April 1955.

2. Mazzawy, R.S., "Surge Induced Structural Loads in Gas Turbines", ASME Journal of Engineering for Power, Vol. 102, pp. 162-168, January 1980.

3. Pinsley, J.E., Guenette, G.R., Epstein, A.H., and Greitzer, E.M., "Active Stabilization of Compressor Surge", Journal of Turbomachinery, Vol. 113, pp. 723-732, 1991.

4. Gysling, D.L., Dugundji, J., Greitzer, E.M., and Epstein, A.H., "Dynamic Control of Centrifugal Compressor Surge Using Tailored Structures", Journal of Turbomachinery, Vol. 113, No. 4, pp. 710-722, 1991.

5. Lavrich, P.L., "Time Resolved Measurements of Rotating Stall in Axial Flow Compressors", MIT GTL Report No. 194, August 1988.

6. Day, I.J., "Stall Inception in Axial Flow Compressors", ASME Paper 91-GT-86, 1991.

7. Moore, F.K., "A Theory of Rotating Stall of Multistage Compressors, Parts I-III", ASME Journal of Engineering for Power, Vol. 106, pp. 313-336, 1984.

8. Moore, F.K. and Greitzer, E.M., "A Theory of Post-Stall Transients in Axial Compressors: Part I - Development of the Equations", ASME Journal of Engineering for Gas Turbines and Power, Vol. 108, pp. 68-76, 1986.

9. McDougall, N.M., Cumpsty, N.A., and Hynes, T.P., "Stall Inception in Axial Compressors", Transactions of the ASME, Vol. 112, pp. 116-125, 1990.

10. Longley, J.P., "Inlet Distortion and Compressor Stability", Ph.D. Thesis, Trinity College, Cambridge University, 1988.

11. Garnier, V.H., "Experimental Investigation of Rotating Waves as a Rotating Stall Inception Indication in Compressors", M.S. Thesis, MIT Dept. of Aeronautics and Astronautics, May 1988.

12. Smith, G.D.J., "Casing Treatment in Axial Compressors", Ph.D. Thesis, Engineering Department, University of Cambridge, April 1980.

13. Ludwig, G.R. and Nenni, J.P., "Tests of an Improved Rotating Stall Control System on a J-85 Turbojet Engine", ASME Paper 80-GT-17, 1980.

14. Reis, W. and Blocker, U., "Possibilities for On-line Surge Suppression by Fast Guide Vane Adjustment in Axial Compressors", AGARD-CP-421, 1980.

15. Epstein, A.H., Ffowcs-Williams, J.E., and Greitzer, E.M., "Active Suppression of Aerodynamic Instabilities in Turbomachines", AIAA Paper 86-1994. Also Journal of Propulsion and Power, Vol. 5, No. 2, pp. 204-211, March-April 1989.

16. Paduano, J.D., "Active Control of Rotating Stall in Axial Compressors", MIT GTL Report No. 208, March 1992.

17. Day, I.J., "Active Suppression of Stall and Surge in Axial Compressors", Proceedings, ASME/IGTI Conference in Orlando, 1991.

18. Eastland, A.H.J., "Investigation of Compressor Performance in Rotating Stall", MIT GTL Report No. 164, June 1982.

19. Gamache, R.N., "Axial Compressor Reversed Flow Performance", Ph.D. Thesis, MIT Dept. of Aeronautics and Astronautics, May 1985.

20. Christianson, M.B., "An Experimental Investigation of a Three-Stage Axial-Flow Compressor with Cantilevered Stators Using Low Aspect Ratio - Redesigned Endwork Blading in All Stages," United Aircraft Research Laboratory Report No. R232752-1, February 1975.

21. Lewis, J.T., "MIT Compressor Re-Stagger", P&WA GPD Correspondence, dated 26 June 1984.

22. Silkowski, P.D., "Aerodynamic Design of Movable Inlet Guide Vanes for Active Control of Rotating Stall", M.S. Thesis, MIT Dept. of Aeronautics and Astronautics, February 1990.

23. Goldstein, R.J., editor, "Thermal Anemometers", Chapter IV, Fluid Mechanics Measurements, Hemisphere Publishing Corporation, New York, 1983.

24. Hynes, T.P. and Greitzer, E.M., "A Method for Assessing Effects of Inlet Flow Distortion on Compressor Stability", ASME Journal of Turbomachinery, Vol. 109, pp. 371-379, July 1987.

25. Ljung, L., System Identification - Theory for the User, Prentice Hall, New Jersey, 1987.

26. Chue, R., Hynes, T.P., Greitzer, E.M., Tan, C.S., and Longley, J.P., "Calculation of Inlet Distortion Induced Compressor Flow Field Instability", International Journal of Heat and Fluid Flow, Vol. 10, No. 3, pp. 211-233, September 1986.

27. Longley, J.P., unpublished notes.

28. Nagano, S., Machida, Y., and Takata, H., "Dynamic Performance of Stalled Blade Rows", Japan Society of Mechanical Engineers Paper #JSME 11, presented at Tokyo Joint International Gas Turbine Conference, Tokyo, Japan, October 1971.

29. Mazzawy, R.S., "Multiple Segment Parallel Compressor Model for Circumferential Flow Distortion", ASME Journal of Engineering for Power, Vol. 99, pp. 228-246, April 1977.

30. Hendricks, G.J. and Gysling, D.L., "A Theoretical Study of Sensor-Actuator Schemes for Rotating Stall Control", AIAA Paper 92-3486, 1992.

31. Åström, K.J., and Wittenmark, B., Computer Controlled Systems - Theory and Design, Prentice-Hall, New Jersey, 1984.

32. Hendricks, G.J., personal communication, 1992.

33 Greitzer, E.M., "Surge and Rotating Stall in Axial Flow Compressors, Part I: Theoretical Compression System Model", ASME Journal of Engineering for Power, Vol. 98, pp. 190-198, April 1976.

APPENDIX A

Data Collection Log

This appendix provides a log of the dates and conditions associated with the collection of the experimental data presented in this thesis. The PID servo-controller settings and the analog-to-digital signal converter, A/D, were the only things changed in the equipment configuration over the course of the experiments. It was verified that the identification of the open-loop compressor dynamics was not influenced by the change in servo settings. In Table 4.1 the PID settings which gave the blades an underdamped servo response are notated with a 1, and the PID settings which gave the blades a nearly critically damped response are notated with a 2. The A/D manufactured by Metrabyte had a 2^{12} bit resolution while the one manufactured by Analogic had a 2^{16} bit resolution. The increased signal resolution was anticipated to improve sensing of modal disturbances, but no improvements in the closed-loop stalling flow coefficient were observed as a result of this equipment change. Section 2.6.1 notes the changes in ϕ_{stall} between experiments. It is important to note that although there were measurable variations in ϕ_{stall} from one experiment to another, the variations were not so large in the course of a single experiment.

Experiment Number	Date	T_{amb} °F	P_{amb} in. Hg	ϕ_{stall}	Servo-Dynamics	A/D	Data Set Figure #
4	03/26/91	77	30.24	0.469	1	Metrabyte	5.18-19
6	04/05/91	83	30.15	0.470	1	Metrabyte	5.7
7	04/10/91	76	29.70	0.469	1	Metrabyte	5.7
11	07/10/91	84	29.86	0.465	1	Metrabyte	4.1, 6-8; B.3-4
12	07/22/91	86	30.05	0.463	2	Metrabyte	5.11
13	08/06/91	80	30.19	0.461	2	Metrabyte	5.12
16	08/23/91	86	30.13	0.460	2	Metrabyte	4.2-4, 6-10; 5.17; B.5-14
23	06/18/92	81	30.20	0.460	2	Analogic	B.1-2
25	06/25/92	81	29.67	0.463	2	Analogic	B.17-18, 23-24; 5.1-5, 13, 20-21
26	06/29/92	84	29.97	0.462	2	Analogic	5.4-5; B.15-16, 19-22, 25-26
28	07/02/92	79	29.97	0.460	2	Analogic	5.14
29	07/03/92	80	30.15	0.461	2	Analogic	5.15
30	07/05/92	78	29.93	0.461	2	Analogic	5.16, 22-23
31	07/06/92	79	29.80	0.460	2	Analogic	5.24-31
32	07/08/92	83	30.12	0.460	2	Analogic	5.6

Table A.1: Data Collection Log

APPENDIX B

Additional Torque, Modal Dynamics, and Flow Field Data

This appendix contains three types of compressor data. Figure B.1 presents data at several SGV stagger angles for the true torque which quantify the work done by the rotor blades on the flow. This same set of data is presented in Figure B.2 in the form of an isentropic pressure rise coefficient ψ_T, defined in Equation 3.1. It is from this data that $\frac{\partial \psi_T}{\partial \gamma}$ can be determined; Table 3.1 gives the functional form of $\frac{\partial \psi_T}{\partial \gamma}$ that was derived using this data set. The second set of data, Figures B.3 through B.14, is a more thorough documentation of the measured open-loop compressor dynamics than was given in Chapter 4. The set of data include measurements of $\hat{\Theta}_n$ at 6% and 2% above ϕ_{stall} and 2% and 6% below ϕ_{stall} for each of the first three modes. It can be observed in the data that the stability of each mode decreased with decreasing ϕ. The last set of data documents the radial variations in the stall inception flow field during optimal first and second mode control and during no control. Figures B.15 through B.26 show both the velocity traces and the SFC's for the flow field at 20%, 50%, and 80% of the radial height of the compressor duct. These figures are discussed in Chapter 5.

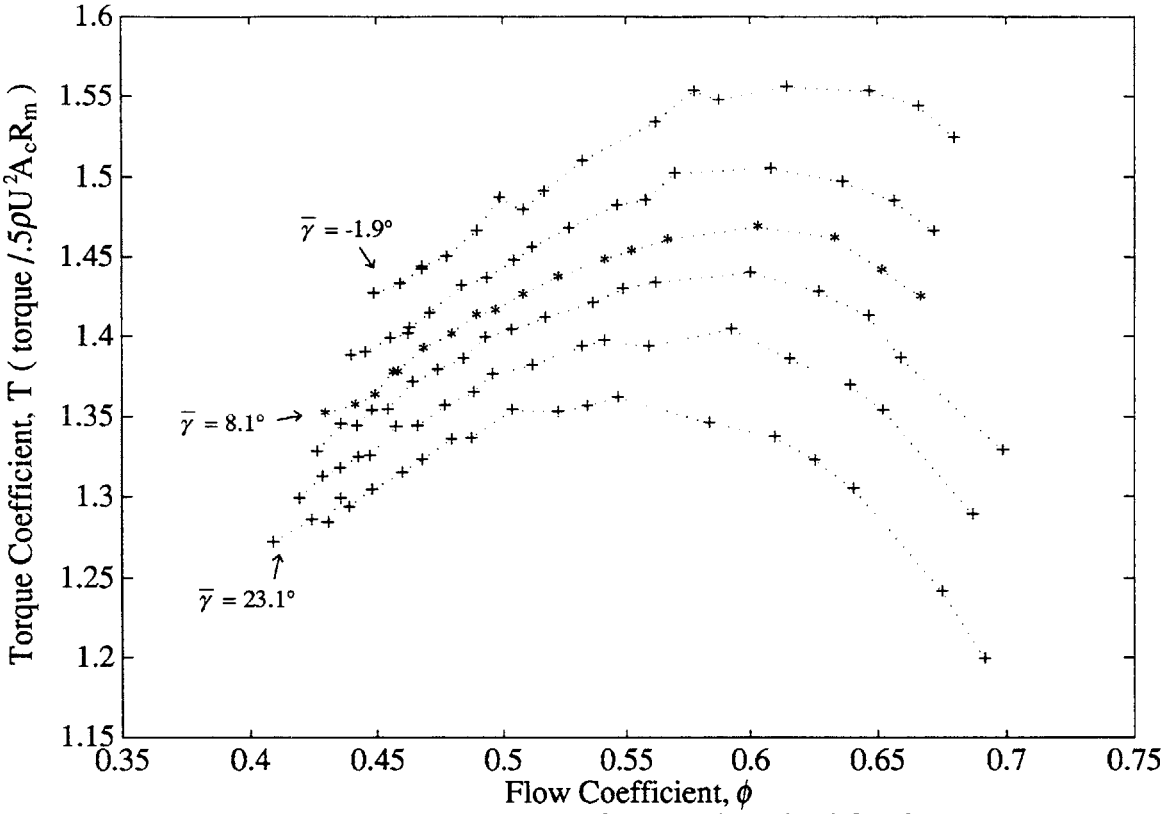

Figure B.1: Compressor Torque Characteristic for SGV Stagger Angles Ranging from -1.9° to 23.1° in 5° Intervals

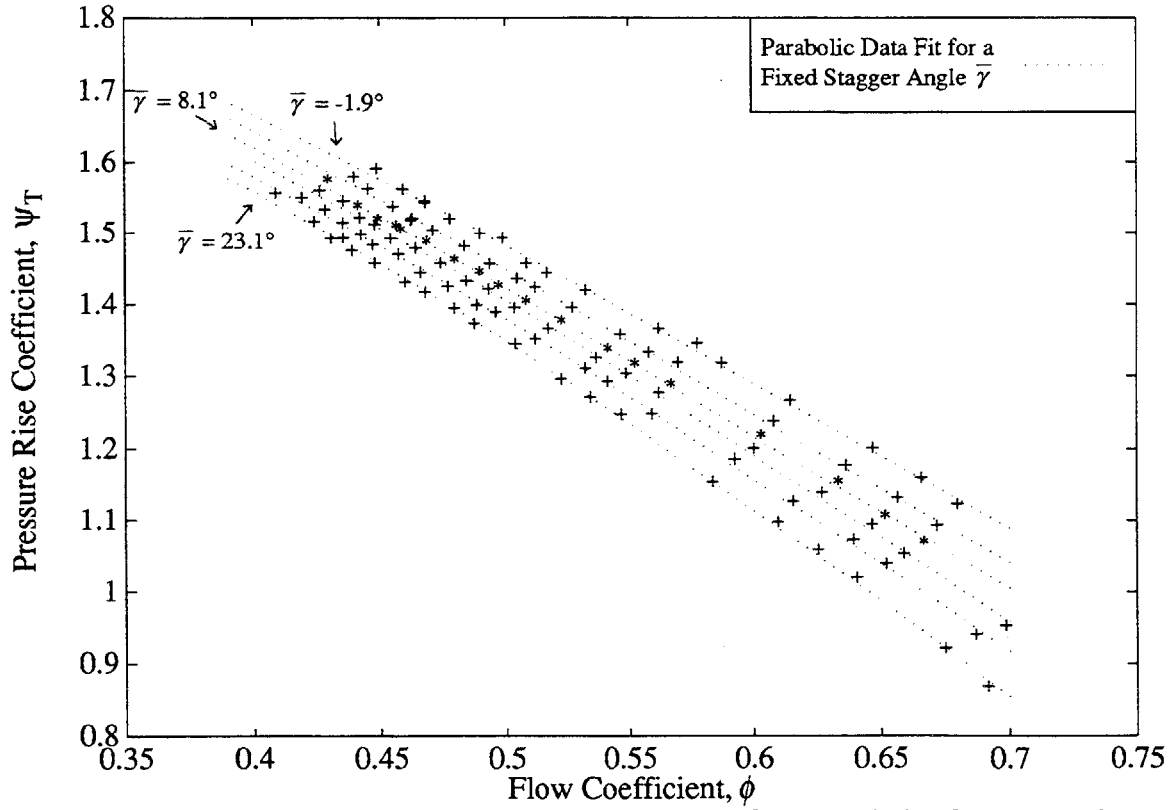

Figure B.2: Compressor Isentropic Pressure Rise Characteristic, Calculated from Torque Characteristic, for SGV Angles Ranging from -1.9° to 23.1° in 5° Intervals

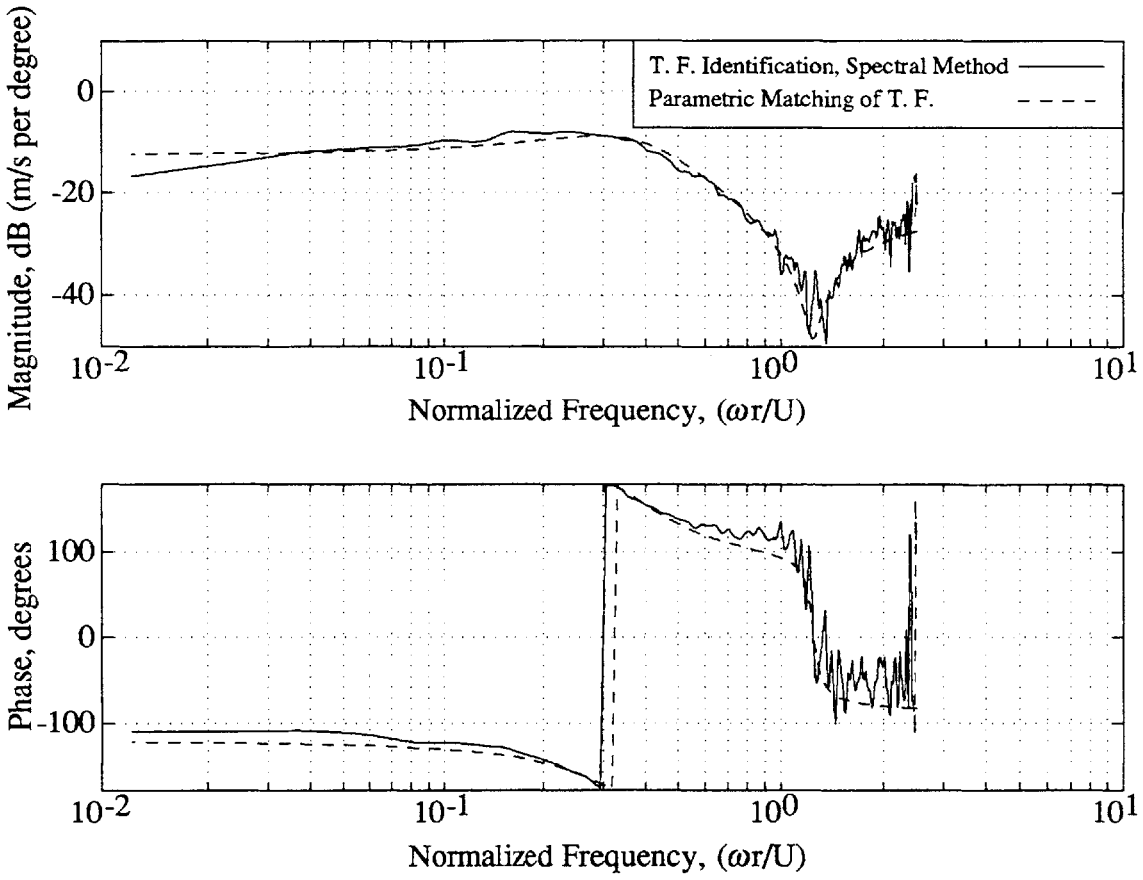

Figure B.3: Estimate of Compressor Transfer Function for Mode 1 at $\phi = .49$ (6% above the stalling flow coefficient)

$$\hat{\Theta}_1(.49) = [\ -.184 \quad .329 \quad -.0709 \quad .00280 \quad -.0573\ ]$$

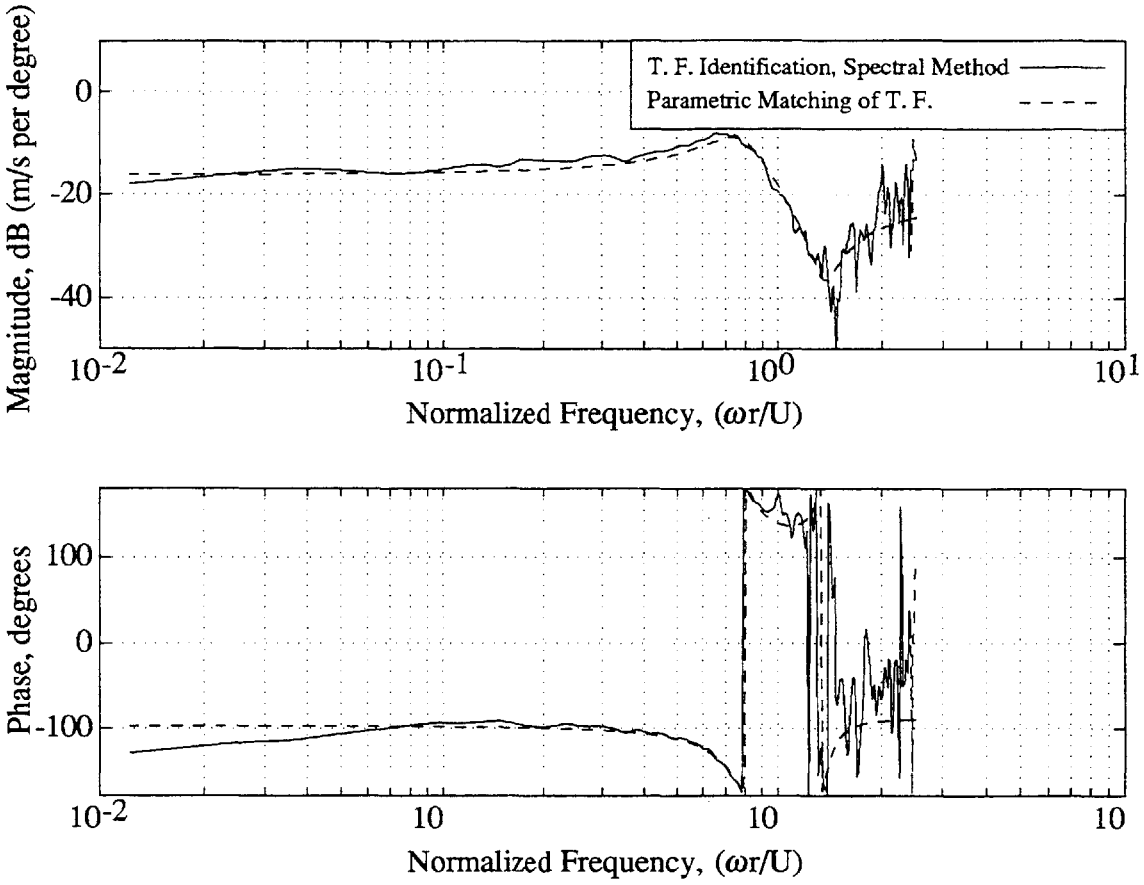

Figure B.4: Estimate of Compressor Transfer Function for Mode 1 at $\phi = .47$ (2% above the stalling flow coefficient)

$$\hat{\Theta}_1(.47) = [\,-.0613 \quad .313 \quad -.0600 \quad .00203 \quad -.0506\,]$$

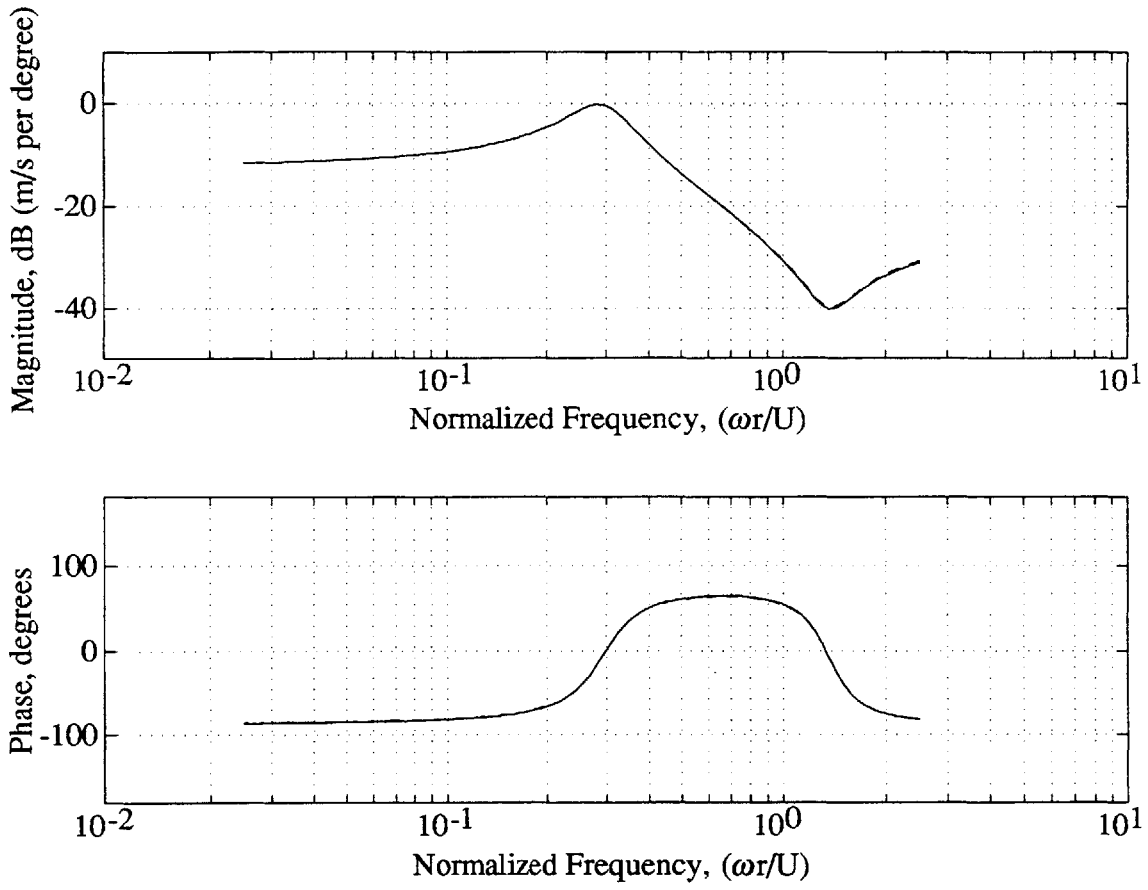

Figure B.5: Estimate of Compressor Transfer Function for Mode 1 at $\phi = .45$ (2% below the stalling flow coefficient)

$$\hat{\Theta}_1(.45) = [\ .0576 \quad .286 \quad -.0565 \quad .00844 \quad -.0421\ ]$$

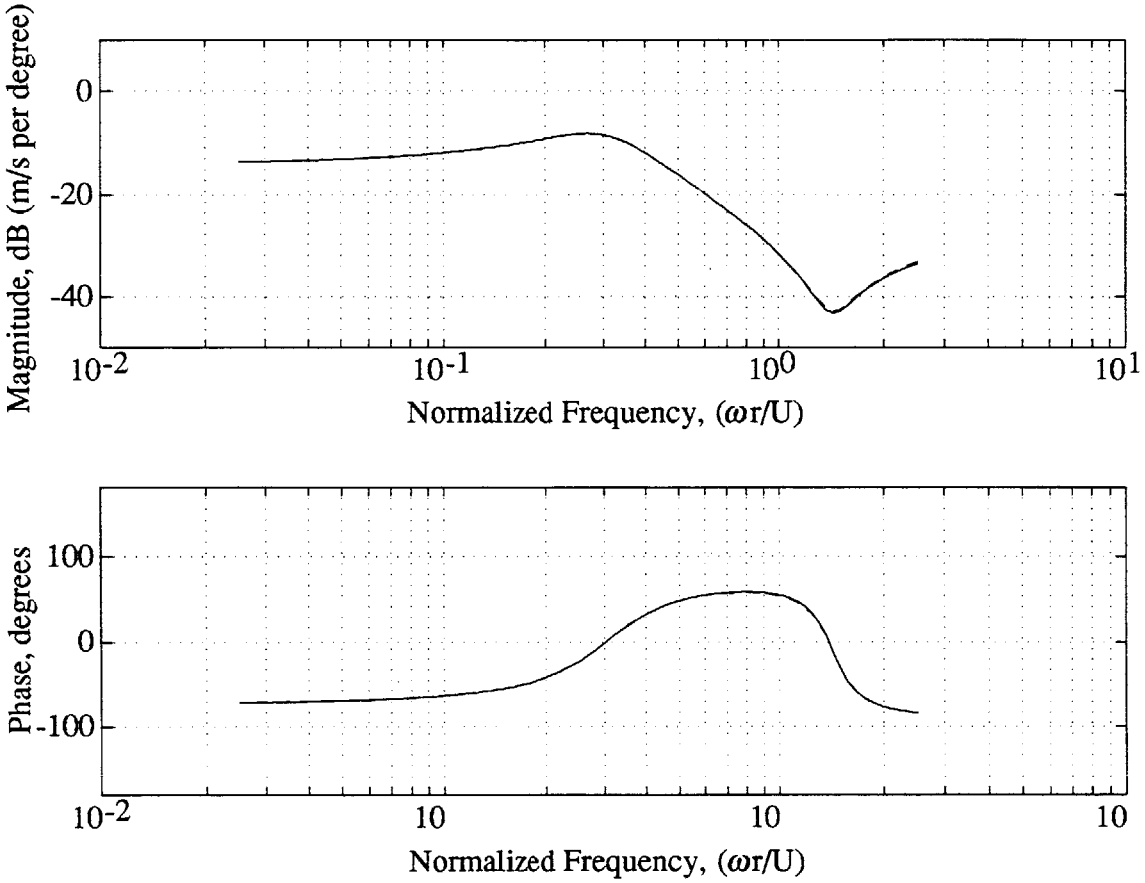

Figure B.6: Estimate of Compressor Transfer Function for Mode 1 at $\phi = .43$ (6% below the stalling flow coefficient)

$$\hat{\Theta}_1(.43) = [\ .124 \quad .282 \quad -.0475 \quad .00625 \quad -.0337\ ]$$

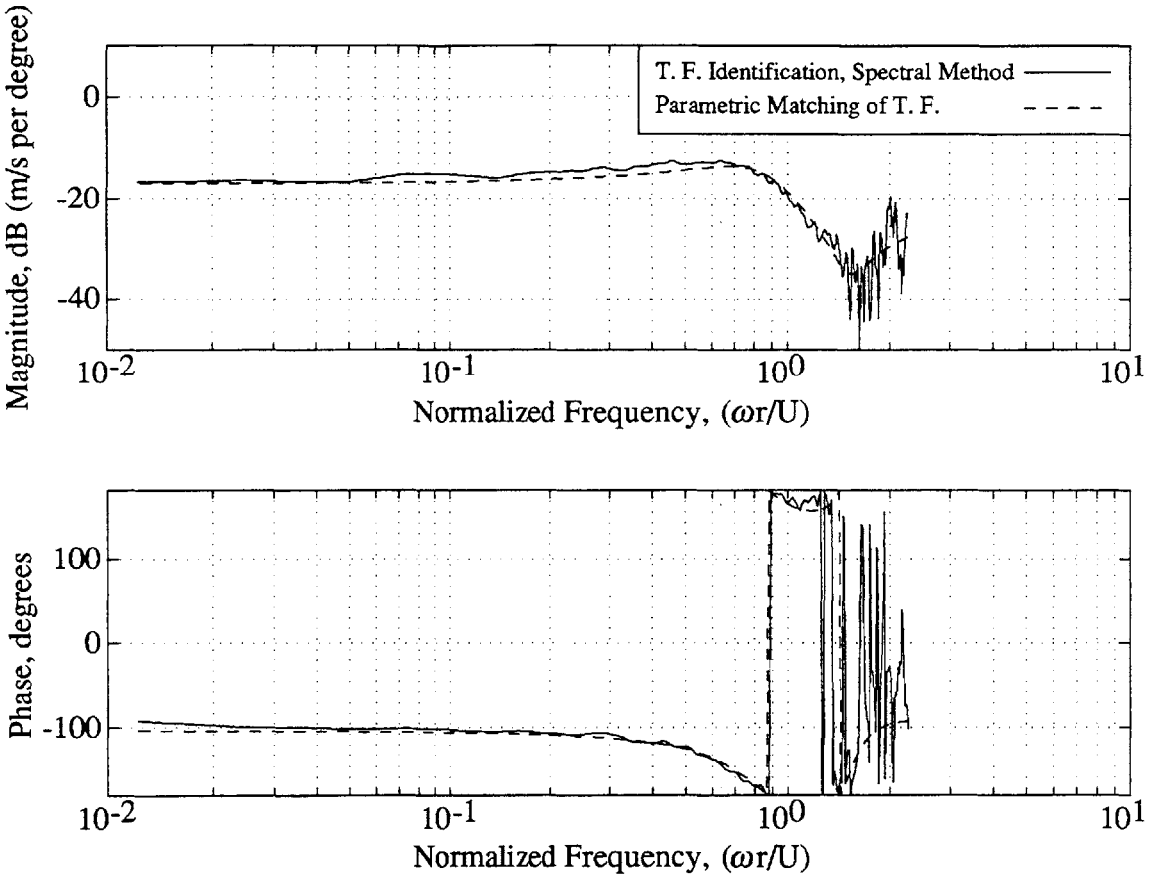

Figure B.7: Estimate of Compressor Transfer Function for Mode 2 at $\phi = .49$ (6% above the stalling flow coefficient)

$$\hat{\Theta}_2(.49) = [\ -.298 \quad .794 \quad -.0950 \quad -.0113 \quad -.0631\ ]$$

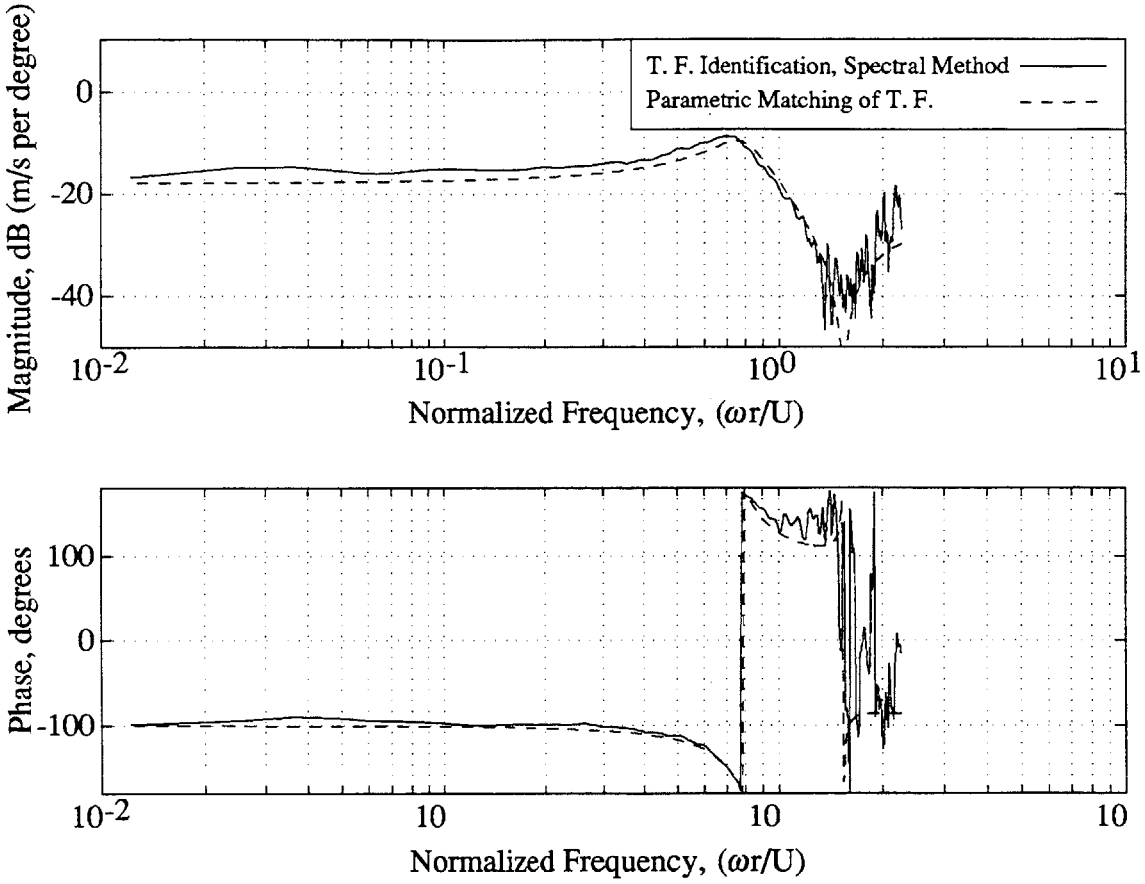

Figure B.8: Estimate of Compressor Transfer Function for Mode 2 at $\phi = .47$ (2% above the stalling flow coefficient)

$$\hat{\Theta}_2(.47) = [\,-.150 \quad .768 \quad -.0806 \quad -.00364 \quad -.0526\,]$$

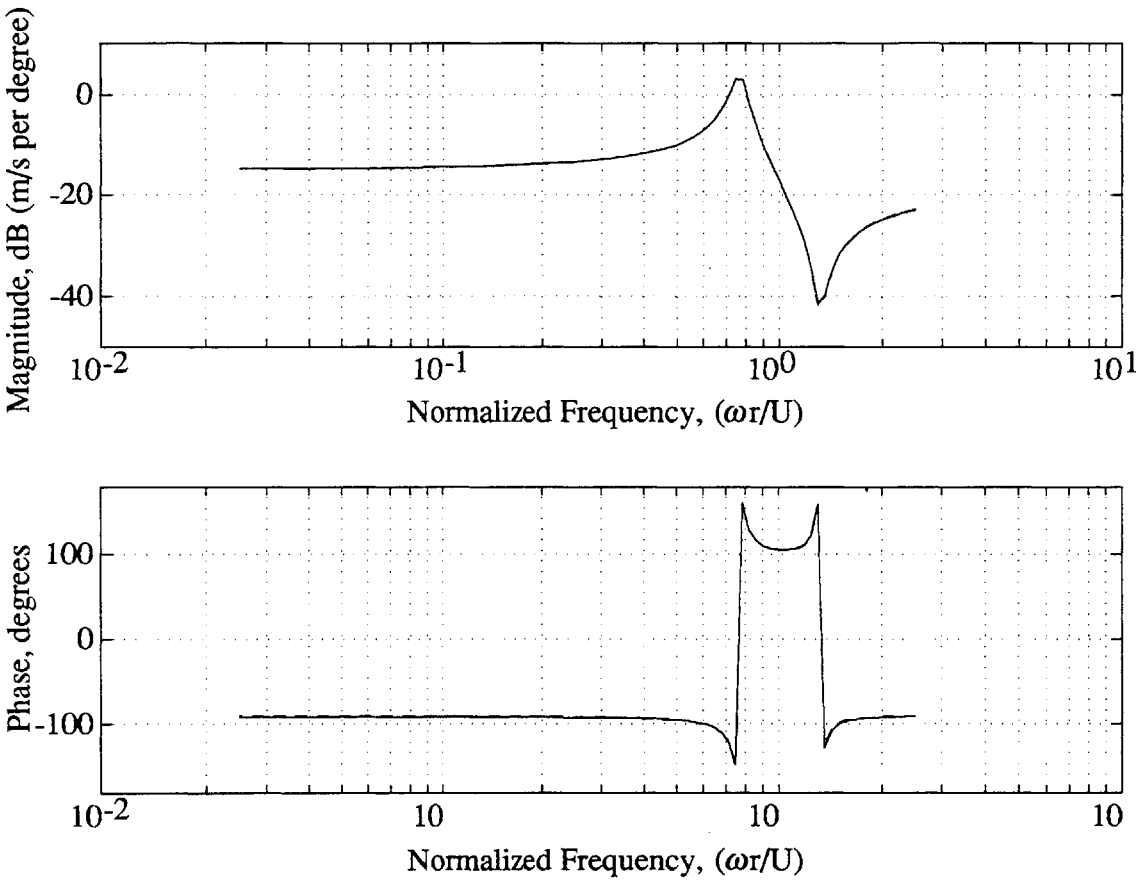

Figure B.9: Estimate of Compressor Transfer Function for Mode 2 at $\phi = .45$ (2% below the stalling flow coefficient)

$$\hat{\Theta}_2(.45) = [\ -.0366 \quad .766 \quad -.109 \quad -.00319 \quad -.0824\ ]$$

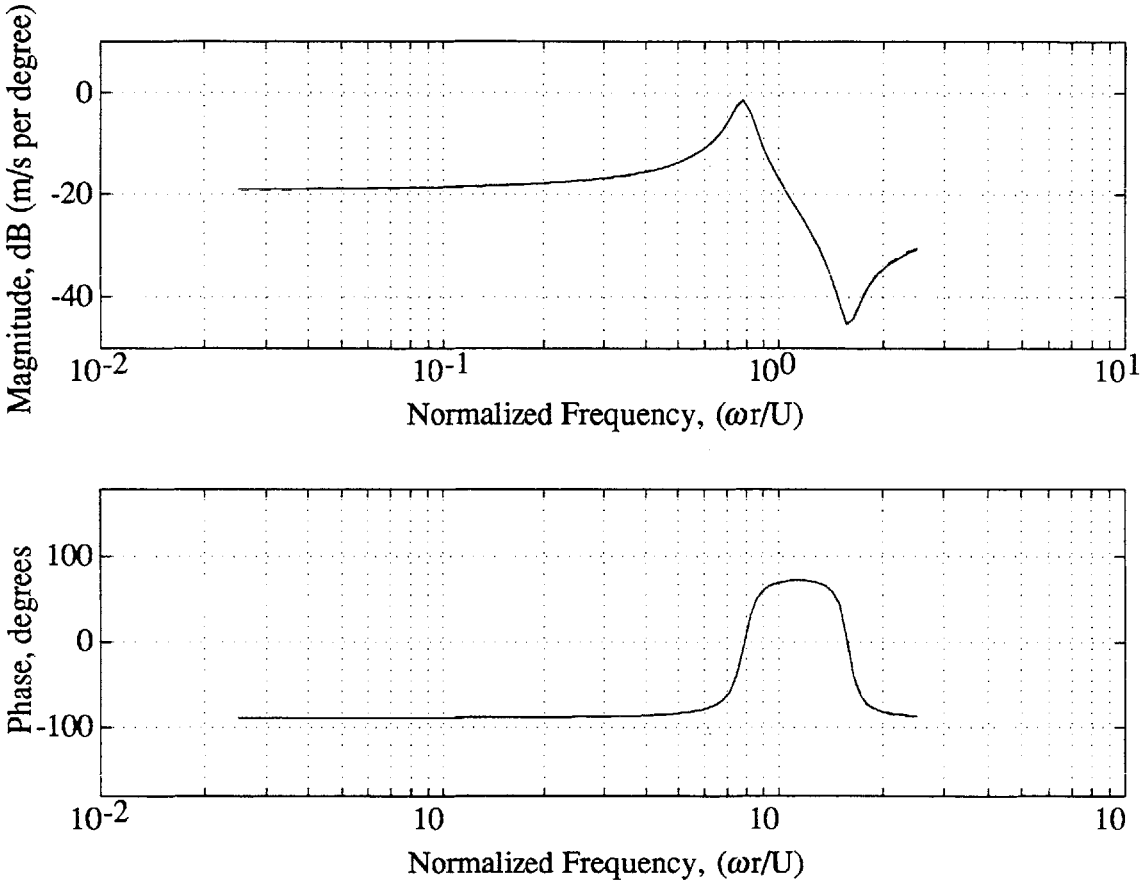

Figure B.10: Estimate of Compressor Transfer Function for Mode 2 at $\phi = .43$ (6% below the stalling flow coefficient)

$$\hat{\Theta}_2(.43) = [\ .510 \quad .781 \quad -.0684 \quad .00345 \quad -.0431\ ]$$

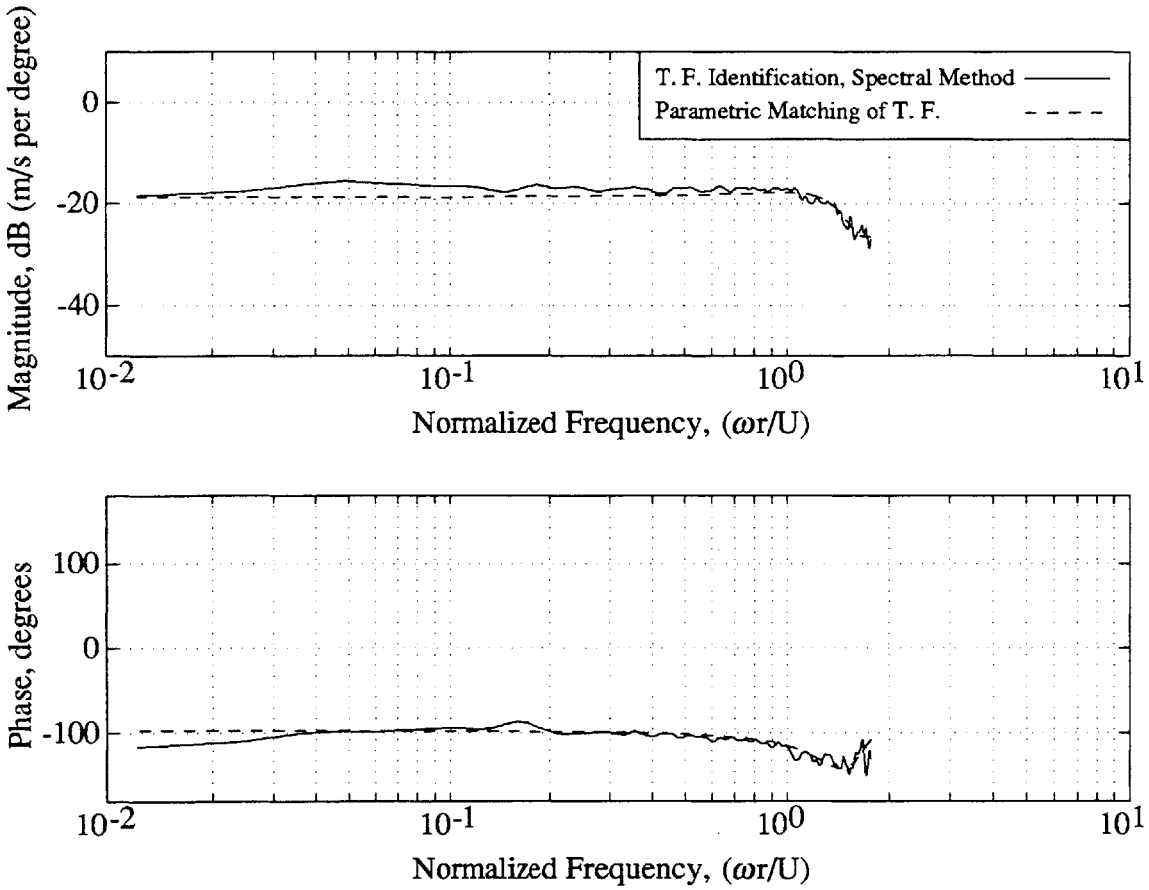

Figure B.11: Estimate of Compressor Transfer Function for Mode 3 at $\phi = .49$ (6% above the stalling flow coefficient)

$$\hat{\Theta}_3(.49) = [\, -.364 \quad 1.37 \quad -.129 \quad -.0176 \quad -.0787 \,]$$

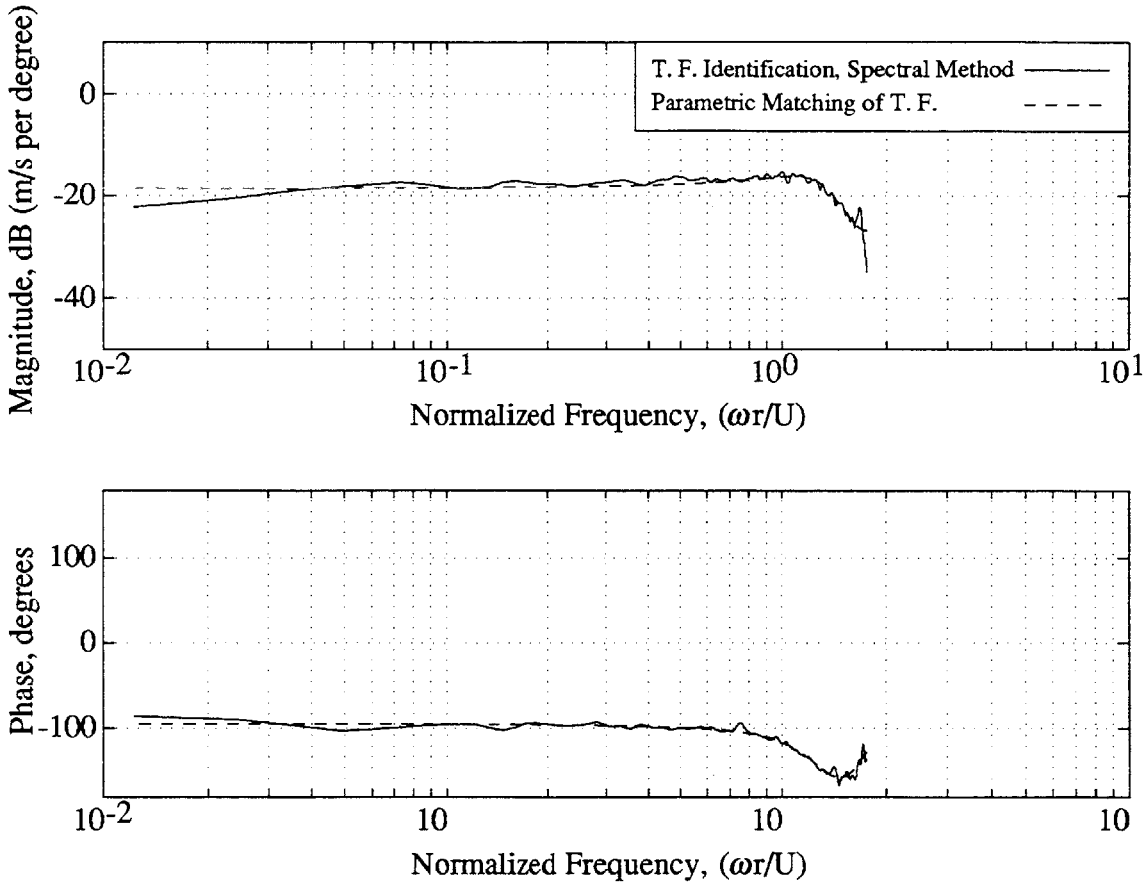

Figure B.12: Estimate of Compressor Transfer Function for Mode 3 at $\phi = .47$ (2% above the stalling flow coefficient)

$$\hat{\Theta}_3(.47) = [\,-.319 \quad 1.29 \quad -.123 \quad -.0192 \quad -.0733\,]$$

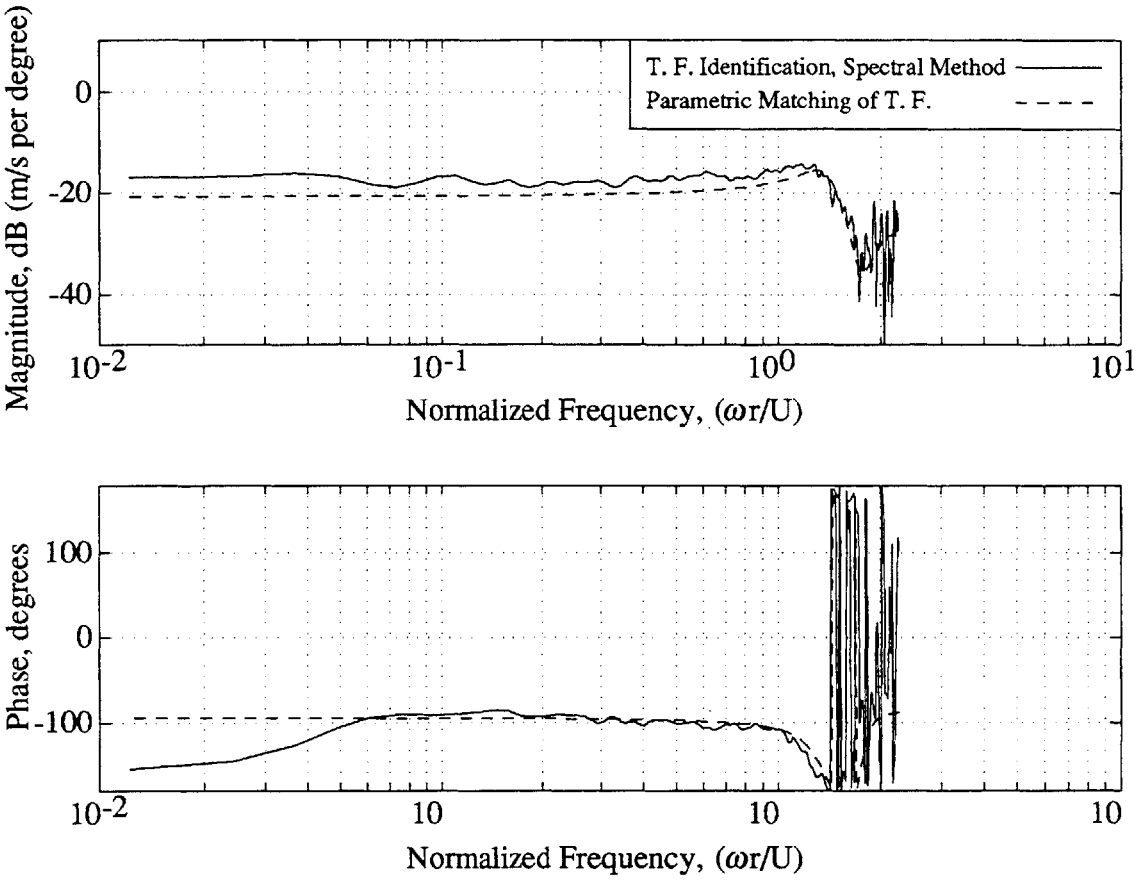

Figure B.13: Estimate of Compressor Transfer Function for Mode 3 at $\phi = .45$ (2% below the stalling flow coefficient)

$$\hat{\Theta}_3(.45) = [\,-.181 \quad 1.38 \quad -.102 \quad -.00529 \quad -.0583\,]$$

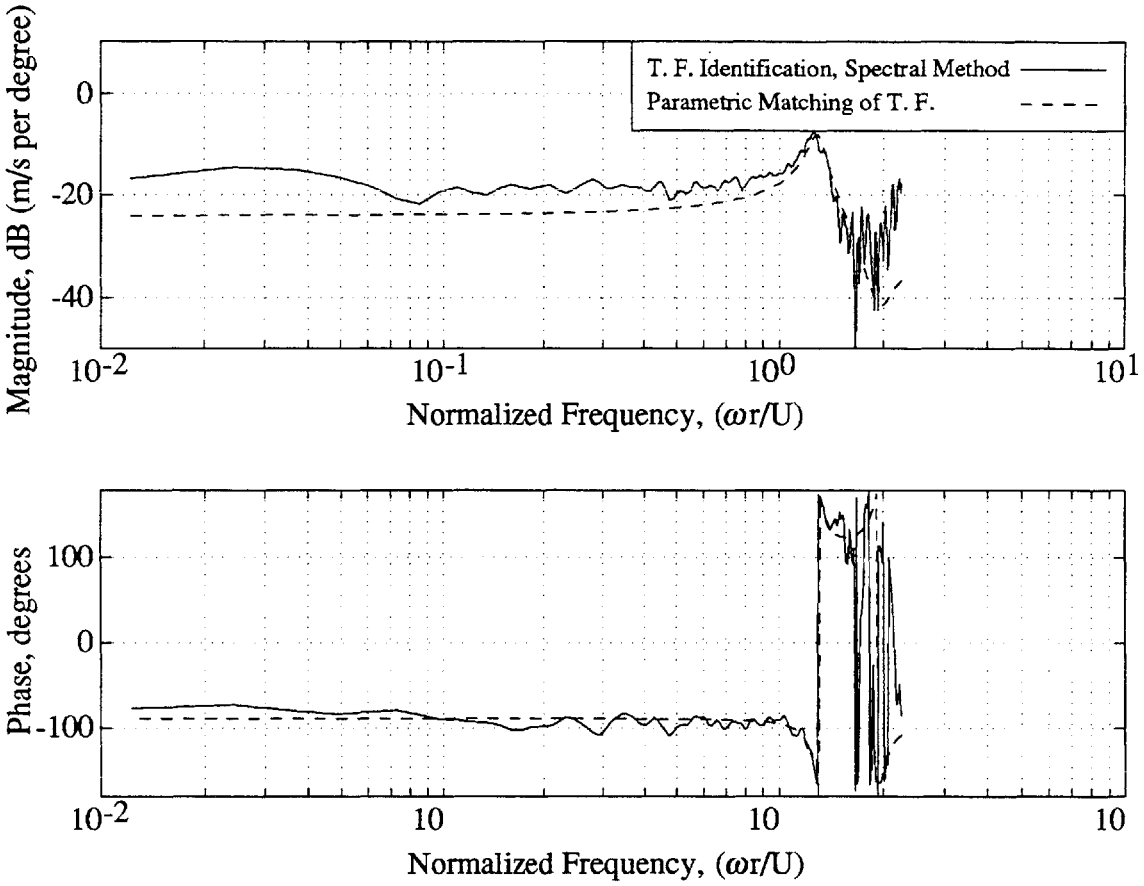

Figure B.14: Estimate of Compressor Transfer Function for Mode 3 at $\phi = .43$ (6% below the stalling flow coefficient)

$$\hat{\Theta}_3(.43) = [\ -.0960 \quad 1.30 \quad -.0651 \quad -.00668 \quad -.0327\ ]$$

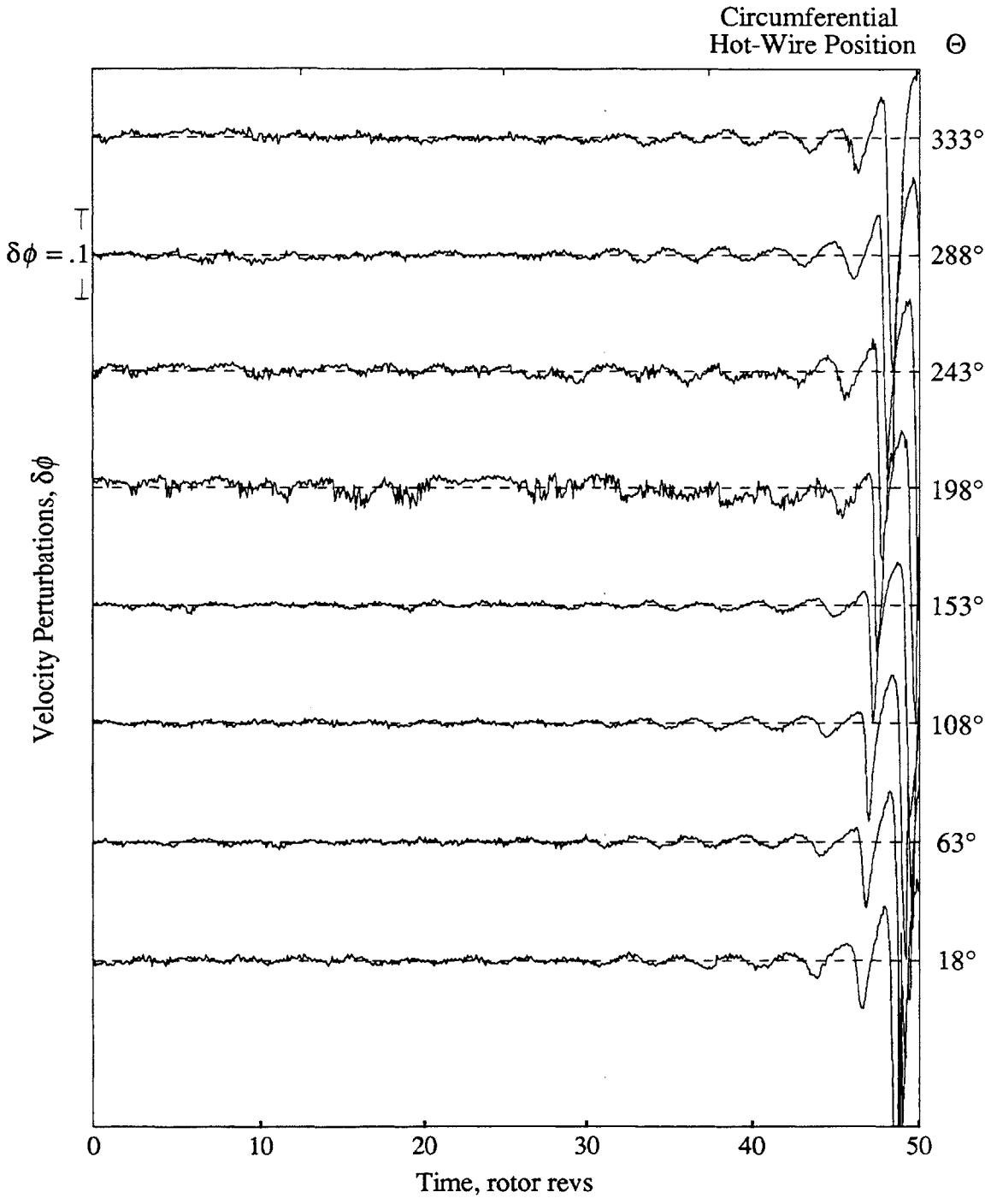

Figure B.15: Stall Inception Flow Field around Compressor Annulus at 20% Span Measured Upstream of the IGV's when $\overline{\phi} = .46$

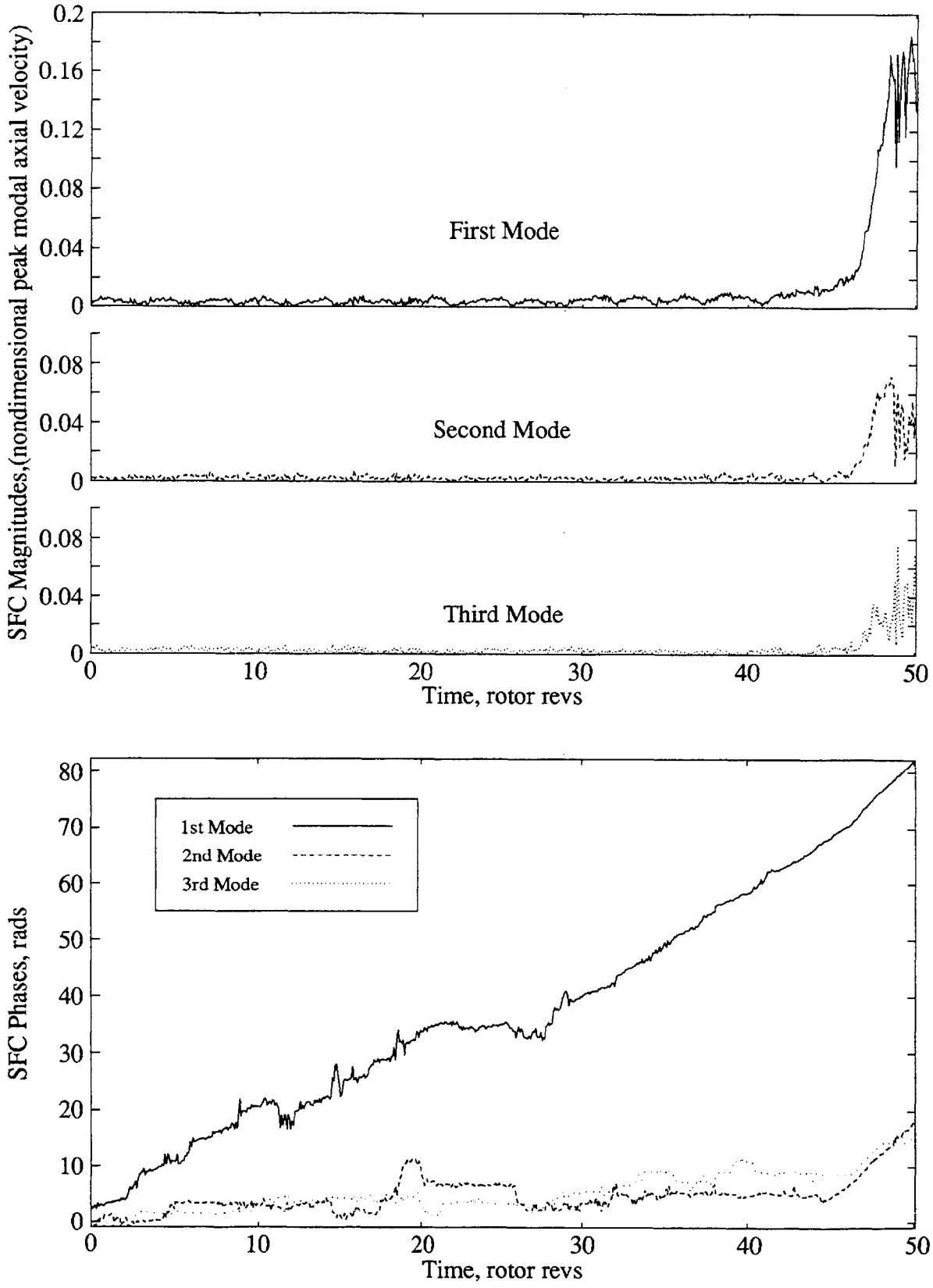

Figure B.16: Magnitude and Phases of the First Three Spatial Fourier Coefficients Calculated from the Stall Inception Flow Field at 20% Span (Data in Figure B.15)

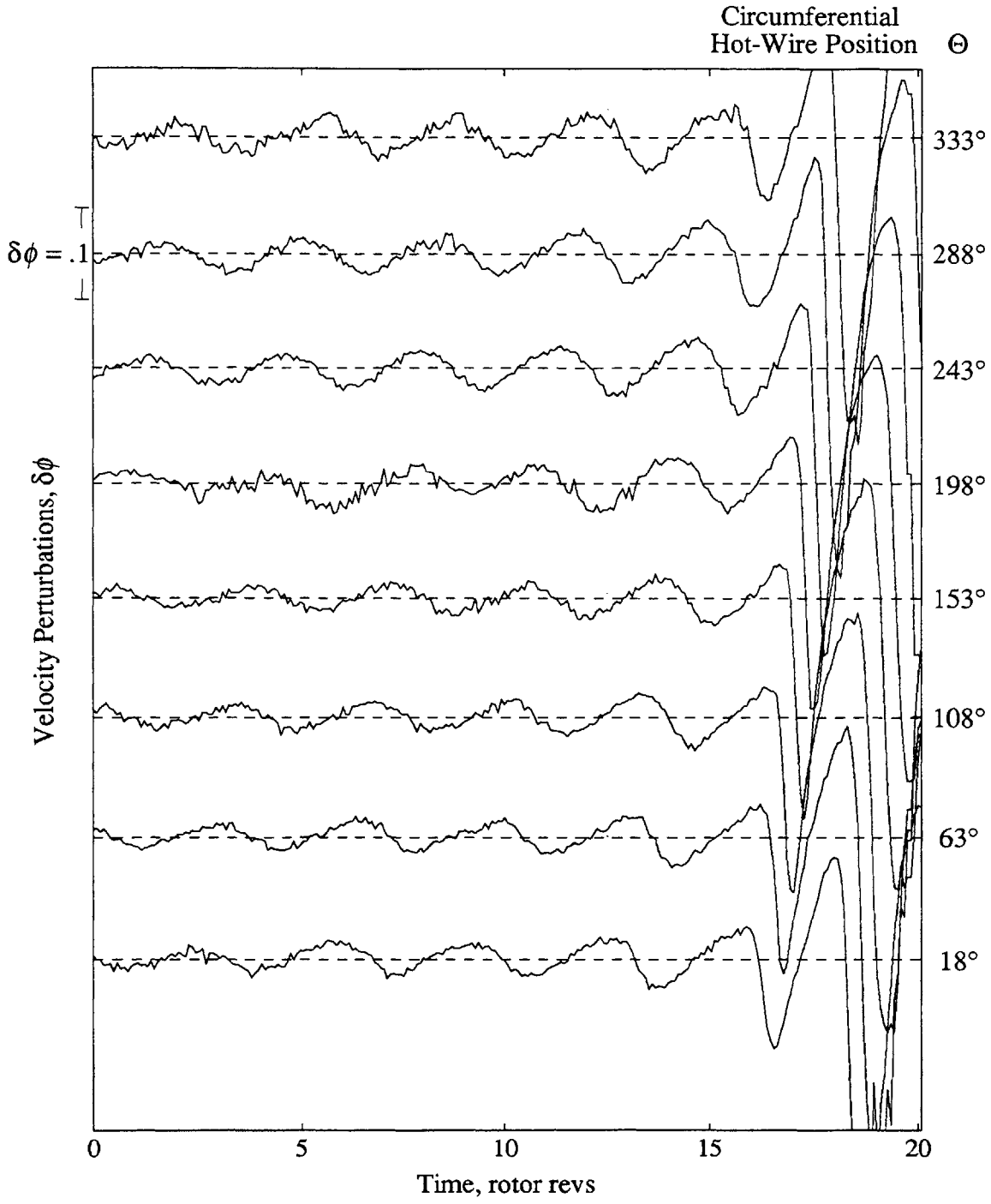

Figure B.17: Stall Inception Flow Field around Compressor Annulus at 50% Span Measured Upstream of the IGV's when $\overline{\phi} = .46$

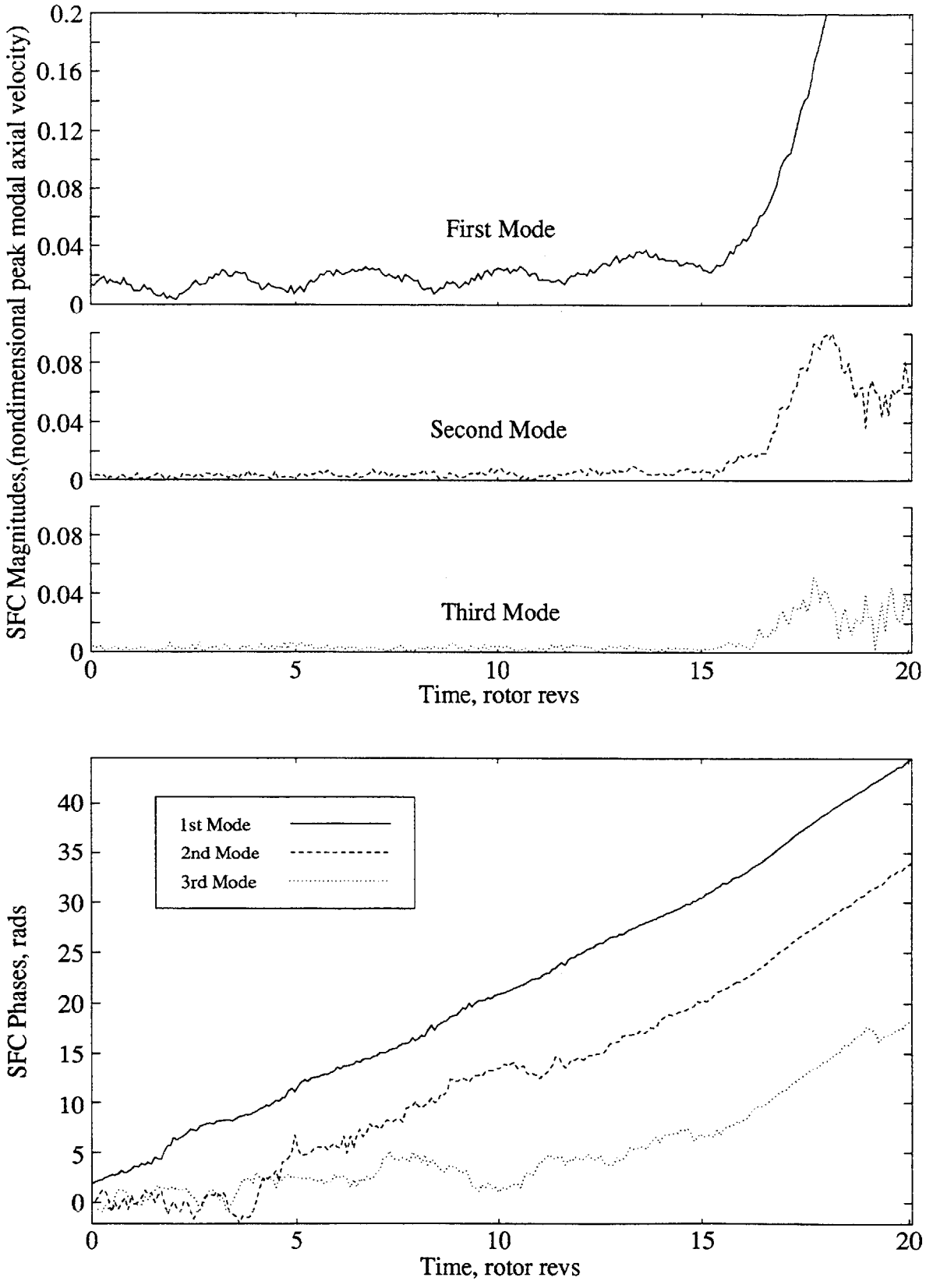

Figure B.18: Magnitude and Phases of the First Three Spatial Fourier Coefficients Calculated from the Stall Inception Flow Field at 50% Span (Data in Figure B.17)

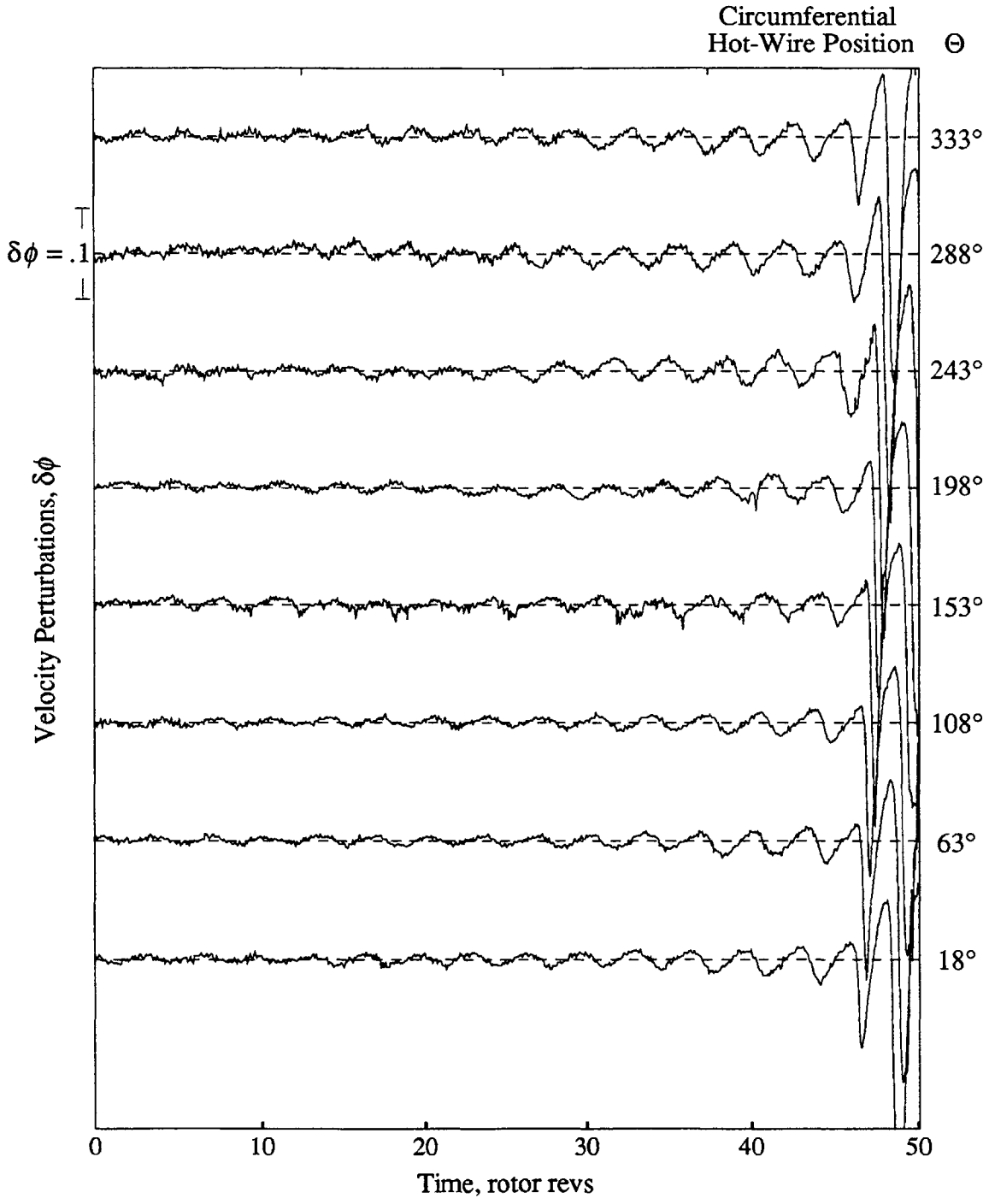

Figure B.19: Stall Inception Flow Field around Compressor Annulus at 80% Span Measured Upstream of the IGV's when $\overline{\phi} = .46$

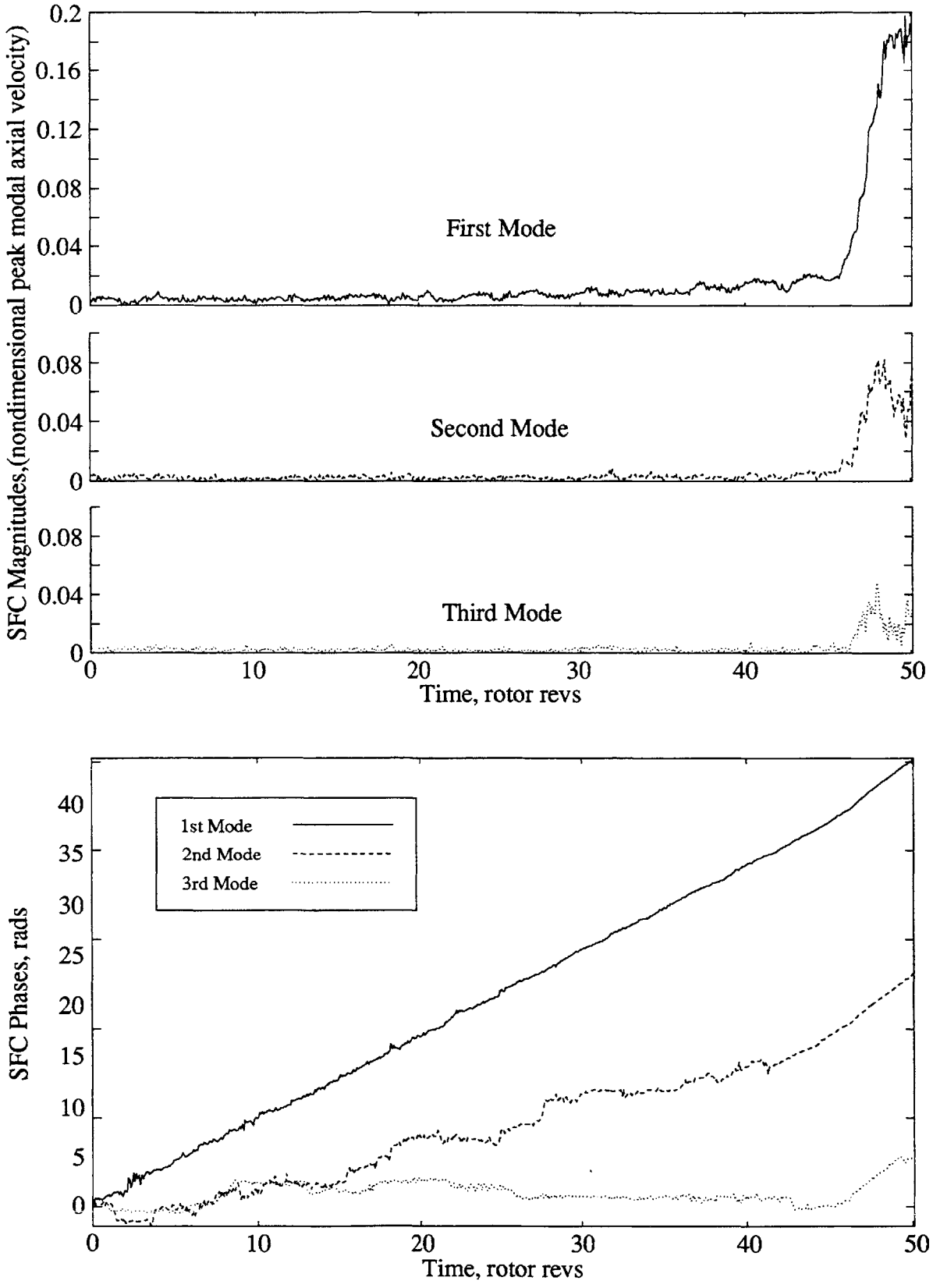

Figure B.20: Magnitude and Phases of the First Three Spatial Fourier Coefficients Calculated from the Stall Inception Flow Field at 80% Span (Data in Figure B.19)

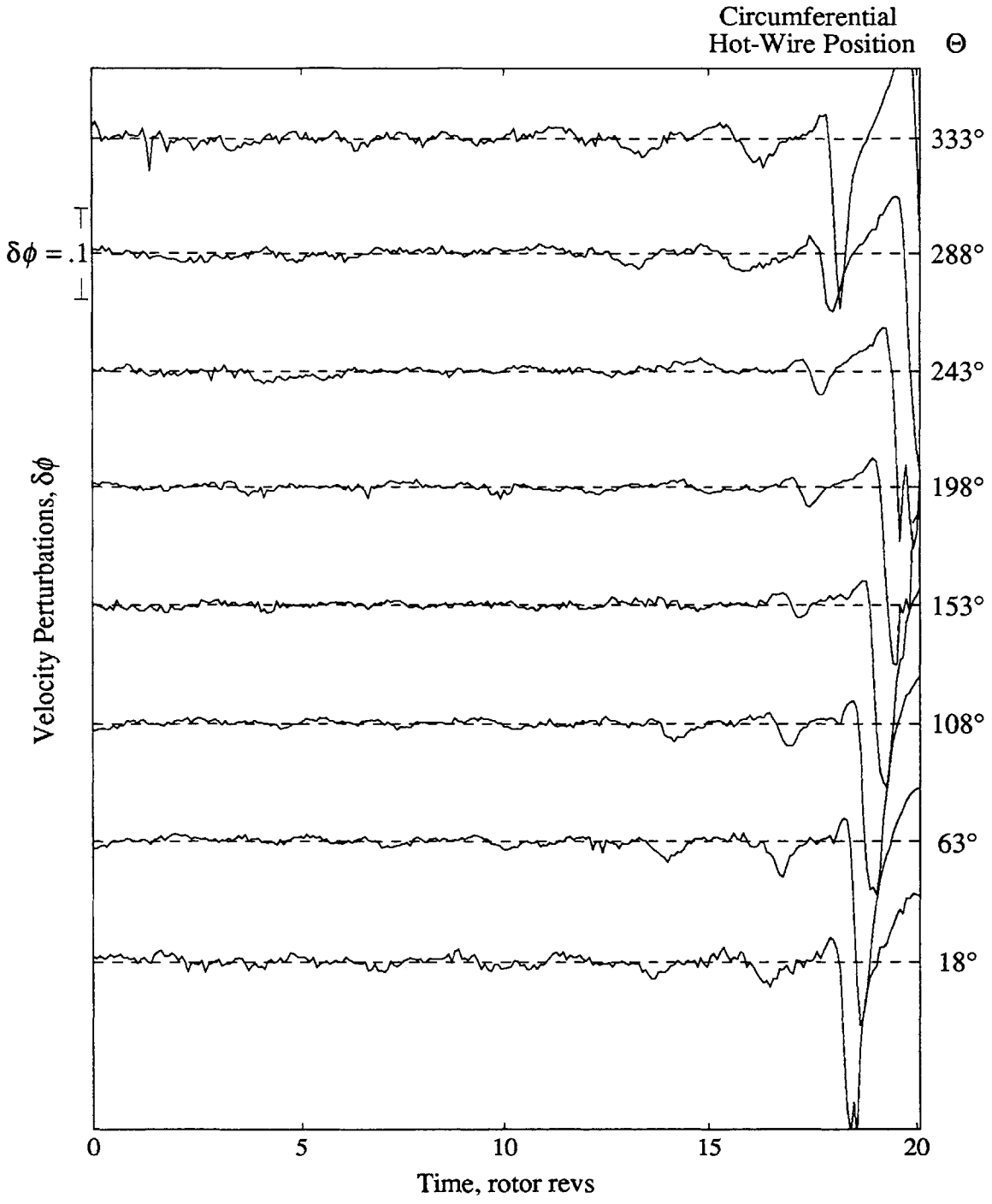

Figure B.21: Stall Inception Flow Field around Compressor Annulus at 20% Span during Optimal 1st and 2nd Mode Control Measured Upstream of the IGV's when $\overline{\phi} = .43$

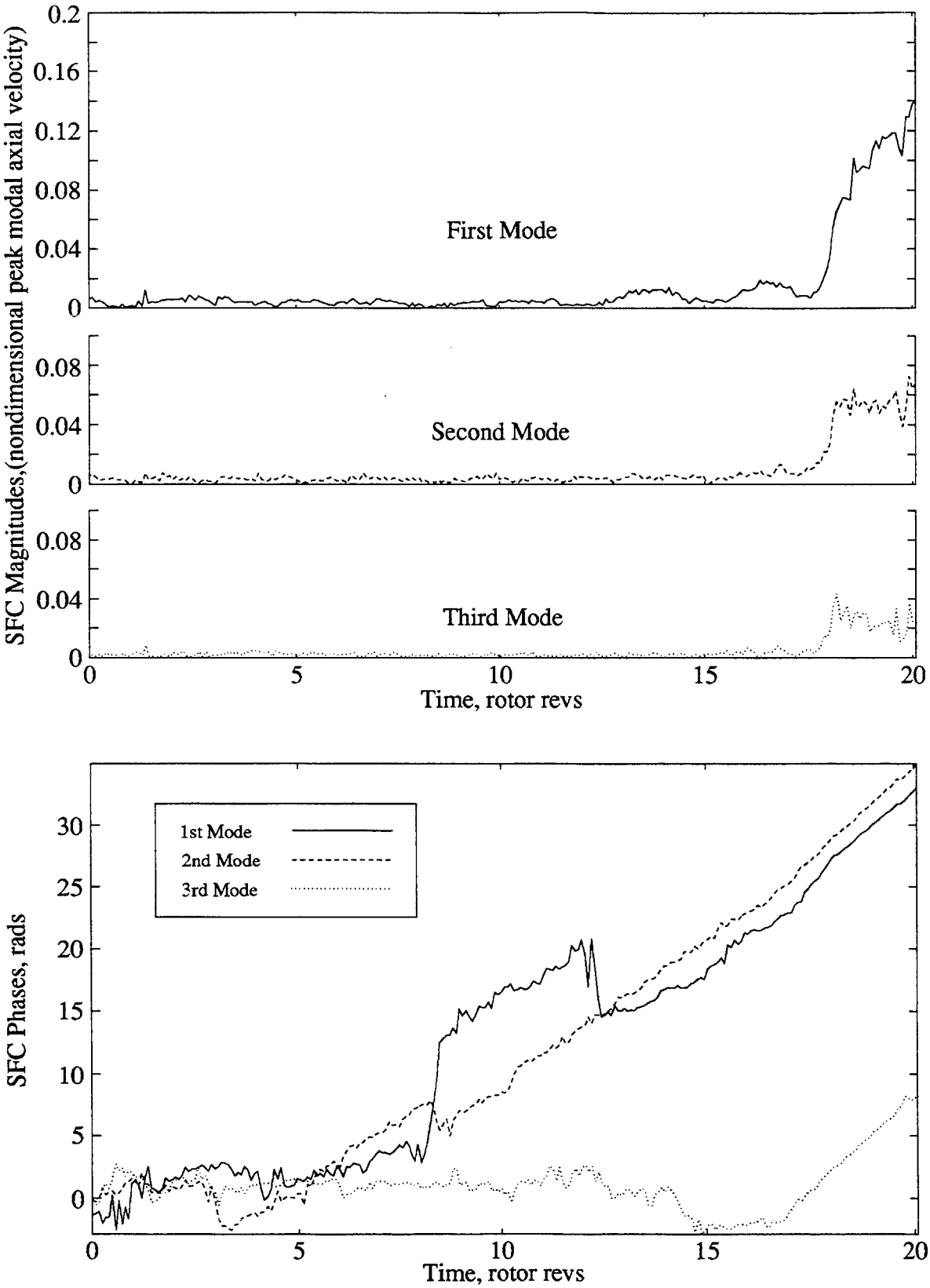

Figure B.22: Magnitude and Phases of the First Three Spatial Fourier Coefficients Calculated from the Stall Inception Flow Field at 20% Span during Optimal 1st and 2nd Mode Control (Data in Figure B.21)

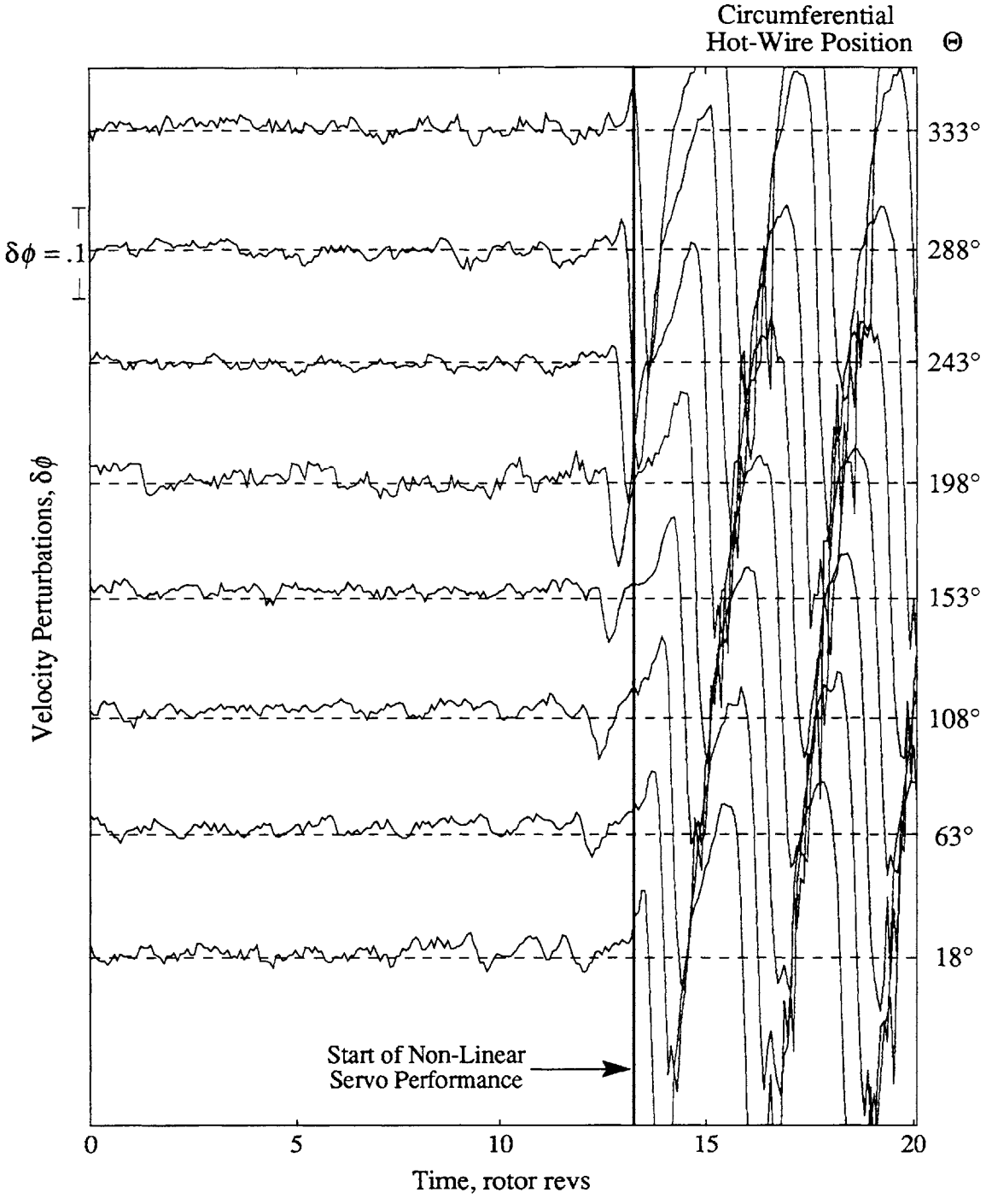

Figure B.23: Stall Inception Flow Field around Compressor Annulus at 50% Span during Optimal 1st and 2nd Mode Control Measured Upstream of the IGV's when $\overline{\phi} = .43$

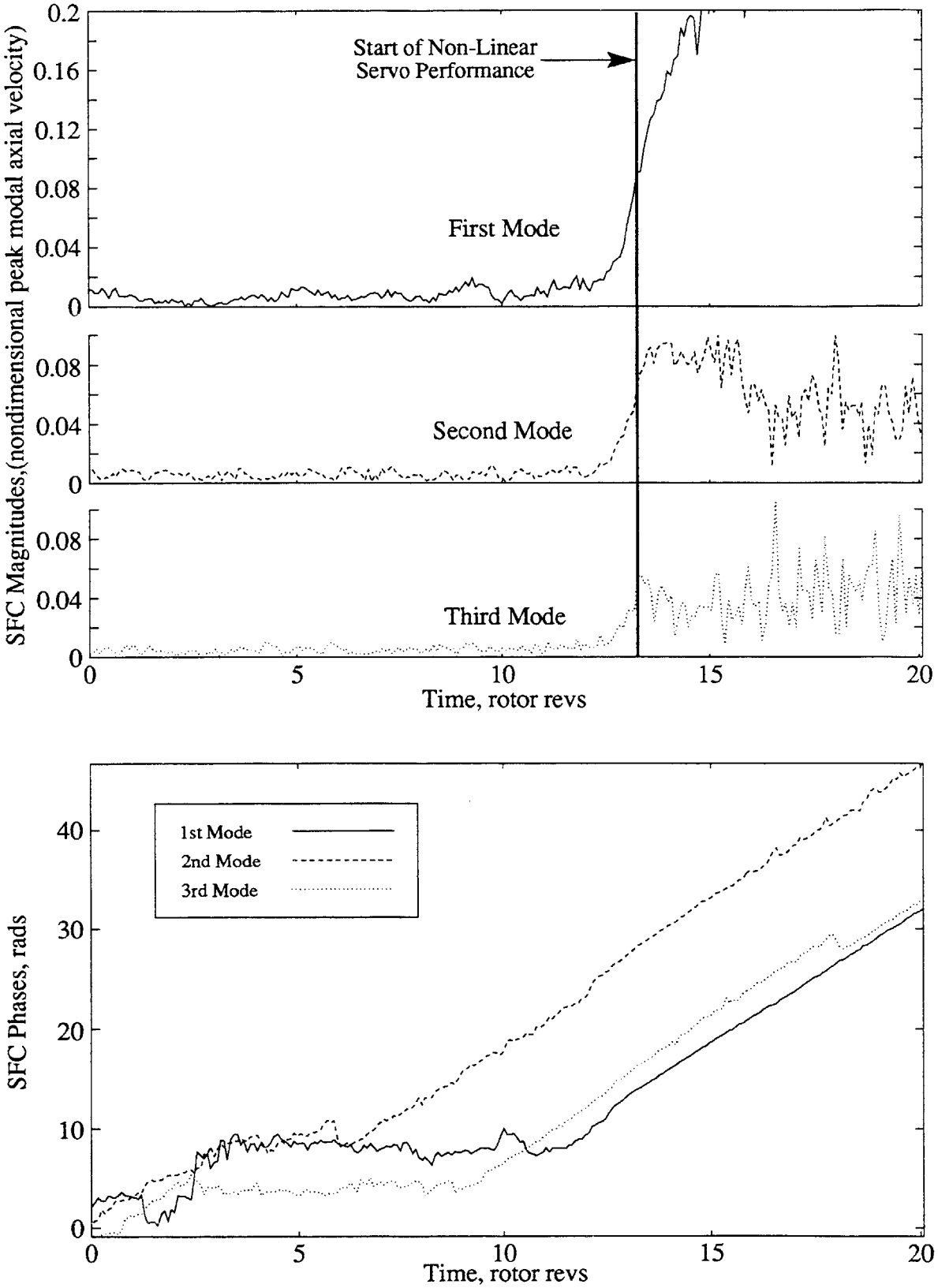

Figure B.24: Magnitude and Phases of the First Three Spatial Fourier Coefficients Calculated from the Stall Inception Flow Field at 50% Span during Optimal 1st and 2nd Mode Control (Data in Figure B.23)

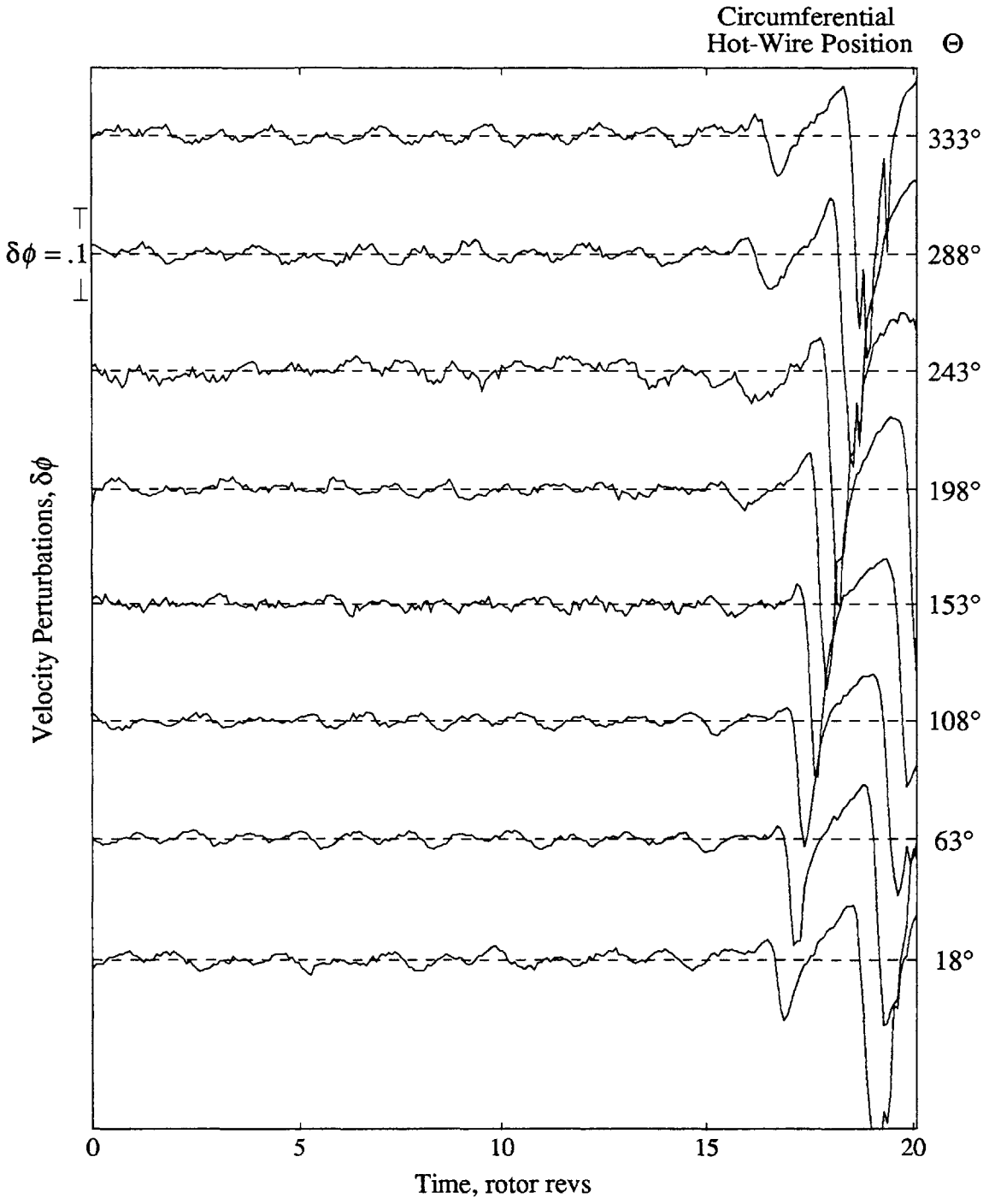

Figure B.25: Stall Inception Flow Field around Compressor Annulus at 80% Span during Optimal 1st and 2nd Mode Control Measured Upstream of the IGV's when $\overline{\phi} = .43$

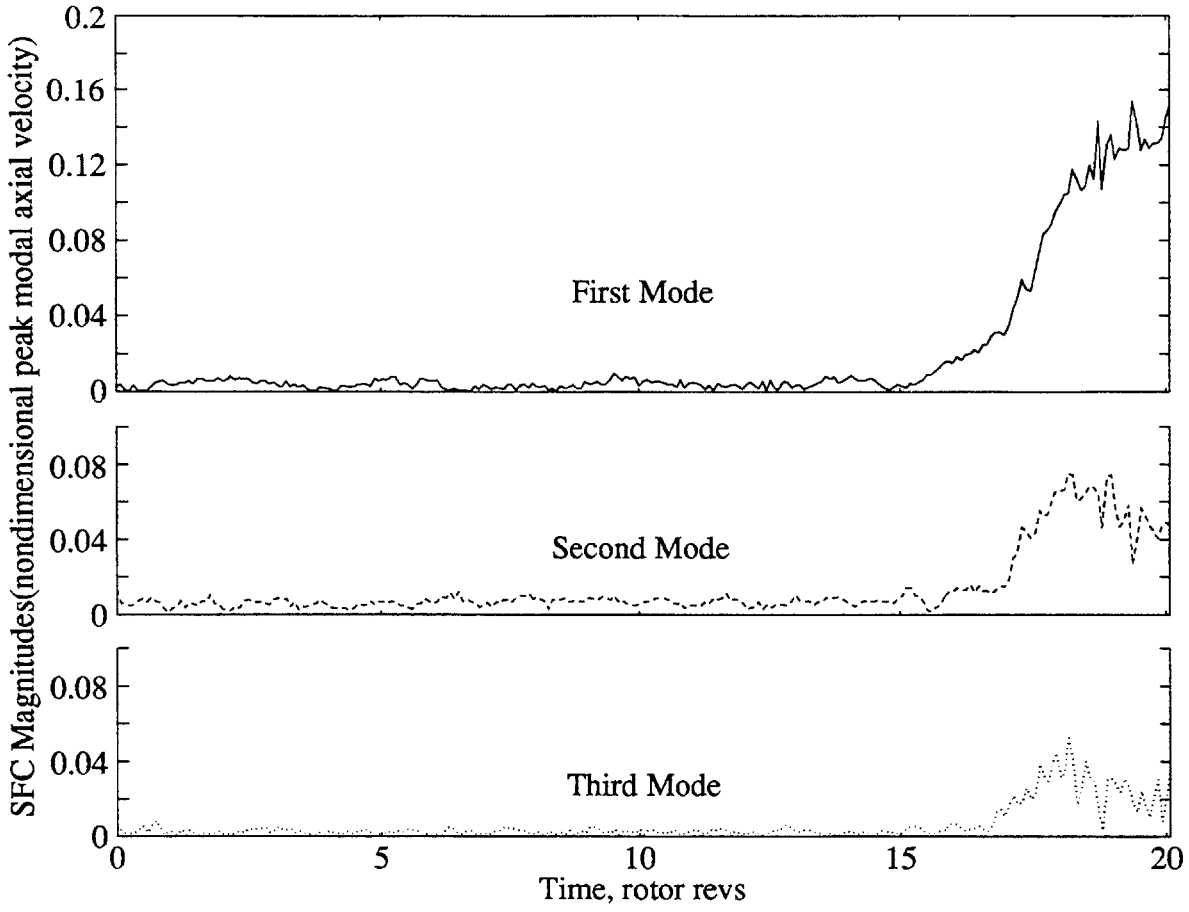

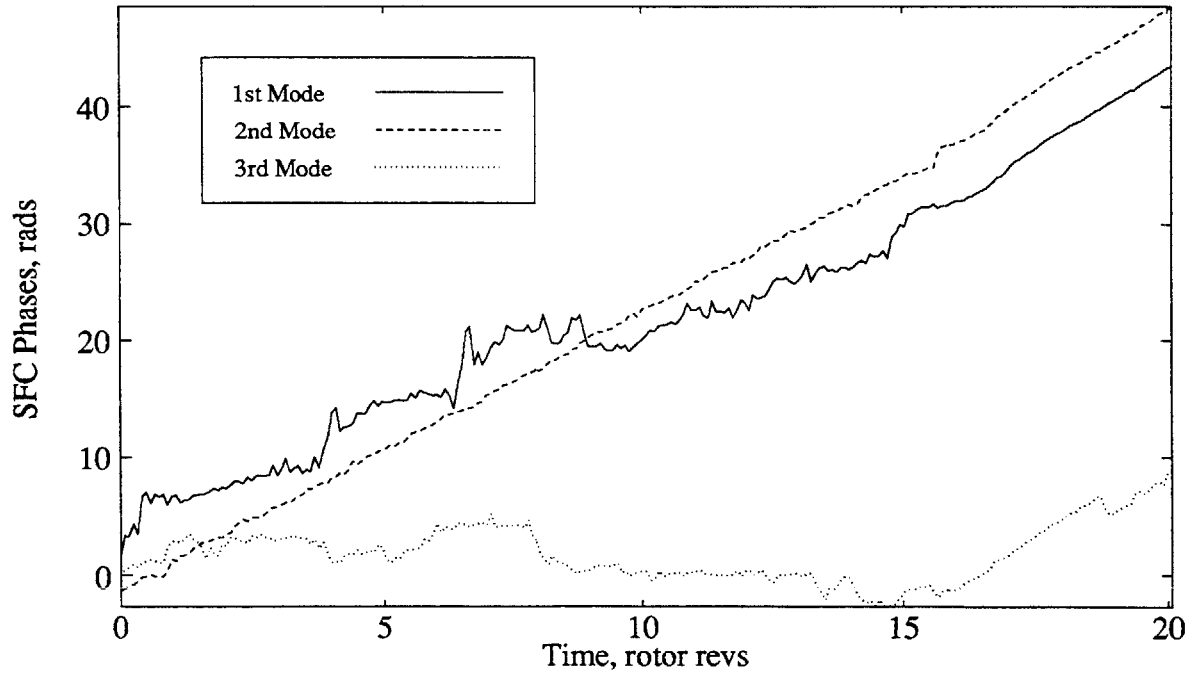

Figure B.26: Magnitude and Phases of the First Three Spatial Fourier Coefficients Calculated from the Stall Inception Flow Field at 80% Span during Optimal 1st and 2nd Mode Control (Data in Figure B.25)

APPENDIX C

Estimating the Ideal Pressure Rise Response to Flow Perturbations

An analytic expression for the instantaneous pressure rise across a blade row is needed in compressor models 3 and 4. These models are especially useful when torque data is not available for the compressor being modeled. This appendix presents the details of the analysis from which $\frac{\partial \psi_i}{\partial \phi}$ was determined.

Consider a rotor downstream of a stator or IGV row (Figure C.1). The flow field is assumed to be 2-dimensional, and flow properties are assumed match those at the mean radius. A expression for the steady-state total pressure rise across a blade row is obtained from first principles. Applying conservation of energy and conservation of angular momentum to the flow across a rotor rotating at velocity U, an expression for the rise in total pressure across the rotor can be written. In writing this it is assumed that the flow is isothermal across the rotor; hence the flow is assumed to be lossless. Additionally, it is assumed that the rotor blades have a zero incidence angle with the flow and perform perfect turning on the flow. The expression for lossless flow across a rotor with zero incidence and zero deviations is

$$\left(P_{t,2} - P_{t,1}\right) = \rho U\left(v_2 - v_1\right). \tag{C.1}$$

The change in total pressure between stations 1 and 2 is related to the change in the angular velocity between the two stations. This expression, although somewhat idealized, is treated in the models as a description of the pressure rise across a blade row immediately after a perturbation in the velocity field has occurred. After a perturbation, the boundary layers on the blades will not yet have changed and will require time to adjust to the new flow conditions. The losses associated with the new flow conditions

will also require time to change. Because of this, the instantaneous change in pressure rise can be approximated by the slope of the ideal pressure rise characteristic. The derivation below clarifies the physical reasoning accompanying this conclusion.

A perturbation in the axial velocity in the ideal rotor shown in Figure C.1 results in a perturbation in pressure rise which can be described by

$$\frac{\delta\left(P_{t,2}-P_{t,1}\right)}{\rho U}=\delta\left(v_2-v_1\right). \tag{C.2}$$

Here the instantaneous response of the blade row has been approximated to be equal to the change in the steady-state performance of the ideal blade row. Figure C.1 clarifies that the change in the flow swirl across the compressor decreases after a positive axial velocity perturbation. This decrease indicates that the total pressure rise across the compressor will decrease as well and that the slope of the pressure rise characteristic will be negative. The following steps indicate how Equation C.2 is transformed so that the right side can be written in terms of γ_R, γ_S and δC_x. The perturbation in the angular velocity is transformed as follows:

$$\frac{\delta\left(P_{t,2}-P_{t,1}\right)}{\rho U}=\left(v_2^*-v_1^*\right)-\left(v_2-v_1\right), \tag{C.3}$$

$$=\left(C_x+\delta C_x\right)\left(\tan\alpha_{R'}^*-\tan\alpha_S\right)-C_x\left(\tan\alpha_{R'}-\tan\alpha_S\right), \tag{C.4}$$

$$=C_x\left(\tan\alpha_{R'}^*-\tan\alpha_{R'}\right)+\delta C_x\left(\tan\alpha_{R'}^*-\tan\alpha_S\right). \tag{C.5}$$

The velocity triangles for the rotor before and after the perturbation are defined by the following:

$$C_x\tan\alpha_{R'}=U-C_x\tan\alpha_R,$$

$$\left(C_x+\delta C_x\right)\tan\alpha_{R'}^*=U-\left(C_x+\delta C_x\right)\tan\alpha_R. \tag{C.6}$$

By substituting these into Equation C.5 the change in total pressure can be written in terms of the blade metal angles γ_R and γ_S:

$$\frac{\delta\left(P_{s,2}-P_{t,1}\right)}{\rho U}=-\delta C_x\left(\tan\alpha_R+\tan\alpha_S\right). \tag{C.7}$$

This basic relationship can be modified to describe the performance of the three-stage axial compressor. First, to express the pressure rise in terms of ψ_i, the downstream static pressure rise needs to be introduced:

$$P_{t\,exit} = P_{s\,exit} + \frac{\rho\left(\vec{V}\right)^2_{exit}}{2}. \tag{C.8}$$

The pressure rise across all three rotors can now be written in nondimensional form as

$$\delta\psi_i + \frac{\left(\vec{V}+\delta\vec{V}\right)^2_{exit} - \left(\vec{V}\right)^2_{exit}}{2U^2} = -\delta\phi\left(\tan\alpha_{R,1} + \tan\gamma + \tan\alpha_{R,2} + \tan\alpha_{S,1} + \tan\alpha_{R,3} + \tan\alpha_{S,2}\right). \tag{C.9}$$

Because velocity disturbances are small, the second order term $\delta\vec{V}^2$ can be ignored and the expression rewritten as

$$\frac{\delta\psi_i}{\delta\phi} = -\left(\phi\left(1+\left(\tan\alpha_{S,3}\right)^2\right) + \tan\alpha_{R,1} + \tan\gamma + \tan\alpha_{R,2} + \tan\alpha_{S,1} + \tan\alpha_{R,3} + \tan\alpha_{S,2}\right). \tag{C.10}$$

This is the same as the slope of the Euler pressure rise equation with respect to ϕ. The Euler compressor equation for the three-stage compressor was listed previously as Equation 3.2. The analytic expression derived here is used to define the slope $\frac{\partial\psi_i}{\partial\phi}$ in Models 3 and 4.

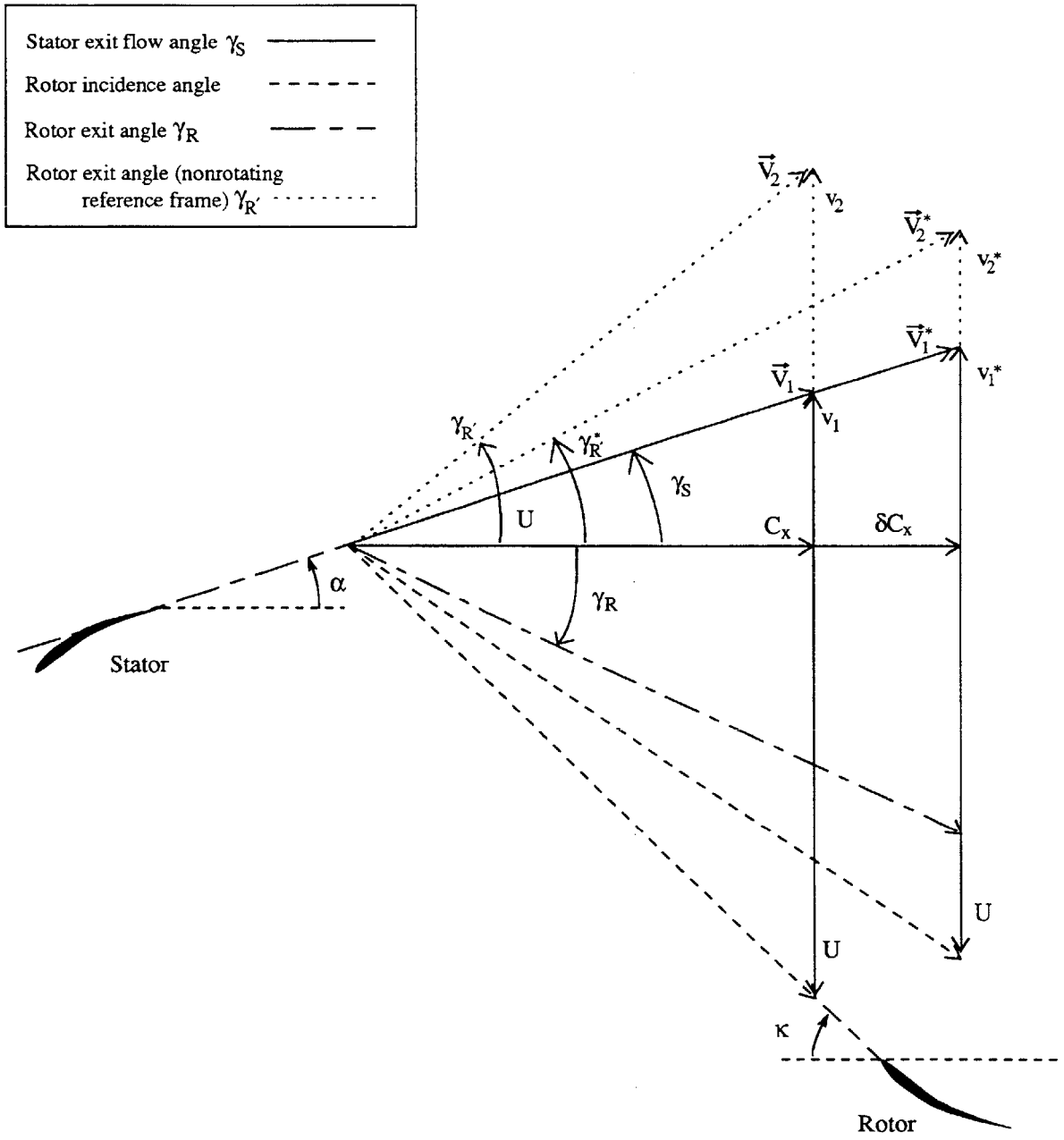

Figure C.1: Rotor Velocity Triangle